DTU Nanotech
Department of Micro- and Nanotechnology

Master Thesis, s021678

Acoustic forces on particles and liquids in microfluidic systems

Peder Skafte-Pedersen

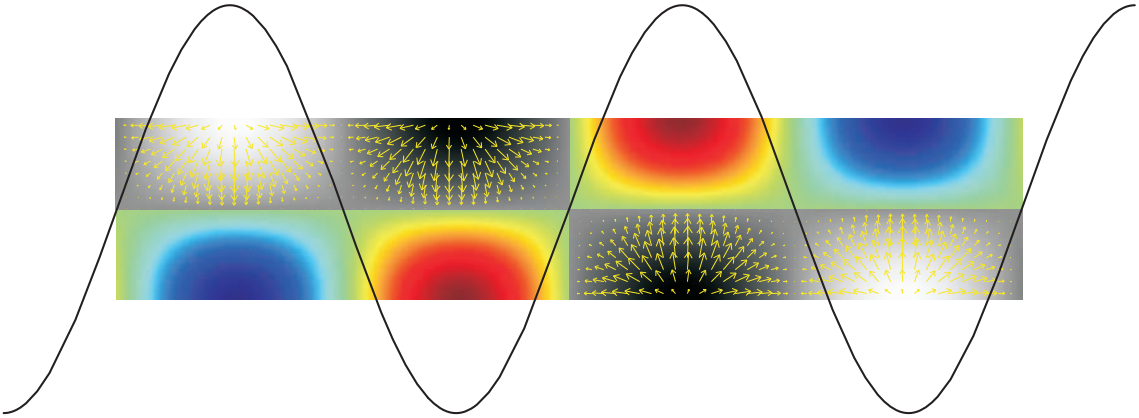

Supervisor: Henrik Bruus

Department of Micro- and Nanotechnology
Technical University of Denmark

31 January 2008

Abstract

Within the field of microfluidics and lab-on-a-chip systems there is an increasing demand for development of novel on-chip tools for particle handling and fluid control in the viscosity-dominated microflow regime. One approach exploits ultrasound in the MHz range, which is equivalent to wavelengths in the mm and sub-mm range well suited for mm-sized microsystems. Since the governing acoustofluidic equations are nonlinear the ultrasound gives rise to steady forces on fluids and particles through the two nonlinear effects known as acoustic streaming and acoustic radiation force, respectively.

In this thesis we treat the theoretical aspects of these two effects by analytical and numerical methods in order to examine and characterize the acoustofluidic dynamics of microfluidic systems at resonance. The fundamental approach is based on a perturbation method to second order.

Three different mechanisms based on viscous damping, boundary layers and transmission losses, respectively, are proposed as sources for the acoustic streaming. The two first have been treated, and by a thorough investigation of the structure of the governing equations it is shown that the contributions based on viscous damping can be neglected in resonance. The boundary layer theory has been shown to give a streaming velocity amplitude of the correct magnitude, but the analysis indicates that it cannot account for the spatial appearance of the experimental reference fields [1].

The acoustic radiation force have been determined in an inviscid approximation for various resonance modes in shallow microfluidic systems by 2D simulations in COMSOL based on first-order acoustic fields. When compared with experimental references [1, 2] we find a satisfactory qualitative correspondence between simulations and measurements for geometrically well-defined systems, allowing us to use the method as a design tool.

Resumé

Inden for mikrofluidik og dets anvendelse i lab-on-a-chip-systemer er der et stigende behov for udviklingen af nye integrerede værktøjer til håndtering og styring af partikler og væsker i det viskositetsdominerede mikrostrømningsregime. En mulighed er at benytte ultralyd i MHz-området, hvilket giver anledning til bølgelængder i størrelsesordenen mm til sub-mm, der er velegnet til brug i mm-skala mikrosystemer. Da de grundlæggende akustofluide ligninger er ikke-lineære, vil ultralyden give anledning til tidsuafhængige kræfter på fluider og partikler i form af de to ikke-lineære effekter kendt som henholdsvist akustisk strømning og akustisk strålingskraft.

I denne afhandling bliver de teoretiske aspekter af disse to effekter behandlet for at undersøge og karakterisere den akustofluide dynamik af systemer i resonans. Den grundlæggende fremgangsmåde bygger på en andenordens perturbationsmetode.

Tre forskellige mekanismer baseret på henholdsvist viskos dæmpning, grænselag, samt transmissionstab bliver foreslået som ophav til den akustiske strømning. De to første mekanismer bliver gennemgået, og ved en grundig analyse af de grundlæggende ligningers struktur er det påvist at bidrag hidrørende fra den viskose dæmpning kan negligeres i resonans. Grænselagsteorien viser sig at give korrekte estimater på størrelsen af den akustiske strømningshastighed, men analysen indikerer, at grænselagsteorien ikke kan redegøre for det rumlige udseende af det eksperimentelle referencefelt [1].

Den akustiske strålingskraft er blevet bestemt som en ikke-viskos tilnærmelse for forskellige resonanstilstande i et fladt mikrofluidsystem ved brug af 2D-simuleringer baseret på førsteordens akustiske felter i Comsol. Sammenligning med eksperimentelle referencer [1, 2] viser tilfredsstillende kvalitativ overensstemmelse mellem simuleringer og målinger for geometrisk veldefinerede systemer, hvorfor vi kan benytte fremgangsmåden som et designværktøj.

Preface

The present thesis is submitted as a fulfillment of the prerequisites for obtaining the Master of Science in Engineering degree at the Technical University of Denmark (DTU). The content is based on work carried out in the Theoretical Microfluidics (TMF) group at the Department of Micro- and Nanotechnology (DTU Nanotech) with a duration of one year from February 2007 corresponding to a credit of 50 ECTS points.

During the project many people have been of great help and inspiration for which I am very grateful. First of all I would like to thank my supervisor Henrik Bruus for outstanding supervision and inspiration, and for always having a few minutes or hours to discuss physics. Furthermore I would like to express my gratitude to Ph.D. student Melker Hagsäter for sharing his knowledge and experience on acoustic microsystems and for providing data and images, as well as to Ph.D. student Thomas Glasdam Jensen for providing me the results from his master project and several discussions on the theoretical issues. I have also had the privilege of being provided with experimental data, designs, ideas and experience for which I would like to acknowledge Ph.D. student Andreas Lenshof and prof. Thomas Laurell from Lund University as well as Ph.D. student Otto Manneberg and assoc. prof. Martin Wiklund from KTH, Stockholm. In the first phase of the project I benefitted from the discussions with B.Sc. students Julie Refsgaard Lawaetz and Sofie Sabine Rose Moth and help on piezoelectricity from M.Sc. student Jesper K. Olsen, which is highly appreciated. Moreover, I would like to thank the TMF group for good company and support and help whenever a problem had to be solved, as well as office mate Simon Jarlgaard, the rest of the office and DTU Nanotech for a positive working atmosphere. Finally I would like to acknowledge the Oticon Foundation for generous financial support allowing me to present some of the results at the 60^{th} Annual Meeting of the Division of Fluid Dynamics of The American Physical Society.

Peder Skafte-Pedersen
Department of Micro- and Nanotechnology
Technical University of Denmark
31 January 2008

Contents

List of Figures

List of Tables

List of symbols

Symbol	Description	Unit
ρ_i	i^{th}-order acoustic mass density	$\mathrm{kg\,m^{-3}}$
p_i	i^{th}-order acoustic pressure	$\mathrm{kg\,m^{-3}}$
v_i	i^{th}-order acoustic velocity	$\mathrm{m\,s^{-1}}$
$\mathbf{v}_i$	i^{th}-order acoustic velocity vector	$\mathrm{m\,s^{-1}}$
$\mathbf{J}_i$	i^{th}-order acoustic mass flux density	$\mathrm{kg\,m^{-2}\,s^{-1}}$
$\mathbf{r}$	Position vector	m
ϕ	Velocity potential	$\mathrm{m^2\,s^{-1}}$
U	Velocity amplitude	$\mathrm{m\,s^{-1}}$
ξ	Mechanical displacement	m
ℓ	Actuator amplitude	m
L	Domain length	m
δ_ν	Momentum diffusion length	m
λ	Wave length	m
$\mathbf{k}$	Wave vector	$\mathrm{m^{-1}}$
k	Wave number	$\mathrm{m^{-1}}$
k_0	Inviscid wave number	$\mathrm{m^{-1}}$
P	Power	$\mathrm{kg\,m^2\,s^{-3}}$
$\mathbf{F}_a$	Acoustic radiation force	$\mathrm{kg\,m\,s^{-2}}$
$\mathbf{F}$	Body force density	$\mathrm{kg\,m^{-2}\,s^{-2}}$
ω	Angular frequency	$\mathrm{s^{-1}}$
f	Frequency	$\mathrm{s^{-1}}$
η	Dynamic viscosity	$\mathrm{kg\,m^{-1}\,s^{-1}}$
ν	Kinematic viscosity	$\mathrm{m^2\,s^{-1}}$
c_a	Speed of sound	$\mathrm{m\,s^{-1}}$
κ	Adiabatic compressibility	$\mathrm{kg^{-1}\,m\,s^2}$
Y	Young's modulus	$\mathrm{kg\,m^{-1}\,s^{-2}}$
Q	Volume flow rate	$\mathrm{m^3\,s^{-1}}$
E	Energy density	$\mathrm{kg\,m^{-1}\,s^{-2}}$
Ψ	Radiation force potential	$\mathrm{kg\,m^2\,s^{-2}}$
$\mathbf{I}_a$	Acoustic intensity	$\mathrm{kg\,s^{-3}}$
$\boldsymbol{\omega}$	Vorticity	$\mathrm{s^{-1}}$
V	Volume	$\mathrm{m^3}$

Symbol	Description	Unit
Z_a	Acoustic impedance	$\mathrm{kg\,m^{-4}\,s^{-1}}$
z_s	Specific acoustic impedance	$\mathrm{kg\,m^{-2}\,s^{-1}}$
z_c	Characteristic impedance	$\mathrm{kg\,m^{-2}\,s^{-1}}$
τ	Characteristic time scale	s
ℓ_d	Characteristic dynamic length scale	m
$\varkappa$	Boundary decay number	$\mathrm{m^{-1}}$
S	Surface area	$\mathrm{m^2}$
t	Time	s
$\mathbf{n}$	Surface outward normal vector	
$\mathbf{t}$	Surface tangential vector	
$\hat{\mathbf{x}}$, $\hat{\mathbf{y}}$, $\hat{\mathbf{z}}$	Rectangular coordinate unit vectors	
$\hat{\boldsymbol{\theta}}$, $\hat{\boldsymbol{\varphi}}$, $\hat{\mathbf{r}}$	Spherical coordinate unit vectors	
ϑ	Wave number ratio	
α	Density ratio	
χ	Compressibility ratio	
ϵ	Main perturbation parameter	
γ	Viscous damping coefficient	
β	Bulk viscosity coefficient	
$\mathcal{R}_I$	Intensity reflection coefficient	
$\mathcal{T}_I$	Intensity transmission coefficient	
$\mathcal{C}$	Radiation coefficient	
$\mathcal{C}_\rho$	Density radiation coefficient	
$\mathcal{C}_\kappa$	Compressibility radiation coefficient	
$\mathcal{E}$	Separation efficiency	
N	Number of particles	
$\boldsymbol{\Gamma}$	Flux vector	
D	Degrees of freedom	
Ω	Computational domain	
$\partial\Omega$	Domain boundary	
∂_i	Partial derivative	
$\tilde{\cdot}$	Time-independent part of $\tilde{\cdot}\,\mathrm{e}^{-\mathrm{i}\omega t}$	
$\langle\cdot\rangle$	Time-average	
$\lvert\cdot\rvert$	Absolute value	
$\mathrm{Re}\{\cdot\}$	Real part	
$\mathrm{Im}\{\cdot\}$	Imaginary part	
i	Imaginary unit	
δ_{nl}	Kronecker delta	
l, m, n	Integer	
P_n	Legendre polynomial	
Re	Reynolds number	
St	Particle Stokes number	

Chapter 1

Introduction

1.1 Background

The field of lab-on-a-chip (LOC) systems is a relatively young research area combining microelectronics, fluid mechanics, optics, biotechnology and other scientific fields with the aim of developing small, fully integrated chemical and biochemical analysis systems on a single microchip. The motivation for development of LOC systems is that such devices have the potential to be considerably faster and simpler to use than conventional laboratories thereby eliminating the need for specialized operators as well as the required sample sizes are greatly reduced. Furthermore, a mass production of single-use chips results in cheap and reliable systems suitable for operation in the field.

However, the development of LOC systems is not a trivial task. Due to the miniaturization, these systems have a far higher surface to volume ratio than the equipment which is nowadays used in conventional laboratories leading to significant changes of the system dynamics. Thus, converting a macroscopic laboratory to a microscopic chip cannot be done simply by scaling down the system but involves rethinking most of the processes and tools. Therefore large efforts are being put into the development of a variety of novel micro components such as on-chip tools for handling of particles and liquids, integrated readout systems, temperature control and the like. This thesis deals with effects covering two of these areas, namely tools and methods for manipulation of particles and liquids, respectively, for which several techniques can be used.

Particle control is a generic term covering processes such as trapping, sorting and transport of particles and can for instance be carried out by magnetophoresis, electrophoresis or dielectrophoresis depending on the specific system. Although good results have been obtained using these techniques they generally have some common disadvantages. First of all they often demand integrated micro structured electrodes or magnetic materials, which complicates and adds costs to fabrication of the chips. Secondly they require the samples to have specific electric or magnetic properties and can due to the electromagnetic fields disrupt the properties of the particles, which is not desirable when one for instance wants to study kinetics of particles such as cells or other biological material in an unperturbed fluid environment.

Fluid control covers areas such as pumping, guiding and mixing fluids, which can be implemented with a variety of passive and active methods ranging from e.g. electroosmotic pumps [3] over micromechanic actuators [4] to geometrically induced mixing [5].

1.2 Acoustofluidics

In this thesis we will investigate another mechanism, namely acoustofluidics being the field dealing with acoustics and related fluid dynamic effects. In particular the two nonlinear effects, acoustic streaming and acoustic radiation force, will be considered.

Streaming is a phenomenon that occurs when sound waves transmitted through a viscous fluid give rise to a time-independent movement of the bulk fluid with a given streaming velocity. In LOC systems this can be used for either pumping or mixing fluids.

Acoustic radiation is a time-independent phenomenon arising in a sound field when particles or other obstacles are present, which thereby get affected by the radiation force. If the acoustic field is well controlled the radiation force can be used for gentle manipulation of cells and other particles in microfluidics.

Both acoustic streaming and radiation have as a physical phenomenon been known for a long time and was described by Faraday [6] followed by theoretical treatment initiated by Rayleigh [7] and King [8] for streaming and radiation, respectively. From the 1940s to 1960s the theoretical treatment of acoustic streaming and radiation was developed further and solved for special cases by amongst others Eckart [9], Markham [10–14], Nyborg [15–18] and Yosioka and Kawasima [19].

1.3 Experimental motivation

Within the past few years the field of acoustofluidics has gained increasing interest for applications in microfluidic systems. Examples of applications cover a variety of functions such as pumps [20], mixers [21–23], heaters [24] and manipulators for particle trapping [25–27] and sorting [28,29]. However, for these devices the majority of the reported results are predominantly based on purely experimental work with little emphasis on theory and modeling.

The systems we are interested in modeling are sketched in Fig. 1.1 and consist of an acoustically hard material often being silicon and glass [1] in which a microfluidic system is etched. This can consist of channels [29] or a combination of channels and resonator chambers [1] commonly filled with water or similar fluids with particles such as cells suspended herein. An external piezoelectric actuator is used to excite the resonance modes of the system giving rise to both radiation and streaming.

These type of systems have several advantages. First of all, by exploiting the resonance mode we are able to build up considerable acoustic amplitudes without requirements for a specific perfect acoustic coupling between chamber and actuator, which thereby do not need to be integrated in the system. This reduces the fabrication costs considerably. Secondly, the acoustic forces have been shown to be gentle towards biological samples and these systems are thereby suitable as a noninvasive tool for long term handling of cells [30].

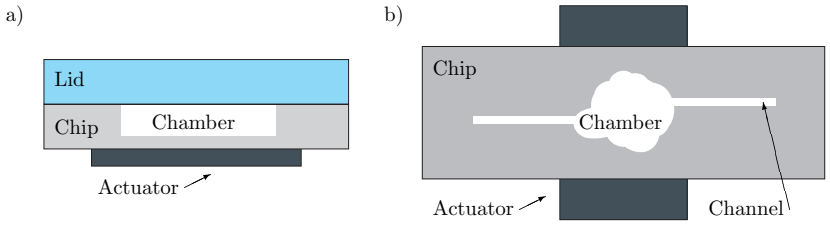

Figure 1.1: Sketch of an acoustic microfluidic resonator system. a) Side view showing a resonance chamber etched into the chip and bonded by a lid. Chip and lid are acoustically hard, commonly silicon and glass [1]. An external piezoelectric actuator clamped underneath the chip excites the resonance modes. b) Top view showing an arbitrarily shaped chamber with inlet and outlet channels. Fluidic access to channels can be made either through bottom or top of chip. The typical dimension are measured in millimeters for the lateral plane and hundreds of microns in chamber depth.

Finally, a resonance mode is typically very well-defined within a given geometry, which can be exploited when designing to obtain a specific acoustic field pattern.

As reference for the theoretical work we will use the paper by Hagsäter *et al.* [1], who have reported on experimental results of streaming and radiation as shown in Fig. 1.2. The two images a) and c) show both streaming and radiation forces occurring simultaneously for the same eigenmode, where the radiation force dominates large particles and the viscous streaming drag is dominating for the small particles as will be shown later. The utilized system is constructed as sketched in Fig. 1.1 where chambers and channels are etched into a 49×15 mm^2 silicon chip sealed by a glass lid. The chamber we will use for reference is a square with side length $L = 2$ mm etched $h = 200$ µm into the 500 µm thick silicon and connected to 400 µm wide channels with a length of 11.84 mm. Under normal operating conditions the wavelength λ obeys the condition $h < \lambda < L$, corresponding to frequencies of a few MHz.

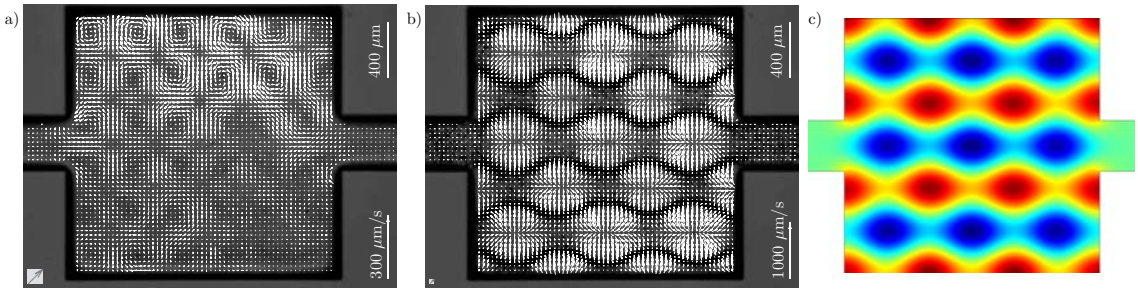

Figure 1.2: Experimental results obtained by particle image velocimetry (PIV) of a) acoustic streaming with 1 µm tracer beads and b) radiation forces on 5 µm beads. The radiation force pushes the large particles towards pressure nodal lines in a resonance mode at 2.17 MHz whereas the streaming dominates for small particles dragging these in a 6×6 vortex pattern. Both effects occur simultaneously, and a) and b) correspond to the same eigenmode illustrated by the simulation c) of the acoustic pressure at 2.23 MHz with arbitrary amplitude; red areas correspond to positive and blue to negative values. Images a) and b) courtesy of Hagsäter *et al.* [1].

Another system that will be used for comparison is a microfluidic separation device developed in the group of Thomas Laurell at Lund University [2, 28, 29, 31]. This will be described more thoroughly in Chap. 8.

1.4 Goal

The project upon which this thesis is based has been formulated in a very open manner with the objective of identifying and treating relevant theoretical issues related to acoustofluidics in resonant microfluidic systems rather than developing a specific LOC system.

Theoretical work has previously been done in this field by former MSc student Thomas Glasdam Jensen (TGJ) [32] with results applied to the specific microfluidic system shown in Fig. 1.2. In the thesis at hand, a thorough treatment of the theoretical background will be presented with the goal of extending the work of TGJ in order to develop general solution schemes suitable for modeling of arbitrarily shaped microfluidic systems operated at acoustic resonance. Both analytical analysis as well as methods and mathematical approaches convenient for implementation with numerical modeling tools will be treated for the computation of acoustic streaming and radiation forces. With such tools it will be possible to perform a systematic optimization of acoustically driven LOC systems, thereby reducing the need for time-consuming experimental trial-and-error development.

1.5 Outline

The work presented in the following is a selection of the work carried out during the master project and some aspects such as actuation models, energy considerations, various mathematical derivations and some simulation results have been left out for clarity. Besides the content of the present thesis the work also has also been presented by the following: a poster session at the Annual Meeting of the Danish Physical Society in June 2007, a contributed talk at the 60^{th} Annual Meeting of the Division of Fluid Dynamics of The American Physical Society in November 2007, a paper submitted to *Lab on a Chip* in February 2008 [2] as well as an accepted talk at the ASME Sixth International Conference on Nanochannels, Microchannels, and Minichannels in June 2008.

In this thesis we begin the by introducing the general theory in Chap. 2 leading from the basic governing equations to formulations suitable for the treatment of time-independent acoustofluidic problems based on a second-order perturbation scheme. With the exception of Sec. 2.4 most of the content of Chap. 2 can be found in various textbooks and papers and will be well-known to readers familiar with the field of second-order acoustofluidics.

In Chap. 3 a few classic examples and concepts of resonance and transmission with and without damping will be presented. Despite their simplicity these examples are very instructive for the understanding of acoustic wave behavior. The chapter is rounded off with a discussion of actuation models.

Having introduced the basic theoretical foundation we proceed to a treatment of the acoustic radiation force in Chap. 4. The chapter begins with the derivation of the gen-

eral radiation force equation and the solution for the force on small particles based on a condensed compilation of the theory presented in older and recent papers. The results are subsequently commented from a physical point of view with emphasis on the issues related to micro systems.

The acoustic streaming is the subject of Chap. 5, where we begin with an analysis based on the inviscid theory. The main part is dedicated to the development of a decomposition method to be used in numerical simulations as the mathematical structure of the acoustic fields do not allow for a direct computation of the streaming based on bulk dynamics. The chapter is finished with an introduction to the fundamentals of second-order boundary layer theory.

A part of more technical nature is given in Chap. 6, which, as a small guide, describes the implementation of physical problems in COMSOL MULTIPHYSICS^{TM} and comments on issues encountered during the implementation of acoustofluidic systems.

In Chap. 7 the theory and numerical methods from previous chapters are combined for the computation of streaming in resonating microfluidic systems. We will touch upon three different mechanisms for streaming whereof two are treated and commented more in-depth.

In order to give a perspective on the possibilities of acoustofluidics we apply some of the theoretical methods and results to a real device in Chap. 8, whereby we can compare theory with experiments.

The thesis is rounded off with a conclusion and outlook in Chap. 9.

Chapter 2

General acoustic theory

In the following the general theoretical foundation for acoustic effects will be given. The starting point is the basic governing equations from which the relevant acoustic equations and concepts will be derived based on a perturbation approach.

2.1 Governing equations

For the treatment of fluid dynamic problems a number of governing equations exist. In the following we will not consider thermal effects and our system can thus be described from conservation of momentum and mass.

The Navier–Stokes equation for conservation of momentum can be formulated in a variety of ways, and in this thesis we will use following formulation valid for a Newtonian, viscous, and compressible fluid [33],

$$\rho\left[\partial_t \mathbf{v} + (\mathbf{v}\cdot\boldsymbol{\nabla})\,\mathbf{v}\right] = -\boldsymbol{\nabla} p + \eta\nabla^2\mathbf{v} + \beta\eta\boldsymbol{\nabla}\left(\boldsymbol{\nabla}\cdot\mathbf{v}\right). \tag{2.1}$$

In contrast to many classical microfluidic problems in the low Reynolds number regime we will make use of both the nonlinear terms as well as compressibility, where the nonlinear terms will be the foundation for the nonlinear effects treated in the following chapters and the compressibility is a basic necessity for the propagation of sound. The value of the bulk viscosity $\beta\eta$ is not easily determined, but in the following we will use the coefficient value $\beta = 5/3$ in accordance with Stokes viscosity equation as described by Markham *et al.* [10]. This value is in reasonable agreement with measurements by e.g. Liebermann [34].

For the conservation of mass we employ the continuity equation being as follows for a compressible medium in a domain without source terms,

$$\partial_t \rho = -\boldsymbol{\nabla}\cdot(\rho\mathbf{v}). \tag{2.2}$$

Besides the conservation equations we will for acoustic problems also need a thermodynamic equation of state expressing pressure as a function of fluid density only [33, 35],

$$p = p(\rho). \tag{2.3}$$

If we assume the acoustic effects to be only minor variations to a quiescent system, pressure p, density ρ and particle velocity $\mathbf{v}$ can be described by a thermal equilibrium state $\{p_0, \rho_0, \mathbf{v}_0\}$ perturbed by higher order terms [15, 33],

$$p = p_0 + p_1 + p_2 + \dots \tag{2.4a}$$
$$\rho = \rho_0 + \rho_1 + \rho_2 + \dots \tag{2.4b}$$
$$\mathbf{v} = \mathbf{0} + \mathbf{v}_1 + \mathbf{v}_2 + \dots, \tag{2.4c}$$

where the last equality have presumed the quiescent zeroth-order state, i.e. $\mathbf{v}_0 \equiv \mathbf{0}$. With this nomenclature we can perform a second-order Taylor expansion of Eq. (2.3) around $p_0 = p(\rho_0)$ to get the following equation of state if only terms up to second order are included

$$p = p_0 + c_a^2\rho_1 + c_a^2\rho_2 + \frac{1}{2}(\partial_\rho c^2)_0\rho_1^2, \tag{2.5}$$

where the quantity c_a has been introduced. This, for an inviscid fluid, isentropic derivative,

$$c_a^2 \equiv \left(\frac{\partial p}{\partial \rho}\right)_s \tag{2.6}$$

is the speed of sound, which we for now consider a constant to first order.

For a dissipative system it will be shown that perturbation can be performed in two parameters formally written as

$$f = \sum_{m=0}^{\infty}\sum_{n=0}^{\infty}\epsilon^m\gamma^n g_{mn} \equiv \sum_{m=0}^{\infty}\sum_{n=0}^{\infty} f_{mn}, \tag{2.7}$$

where f is any of p, ρ and $\mathbf{v}$ and the main perturbation parameter ϵ and secondary perturbation parameter γ will be defined in the following. The last equality implies that from now on the perturbation parameters will not be explicitly stated as is neither done in Eqs. (2.4). Since ϵ is the leading parameter, the assignation first-order and second-order relate only to the order in ϵ, and often perturbation in γ is not performed in which case only one index will occur.

With the governing scale for the dynamics of propagation of sound in any medium being c_a, the main perturbation parameter ϵ must relate the velocity $\mathbf{v}$ of the particles to the governing velocity,

$$\epsilon \equiv \frac{|\mathbf{v}|}{c_a}, \tag{2.8}$$

where linearization demands $\epsilon \ll 1$. The secondary parameter γ, which will be derived in Sec. 2.3.1, is denoted the viscous damping coefficient as it depends on the viscous effects. For an inviscid system $\gamma = 0$ and inviscid quantities are therefore written as f_{m0}.

The first-order perturbations p_1, ρ_1, $\mathbf{v}_1$ or their inviscid counterparts p_{10}, ρ_{10}, and $\mathbf{v}_{10}$ are the quantities most often encountered in acoustics and give rise to the field of time-dependent linear acoustics. The terms of second order and higher lead to time-independent

effects with the most important being the acoustic radiation force and acoustic streaming, which will be the main subject of the thesis from Chap. 4 and onwards. Based on the perturbation ansatz in Eqs. (2.4) we can continue to derive the approximated governing equations up to second order, being the accuracy necessary and sufficient for treatment of acoustic streaming and radiation.

2.1.1 Perturbed governing equations

Inserting the series from Eqs. (2.4) into Eqs. (2.1), (2.2) and (2.3) yields the following when only keeping zeroth order-terms and remembering that $\mathbf{v}_0 = \mathbf{0}$,

$$\mathbf{0} = -\boldsymbol{\nabla} p_0 \tag{2.9}$$

$$\partial_t \rho_0 = 0 \tag{2.10}$$

$$p = p_0. \tag{2.11}$$

It is evident that the only solutions satisfying the governing equations to zeroth order, Eqs. (2.9), (2.10) and (2.11) are constant zeroth-order terms. As they do not depend on viscosity, only one index is necessary for zeroth-order terms.

A perturbation and linearization in ϵ to first order is readily seen to give the following first-order approximations of Eqs. (2.1), (2.2) and (2.3)

$$\rho_0 \partial_t \mathbf{v}_1 = -c_a^2 \boldsymbol{\nabla} \rho_1 + \eta \nabla^2 \mathbf{v}_1 + \beta \eta \boldsymbol{\nabla} (\boldsymbol{\nabla} \cdot \mathbf{v}_1) \tag{2.12}$$

$$\partial_t \rho_1 = -\rho_0 \boldsymbol{\nabla} \cdot \mathbf{v}_1 \tag{2.13}$$

$$p_1 = c_a^2 \rho_1. \tag{2.14}$$

It should be noticed that $\boldsymbol{\nabla} p_1$ is expressed in terms of ρ_1 using Eq. (2.5) and the constant zeroth-order terms have been pulled outside the differential operators.

Using the same approach the governing equations to second order become

$$\rho_0 \partial_t \mathbf{v}_2 = -\rho_1 \partial_t \mathbf{v}_1 - \rho_0 (\mathbf{v}_1 \cdot \boldsymbol{\nabla}) \mathbf{v}_1 - \boldsymbol{\nabla} p_2 + \eta \nabla^2 \mathbf{v}_2 + \beta \eta \boldsymbol{\nabla} (\boldsymbol{\nabla} \cdot \mathbf{v}_2) \tag{2.15}$$

$$\partial_t \rho_2 = -\rho_0 \boldsymbol{\nabla} \cdot \mathbf{v}_2 - \boldsymbol{\nabla} \cdot (\rho_1 \mathbf{v}_1) \tag{2.16}$$

$$p_2 = c_a^2 \rho_2 + \frac{1}{2} (\partial_\rho c^2)_0 \rho_1^2. \tag{2.17}$$

We now observe that both in the Navier–Stokes and the continuity equation, Eqs. (2.15) and (2.16), terms containing products of first-order quantities appear. For a harmonically driven system, that is time dependence $\cos \omega t$ or $\sin \omega t$, this will give rise to second-order terms with a doubled frequency but more importantly also a time-independent component as is realized from the following trigonometric identity,

$$(\cos \omega t)^2 = \frac{1}{2} \cos 2\omega t + \frac{1}{2}. \tag{2.18}$$

Thus, the governing equations indicate how first-order terms may give rise to steady second-order effects.

Although Eqs. (2.9) to (2.17) constitute the basic set of equations for the field of acoustofluidics it is profitable to reformulate them, which will be done in the following, where we begin with linear acoustics for inviscid fluids.

2.2 Linear acoustics without damping

If viscosity is neglected, the system will in our model be undamped and the first-order equations are

$$\rho_0 \partial_t \mathbf{v}_{10} = -\boldsymbol{\nabla} p_{10} = -c_a^2 \boldsymbol{\nabla} \rho_{10} \tag{2.19}$$

$$\partial_t \rho_{10} = -\rho_0 \boldsymbol{\nabla} \cdot \mathbf{v}_{10} \tag{2.20}$$

$$p_{10} = c_a^2 \rho_{10}, \tag{2.21}$$

where the Navier–Stokes equation has reduced to Euler's equation of motion [36].

We can now derive the linear wave equation for the first-order density by taking the divergence of Eq. (2.19) and subsequently exploit commutation between temporal and spatial differential operators,

$$\partial_t \boldsymbol{\nabla} \cdot (\rho_0 \mathbf{v}_{10}) = -c_a^2 \boldsymbol{\nabla} \cdot (\boldsymbol{\nabla} \rho_{10}), \tag{2.22}$$

Combining with Eq. (2.13) and utilizing $\boldsymbol{\nabla} \cdot \boldsymbol{\nabla} = \nabla^2$ we can now write

$$\partial_t (-\partial_t \rho_{10}) = -c_a^2 \boldsymbol{\nabla} \cdot (\boldsymbol{\nabla} \rho_{10}), \tag{2.23}$$

which is readily reduced to the linear wave equation in density for an inviscid fluid.

$$\partial_t^2 \rho_{10} = c_a^2 \nabla^2 \rho_{10}, \tag{2.24}$$

From Eq. (2.21) it is immediately realized that a corresponding wave equation exists for p_{10}. Similar manipulations with Eqs. (2.13), (2.14) and (2.19) give rise to a wave equation for $\mathbf{v}_{10}$ as follows. Taking the gradient of Eq. (2.20) and interchanging temporal and spatial operators we find

$$\partial_t \boldsymbol{\nabla} \rho_{10} = -\rho_0 \boldsymbol{\nabla} (\boldsymbol{\nabla} \cdot \mathbf{v}_{10}). \tag{2.25}$$

Substituting $\boldsymbol{\nabla} \rho_{10}$ from Eq. (2.19) gives

$$\partial_t \left(-\frac{\rho_0}{c_a^2} \partial_t \mathbf{v}_{10} \right) = -\rho_0 \boldsymbol{\nabla} (\boldsymbol{\nabla} \cdot \mathbf{v}_{10}), \tag{2.26}$$

which can be rewritten by use of the vector identity $\boldsymbol{\nabla} \times (\boldsymbol{\nabla} \times \mathbf{v}) = \boldsymbol{\nabla} (\boldsymbol{\nabla} \cdot \mathbf{v}) - \nabla^2 \mathbf{v}$,

$$\partial_t^2 \mathbf{v}_{10} = c_a^2 \left[\nabla^2 \mathbf{v}_{10} + \boldsymbol{\nabla} \times (\boldsymbol{\nabla} \times \mathbf{v}_{10}) \right]. \tag{2.27}$$

As $\mathbf{v}_{10}$ is a harmonic term with no time-independent component, $\mathbf{v}_{10}$ is irrotational as can be seen from Eq. (2.19). Therefore we can write up a vector wave equation for $\mathbf{v}_{10}$,

$$\partial_t^2 \mathbf{v}_{10} = c_a^2 \nabla^2 \mathbf{v}_{10}. \tag{2.28}$$

The three first-order quantities fulfil the same type of equation and it is therefore obvious to introduce a general scalar potential from which the pressure, density and velocity can

be derived. Since $\mathbf{v}_{10}$ is irrotational, it is permissible to express the velocity by a scalar potential

$$\mathbf{v}_{10} \equiv \boldsymbol{\nabla}\phi_{10}. \tag{2.29}$$

Inserting this in Euler's equation of motion Eq. (2.19) can after an integration and minor algebraic manipulation be shown to give

$$\rho_{10} = -\frac{\rho_0}{c_a^2}\partial_t\phi_{10}. \tag{2.30}$$

From the equation of state Eq. (2.14) we thus find

$$p_{10} = -\rho_0\partial_t\phi_{10}. \tag{2.31}$$

Eqs. (2.29), (2.30) and (2.31) now constitute the connection between all three first-order quantities and the first-order potential. By trivial algebra it is easy to show that the potential of course fulfills the wave equation

$$\partial_t^2\phi_{10} = c_a^2\nabla^2\phi_{10}. \tag{2.32}$$

2.2.1 Plane waves and the Helmholtz equation

One commonly encountered solution to Eq. (2.32) is the harmonic plane wave, which in complex notation can be expressed as

$$\phi_{10} = \phi_{10a}\mathrm{e}^{\mathrm{i}(\mathbf{k}_0\cdot\mathbf{r}-\omega t)} + \phi_{10b}\mathrm{e}^{\mathrm{i}(-\mathbf{k}_0\cdot\mathbf{r}-\omega t)}, \tag{2.33}$$

where ϕ_{10a} and ϕ_{10b} are amplitudes determined by the initial and boundary conditions, ω is the angular frequency, and $\mathbf{k}_0$ is the wave propagation vector. In order for Eq. (2.33) to be a valid solution, the following dispersion relation must be fulfilled,

$$\omega^2 = c_a^2|\mathbf{k}_0|^2 \tag{2.34}$$

$$\omega = c_a k_0. \tag{2.35}$$

The plane wave can be reformulated to the expression given as

$$\phi_{10} = \tilde{\phi}_{10}(\mathbf{r})\mathrm{e}^{-\mathrm{i}\omega t}, \tag{2.36}$$

where we have introduced the notation $f_{1n}(\mathbf{r},t) = \tilde{f}_{1n}(\mathbf{r})\mathrm{e}^{-\mathrm{i}\omega t}$, which will be used in the following. Inserting the solution Eq. (2.36) into Eq. (2.32) we find

$$\partial_t^2\tilde{\phi}_{10}(\mathbf{r})\mathrm{e}^{-\mathrm{i}\omega t} = c_a^2\nabla^2\tilde{\phi}_{10}(\mathbf{r})\mathrm{e}^{-\mathrm{i}\omega t}. \tag{2.37}$$

As the time-derivative for harmonic motion in complex notation becomes $\partial_t \rightarrow -\mathrm{i}\omega$, this leads to

$$-\omega^2\tilde{\phi}_{10}(\mathbf{r})\mathrm{e}^{-\mathrm{i}\omega t} = c_a^2\nabla^2\tilde{\phi}_{10}(\mathbf{r})\mathrm{e}^{-\mathrm{i}\omega t}, \tag{2.38}$$

which with the use of the dispersion relation, Eq. (2.35), gives the following,

$$\nabla^2 \tilde{\phi}_{10}(\mathbf{r}) = -k_0^2 \tilde{\phi}_{10}(\mathbf{r}). \tag{2.39}$$

This equation, which of course also applies to pressure, density, and velocity, is the Helmholtz equation and constitutes the basis for a classical eigenvalue problem with eigenvalues k_0^2. From the dispersion relation Eq. (2.35) the corresponding eigenfrequencies can be found. The Helmholtz equation will be widely used for determination of eigenmodes, i.e. resonance states, in a given system as will be shown later.

2.2.2 Energy and intensity

Besides knowledge of the three fields ρ_{10}, p_{10} and $\mathbf{v}_{10}$ it can also be beneficial to consider the energy inherent in a given acoustic field, which for instance will be seen in the treatment of the acoustic radiation force in Chap. 4. The kinetic energy density E_{kin} is given in terms of the particle velocity as

$$E_{\text{kin}} = \frac{1}{2}\rho_0 v_{10}^2. \tag{2.40}$$

The potential energy density E_{pot} stems from the energy stored due to compression and dilatation and can be found from

$$dE_{\text{pot}} = -\frac{p_{10} dV}{V}. \tag{2.41}$$

The potential energy density can thus be calculated as

$$E_{\text{pot}} = -\int_{V_0}^{V} \frac{p_{10}}{V} dV. \tag{2.42}$$

By exploiting the conservation of mass and the definition of the speed of sound Eq. (2.6) it can be shown that the first-order potential energy density can be expressed in terms of the pressure [35],

$$E_{\text{pot}} = \frac{1}{2}\frac{p_{10}^2}{c_a^2 \rho_0}. \tag{2.43}$$

Hereby the total acoustic energy density $E = E_{\text{kin}} + E_{\text{pot}}$ can now be written as

$$E = \frac{1}{2}\rho_0 \left[v_{10}^2 + \frac{p_{10}^2}{c_a^2 \rho_0^2} \right]. \tag{2.44}$$

Thus, kinetic energy has maximum at velocity maxima and potential energy at pressure maxima. In an un-attenuated standing wave, pressure and velocity are phase shifted by $\pi/2$ as will be shown in Chap. 3 and we thereby have maxima of kinetic and potential energy density at pressure nodes and antinodes, respectively.

As dissipation is not present in inviscid fluids, we can express conservation of energy through the energy density flux commonly encountered as the acoustic intensity $\mathbf{I}_a$ [36],

$$\partial_t E = -\boldsymbol{\nabla} \cdot \mathbf{I}_a. \tag{2.45}$$

Using the wave equation it is easy to show that the intensity can be expressed by the following pressure and velocity relation,

$$\mathbf{I}_a = p_{10}\mathbf{v}_{10}. \tag{2.46}$$

This quantity can be used in characterization of transmission phenomena as will be shown in Chap. 3.

2.3 Linear acoustics with damping

In the previous section we have neglected any damping to find the linearized wave and Helmholtz equations. This lossless assumption is applicable for wide range of acoustic applications, but in reality there will always be absorption due to e.g. viscosity, heat conduction and interactions with other domains [35] in a given system. In our model we will focus on dissipation caused by viscous effects.

The starting point for analyzing the impact of viscosity is the first-order Navier–Stokes equation given in Eq. (2.12). As in Sec. 2.2 we take the divergence of the momentum equation, now with inclusion of the viscous terms,

$$\rho_0 \partial_t \boldsymbol{\nabla} \cdot \mathbf{v}_1 = -c_a^2 \nabla^2 \rho_1 + \boldsymbol{\nabla} \cdot \left[\eta \nabla^2 \mathbf{v}_1 + \beta \eta \boldsymbol{\nabla} (\boldsymbol{\nabla} \cdot \mathbf{v}_1) \right]. \tag{2.47}$$

From the identity $\boldsymbol{\nabla} \cdot \boldsymbol{\nabla}(\boldsymbol{\nabla} \cdot \mathbf{v}) = \nabla^2(\boldsymbol{\nabla} \cdot \mathbf{v}) = \boldsymbol{\nabla} \cdot (\nabla^2 \mathbf{v})$ we obtain

$$\rho_0 \partial_t \boldsymbol{\nabla} \cdot \mathbf{v}_1 = -c_a^2 \nabla^2 \rho_1 + [1 + \beta]\, \eta \nabla^2 (\boldsymbol{\nabla} \cdot \mathbf{v}_1). \tag{2.48}$$

Exploiting the continuity equation Eq. (2.13) to replace $\boldsymbol{\nabla} \cdot \mathbf{v}_1$, we obtain a partial differential equation (PDE) in ρ_1,

$$\partial_t^2 \rho_1 = c_a^2 \nabla^2 \rho_1 + \frac{1}{\rho_0} [1 + \beta] \eta \nabla^2 (\partial_t \rho_1). \tag{2.49}$$

This is the modified wave equation for ρ_1 with viscosity taken into account. Combining the equation of state Eq. (2.14) with Eq. (2.49) we get the similar wave equation for the pressure p_1,

$$\partial_t^2 p_1 = c_a^2 \nabla^2 p_1 + \frac{1}{\rho_0} [1 + \beta] \eta \nabla^2 (\partial_t p_1), \tag{2.50}$$

whereas we in the general case cannot construct a modified wave equation for $\mathbf{v}_1$. This is only possible for the special case of irrotational velocity fields.

2.3.1 The lossy Helmholtz equation

If we in analogy with the inviscid case assume a harmonic solution of the form

$$p_1 = \tilde{p}_1(\mathbf{r})\mathrm{e}^{-\mathrm{i}\omega t}, \tag{2.51}$$

and insert this into the viscous wave equation Eq. (2.50) we readily find

$$\nabla^2 p_1 = -\frac{\omega^2}{c_a^2}\left[1 - \frac{\mathrm{i}(1+\beta)\eta\omega}{\rho_0 c_a^2}\right]^{-1} p_1. \tag{2.52}$$

This equation, which also holds for $\tilde{p}_1$, ρ_1, and $\tilde{\rho}_1$, is known as the lossy Helmholtz equation [35] and introduces the very important viscous damping coefficient γ,

$$\gamma \equiv \frac{(1+\beta)\eta\omega}{\rho_0 c_a^2}. \tag{2.53}$$

Considering the medium to be water under influence of ultrasonics in the low MHz range, we find from a quick order of magnitude estimation γ to be on the order of

$$\gamma \approx \frac{10^{-3}\ \mathrm{Pa\,s} \times 2\pi \times 10^6\ \mathrm{s}^{-1}}{10^3\ \mathrm{kg\,m}^{-3} \times 15^2 \times 10^4\ \mathrm{m}^2\,\mathrm{s}^{-2}} \approx 10^{-5}. \tag{2.54}$$

A series expansion of Eq. (2.52) is therefore applicable. To first order the Taylor expansion of $(1-x)^{-1}$ is $(1+x)$ and thereby we find

$$\nabla^2 p_1 \approx -p_1 \frac{\omega^2}{c_a^2}\left[1 + \mathrm{i}\gamma\right]. \tag{2.55}$$

By a second expansion we can make the following approximation leading to the modified Helmholtz equation,

$$\nabla^2 p_1 \approx -k_0^2\left[1 + \mathrm{i}\frac{\gamma}{2}\right]^2 p_1, \tag{2.56}$$

where k_0 is the wave number known from the undamped Helmholtz equation, Eq. (2.39). One solution to the modified Helmholtz equation is the damped plane traveling wave found directly from the corresponding inviscid solution by replacing k_0 with $k_0\left(1 + \mathrm{i}\frac{\gamma}{2}\right)$,

$$p_1 = a\mathrm{e}^{\mathrm{i}(k_0 x - \omega t)}\mathrm{e}^{-\frac{1}{2}k_0\gamma x}, \tag{2.57}$$

where a is a real pressure amplitude and we identify the exponential decay due to the damping term $\frac{1}{2}k_0\gamma$. Since the system is now dissipative it cannot be sustained without energy supply and is thus not suitable for eigenvalue determination without a driving force.

2.4 First-order analysis by double perturbation

From Eq. (2.29) we know that $\mathbf{v}_{10}$ can be expressed as a gradient. However, when including viscosity we cannot be sure that $\mathbf{v}_1$ is irrotational, and in that case we can instead choose to decompose $\mathbf{v}_1$ after a gradient and some remaining unknown velocity $\mathbf{v}_{1r}$. By algebraic manipulation we can show that in the general case $\mathbf{v}_1$ can be expressed by

$$\mathbf{v}_1 = \boldsymbol{\nabla}\phi_1 + \boldsymbol{\nabla} \times \mathbf{A}_1, \tag{2.58}$$

where $\mathbf{A}_1$ is a vector potential and ϕ_1 is given by

$$\phi_1 = -\frac{\mathrm{i}c_a^2(1-\mathrm{i}\gamma)}{\omega\rho_0}\rho_1. \tag{2.59}$$

That is, $\mathbf{v}_1$ can be decomposed after a scalar and vector potential as described by the fundamental theorem of vector calculus but without the demand for a decaying vector field or a restriction to a Lipschitz domain. The full derivation can be found in App. A.

Although decomposition can often be of help in mathematical analysis we can employ an even more powerful method for systems with low viscous damping. As Eq. (2.54) showed that γ is very low for the systems of interest and non-existing for inviscid systems it is a natural choice to use it as the perturbation parameter presented in Eq. (2.7). Due to the magnitude of γ we can safely discard terms of second order and higher in γ, whereby a double perturbation analogy to the series in Eqs. (2.4) can be obtained to first order in both ϵ and γ,

$$p = p_0 + p_{10} + p_{11} + \mathcal{O}(\epsilon\gamma^2) + \mathcal{O}(\epsilon^2) \tag{2.60a}$$

$$\rho = \rho_0 + \rho_{10} + \rho_{11} + \mathcal{O}(\epsilon\gamma^2) + \mathcal{O}(\epsilon^2) \tag{2.60b}$$

$$\mathbf{v} = \mathbf{0} + \mathbf{v}_{10} + \mathbf{v}_{11} + \mathcal{O}(\epsilon\gamma^2) + \mathcal{O}(\epsilon^2). \tag{2.60c}$$

2.4.1 Governing equations

From Sec. 2.2 we already know the governing equations to zeroth order in γ whereby we can deduce the following relation between velocity and density for harmonic fields

$$\mathbf{v}_{10} = -\frac{\mathrm{i}c_a^2}{\omega\rho_0}\boldsymbol{\nabla}\rho_{10}. \tag{2.61}$$

We now have to set up equations for determination of ρ_{11} and $\mathbf{v}_{11}$. The continuity equation to first order in ϵ is

$$\partial_t\rho_{10} + \partial_t\rho_{11} = -\rho_0\boldsymbol{\nabla}\cdot\mathbf{v}_{10} - \rho_0\boldsymbol{\nabla}\cdot\mathbf{v}_{11}. \tag{2.62}$$

The Navier–Stokes equation becomes

$$\rho_0\partial_t(\mathbf{v}_{10}+\mathbf{v}_{11}) = -c_a^2\boldsymbol{\nabla}(\rho_{10}+\rho_{11}) + \eta\nabla^2(\mathbf{v}_{10}+\mathbf{v}_{11}) + \beta\eta\boldsymbol{\nabla}(\boldsymbol{\nabla}\cdot(\mathbf{v}_{10}+\mathbf{v}_{11})). \tag{2.63}$$

As the terms $\eta\nabla^2\mathbf{v}_{11} + \beta\eta\boldsymbol{\nabla}(\boldsymbol{\nabla}\cdot\mathbf{v}_{11})$ are of the order $\mathcal{O}(\epsilon\gamma^2)$, we can discard these and thus the Navier–Stokes equation reduces to

$$\rho_0\partial_t(\mathbf{v}_{10}+\mathbf{v}_{11}) = -c_a^2\boldsymbol{\nabla}(\rho_{10}+\rho_{11}) + \eta\nabla^2\mathbf{v}_{10} + \beta\eta\boldsymbol{\nabla}(\boldsymbol{\nabla}\cdot\mathbf{v}_{10}). \tag{2.64}$$

Subtract the viscous and inviscid equations to get a pair of equations for $\mathbf{v}_{11}$ and ρ_{11}

$$\partial_t\rho_{11} = -\rho_0\boldsymbol{\nabla}\cdot\mathbf{v}_{11}, \tag{2.65}$$

for continuity and similarly for the Navier–Stokes equation

$$\rho_0\partial_t\mathbf{v}_{11} = -c_a^2\boldsymbol{\nabla}\rho_{11} + \eta\nabla^2\mathbf{v}_{10} + \beta\eta\boldsymbol{\nabla}(\boldsymbol{\nabla}\cdot\mathbf{v}_{10}). \tag{2.66}$$

Now, all terms are of the order $\epsilon\gamma$ and the force density $\mathbf{F}_{11}$ containing inviscid terms to be found from the inviscid Helmholtz equation is

$$\mathbf{F}_{11} \equiv \eta\nabla^2\mathbf{v}_{10} + \beta\eta\boldsymbol{\nabla}(\boldsymbol{\nabla}\cdot\mathbf{v}_{10}). \tag{2.67}$$

Hereby Eq. (2.66) reduces to the following linear PDE with a known body force density,

$$\rho_0\partial_t\mathbf{v}_{11} = -c_a^2\boldsymbol{\nabla}\rho_{11} + \mathbf{F}_{11}. \tag{2.68}$$

2.4.2 Structure of viscous parts

We know from Eq. (2.61) that $\mathbf{v}_{10}$ can be expressed by a gradient field. Inserting this into Eq. (2.67) we find after a minor algebraic work

$$\mathbf{F}_{11} = -\frac{\gamma\rho_0 c_a^2}{\omega}\boldsymbol{\nabla}\left[\nabla^2\left(\frac{\mathrm{i}c_a^2}{\omega\rho_0}\rho_{10}\right)\right], \tag{2.69}$$

where we have used the expression for γ given in Eq. (2.53). Combining this with Eq. (2.68) and employing the harmonic time-operator $\partial_t \to -\mathrm{i}\omega$ in conjunction with the Helmholtz equation, Eq. (2.39), for ρ_{10} can be shown to give

$$\mathbf{v}_{11} = -\frac{c_a^2}{\rho_0\omega}\boldsymbol{\nabla}\left(\mathrm{i}\rho_{11} + \gamma\rho_{10}\right) \tag{2.70}$$

and it is thus clear that with the secondary perturbation we have limited the first-order velocity to contain only gradient terms. Hereby $\mathbf{v}_1$ can be shown to fulfill a Helmholtz equation.

Alternatively we can isolate ρ_{11} by substituting the new expression for $\mathbf{v}_{11}$ into the continuity equation, Eq. (2.65) and using $\partial_t \to -\mathrm{i}\omega$ for harmonic fields,

$$\rho_{11} = -\frac{\mathrm{i}\rho_0}{\omega}\boldsymbol{\nabla}\cdot\left(-\frac{c_a^2}{\rho_0\omega}\boldsymbol{\nabla}\left(\mathrm{i}\rho_{11} + \gamma\rho_{10}\right)\right). \tag{2.71}$$

Using the Helmholtz equation for ρ_{10} together with the definition of the wave number Eq. (2.35) we find

$$\nabla^2\rho_{11} = -k_0^2\rho_{11} - \mathrm{i}\gamma k_0^2\rho_{10}, \tag{2.72}$$

which can be recognized as an inhomogeneous variant of the Helmholtz equation, where the eigenvalue problem has been transformed into an ordinary linear inhomogeneous differential equation.

A similar equation can be derived for $\mathbf{v}_{11}$, if we exploit $\boldsymbol{\nabla} \times \mathbf{v}_{11} = \mathbf{0}$ to rewrite the harmonic equivalent of Eq. (2.65),

$$\nabla^2 \mathbf{v}_{11} = \frac{\mathrm{i}\omega}{\rho_0} \boldsymbol{\nabla} \rho_{11} \tag{2.73}$$

Inserting this into the Navier–Stokes equation Eq. (2.66) and using that $\mathbf{v}_{10}$ is irrotational it is a trivial task to derive the following,

$$\nabla^2 \mathbf{v}_{11} = -k_0^2 \mathbf{v}_{11} - \mathrm{i}\gamma k_0^2 \mathbf{v}_{10}. \tag{2.74}$$

The equations presented in this section can in certain cases be used to determine the viscous solution to a corresponding inviscid field as will be demonstrated later.

2.4.3 First-order velocity in terms of density

By Eqs. (2.61) and (2.70) we have now shown that the entire first-order velocity $\mathbf{v}_1$ for low damping can be found from a scalar potential. Substituting $\mathbf{v}_1 = \boldsymbol{\nabla}\phi_1$ into the Navier–Stokes and continuity equation and combining these gives us for harmonic fields

$$-\mathrm{i}\omega\rho_0 \boldsymbol{\nabla}\phi_1 = -c_a^2 \boldsymbol{\nabla}\rho_1 + \frac{\mathrm{i}\omega\eta(1+\beta)}{\rho_0} \boldsymbol{\nabla}\rho_1. \tag{2.75}$$

By using the expression for γ defined in Eq. (2.53) and writing $\boldsymbol{\nabla}\phi_1 = \mathbf{v}_1$ we can hereby show that $\mathbf{v}_1 \propto \boldsymbol{\nabla}\rho_1$ to first order in ϵ and γ,

$$\mathbf{v}_1 = -\frac{\mathrm{i}c_a^2(1-\mathrm{i}\gamma)}{\rho_0\omega} \boldsymbol{\nabla}\rho_1. \tag{2.76}$$

This relation can be used in Chap. 5 for decomposition of the second-order equations.

2.5 Second-order acoustics without viscosity

With the Helmholtz equations derived in the previous sections we can, with suitable boundary conditions, determine the acoustic resonances in which our systems are to be driven. However, as we are interested in the time-independent acoustofluidic effects we must perturb to at least second order in ϵ. From Sec. 2.1 we know the governing equations to second order given by Eqs. (2.15), (2.16) and (2.17).

2.5.1 Second-order pressure

Neglecting viscosity gives us the following Navier–Stokes equation to second order,

$$\rho_0 \partial_t \mathbf{v}_{20} + \rho_{10} \partial_t \mathbf{v}_{10} + \rho_0 \left(\mathbf{v}_{10} \cdot \boldsymbol{\nabla}\right) \mathbf{v}_{10} = -\boldsymbol{\nabla} p_{20}. \tag{2.77}$$

In the inviscid case we are allowed to use the scalar potential ϕ_{10} introduced in Eq. (2.29). Expressing $\mathbf{v}_{10}$ and ρ_{10} in terms of ϕ_{10} we find

$$\rho_{10}\partial_t \mathbf{v}_{10} = -\frac{\rho_0}{c_a^2}\partial_t\phi_{10}\partial_t(\boldsymbol{\nabla}\phi_{10}). \tag{2.78}$$

As $\boldsymbol{\nabla}(\partial_t\phi_{10}\partial_t\phi_{10}) = 2\partial_t\phi_{10}\boldsymbol{\nabla}(\partial_t\phi_{10}) = 2\partial_t\phi_{10}\partial_t(\boldsymbol{\nabla}\phi_{10})$ we can rewrite Eq. (2.78) to

$$\rho_{10}\partial_t \mathbf{v}_{10} = -\frac{\rho_0}{2c_a^2}\boldsymbol{\nabla}\left(\partial_t\phi_{10}\right)^2. \tag{2.79}$$

Similarly we have, as $\mathbf{v}_{10}$ is irrotational, that

$$\rho_0(\mathbf{v}_{10}\cdot\boldsymbol{\nabla})\mathbf{v}_{10} = \frac{1}{2}\rho_0\boldsymbol{\nabla}\left|\boldsymbol{\nabla}\phi_{10}\right|^2. \tag{2.80}$$

Following Yosioka and Kawasima [19] $\mathbf{v}_{20}$ is irrotational in the inviscid case and can thus be expressed by a scalar potential ϕ_{20}. Hereby we can express $\boldsymbol{\nabla}p_{20}$ exclusively by scalar potentials by combining Eqs. (2.77), (2.79) and (2.80)

$$\boldsymbol{\nabla}p_{20} = -\rho_0\partial_t\boldsymbol{\nabla}\phi_{20} - \frac{1}{2}\rho_0\boldsymbol{\nabla}\left|\boldsymbol{\nabla}\phi_{10}\right|^2 + \frac{1}{2}\frac{\rho_0}{c_a^2}\boldsymbol{\nabla}(\partial_t\phi_{10})^2. \tag{2.81}$$

If we combine Euler's equation, Eq. (2.19), with Eq. (2.81) the first and second-order pressure gradients can now be expressed as

$$\boldsymbol{\nabla}p_{10} + \boldsymbol{\nabla}p_{20} = -\rho_0\left(\partial_t\boldsymbol{\nabla}\phi_{10} + \partial_t\boldsymbol{\nabla}\phi_{20}\right) - \frac{1}{2}\rho_0\boldsymbol{\nabla}\left|\boldsymbol{\nabla}\phi_{10}\right|^2 + \frac{1}{2}\frac{\rho_0}{c_a^2}\boldsymbol{\nabla}(\partial_t\phi_{10})^2. \tag{2.82}$$

As any deviation from the steady state is caused by the acoustic field, we can immediately remove the gradients to get the deviation $\delta p \equiv p_{10} + p_{20}$ from the static pressure p_0

$$\delta p = -\rho_0(\partial_t\phi_{10} + \partial_t\phi_{20}) - \frac{1}{2}\rho_0\left|\boldsymbol{\nabla}\phi_{10}\right|^2 + \frac{1}{2}\frac{\rho_0}{c_a^2}(\partial_t\phi_{10})^2. \tag{2.83}$$

This result will be the foundation for calculation of the acoustic radiation force in Chap. 4. We observe how the energy plays a role in the radiation force since the last two terms represent the difference of potential and kinetic energy densities.

2.5.2 Time-averaging

It is clear that we now have products of first-order terms in the expression for δp, which therefore contains time independent components as shown in Eq. (2.18) for a harmonically driven system. As we in general are only interested in the time-averaged second-order quantities it is a natural choice to time-average the governing equations, which will be used extensively in the coming sections. For harmonic first-order fields the time-average, which we denote with the notation $\langle\cdot\rangle$, is easily computed by [33],

$$\langle f_1 g_1\rangle = \frac{1}{2}\mathrm{Re}\left\{\tilde{f}_1\tilde{g}_1^*\right\}, \tag{2.84}$$

where f_1 and g_1 are any of the first-order fields with or without secondary perturbation in γ and the asterisk indicates complex conjugation.

Hereby the two first terms will vanish in the steady state system described by Eq. (2.83) when time-averaged and we can express the time-averaged second-order pressure as

$$\langle p_{20} \rangle = -\left\langle \frac{1}{2}\rho_0 \left|\boldsymbol{\nabla}\phi_{10}\right|^2 \right\rangle + \left\langle \frac{1}{2}\frac{\rho_0}{c_a^2}(\partial_t \phi_{10})^2 \right\rangle, \tag{2.85}$$

Eq. (2.85) shows us that in the inviscid case $\langle p_{20} \rangle$ can be determined directly from the first-order fields without the need for solving a second-order equation.

2.5.3 Streaming velocity and boundary conditions

When we refer to the term streaming velocity, the quantity in question is the time-averaged second-order velocity. Thus, we can restrict ourselves to treat the time-averaged governing equations. For a harmonically driven system in steady state any time-derivatives will vanish when time-averaged. Thus, in the inviscid case we deduce from Eqs. (2.16) and (2.77) the governing equations to be

$$\boldsymbol{\nabla} \cdot \langle \mathbf{v}_{20} \rangle = -\frac{1}{\rho_0}\boldsymbol{\nabla} \cdot \langle \rho_{10}\mathbf{v}_{10} \rangle \tag{2.86}$$

$$\langle \rho_{10}\partial_t \mathbf{v}_{10} \rangle + \langle \rho_0 \left(\mathbf{v}_{10} \cdot \boldsymbol{\nabla}\right)\mathbf{v}_{10} \rangle = -\langle \boldsymbol{\nabla} p_{20} \rangle . \tag{2.87}$$

Here we should notice two aspects; first of all we only need two governing equations in the time-averaged formulation since the second-order density does not figure in any of Eqs. (2.86) and (2.87). This simplifies matters as we now do not need to concern the unknown derivatives in Eq. (2.17). Secondly we find that $\langle \mathbf{v}_{20} \rangle$ does not figure in the Navier–Stokes equation and thus no direct coupling between $\langle p_{20} \rangle$ and $\langle \mathbf{v}_{20} \rangle$ exists in the inviscid case, which is not surprising as the second-order velocity can be ascribed to the momentum transfer due to viscous stress and attenuation.

Having in mind that we consider compressible media the velocity is not well-defined but should be based on the momentum being a more fundamental quantity [33]. Thus, our boundary conditions should also be applied to the momentum, which we can express through the mass flux density

$$\mathbf{J} \equiv \rho \mathbf{v}. \tag{2.88}$$

The time-averaged mass flux density to second order is given by

$$\langle \mathbf{J}_{20} \rangle \equiv \rho_0 \langle \mathbf{v}_{20} \rangle + \langle \rho_{10}\mathbf{v}_{10} \rangle , \tag{2.89}$$

and we now recognize the continuity equation, Eq. (2.86), in terms of the mass flux density as

$$\boldsymbol{\nabla} \cdot \langle \mathbf{J}_{20} \rangle = \mathbf{0}. \tag{2.90}$$

Analogous expressions to Eqs. (2.89) and (2.90) of course also holds for viscous fields. Using this convention we shall in Sec. 5.1 see that from the continuity equation we can actually get a streaming velocity even in the inviscid case as was also pointed out by Markham [11].

2.6 Second-order acoustics with viscosity

In order to couple the time-averaged Navier–Stokes and continuity equations we must include the effects of viscosity. The time-averaged Navier–Stokes and continuity equations are from Eqs. (2.15) and (2.16) found to be

$$\rho_0 \boldsymbol{\nabla} \cdot \langle \mathbf{v}_2 \rangle = -\boldsymbol{\nabla} \cdot \langle \rho_1 \mathbf{v}_1 \rangle \tag{2.91}$$

$$\boldsymbol{\nabla} \langle p_2 \rangle = -\langle \rho_1 \partial_t \mathbf{v}_1 \rangle - \rho_0 \langle (\mathbf{v}_1 \cdot \boldsymbol{\nabla}) \mathbf{v}_1 \rangle + \eta \nabla^2 \langle \mathbf{v}_2 \rangle + \beta\eta \langle \boldsymbol{\nabla} (\boldsymbol{\nabla} \cdot \mathbf{v}_2) \rangle \tag{2.92}$$

If we consider the two first terms on the right hand side of Eq. (2.92), these are known from the first-order solution and can thereby be considered a body force density driving the second-order system. To ease notation we therefore introduce the body force density $\mathbf{F}$. With common differentiation rules it is easily shown that

$$\rho_1 \partial_t \mathbf{v}_1 = \partial_t (\rho_1 \mathbf{v}_1) - \mathbf{v}_1 \partial_t \rho_1. \tag{2.93}$$

Using the first-order continuity equation Eq. (2.13) we thereby find

$$\rho_1 \partial_t \mathbf{v}_1 = \partial_t (\rho_1 \mathbf{v}_1) + \rho_0 \mathbf{v}_1 (\boldsymbol{\nabla} \cdot \mathbf{v}_1), \tag{2.94}$$

which is readily reduced to the following by time-averaging

$$\langle \rho_1 \partial_t \mathbf{v}_1 \rangle = \rho_0 \langle \mathbf{v}_1 (\boldsymbol{\nabla} \cdot \mathbf{v}_1) \rangle . \tag{2.95}$$

Hereby we can introduce the time-averaged body force density $\langle \mathbf{F} \rangle$ expressed in terms of the first-order velocity $\mathbf{v}_1$

$$\langle \mathbf{F} \rangle \equiv \rho_0 \langle \mathbf{v}_1 (\boldsymbol{\nabla} \cdot \mathbf{v}_1) \rangle + \rho_0 \langle (\mathbf{v}_1 \cdot \boldsymbol{\nabla}) \mathbf{v}_1 \rangle . \tag{2.96}$$

This can be inserted in Eq. (2.92), which now obviously appears as a linear partial differential equation with a known body force,

$$\boldsymbol{\nabla} \langle p_2 \rangle = -\langle \mathbf{F} \rangle + \eta \nabla^2 \langle \mathbf{v}_2 \rangle + \beta\eta \langle \boldsymbol{\nabla} (\boldsymbol{\nabla} \cdot \mathbf{v}_2) \rangle . \tag{2.97}$$

With the derivations made in the previous sections we now have the basic compilation of equations necessary for treating acoustic streaming and radiation in both viscous and inviscid cases. Before proceeding with more elaborate analysis of the second-order equations we shall now consider some examples of solutions to the basic first-order equations.

Chapter 3

First-order theory: Resonance and actuation

In the following the concepts of resonance and transmission will be introduced and demonstrated through simple instructive examples. These serve for an understanding of the general wave behavior in damped and undamped systems and can set a basis for development of more extensive actuator models.

3.1 Resonances in single-domain systems

3.1.1 Double actuation of inviscid 1D system

Let us consider how to model a microfluidic system excited by a piezoelectric actuator. If we as a first simple example consider a one-dimensional system, we could imagine that the actuator would give rise to a harmonic movement of the walls enclosing the fluidic domain in analogy to the approach in [33]. In Fig. 3.1 such a system is conceptually sketched, where the walls are assumed to move back and forth with opposite phase. By letting the maximum displacement of the walls be $\xi_{\max} = \ell$ we can for a harmonic actuation in complex notation choose that $\xi = \pm \mathrm{i}\ell \mathrm{e}^{-\mathrm{i}\omega t}$ at $x = \pm L$, respectively. Thus, the velocity of

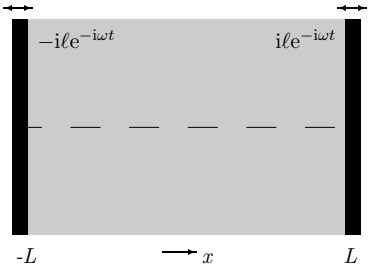

Figure 3.1: 1D system actuated by two actuators in anti phase with displacement $\xi = \pm \mathrm{i}\ell \mathrm{e}^{-\mathrm{i}\omega t}$ at $x = \pm L$, respectively. Figure adapted from [33].

the walls is easily found by differentiation in t to be

$$v_{\text{wall}} = \pm\omega\ell \mathrm{e}^{-\mathrm{i}\omega t}, \qquad x \in \partial\Omega. \tag{3.1}$$

As plane waves are generated by each wall the general solution to the inviscid wave equation in the domain can be formulated as a superposition of two plane waves propagating in opposite directions,

$$v_{10} = a\mathrm{e}^{\mathrm{i}(k_0 x - \omega t)} + b\mathrm{e}^{\mathrm{i}(-k_0 x - \omega t)}, \qquad x \in \Omega \tag{3.2}$$

where k_0 is the wave number given by Eq. (2.35), a and b unknown amplitudes, and v_{10} is a function of x and t only. If we assume total reflection at the walls, the two unknown coefficients can be determined from the boundary conditions stating continuity of the mass flux density at the walls. To first order this is equivalent to continuity in the velocity, and from Eqs. (3.1) and (3.2) we find the boundary conditions

$$-\omega\ell = a\mathrm{e}^{-\mathrm{i}k_0 L} + b\mathrm{e}^{\mathrm{i}k_0 L} \tag{3.3a}$$

$$\omega\ell = a\mathrm{e}^{\mathrm{i}k_0 L} + b\mathrm{e}^{-\mathrm{i}k_0 L}. \tag{3.3b}$$

These symmetric conditions are easily solved for a and b to give

$$a = -b = -\frac{\mathrm{i}\omega\ell}{2\sin k_0 L}, \tag{3.4}$$

and thereby we find the solution to be a standing wave expressed by

$$v_{10} = \omega\ell \frac{\sin k_0 x}{\sin k_0 L} \mathrm{e}^{-\mathrm{i}\omega t} \tag{3.5}$$

From Eq. (2.29) we can express the velocity potential ϕ_1 of Eq. (3.5) as

$$\phi_{10} = -\frac{\omega\ell}{k_0} \frac{\cos k_0 x}{\sin k_0 L} \mathrm{e}^{-\mathrm{i}\omega t} \tag{3.6}$$

and the pressure is readily found from Eq. (2.31)

$$p_{10} = -\mathrm{i}\rho_0 c_a^2 k_0 \ell \frac{\cos k_0 x}{\sin k_0 L} \mathrm{e}^{-\mathrm{i}\omega t} \tag{3.7}$$

By examination of Eqs. (3.5) and (3.7) it is observed that a resonance occurs for

$$k_0 L = m\pi, \qquad m \in \mathbb{N}, \tag{3.8}$$

where we in this undamped system have diverging pressure and velocity. This hints that if a microfluidic system is constructed in such a way that a resonant state can be created, wave patterns of significant magnitude can be established without strict demands for a well coupled actuator.

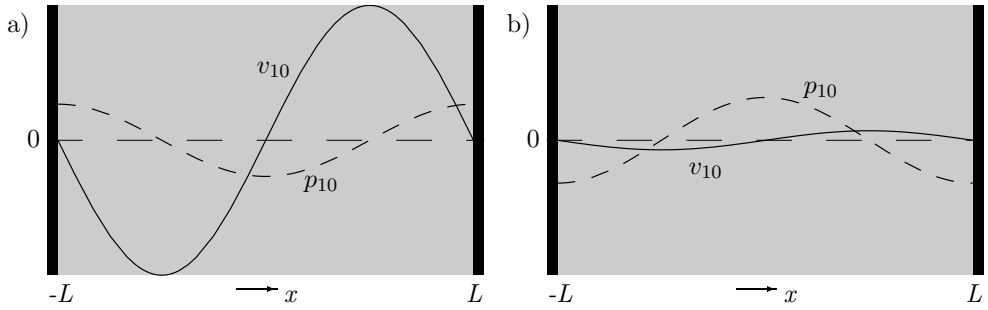

Figure 3.2: The doubly actuated system close to resonance at two different times in arbitrary units. Pressure is shown as a dashed line and velocity as a solid line.

Taking the real parts of Eqs. (3.5) and (3.7) to get the real physical velocity and pressure, we find

$$\mathrm{Re}\{v_{10}\} = \ell\omega \frac{\sin(k_0 x)}{\sin k_0 L} \cos(\omega t) \tag{3.9a}$$

$$\mathrm{Re}\{p_{10}\} = -\rho_0 c_a^2 k_0 \ell \frac{\cos(k_0 x)}{\sin(k_0 L)} \sin(\omega t), \tag{3.9b}$$

which for a frequency close to resonance can give the situation plotted in Fig. 3.2. As expected from basic acoustic theory [36] we find a $\frac{1}{2}\pi$ phase shift between pressure and velocity in both space and time resulting in zero time-averaged energy flux as deduced from Eqs. (2.46) and (2.84). Furthermore it is observed that close to resonance the velocity can be approximated by a standing wave with nodes at the ends similarly as is also the case for a closed resonator pipe.

3.1.2 Eigenmodes in non-actuated systems

Although resonance frequencies occur in the previous example we notice that the frequency can be chosen arbitrarily. If the walls on the other hand are either infinitely acoustically hard corresponding to zero velocity or infinitely soft corresponding to zero pressure we get the classic examples of a closed or open resonator.

Due to the homogeneous Dirichlet or Neumann conditions it is easy to show that waves in such a resonator has no defined amplitude but restrictions on the frequencies, which become quantized into a discrete eigenfrequency spectrum. This is the condition we will exploit from Chap. 6 and onwards for determination of eigenmodes fulfilling the Helmholtz equation Eq. (2.39). For now we will not solve for any eigenmodes but only notice that the eigenfrequencies can be estimated from the geometry, since the wavelengths in resonance approximately are fractions of the domain dimensions. Letting these be L_0, H_0 and W_0, the dispersion relation Eq. (2.35) can be exploited to make the estimate for resonance angular frequencies

$$\omega^2 = c_a^2 \left[\left(\frac{2l\pi}{L_0}\right)^2 + \left(\frac{2m\pi}{H_0}\right)^2 + \left(\frac{2n\pi}{W_0}\right)^2 \right], \qquad (l,m,n) \in \mathbb{N}. \tag{3.10}$$

Despite its simplicity this expression will in Chap. 8 be shown to be valuable for describing and analyzing the dynamics of a specific microfluidic device.

3.1.3 Actuation of viscous system

In a real microfluidic system the primary medium of concern is water and we do therefore have viscous damping in contrast to the example treated in Sec. 3.1.1. If we consider the same system with two actuators we can choose either to repeat the analysis using the governing viscous equations or we can exploit the similarity of the inviscid and lossy Helmholtz equations given by Eqs. (2.39) and (2.52).

We will apply the latter approach and define the viscous wavenumber k as

$$k \equiv \frac{\omega}{c_a\sqrt{1-\mathrm{i}\gamma}}, \tag{3.11}$$

whereby we can rewrite the lossy Helmholtz equation given by Eq. (2.52) to

$$\nabla^2 p_1 = -k^2 p_1. \tag{3.12}$$

Since this is structurally equivalent to the inviscid Helmholtz equation and we have justified $\boldsymbol{\nabla}\times\mathbf{v}_1 = \mathbf{0}$ in Eq. (2.76) for $\gamma \ll 1$ we can simply compute the viscous analogy to Eqs. (3.5) and (3.7) by replacing k_0 with k,

$$v_1 = \omega\ell\frac{\sin kx}{\sin kL}\mathrm{e}^{-\mathrm{i}\omega t} \tag{3.13a}$$

$$p_1 = -\mathrm{i}\rho_0 c_a^2 k\ell\frac{\cos kx}{\sin kL}\mathrm{e}^{-\mathrm{i}\omega t}, \tag{3.13b}$$

and it is seen that the solution still complies with the boundary condition Eq. (3.1). Due to the small magnitude of γ it is from Eq. (3.11) evident that the shift in resonance frequency caused by viscosity is inconsiderable and can with a good approximation be neglected. Hereby we maintain the resonance condition from Eq. (3.8) to a high accuracy, but with k being complex we can also deduce that the fields will not diverge at resonance as the sine term in the denominator is non-zero under these conditions.

For an easier perception of the structure of the viscous solution it is advantageous to turn to the series expanded Helmholtz equation in Eq. (2.56) from where we find $k^2 \approx k_0^2\left[1+\mathrm{i}\frac{\gamma}{2}\right]^2$. Inserting this in Eqs. (3.13) and expanding numerator and denominator to first order in γ gives us the approximation

$$v_1(x,t) \approx \omega\ell\frac{\sin k_0x + \mathrm{i}\frac{1}{2}\gamma k_0 x\cos k_0x}{\sin k_0L + \mathrm{i}\frac{1}{2}\gamma k_0 L\cos k_0L}\mathrm{e}^{-\mathrm{i}\omega t} \tag{3.14a}$$

$$p_1(x,t) \approx -\mathrm{i}\rho_0 c_a^2 k_0\ell\frac{\cos k_0x - \mathrm{i}\frac{1}{2}\gamma k_0 x\sin k_0x}{\sin k_0L + \mathrm{i}\frac{1}{2}\gamma k_0 L\cos k_0L}\mathrm{e}^{-\mathrm{i}\omega t}. \tag{3.14b}$$

Substituting the resonance wave number Eq. (3.8) for k_0 we can thereby determine the expected viscous fields at the desired operating condition

$$v_1 \approx \omega\ell(-1)^m \left[-\frac{2\mathrm{i}}{\gamma m\pi}\sin\left(\frac{m\pi}{L}x\right) + \frac{x}{L}\cos\left(\frac{m\pi}{L}x\right)\right] \mathrm{e}^{-\mathrm{i}\omega t} \tag{3.15}$$

$$p_1 \approx -\mathrm{i}\rho_0 c_a^2 \frac{m\pi}{L}\ell(-1)^m \left[\frac{2\mathrm{i}}{\gamma m\pi}\cos\left(\frac{m\pi}{L}x\right) + \frac{x}{L}\sin\left(\frac{m\pi}{L}x\right)\right] \mathrm{e}^{-\mathrm{i}\omega t}, \tag{3.16}$$

where we have exploited $\sin m\pi = 0$ and $\cos m\pi = (-1)^m$. It is now clear that a high but bounded amplitude on the order of

$$|v_1| \sim \left|\frac{\omega\ell}{\gamma}\right|, \tag{3.17}$$

is present at resonance as well as the $\frac{1}{2}\pi$ phase shift between pressure and velocity has been perturbed. Since the sine term dominates the velocity the major part of the this is equivalent to a standing wave at static walls and the moving wall boundary condition is fulfilled by the small phase shifted component.

Assuming the walls to be piezoelectric actuators the Ferroperm Pz27 types used by Hagsäter *et al.* [1] can be shown to have a typical unloaded displacement amplitude [37] of $\ell \sim 10^{-9}$ m. A quick order of magnitude estimate for the maximum velocity at a typical frequency in the low MHz range gives the following when using the value of γ from Eq. (2.54)

$$|v_1| \approx \frac{2\pi \times 10^6\ \mathrm{s}^{-1} \times 10^{-9}\ \mathrm{m}}{10^{-5}} \approx 6 \times 10^2\ \mathrm{m\,s}^{-1}. \tag{3.18}$$

Similarly the maximum resonance pressure can be estimated to be

$$|p_1| \approx \frac{10^3\ \mathrm{kg\ m}^{-3}\ 15^2 \times 10^2\ \mathrm{m}^2\,\mathrm{s}^{-2}\ 10^{-9}\ \mathrm{m}}{10^{-3}\ \mathrm{m} \times 10^{-5}} \approx 2 \times 10^8\ \mathrm{Pa}. \tag{3.19}$$

It first sight these amplitudes seem very large, and for comparison Nyborg [15] states reasonable first-order velocities to be on the order of $10^{-4}c_a$ in general, which is also in agreement with microfluidic experiments by Spengler *et al.* [38]. Thus, this naive boundary model exceeds the realistic acoustic amplitude with more than three orders of magnitude. Although taking viscous damping into account eliminates the divergence, the excessive first-order fields calls for the development of a better actuation model. Perspectives on this will be given in Sec. 3.3.

3.1.4 An example of an irrotational 2D solution

For acoustic modeling of microfluidic systems we must extend the theory to at least two dimensions. Using the square chamber in Fig. 1.2 as a basis we can approximate this with a simple 2×2 mm^2 square with hard walls at $(x, y) = (\pm L, \pm L)$. We will now determine if a physically prudent analytical irrotational velocity field can be found.

Strictly speaking the boundary conditions should for a viscous system be no-slip in $\mathbf{v}_1$ at all domain boundaries. But for an oscillating system the extent of a first-order boundary

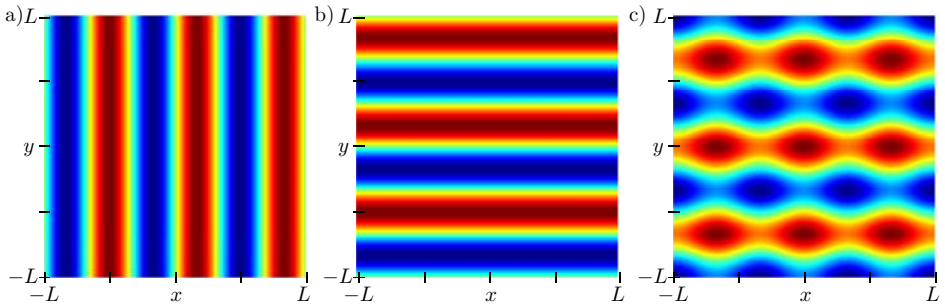

Figure 3.3: Surface plots of the dominating terms of the analytical first-order fields given by Eqs. (3.23a), (3.23b) and (3.24) at $t = 0$. a) shows v_{1x}, b) v_{1x}, and c) p_1 for an amplitude ratio of $r = 3$ and modenumber $m = 3$ corresponding to $f = 2.2$ MHz for a water filled chamber with $L = 10^{-3}$. The absolute amplitude is arbitrarily chosen, but their relative scaling follows Eqs. (3.23a), (3.23b) and (3.24). Red areas are local maxima and blue are minima.

layer is limited since the direction of the flow changes within each cycle. The thickness of the boundary layer can be given in terms of the momentum diffusion length δ_ν and is governed by the kinematic viscosity ν. In an oscillating flow the first-order boundary layer, which can be built up within half a cycle can thereby be estimated from [39],

$$\delta_\nu = \sqrt{\frac{2\nu}{\omega}}. \tag{3.20}$$

For frequencies in the low MHz range the momentum diffusion length of water will be

$$\delta_\nu \sim 10^{-6}\ \text{m}, \tag{3.21}$$

which is an insignificant correction to the overall first-order field. Hereby we can for the treatment of first-order bulk dynamics in a mm-sized chamber apply a less restrictive slip condition and determine the x- and y-velocities v_{1x} and v_{1y} solely from boundary conditions normal to their propagation direction.

In Jensen [32] the following simple set of boundary conditions are proposed to determine an analytical solution approximating the eigenmode shown in Fig. 1.2 c), which we will replicate,

$$v_{1x}(L) = \omega\ell \mathrm{e}^{-\mathrm{i}\omega t} \qquad v_{1x}(-L) = -\omega\ell \mathrm{e}^{-\mathrm{i}\omega t} \tag{3.22a}$$
$$v_{1y}(L) = r\omega\ell \mathrm{e}^{-\mathrm{i}\omega t} \qquad v_{1y}(-L) = -r\omega\ell \mathrm{e}^{-\mathrm{i}\omega t}, \tag{3.22b}$$

where ℓ is the wall displacement and r an arbitrary real amplitude factor. Since v_{1x} and v_{1y} can be solved independently of each other in this simple case, we can use the solution Eq. (3.13a) from the one-dimensional analysis directly and find for the velocity

$$v_{1x} = \omega\ell \frac{\sin kx}{\sin kL} \mathrm{e}^{-\mathrm{i}\omega t} \tag{3.23a}$$
$$v_{1y} = r\omega\ell \frac{\sin ky}{\sin kL} \mathrm{e}^{-\mathrm{i}\omega t}. \tag{3.23b}$$

The pressure field can be deduced from Eq. (3.12) in combination with Eqs. (3.23) and is easily found to be

$$p_1 = -\mathrm{i}\rho_0 c_a^2 k\ell \frac{1}{\sin kL} \left(\cos kx + r\cos ky\right) \mathrm{e}^{-\mathrm{i}\omega t}. \tag{3.24}$$

If, as in Jensen [32], the amplitude factor is chosen to $r = 3$ the dominating standing wave terms can be plotted as shown in Fig. 3.3, and we see a satisfactory correspondence between the simulation in Fig. 1.2 and the analytical solution. This solution will serve as our analytical reference mode in the coming chapters.

3.2 Wave propagation in multiple domains

A microfluidic device is of course not simply a chamber surrounded by infinitely hard boundaries but consists of a variety of materials through which sound waves can be transmitted. In the following will be given a few examples of the conditions and methods used to treat the more extended models. For simplicity viscous damping is neglected but the examples can be generalized with inclusion of damping mechanisms.

3.2.1 Impedance

For an easier treatment of transmission problems it can be an advantage to introduce impedance analysis. In general impedance is a measure of how a system responds to a given load and is used in several areas such as electronics, mechanics and acoustics. In acoustics, the basic definition of acoustic impedance Z_a is the ratio of complex sound pressure p_{10} to the surface integral over a surface S of the normal component of the particle velocity [36] and is an important measure used in transmission calculations,

$$Z_a \equiv \frac{p_{10}}{\int_S \mathbf{v}_{10} \cdot \mathbf{n} dS}. \tag{3.25}$$

This impedance is often used for analyzing the behavior of acoustic components such as wave guides, ducts and resonators [35].

Similarly we have the specific acoustic impedance z_s, which is not a function of the geometry of a given system but only the medium and wave type. This impedance is given by

$$z_s \equiv \frac{p_{10}}{v_{10}}. \tag{3.26}$$

If the wave is not depending on the coordinates over which the surface integral in Eq. (3.25) is evaluated, corresponding to e.g. plane or standing waves in a tube, we see that Eqs. (3.25) and (3.26) are related by

$$z_s = Z_a S. \tag{3.27}$$

For a plane wave we can easily find z_s, where we for simplicity consider a wave traveling in the positive x-direction, $v_{10} \propto \mathrm{e}^{\mathrm{i}k_0 x}\mathrm{e}^{-\mathrm{i}\omega t}$. Combined with the continuity equation, Eq. (2.13), we find

$$-\mathrm{i}\rho_0\omega v_{10} = -\mathrm{i}k_0 p_{10}. \tag{3.28}$$

Using the definition of specific impedance Eq. (3.26) we now get the important result

$$z_{s,\mathrm{plane}} = \rho_0 c_a \equiv z_c \tag{3.29}$$

This is a characteristic quantity of a given medium, which has been named the characteristic impedance, [35, 36] and will in the following be shown useful for description of transmission phenomena for plane waves, where transmission and reflection depend on the matching of characteristic impedances.

Other impedances such as radiation impedance [35] can also be encountered, but are left out as they are not of particular interest for this area of acoustics.

3.2.2 Traveling waves in two domains

A first step to develop more realistic acoustic models is to analyze how waves travel through several domains. The most classical example found in acoustics textbooks [35] is the situation outlined in Fig. 3.4, where two domains, A and B, have different speed of sound c_A, c_B and zeroth-order density ρ_{0A}, ρ_{0B} and thus different conditions for wave propagation.

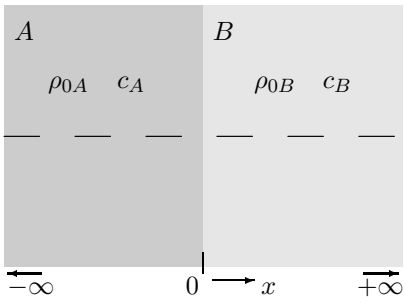

Figure 3.4: Two domains with different physical parameters affecting a wave traveling from domain A to B.

Letting a plane traveling wave propagate from A to B, it is evident that if domain B is not infinitely acoustically hard, a part of the incoming wave will be transmitted into B whereas the rest will be reflected. Assuming both domains to be infinitely long, we can now deduce that for normal incidence the wave in domain A can be described by a linear combination of left and right going plane waves, whereas only right going waves are present in domain B. In terms of a normalized velocity potential we can thus state

$$\phi_{10A}(x,t) = \mathrm{e}^{\mathrm{i}(k_{0A}x-\omega t)} + a\mathrm{e}^{\mathrm{i}(-k_{0A}x-\omega t)} \tag{3.30a}$$

$$\phi_{10B}(x,t) = b\mathrm{e}^{\mathrm{i}(k_{0B}x-\omega t)}, \tag{3.30b}$$

where the two unknown coefficients a and b are to be determined from the boundary conditions.

Considering the two domains to be fluids we must to first order require continuity in the normal velocity in order for the fluids to stay in contact at all times and secondly continuity in pressure as to avoid a net force on the interface. From Eqs. (2.29) and (2.31) we know the relation between potential, pressure and velocity, so the boundary conditions can readily be written as,

$$\partial_x \phi_{10A}(0,t) = \partial_x \phi_{10B}(0,t) \tag{3.31}$$

$$\rho_{0A} \partial_t \phi_{10A}(0,t) = \rho_{0B} \partial_t \phi_{10B}(0,t). \tag{3.32}$$

Inserting the general wave functions from Eqs. (3.30) we find that continuity in velocity and pressure gives rise to the following amplitude relations

$$1 - a = \frac{k_{0B}}{k_{0A}} b \tag{3.33}$$

$$1 + a = \frac{\rho_{0B}}{\rho_{0A}} b. \tag{3.34}$$

Eqs. (3.33) and (3.34) are easily solved for the reflection and transmission amplitudes a and b and using the fact, that the wave number can be written in terms of the sound velocity in a domain X

$$k_{0X} = \frac{\omega}{c_X}, \tag{3.35}$$

where c_X is the speed of sound in domain X and ω is the same in all domains, we find

$$a = \frac{z_{cB} - z_{cA}}{z_{cA} + z_{cB}}, \tag{3.36a}$$

$$b = \frac{2 z_{cB}}{z_{cA} + z_{cB}} \frac{\rho_{0A}}{\rho_{0B}}. \tag{3.36b}$$

This simple example, shows us how phase shifts of π in the reflected wave can be induced depending on the ratio of the specific impedances. Another measure of the transmission than the coefficients a and b can be given by defining the intensity reflection and transmission coefficients $\mathcal{R}_I$ and $\mathcal{T}_I$ [35],

$$\mathcal{R}_I \equiv \frac{\left\langle I_{a,r} \right\rangle}{\left\langle I_{a,i} \right\rangle}, \qquad \mathcal{T}_I \equiv \frac{\left\langle I_{a,t} \right\rangle}{\left\langle I_{a,i} \right\rangle}, \tag{3.37a}$$

where indices, r, i and t refer to reflected, incident and transmitted wave, respectively. From the definition of acoustic intensity Eq. (2.46) and the potential amplitudes Eqs. (3.36) we can calculate

$$\mathcal{R}_I = \left(\frac{z_{cB} - z_{cA}}{z_{cA} + z_{cB}} \right)^2 \tag{3.38}$$

$$\mathcal{T}_I = \frac{4 z_{cA} z_{cB}}{\left(z_{cA} + z_{cB} \right)^2}. \tag{3.39}$$

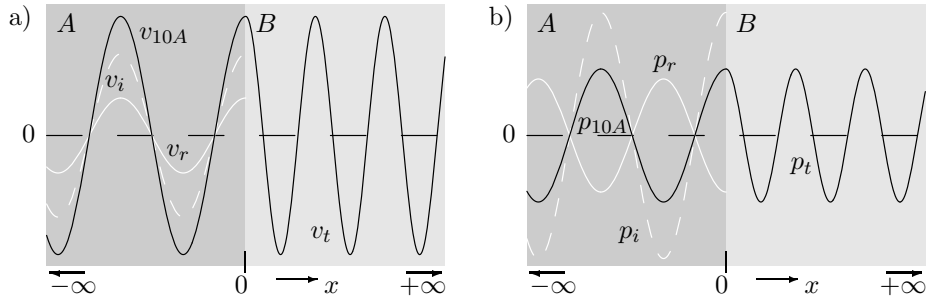

Figure 3.5: The velocity and a) pressure b) distribution in a system where a plane traveling wave is sent into the interface from the left. Incident waves p_i, v_i are dashed and white whereas reflected waves are solid white. The resulting waves v_{10A} and p_{10A} are black and we observe that these obey the boundary conditions.

Upon inspection we see that the intensity as expected is conserved since $\mathcal{R}_I + \mathcal{T}_I = 1$. The physical consequence of these results can easily be interpreted by examining a few limiting cases. If the two domains are occupied by the same material it is evident that we have full transmission as the boundary is acoustically nonexisting. Likewise if e.g. $c_B \to 0$, we do not have transmission, but full reflection resulting in a standing wave in domain A.

With the coefficients we can now plot the pressure and velocity as done in Fig. 3.5, where the real, physical part is visualized. The continuity of both pressure and velocity is clearly seen, and we also observe that the reflected pressure wave have a phase shift of π relative to the incoming wave as opposed to the velocity since $z_{cA} > z_{cB}$. Furthermore we notice that the pressure and velocity are no longer $\frac{1}{2}\pi$ out of phase as in a classic inviscid resonator since the reflection surface is not perfectly hard and the domains are infinite.

For a microsystem of the type presented in Fig. 1.1 the typical acoustic material parameters will be the ones shown in Table. 3.1 from where we notice a significant mismatch in the characteristic impedance the domains in between. From Eq. (3.39) we can estimate the transmission coefficients from water to silicon and silicon to air as $\mathcal{T}_{I,\mathrm{w}\to\mathrm{s}} = 0.26$ and $\mathcal{T}_{I,\mathrm{s}\to\mathrm{a}} = 8.0 \times 10^{-5}$, which is an indication of good resonance properties.

Property	ρ_0	c_a	z_c
Unit	$\mathrm{kg\,m^{-3}}$	$\mathrm{m\,s^{-1}}$	$\mathrm{kg\,m^{-2}\,s^{-1}}$
Silicon	2331	8490	1.98×10^7
Water	998	1483	1.48×10^6
Air	1.161	343.4	397

Table 3.1: Material parameters for water silicon and air. Conditions are T=300 K and p_0=10^5 Pa for air and T = 20°C for water and silicon. Values for water and air from [40] and for silicon from [32]. Specific impedance is calculated by $z_c = \rho_0 c_a$.

3.2.3 Transmission through a domain

The previous example can of course be generalized to include several domains. However the overall method for solving the systems is the same, namely to set up the general solutions to the wave equation in each domain and solve the coupled system by continuity in pressure and velocity.

We finish off our transmission examples by a small instructive demonstration of the consequences of placing a foreign object in a standing wave field. The general geometry resembles the initial resonator example with two actuators. Now, however, a sheet of a different material with width d has been placed a distance h from the center of the system thus dividing it into three domains A, B and C as seen in Fig. 3.2, where A and C are of the same material.

In all three domains we now have the general solution as a linear combination of two plane traveling waves which in terms of complex potentials can be written as

$$\phi_{1A} = a_A \mathrm{e}^{\mathrm{i}(k_{0A}x-\omega t)} + b_A \mathrm{e}^{\mathrm{i}(-k_{0A}x-\omega t)} \tag{3.40}$$

$$\phi_{1B} = a_B \mathrm{e}^{\mathrm{i}(\vartheta k_{0A}x-\omega t)} + b_B \mathrm{e}^{\mathrm{i}(-\vartheta k_{0A}x-\omega t)} \tag{3.41}$$

$$\phi_{1C} = a_C \mathrm{e}^{\mathrm{i}(k_{0A}x-\omega t)} + b_C \mathrm{e}^{\mathrm{i}(-k_{0A}x-\omega t)}, \tag{3.42}$$

where we have introduced the wave number ratio $\vartheta \equiv k_B/k_A$. The problem can be solved by the pressure and velocity continuity conditions at $x = h$ and $x = h + d$ and the known velocity at the actuators at $x = \pm L$, but since the solution process is trivial and the results not easily interpretable we restrict the results to the plots shown in Fig. 3.6.

From Fig. 3.6 a) it can be seen that the introduction of a relatively large piece of foreign material heavily changes the standing wave. If we on the other hand decrease the thickness of the slab the system converges towards the initial resonance without foreign objects.

This example illustrates how it can be expected that the introduction of a small amount of particles or cells in a microfluidic resonator system will not change the dynamics of the system. The examples in Fig. 3.6 are of course only a qualitative demonstration of

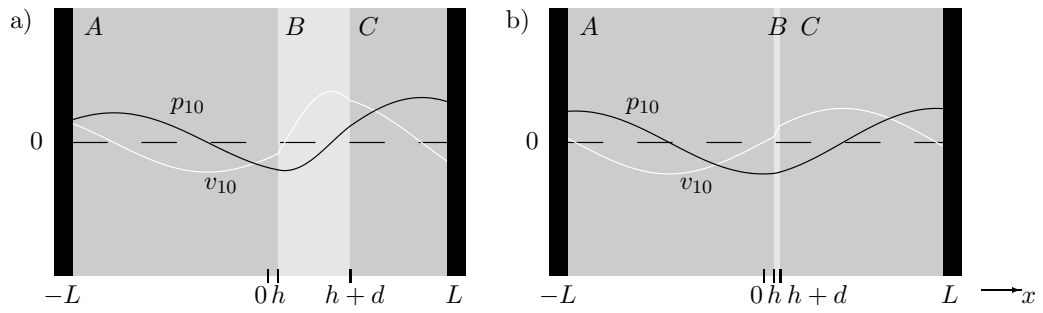

Figure 3.6: A doubly actuated system with a homogeneous domain, A and C, separated by a slab, B, of different material. The system is actuated at a frequency corresponding to resonance of a chamber without slab. For the thin slab the situation depicted in Fig. 3.2 is approached. Pressure is shown as the solid black line and velocity as the solid white line. Amplitudes are arbitrary.

the mechanism, but if one is to handle a dense concentration of particles in a confined microsystem it might be worth estimating if the resonance mode will be significantly affected.

3.3 Approaches for improved actuation models

In Eqs. (3.18) and (3.19) we found the amplitude of the resonating system to be far higher than physically reasonable since we assumed the piezoelectric actuator to be both perfectly coupled and lossless as well as able to deliver its unloaded displacement into a system at resonance. None of these simplifications hold in the real life, however, and better models are to be made if we want a more precise estimate of the amplitude.

During the project various methods and models have been proposed and investigated. The most simple approaches include combined displacement and pressure restrictions as well as limitations on the actuator power. Another model based on a force driven mechanical actuator can be found in App. B.

Finally a complete 1D model was developed coupling various domains governed by both inviscid and viscous wave equations to an air backed piezoelectric actuator domain governed by a wave equation covering mechanical and electrodynamic effects. Hereby it was from frequency sweeps possible to establish a direct correlation between the applied actuator voltage and acoustic resonance amplitudes. By varying the number and geometry of layers to simulate different coupling properties through amongst other things an air film and ultrasonics gel the model did show that coupling issues from the actuator to the resonating chamber can reduce the amplitude to the reported values [15,38] and even lower.

Although the model contains quite an amount of interesting physics we will not describe it here since it is a bit too extensive to be covered briefly and not of importance for the following chapters as it can primarily be used for determination of the amplitude. In the remainder of the thesis we will therefore simply assume a first-order velocity amplitude of $|\mathbf{v}_1| \sim 10^{-4} c_a$, which will be compared to experimental results in Chap. 8.

Having described the general first-order wave dynamics in viscous systems, we can now proceed to the second-order effects.

Chapter 4

Second-order theory: Radiation force

In literature one often finds the terms acoustic radiation pressure and radiation force. Unfortunately the nomenclature is not clear and in some cases the radiation pressure refers to the second-order pressure p_2 and other times to the hereto connected steady forces exerted on objects [8,19,41–43]. In this thesis we use the term second-order pressure to describe p_2, acoustic radiation as a general phenomenological term, and radiation force for the actual force.

In the following the general expression for the steady state radiation force on deformable free floating objects in an inviscid fluid will be derived. The derivation is accurate to second order in pressure and velocity and follows the theory initially outlined by King [8] in 1934 and extended to compressible objects by Yosioka and Kawasima [19] in 1955. However, as was later pointed out by Hasegawa *et al.* [42] in 2000 the early papers have some lacks of amongst other things on the continuity of argumentation and derivation of the general expressions, some of which will be taken into account in the following based on [42].

4.1 Radiation force on objects in general

The time-averaged acoustic radiation force $\langle \mathbf{F}_a \rangle$ on an object in the acoustic field is found by integrating the pressure over its surface. If the object is freely suspended in the liquid, the surface will oscillate in time due to the first-order pressure and the surface S to be integrated over is thus a function of time,

$$\langle \mathbf{F}_a \rangle = \left\langle -\int_{S(t)} \delta p \mathbf{n} dS \right\rangle, \tag{4.1}$$

where $\mathbf{n}$ is the outwards normal vector of the object and δp is the excess pressure defined in Eq. (2.83). From Eq. (2.83) we thereby get the force

$$\begin{aligned}\langle \mathbf{F}_a \rangle = &\left\langle \int_{S(t)} \rho_0 \partial_t \phi_{10} \mathbf{n} dS \right\rangle + \left\langle \int_{S_0} \rho_0 \partial_t \phi_{20} \mathbf{n} dS \right\rangle \\ &+ \frac{1}{2}\rho_0 \left\langle \int_{S_0} |\boldsymbol{\nabla}\phi_{10}|^2 \mathbf{n} dS \right\rangle - \frac{1}{2}\frac{\rho_0}{c_a^2} \left\langle \int_{S_0} (\partial_t \phi_{10})^2 \mathbf{n} dS \right\rangle . \end{aligned} \tag{4.2}$$

As the integrands in the last terms are of second order it is sufficient to integrate these over the equilibrium position S_0. Furthermore we readily observe for a system in steady state

$$\left\langle \int_{S_0} \rho_0 \partial_t \phi_{20} \mathbf{n} dS \right\rangle = \mathbf{0}, \tag{4.3}$$

as the integration domain is time-independent, which leaves three integrals to be evaluated.

4.1.1 The Reynolds transport theorem

In order to evaluate the first integral with both time-dependent integrand and surface in Eq. (4.2) we can exploit the Reynolds transport theorem, which is often encountered in fluid mechanics, see e.g. White [44].

Consider an arbitrary property ς in a volume V dependent on time as shown in Fig. 4.1. By a limiting process we can find the time change of the system as

$$\frac{d}{dt}\int_{V(t)} \varsigma(t) dV = \lim_{\delta t \to 0} \left(\frac{\int_{V(t+\delta t)} \varsigma(t+\delta t) dV - \int_{V(t)} \varsigma(t) dV}{\delta t} \right), \tag{4.4}$$

where we can rewrite the right hand side as follows

$$\lim_{\delta t \to 0} \left(\frac{\int_{V(t+\delta t)} \varsigma(t+\delta t) dV - \int_{V(t)} \varsigma(t) dV - \int_{V(t)} \varsigma(t+\delta t) dV + \int_{V(t)} \varsigma(t+\delta t) dV}{\delta t} \right). \tag{4.5}$$

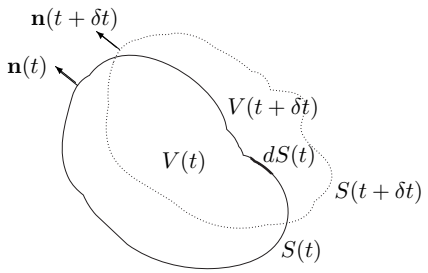

Figure 4.1: Arbitrary volume V with surface S and surface element dS at times t and $t+\delta t$ for derivation of Reynolds transport theorem.

As the second and fourth term in Eq. (4.5) have the same integration limit, these can be rewritten to a differentiation inside the integral,

$$\lim_{\delta t\to 0}\left(\frac{\int_{V(t)}\varsigma(t+\delta t)dV-\int_{V(t)}\varsigma(t)dV}{\delta t}\right)=\int_{V(t)}\partial_t\varsigma(t)dV. \tag{4.6}$$

The two remaining integrals have a common integrand and can thus be combined to a single integral by changing integration limits

$$\lim_{\delta t\to 0}\left(\frac{\int_{V(t+\delta t)}\varsigma(t+\delta t)dV-\int_{V(t)}\varsigma(t+\delta t)dV}{\delta t}\right)=\lim_{\delta t\to 0}\left(\frac{\int_{V(t+\delta t)-V(t)}\varsigma(t+\delta t)dV}{\delta t}\right). \tag{4.7}$$

It is now convenient to express the volume element dV in terms of the fluid inflow. If fluid is allowed to enter and leave the volume, the change will, by a normal velocity $\mathbf{v}\cdot\mathbf{n}$ be given by

$$dV=V(t+\delta t)-V(t)=\mathbf{v}\cdot\mathbf{n}\delta t dS, \tag{4.8}$$

where dS is the surface element shown in Fig. 4.1. Combining Eqs. (4.5), (4.6), (4.7) and (4.8) evaluated for $\delta t\to 0$ we now have

$$\frac{d}{dt}\int_{V(t)}\varsigma(t)dV=\int_{S(t)}\varsigma(t)\mathbf{v}\cdot\mathbf{n}dS+\int_{V(t)}\partial_t\varsigma(t)dV. \tag{4.9}$$

Applying Gauss' theorem we can rewrite Eq. (4.9) to the common form encountered as the Reynolds transport theorem.

$$\frac{d}{dt}\int_{V(t)}\varsigma(t)dV=\int_{V(t)}\left[\partial_t\varsigma(t)+\boldsymbol{\nabla}\cdot(\varsigma(t)\mathbf{v})\right]dV. \tag{4.10}$$

This equation commonly appears as an integral formulation for conservation of momentum obtained when $\varsigma=\rho\mathbf{v}$.

4.1.2 Rewriting time-dependent integral

We now use the surface integral form of the Reynolds transport theorem Eq. (4.9) on the momentum and define the magnitude of normal velocity $\mathbf{v}_{10}\cdot\mathbf{n}\equiv v_n$ to get

$$\frac{d}{dt}\int_{V(t)}\rho_0\mathbf{v}_{10}dV=\int_{S(t)}\rho_0\mathbf{v}_{10}v_n dS+\int_{V(t)}\partial_t(\rho_0\mathbf{v}_{10})dV. \tag{4.11}$$

Following the approach by Hasegawa *et al.* [42] we consider the configuration given in Fig. 4.2 where a deformable object with surface $S(t)$ is positioned in a domain enclosed by a fictional fixed surface R. The surface integral must now take both $S(t)$ and R into account and we get

$$\frac{d}{dt}\int_{V(t)}\rho_0\mathbf{v}_{10}dV=\int_{V(t)}\partial_t(\rho_0\mathbf{v}_{10})dV+\int_{S(t)}\rho_0\mathbf{v}_{10}v_n dS+\int_{R}\rho_0\mathbf{v}_{10}v_n dR. \tag{4.12}$$

As R is fixed, $\mathbf{v}_{10} \cdot \mathbf{n}_R = 0$ on R. On $S(t)$ we have $v_n = -v_{10n}$ as $S(t)$ is inside the domain $V(t)$ having $\mathbf{n}$ pointing the opposite direction of a normal vector of $V(t)$. Now use $\partial_t(\rho_0 \mathbf{v}_{10}) = -\boldsymbol{\nabla} p_{10}$ from Euler's equation of motion Eq. (2.19),

$$-\frac{d}{dt}\int_{V(t)} \rho_0 \mathbf{v}_{10} dV = -\int_{V(t)} \boldsymbol{\nabla} p_{10} dV - \int_{S_0} \rho_0 \mathbf{v}_{10} v_{10n} dS, \tag{4.13}$$

where we have replaced $S(t)$ with S_0 for integrands of second order. Using Gauss' theorem, we can rewrite the volume integral remembering that the sign changes as the normal vector $\mathbf{n}$ points into the domain,

$$-\frac{d}{dt}\int_{V(t)} \rho_0 \mathbf{v}_{10} dV = \int_{S(t)} p_{10} \mathbf{n} dS - \int_{S_0} \rho_0 \mathbf{v}_{10} v_{10n} dS - \int_R p_{10} \mathbf{n}_R dR. \tag{4.14}$$

The term $\int_R p_{10} \mathbf{n}_R dR$ time averages to zero as p_{10} is a first order periodic term and R is constant. Likewise the left hand side of Eq. (4.14) vanishes by time averaging as we are in steady state. Thus we are left with

$$\left\langle \int_{S(t)} p_{10} \mathbf{n} dS \right\rangle = \left\langle \int_{S_0} \rho_0 \mathbf{v}_{10} v_n dS \right\rangle = -\left\langle \int_{S(t)} \rho_0 \partial_t \phi_{10} \mathbf{n} dS \right\rangle, \tag{4.15}$$

where the last equality comes from Eq. (2.31). Combining Eqs. (4.2), (4.3) and (4.15) we can now express the radiation force to second order on a freely suspended compressible object in a sound field in terms of first-order quantities integrated over the equilibrium position of the object surface,

$$\langle \mathbf{F}_a \rangle = -\left\langle \int_{S_0} \rho_0 \boldsymbol{\nabla} \phi_{10} v_n dS \right\rangle + \frac{1}{2}\rho_0 \left\langle \int_{S_0} |\boldsymbol{\nabla} \phi_{10}|^2 \mathbf{n} dS \right\rangle - \frac{1}{2}\frac{\rho_0}{c_a^2} \left\langle \int_{S_0} (\partial_t \phi_{10})^2 \mathbf{n} dS \right\rangle. \tag{4.16}$$

The first term stems from the moving boundary interacting with the first-order fields, whereas the last two terms are identified as integrals over the difference of the acoustic energy densities.

It should be noticed that this expression, in contrast to the ones most often referred in experimental papers [30,31,38,45], is a general result applicable for any geometry without restrictions to the size of the object relatively to the wavelength.

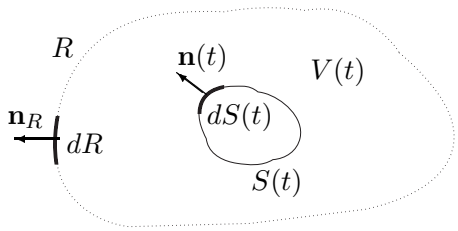

Figure 4.2: Deformable object with surface $S(t)$ in a domain $V(t)$ enclosed by a fictional fixed surface R. Figure adapted from [42].

4.2 Introduction by 1D dynamics

When calculating the potentials in Eq. (4.16) it is often advisable and necessary to choose fairly simple geometries and acoustic fields. A good place to start if one wants to extract the general behavior of the radiation force could be to consider the geometry previously shown in Fig. 3.6 with an infinitely wide plate of finite thickness positioned in a plane wave along the x-axis for which we now outline a solution scheme.

In this one-dimensional case the normal velocity at the plate is equal to the first-order velocity and the tangential velocity is non existing as the waves have normal incidence on the plate. Thus, we can write up the radiation force along the x-direction from Eq. (4.16) as

$$\langle F_a \rangle = -\left\langle \frac{1}{2}\rho_0 \int_{S_0} |\boldsymbol{\nabla}\phi_{10}|^2 \,\mathbf{n} dS \right\rangle - \left\langle \frac{1}{2}\frac{\rho_0}{c_a^2} \int_{S_0} (\partial_t \phi_{10})^2 \mathbf{n} dS \right\rangle . \tag{4.17}$$

Since the integrands are independent of the integration variables and we have the normal vectors $\mathbf{n} = -\hat{\mathbf{x}}$ and $\mathbf{n} = \hat{\mathbf{x}}$ at $x = h$ and $x = h + d$, respectively, we can easily find the radiation force to be

$$\begin{aligned} \langle F_a \rangle = &\left\langle \rho_0 \left|\boldsymbol{\nabla}\phi_{10A}\right|^2_{x=h} \right\rangle + \left\langle \frac{1}{2}\frac{\rho_0}{c_a^2} (\partial_t \phi_{10A})^2_{x=h} \right\rangle \\ &- \left\langle \rho_0 \left|\boldsymbol{\nabla}\phi_{10C}\right|^2_{x=h+d} \right\rangle - \left\langle \frac{1}{2}\frac{\rho_0}{c_a^2} (\partial_t \phi_{10C})^2_{x=h+d} \right\rangle . \end{aligned} \tag{4.18}$$

The result and computations can be simplified if we express Eq. (4.18) in terms of the plate potential ϕ_{10B} as will also be exploited in the following section. Hereby a time-harmonic field can be shown to give

$$\langle F_a \rangle = \frac{1}{4}\left|\boldsymbol{\nabla}\tilde{\phi}_{10B}\right|^2_{x=h} + \frac{1}{4}\frac{\rho_0}{c_a^2}\alpha^2 \left(-\omega\tilde{\phi}_{10B}\right)^2_{x=h} - \frac{1}{4}\left|\boldsymbol{\nabla}\tilde{\phi}_{10B}\right|^2_{x=h+d} - \frac{1}{4}\frac{\rho_0}{c_a^2}\alpha^2 \left(\tilde{\phi}_{10B}\right)_{x=h+d}, \tag{4.19}$$

where the density ratio α is defined in Eq. (4.27). What now remains is simply to insert the relevant potentials, which can be found using the same conditions as the transmission examples in Chap. 3. However, we will not report on the results here, since the geometry is unlikely to be found in microsystems and we do not gain any physical insight that will not be covered by the next sections.

4.3 Force on spheres

Since we in microsystems are interested in manipulating small particles as cells and the like we now go to three dimensions and consider a spherical object of radius a placed in a spherically described coordinate system as outlined in Fig. 4.3. The derivation of the force follows the calculations given by Yosioka and Kawasima [19] and is mathematically quite laborious. For the sake of clarity we only present an excerpt of the calculations in the following and refer to App. C and [19] for more mathematical details.

If we assume a plane acoustic wave along the z-axis, that is along $\theta = 0$, there will be no φ-dependence. By projection along $\hat{\mathbf{z}}$ in spherical coordinates we find for normal and tangential components, respectively, that

$$\mathbf{n} \cdot \hat{\mathbf{z}} = \hat{\mathbf{r}} \cdot \hat{\mathbf{z}} = \cos\theta \tag{4.20a}$$

$$\mathbf{t} \cdot \hat{\mathbf{z}} = \hat{\boldsymbol{\theta}} \cdot \hat{\mathbf{z}} = -\sin\theta. \tag{4.20b}$$

This can be combined with the expression for the gradient in spherical coordinates with no φ-dependence,

$$\boldsymbol{\nabla}\phi_{10} = \hat{\mathbf{r}}\partial_r\phi_{10} + \hat{\boldsymbol{\theta}}\frac{1}{r}\partial_\theta\phi_{10}, \tag{4.21}$$

which allows us to split the z-component of the radiation force Eq. (4.16) into four terms

$$\langle \mathbf{F}_a \rangle \cdot \hat{\mathbf{z}} = \langle F_r \rangle + \langle F_{\theta r} \rangle + \langle F_\theta \rangle + \left\langle F_\phi \right\rangle. \tag{4.22}$$

The calculation of the four terms is straight forward and can be shown to give

$$\langle F_r \rangle = -\pi a^2 \rho_0 \left\langle \int_0^\pi (\partial_r \phi_{10})^2_{r=a} \cos\theta \sin\theta d\theta \right\rangle \tag{4.23a}$$

$$\langle F_{\theta r} \rangle = 2\pi a \rho_0 \left\langle \int_0^\pi (\partial_r \phi_{10})_{r=a} (\partial_\theta \phi_{10})_{r=a} \sin^2\theta d\theta \right\rangle \tag{4.23b}$$

$$\langle F_\theta \rangle = \pi \rho_0 \left\langle \int_0^\pi (\partial_\theta \phi_{10})^2_{r=a} \cos\theta \sin\theta d\theta \right\rangle \tag{4.23c}$$

$$\left\langle F_\phi \right\rangle = -\pi a^2 \frac{\rho_0}{c_a^2} \left\langle \int_0^\pi (\partial_t \phi_{10})^2_{r=a} \cos\theta \sin\theta d\theta \right\rangle. \tag{4.23d}$$

Since the spherical particle is impinged by the acoustic wave, another wave propagating from the particle will be induced. Hereby the potential outside the particle will consist of both the incoming potential ϕ_{10i} and the scattered ϕ_{10s}

$$\phi_{10} = \phi_{10i} + \phi_{10s}. \tag{4.24}$$

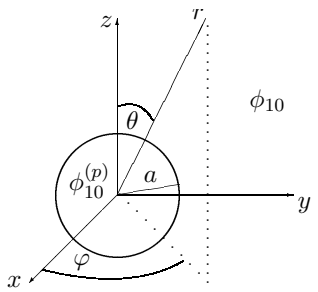

Figure 4.3: A spherical particle of radius a placed in a coordinate system. A plane acoustic field is aligned along the z-axis. The acoustic fields have velocity potential ϕ_{10} and $\phi_{10}^{(p)}$ outside and inside the particle, respectively.

The potential $\phi_{10}^{(p)}$, where the superscript $^{(p)}$ is the notation for any quantity inside the particle, shows up to be simpler than the potential outside the particle and thereby it is advantageous to rewrite Eqs. (4.23) in terms of $\phi_{10}^{(p)}$. This is done by employing our well-known boundary conditions being continuity in normal velocity and pressure at the interface. From this we can find the following,

$$\langle F_r \rangle = -\pi a^2 \rho_0 \left\langle \int_{-1}^{1} (\partial_r \phi_{10}^{(p)})^2 \mu d\mu \right\rangle \tag{4.25a}$$

$$\langle F_{r\theta} \rangle = -2\pi a \alpha \rho_0 \left\langle \int_{-1}^{1} (\partial_r \phi_{10}^{(p)})(\partial_\mu \phi_{10}^{(p)})(1-\mu^2) d\mu \right\rangle \tag{4.25b}$$

$$\langle F_\theta \rangle = \pi \rho_0 \alpha^2 \left\langle \int_{-1}^{1} (\partial_\mu \phi_{10}^{(p)})^2 (1-\mu^2) \mu d\mu \right\rangle \tag{4.25c}$$

$$\left\langle F_\phi \right\rangle = -\pi a^2 \alpha^2 \frac{\rho_0}{c_a^2} \left\langle \int_{-1}^{1} \left(\partial_t \phi_{10}^{(p)}\right)^2 \mu d\mu \right\rangle, \tag{4.25d}$$

where we have introduced the variable transformation $\mu = \cos\theta$, $d\mu = -\sin\theta d\theta$.

4.3.1 Radiation force for small spherical particles

The scattering problem in spherical coordinates is mathematically well-known, and the theoretical foundation and application to acoustics can be found in e.g. [19, 46, 47]. From these references it can be shown that the potential inside the particle can be expressed by

$$\phi_{10}^{(p)} = \sum_{n=0}^{\infty} (2n+1) \mathrm{e}^{\mathrm{i}\omega t} (-\mathrm{i})^n B_n j_n(k_0^{(p)} a) P_n(\cos\theta). \tag{4.26}$$

Here j_n are spherical Bessel functions of first kind, P_n Legendre polynomials and B_n a constant to be determined from the boundary conditions in pressure and velocity, which is done with the help of various mathematical relations for Bessel functions and Legendre polynomials. However, these are quite cumbersome calculations, which do not aid the physical insight and therefore we proceed directly to the result appropriate for microsystems.

We now introduce the coefficients

$$\alpha \equiv \frac{\rho_0^{(p)}}{\rho_0} \tag{4.27}$$

$$\vartheta \equiv \frac{k_0}{k_0^{(p)}}, \tag{4.28}$$

and assume $(k_0 a)^2 \ll 1$, $(k_0^{(p)} a)^2 \ll 1$ and $\alpha = \mathcal{O}(1)$, which complies with the particles used for characterizing microfluidic chips when suspended in water under influence of low MHz radiation having $(k_0 a)^2 \sim (k_0^{(p)} a)^2 \sim 10^{-6}$ and $\alpha \sim 1$. With these restrictions the radiation force for a standing wave potential given by $\phi_{10i} = U k_0^{-1} \cos k_0 z \mathrm{e}^{-\mathrm{i}\omega t}$, where U is a first-order velocity amplitude, will be the following

$$\langle \mathbf{F}_a \rangle \cdot \hat{\mathbf{z}} = 4\pi a^3 U^2 k_0 \rho_0 \mathcal{C}(\alpha, \vartheta) \sin(2k_0 z), \tag{4.29}$$

where $\mathcal{C}(\alpha, \vartheta)$ is a dimensionless material dependent radiation coefficient defined as

$$\mathcal{C}(\alpha, \vartheta) = \frac{-2 + 5\alpha}{3 + 6\alpha} - \frac{1}{3\alpha\vartheta^2}. \tag{4.30}$$

It is from Eq. (2.44) quite easy to show that the average acoustic energy $\langle E \rangle$ in a plane standing wave is given by $\langle E \rangle = U^2 \rho_0$. If we substitute this into Eq. (4.29) we can now write the force as [19],

$$\langle \mathbf{F}_a \rangle \cdot \hat{\mathbf{z}} = 4\pi a^3 \langle E \rangle \omega c_a^{-1} \mathcal{C}(\alpha, \vartheta) \sin(2k_0 z). \tag{4.31}$$

The first property we notice is the strong geometric scaling being important when varying the size of the particles, which will be treated in further detail in Chap. 8. Secondly the force has a doubling of spatial periodicity in the pressure field since it is a second-order effect, but more importantly it can change sign depending on the material parameters as can be seen from Eq. (4.30).

We also find the force to be dependent on the energy, which is not surprising considering the initial expression given in Eq. (4.16). Furthermore force can in general be derived from an energy potential, which we recognize in Eq. (4.31) as $\boldsymbol{\nabla} \langle E \rangle \sim 2k_0 \langle E \rangle = 2\omega c_a^{-1} \langle E \rangle$. Given the general condition $k_0 a \ll 1$ is fulfilled we can thereby increase the force on the particle by increasing the frequency being equivalent to an increased energy gradient. This shows us that microfluidic systems are particularly well suited for exploitation of radiation forces due to the high frequencies necessary to match wavelengths with device dimensions. Ultrasonic frequencies can of course also be used in macroscopic systems, but microsystems allow for a better control and design of the standing wave fields.

Since the force can be expressed in terms of energy we must expect a system in equilibrium to strive for a minimum energy configuration by displacing the particles to the most favorable position. From Sec. 3.1.1 we know that velocity and pressure in a standing wave are phase shifted by $\frac{1}{2}\pi$ and have kinetic energy maxima at pressure nodes and potential energy maxima at antinodes. We can now perform a small investigation of the material parameters by introducing the compressibility $\kappa = \rho_0^{-1} c_a^{-2}$ [48]. Hereby we find the last term in Eq. (4.30) to be a compressibility ratio

$$\chi \equiv \alpha\vartheta^2 = \frac{\kappa}{\kappa^{(p)}}. \tag{4.32}$$

Setting $\alpha = 1$ or $\chi = 1$ corresponding to equal density or compressibility, respectively, we find Eq. (4.30) to be

$$\mathcal{C} = \frac{1}{3}\left(1 - \frac{1}{\chi}\right), \qquad \alpha = 1 \tag{4.33a}$$

$$\mathcal{C} = \frac{-1 + \alpha}{1 + 2\alpha}, \qquad \chi = 1. \tag{4.33b}$$

From Fig. 4.4 we realize that for $\mathcal{C} > 0$ particles will be forced towards the pressure nodes and to the antinodes for $\mathcal{C} < 0$, respectively. Hereby we can for the situations with one of the ratios fixed at unity in Eqs. (4.33) deduce that particles with higher mass

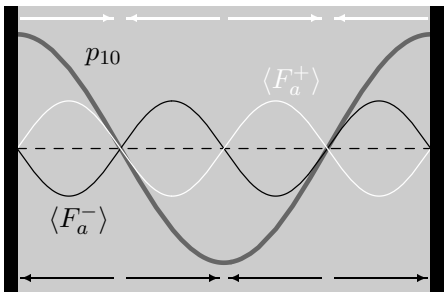

Figure 4.4: Radiation force amplitude as given by Eq. (4.31) in a plane standing pressure wave. $\langle F_a^- \rangle$ denotes $\mathcal{C} < 0$ and $\langle F_a^+ \rangle$ denotes $\mathcal{C} > 0$. We see that F_a^+ forces the particles towards pressure nodes and F_a^- towards antinodes.

density than the medium are attracted to the pressure nodes whereas particles with a higher compressibility are forced to the pressure antinodes. Thus, generally dense particles are attracted to pressure nodes whereas lighter, compressible particles are pushed to the antinodes. This has for instance been exploited to separate red blood cells, erythrocytes, and fat particles, lipids [29,31]. In the experimental measurements shown in Fig. 1.2 b) we can see this behavior for polymer particles, where these aggregate in the pressure nodes.

4.4 Extended models for the radiation force

As the result given in Eq. (4.31) is essentially the gradient of the acoustic energy field with a material dependent coefficient it is reasonable to believe that the result can be extended from plane standing waves to an arbitrary acoustic field. This has been done in a paper by Gor'kov [49], who elegantly derives a general radiation force expression for small particles obeying the same restrictions in an inviscid fluid as in the previous sections.

We shall not consider the details in the derivation but merely state the result, which holds for any field except purely or approximately plane traveling waves [49],

$$\langle \mathbf{F}_a \rangle = -\boldsymbol{\nabla} \Psi \tag{4.34}$$

with the potential Ψ given as

$$\Psi \equiv 2\pi a^3 \rho_0 \left(\frac{\langle p_{10}^2 \rangle}{3\rho_0^2 c_a^2} \mathcal{C}_\kappa + \frac{\langle |\mathbf{v}_{10}|^2 \rangle}{2} \mathcal{C}_\alpha \right), \tag{4.35}$$

The two coefficients $\mathcal{C}_\kappa$ and $\mathcal{C}_\alpha$ can be expressed be

$$\mathcal{C}_\kappa = 1 - \frac{1}{\chi} \tag{4.36a}$$

$$\mathcal{C}_\rho = \frac{2(1-\alpha)}{1+2\alpha}. \tag{4.36b}$$

Now, these coefficients are recognized from Eqs. (4.33) and the same analysis regarding the direction of the force can therefore be performed. Furthermore, Eqs. (4.34) and (4.35)

can be shown to resemble Eq. (4.31) for a plane standing wave [49]. With the gradient explicitly written in Eq. (4.34) it can be realized that the force is zero for local extrema of Ψ, but the only stable positions for particles to aggregate will be at the local minima of Ψ.

In Chap. 8 we will apply Eq. (4.34) to experimental results of a microfluidic separation chip.

4.4.1 Neglected effects

In the preceding sections we have only treated an ideal, inviscid system. However, other effects might have to be considered under certain conditions. For a viscous microsystem operated in the MHz range two effects potentially having an impact on the radiation force are related to viscous effects and aggregation of clusters.

The influence of viscosity has been studied by for instance Westervelt [50] and Doinikov [51–53], who have treated the theory for both viscous and thermal dissipation. In the following we will not consider the viscous effects but merely notice that besides the two length scales, wavelength λ and particle size a governing the inviscid case, the viscosity introduces another length scale in terms of the momentum diffusion length δ_ν. As also noted in [38] the dynamics can change when the two or all of the length scales become comparable.

In the systems of our interest we always have $\lambda \gg a, \delta_\nu$. Yet, as $\delta_\nu \sim 10^{-6}$ m we might approach the limit $a/\delta_\nu \sim \mathcal{O}(1)$ for small particles like the ones used in Fig. 1.2 a) whereby viscosity can be important if the radiation force is the dominating force on the particle.

Besides the viscous effects we have also neglected any inter-particle reactions. These forces, known as Bjerknes forces [54, 55], scale strongly with the inverse of the mutual distance and it is thus a reasonable assumption to neglect the effect for a dilute solution with particles evenly distributed. Yet, as the radiation force drives the particles to either nodal or anti nodal lines notable inter-particle effects due to interference of the scattered sound waves can be anticipated. When we treat an actual system in Chap. 8 this will not be the most important issue, but for systems designated to compile a large amount of particles in a confined area it should be considered if inter-particle forces should be included in the model.

Chapter 5

Second-order theory: Streaming

We will now consider the acoustic streaming based on two approaches. First we shall disregard any boundary layer effects and perform an analysis and decomposition of the equations in order the solve the streaming based on viscous losses and first-order dynamics in the bulk fluid. Afterwards the fundamentals of boundary layer theory will be presented, giving rise to streaming based on boundary effects.

5.1 Inviscid introduction

In Sec. 2.5.1 we found that $\langle \mathbf{v}_{20} \rangle$ did only appear in the continuity equation. Thus, in this section we restrict ourselves to Eq. (2.86) to investigate if any valuable information can be obtained only from this with suitable boundary conditions. As shortly noted in Sec. 2.5.3 the boundary conditions for a compressible flow transforms from the velocity to the mass flux density. In any domain enclosed by boundaries we would thus apply a no-flux condition in analogy to the work by Jensen [32],

$$\langle \mathbf{J}_{20} \rangle = \mathbf{0}, \qquad \forall\, (x, y, z) \in \partial\Omega. \tag{5.1}$$

Based on the continuity equation, Eq. (2.86), we introduce the following guess on $\langle \mathbf{v}_{20} \rangle$

$$\langle \mathbf{v}_{20} \rangle = -\frac{1}{\rho_0} \langle \rho_{10} \mathbf{v}_{10} \rangle + \langle \mathbf{v}_{20\mathrm{inc}} \rangle \,, \tag{5.2}$$

which gives an incompressible continuity equation in $\langle \mathbf{v}_{20\mathrm{inc}} \rangle$,

$$\boldsymbol{\nabla} \cdot \langle \mathbf{v}_{20\mathrm{inc}} \rangle = 0, \qquad \forall\, (x, y, z) \in \Omega. \tag{5.3}$$

With the introduction of $\langle \mathbf{v}_{20\mathrm{inc}} \rangle$ the no-flux boundary condition Eq. (5.1) converts to a Dirichlet condition on $\langle \mathbf{v}_{20\mathrm{inc}} \rangle$,

$$\langle \mathbf{v}_{20\mathrm{inc}} \rangle = \mathbf{0}, \qquad \forall\, (x, y, z) \in \partial\Omega. \tag{5.4}$$

If we further choose to decompose the incompressible component by

$$\langle \mathbf{v}_{20\mathrm{inc}} \rangle = \boldsymbol{\nabla} \langle \phi_{20} \rangle + \boldsymbol{\nabla} \times \langle \mathbf{A}_{20} \rangle \,, \tag{5.5}$$

it is readily realized that the continuity equation gives a Laplace equation with an inhomogeneous Neumann conditions for $\langle\phi_{20}\rangle$

$$\nabla^2 \langle\phi_2\rangle = 0, \qquad \forall\,(x,y,z) \in \Omega \tag{5.6a}$$

$$\boldsymbol{\nabla} \langle\phi_2\rangle = -\boldsymbol{\nabla} \times \langle\mathbf{A}_2\rangle\,, \qquad \forall\,(x,y,z) \in \partial\Omega, \tag{5.6b}$$

whereby $\langle\phi_2\rangle$ is determined exclusively by the boundary conditions. In the following, however, we shall restrict ourselves to the notation $\langle\mathbf{v}_{20\mathrm{inc}}\rangle$.

It is easy to realize that at least one solution satisfying Eqs. (5.3) and (5.4) is a trivial incompressible velocity

$$\mathbf{v}_{20} = \mathbf{0}, \tag{5.7}$$

in which case we get the following streaming velocity

$$\langle\mathbf{v}_{20}\rangle = -\frac{1}{\rho_0}\langle\rho_{10}\mathbf{v}_{10}\rangle\,. \tag{5.8}$$

This result corresponds to the one described by Markham[1] [11], who computes $\langle\mathbf{v}_{20}\rangle$ from a harmonic plane traveling wave. Representing this by $v_{10} = U\cos(k_0 x - \omega t)$, where the amplitude U is a real quantity, it can from Eqs. (2.20), (2.35) and (5.8) be shown that

$$\langle v_{20\mathrm{travel}}\rangle = -\frac{U^2}{2c_a} \tag{5.9}$$

in analogy to Markham [11]. If we use our previously assumed velocity of $U \sim 10^{-4}c_a$ we obtain $\langle v_{20\mathrm{travel}}\rangle \sim 10^{-5}\ \mathrm{m\,s^{-1}}$, which is in fair agreement with measurements [1].

However, rather than traveling waves, we are interested in standing waves. For these waves given by e.g. $v_{10} = U\cos(k_0 x)\mathrm{e}^{-\mathrm{i}\omega t}$, the result is radically changed as we due to the phase shift of $\pi/2$ between first-order velocity and density now have

$$\left\langle \mathbf{v}_{20\mathrm{standing}} \right\rangle = 0. \tag{5.10}$$

From this it can be inferred that the streaming velocity based on bulk dynamics has no compressible component in a perfect lossless standing wave, and hence the compressible contribution with the inclusion of viscosity must scale with γ. On the contrary we cannot conclude that the incompressible component in the inviscid case obeys the same scaling as part of this due to Eqs. (5.6) is determined from the boundaries. With these introductory considerations we will now proceed to the more thorough viscous theory.

5.2 Viscous bulk streaming

In the following the case of streaming based on bulk dynamics will be treated. From Eqs. (2.81) and (2.97) we can infer that the time-averaged second-order body force density

[1] Markham's result, however, has opposite sign. This might be a misprint and is not of importance.

$\langle \mathbf{F} \rangle$ in the Navier–Stokes equation can be expressed by a gradient $\langle \mathbf{F} \rangle = \boldsymbol{\nabla} \langle \Phi_F \rangle$ for $\gamma = 0$. As γ is the typical measure for the viscous effects, we must thus expect that in the viscous case the dominating part of $\langle \mathbf{F} \rangle$ will be a gradient field as well.

If we insert the guess $\langle \mathbf{F} \rangle = \boldsymbol{\nabla} \langle \Phi_F \rangle + \left\langle \mathbf{B}_\gamma \right\rangle$, the governing second-order equations can from Eqs. (2.91) and (2.97) be formulated as

$$\boldsymbol{\nabla} \cdot \langle \mathbf{v}_2 \rangle = -\frac{1}{\rho_0} \boldsymbol{\nabla} \cdot \langle \rho_1 \mathbf{v}_1 \rangle \tag{5.11}$$

$$\boldsymbol{\nabla} \langle p_2 \rangle = -\boldsymbol{\nabla} \langle \Phi_F \rangle - \left\langle \mathbf{B}_\gamma \right\rangle + \eta \nabla^2 \langle \mathbf{v}_2 \rangle + \beta\eta \langle \boldsymbol{\nabla} (\boldsymbol{\nabla} \cdot \mathbf{v}_2) \rangle \,. \tag{5.12}$$

Using the viscous analogy to Eq. (5.2) for $\langle \mathbf{v}_2 \rangle$ gives the following structure of the Navier–Stokes equation,

$$\boldsymbol{\nabla} \langle p_2 \rangle + \boldsymbol{\nabla} \langle \Phi_F \rangle = -\left\langle \mathbf{B}_\gamma \right\rangle - \frac{\eta}{\rho_0} \nabla^2 \langle \rho_1 \mathbf{v}_1 \rangle - \frac{\beta\eta}{\rho_0} \boldsymbol{\nabla} (\boldsymbol{\nabla} \cdot \langle \rho_1 \mathbf{v}_1 \rangle) + \eta \nabla^2 \langle \mathbf{v}_{2\mathrm{inc}} \rangle \,. \tag{5.13}$$

Hereby it is observed that we have terms known from the first-order fields on both sides of the equation. Regarding the magnitude of these, the driving term $\boldsymbol{\nabla} \langle \Phi_F \rangle$ on the left-hand side does not depend on γ, whereas the corresponding terms on the right-hand side do.

If we initially make the erroneous assumption that all driving terms can be expressed as gradients, it is easy to realize that both the continuity equation, Navier–Stokes equation, and the no-flux condition are satisfied for $\langle \mathbf{v}_{2\mathrm{inc}} \rangle = \mathbf{0}$. From this we can deduce that with the chosen boundary conditions in the viscous system the value of $\langle \mathbf{v}_{2\mathrm{inc}} \rangle$ is governed by the components of the right-hand side body force density terms, which are not irrotational.

For analytical calculations this does not pose a problem, but if we attempt to solve the initial Navier–Stokes equation given in Eq. (2.97) directly by numerical tools we can expect computational difficulties. This is due to the fact that we solve for both second-order pressure and velocity in the same system driven by a body force with the gradient $\boldsymbol{\nabla} \langle \Phi_F \rangle$ controlling the pressure and the minor components governing the streaming velocity. As these components scale with γ, we thereby attempt to simultaneously resolve quantities of two different orders of magnitude, which, depending on the numerical method and the value of γ, can be impossible. In the following sections we will develop a method to evade this problem by decomposing the time-averaged Navier–Stokes equation in order to separate terms of significantly different order of magnitude. Hereby we can solve for the second-order velocity from an equation, where all terms are of the same order of magnitude.

5.2.1 Analysis for irrotational first-order velocity

To a first extent we treat the situation, where the first-order velocity is based on the gradient of a scalar potential, since this was shown plausible in Chap. 2 and gives rise to the simple relation between $\mathbf{v}_1$ and ρ_1 given by Eq. (2.76).

The Navier–Stokes equation to second order is known from Eq. (2.92)

$$\langle \rho_1 \partial_t \mathbf{v}_1 \rangle + \rho_0 \langle (\mathbf{v}_1 \cdot \boldsymbol{\nabla}) \mathbf{v}_1 \rangle = -\boldsymbol{\nabla} \langle p_2 \rangle + \eta \nabla^2 \langle \mathbf{v}_2 \rangle + \beta\eta \boldsymbol{\nabla} \langle \boldsymbol{\nabla} \cdot \mathbf{v}_2 \rangle \,, \tag{5.14}$$

where the second term on the left hand side can be rewritten to a gradient, if $\mathbf{v}_1$ is given by a scalar potential,

$$\langle \rho_1 \partial_t \mathbf{v}_1 \rangle + \frac{\rho_0}{2} \boldsymbol{\nabla} \left\langle |\mathbf{v}_1|^2 \right\rangle = -\boldsymbol{\nabla} \langle p_2 \rangle + \eta \nabla^2 \langle \mathbf{v}_2 \rangle + \beta\eta \boldsymbol{\nabla} \langle \boldsymbol{\nabla} \cdot \mathbf{v}_2 \rangle \,. \tag{5.15}$$

Using the incompressible velocity analogous to the calculations in Sec. 5.1, we can reformulate the Navier–Stokes equation to

$$\boldsymbol{\nabla} \langle p_2 \rangle + \frac{\rho_0}{2} \boldsymbol{\nabla} \left\langle |\mathbf{v}_1|^2 \right\rangle + \frac{\beta\eta}{\rho_0} \boldsymbol{\nabla} \langle \boldsymbol{\nabla} \cdot (\rho_1 \mathbf{v}_1) \rangle = -\langle \rho_1 \partial_t \mathbf{v}_1 \rangle + \eta \nabla^2 \langle \mathbf{v}_{2\mathrm{inc}} \rangle - \frac{\eta}{\rho_0} \nabla^2 \langle \rho_1 \mathbf{v}_1 \rangle \,, \tag{5.16}$$

where all obvious gradient terms have been collected at the left-hand side. This allows us to define a new pressure gradient

$$\boldsymbol{\nabla} \langle p_{2\mathrm{effi}} \rangle \equiv \boldsymbol{\nabla} \langle p_2 \rangle + \frac{\rho_0}{2} \boldsymbol{\nabla} \left\langle |\mathbf{v}_1|^2 \right\rangle + \frac{\beta\eta}{\rho_0} \boldsymbol{\nabla} \langle \boldsymbol{\nabla} \cdot (\rho_1 \mathbf{v}_1) \rangle \,. \tag{5.17}$$

Hereby Eq. (5.16) can be simplified to the following equation

$$\boldsymbol{\nabla} \langle p_{2\mathrm{effi}} \rangle = -\langle \rho_1 \partial_t \mathbf{v}_1 \rangle + \eta \nabla^2 \langle \mathbf{v}_{2\mathrm{inc}} \rangle - \frac{\eta}{\rho_0} \nabla^2 \langle \rho_1 \mathbf{v}_1 \rangle \,, \tag{5.18}$$

where $\langle \mathbf{v}_{2\mathrm{inc}} \rangle$ and $\langle p_{2\mathrm{effi}} \rangle$ are the unknowns driven by the body force terms

$$\langle \mathbf{F}_{\mathrm{eff}} \rangle = -\langle \rho_1 \partial_t \mathbf{v}_1 \rangle - \frac{\eta}{\rho_0} \nabla^2 \langle \rho_1 \mathbf{v}_1 \rangle \,, \tag{5.19}$$

which we have shown to be a gradient for $\gamma = 0$. Now, we know from Eq. (2.76)

$$\mathbf{v}_1 = K \boldsymbol{\nabla} \rho_1 \tag{5.20}$$

$$\partial_t \mathbf{v}_1 = -\mathrm{i}\omega K \boldsymbol{\nabla} \rho_1, \tag{5.21}$$

where we have used the harmonic $\mathrm{e}^{-\mathrm{i}\omega t}$ convention and defined the complex pre-factor

$$K \equiv \frac{-\mathrm{i}(1 - \mathrm{i}\gamma) c_a^2}{\rho_0 \omega}. \tag{5.22}$$

Thus, the body force density Eq. (5.19) can be rewritten to

$$\langle \mathbf{F}_{\mathrm{eff}} \rangle = \left\langle \rho_1 \left(\frac{(1 - \mathrm{i}\gamma) c_a^2}{\rho_0} \boldsymbol{\nabla} \rho_1 \right) \right\rangle + \frac{\eta}{\rho_0} \nabla^2 \left\langle \rho_1 \left(\frac{\mathrm{i}(1 - \mathrm{i}\gamma) c_a^2}{\rho_0 \omega} \boldsymbol{\nabla} \rho_1 \right) \right\rangle . \tag{5.23}$$

At first sight Eq. (5.23) appears to be a gradient if we do a little relocation of the complex pre-factors and apply general differentiation rules. Yet, it should be emphasized that although this is tempting in the complex notation, it is in general not allowed mathematically to interchange fields and operators. Therefore we must perform a more laborious analysis.

5.2.2 Expand body force density

Now we take the terms from the body force density Eq. (5.19) and expand them in order to separate small and large components. Beginning with the first term we can rewrite this using Eqs. (2.84) and (5.21),

$$\langle \rho_1 \partial_t \mathbf{v}_1 \rangle = -\frac{c_a^2}{2\rho_0} \mathrm{Re}\left\{ \tilde{\rho}_1 (1 + \mathrm{i}\gamma) \boldsymbol{\nabla} \tilde{\rho}_1^* \right\}. \tag{5.24}$$

Exploit the general relation complex relation

$$\mathrm{Re}\left\{ ab^* \right\} = \mathrm{Re}\left\{ a \right\} \mathrm{Re}\left\{ b \right\} + \mathrm{Im}\left\{ a \right\} \mathrm{Im}\left\{ b \right\}, \tag{5.25}$$

which gives rise to the following,

$$\langle \rho_1 \partial_t \mathbf{v}_1 \rangle = -\frac{c_a^2}{2\rho_0} \left[\mathrm{Re}\left\{ \tilde{\rho}_1 \right\} \mathrm{Re}\left\{ (1 - \mathrm{i}\gamma) \boldsymbol{\nabla} \tilde{\rho}_1 \right\} + \mathrm{Im}\left\{ \tilde{\rho}_1 \right\} \mathrm{Im}\left\{ (1 - \mathrm{i}\gamma) \boldsymbol{\nabla} \tilde{\rho}_1 \right\} \right]. \tag{5.26}$$

If we expand the complex expressions and use this together with commutation of differential and complex operators, that is $\mathrm{Im}\left\{ \boldsymbol{\nabla} \tilde{\rho}_1 \right\} = \boldsymbol{\nabla} \mathrm{Im}\left\{ \tilde{\rho}_1 \right\}$ and likewise for the real part, we end up with the following after elaborate but trivial algebra,

$$-\frac{2\rho_0}{c_a^2} \langle \rho_1 \partial_t \mathbf{v}_1 \rangle = \boldsymbol{\nabla} \left\langle \left| \tilde{\rho}_1 \right|^2 \right\rangle + \gamma \left[\mathrm{Re}\left\{ \tilde{\rho}_1 \right\} \boldsymbol{\nabla} \mathrm{Im}\left\{ \tilde{\rho}_1 \right\} - \mathrm{Im}\left\{ \tilde{\rho}_1 \right\} \boldsymbol{\nabla} \mathrm{Re}\left\{ \tilde{\rho}_1 \right\} \right]. \tag{5.27}$$

As $\tilde{\rho}_1$ is real in a standing wave for $\gamma = 0$, $\mathrm{Im}\left\{ \tilde{\rho}_1 \right\}$ must scale with γ and the dominating term is as expected a gradient, whereas the remaining terms are an order of γ^2 smaller. Thus, the dominating term can be combined with $\boldsymbol{\nabla} \langle p_{2\mathrm{eff}} \rangle$.

Now we can proceed to the second term in Eq. (5.19), again using Eqs. (2.84) and (5.21) for the initial step,

$$\frac{\eta}{\rho_0} \nabla^2 \langle \rho_1 \mathbf{v}_1 \rangle = -\frac{\eta c_a^2}{2\rho_0^2 \omega} \nabla^2 \mathrm{Re}\left\{ \tilde{\rho}_1 (\mathrm{i} - \gamma) \boldsymbol{\nabla} \tilde{\rho}_1^* \right\}. \tag{5.28}$$

From the relation in Eq. (5.25) we get

$$-\frac{2\rho_0 \omega}{c_a^2} \nabla^2 \langle \rho_1 \mathbf{v}_1 \rangle = \nabla^2 \left(\mathrm{Re}\left\{ \tilde{\rho}_1 \right\} \mathrm{Re}\left\{ (\gamma + \mathrm{i}) \boldsymbol{\nabla} \tilde{\rho}_1 \right\} + \mathrm{Im}\left\{ \tilde{\rho}_1 \right\} \mathrm{Im}\left\{ (\gamma + i) \boldsymbol{\nabla} \tilde{\rho}_1 \right\} \right), \tag{5.29}$$

where the complex terms can be expanded to the following,

$$\mathrm{Re}\left\{ (\gamma + i) \boldsymbol{\nabla} \tilde{\rho}_1 \right\} = \gamma \mathrm{Re}\left\{ \boldsymbol{\nabla} \tilde{\rho}_1 \right\} - \mathrm{Im}\left\{ \boldsymbol{\nabla} \tilde{\rho}_1 \right\} \tag{5.30a}$$

$$\mathrm{Im}\left\{ (\gamma + i) \boldsymbol{\nabla} \tilde{\rho}_1 \right\} = \gamma \mathrm{Im}\left\{ \boldsymbol{\nabla} \tilde{\rho}_1 \right\} + \mathrm{Re}\left\{ \boldsymbol{\nabla} \tilde{\rho}_1 \right\}. \tag{5.30b}$$

Combining Eq. (5.29) and Eqs. (5.30) we see, as $|\mathrm{Im}\left\{ \tilde{\rho}_1 \right\}| \sim \gamma |\mathrm{Re}\left\{ \tilde{\rho}_1 \right\}|$, that all terms are of the order of magnitude $\nabla^2 \gamma |\mathrm{Re}\left\{ \tilde{\rho}_1 \right\}|^2$ or lower. Further laborious rewriting can be shown to give

$$\begin{aligned} \frac{2\rho_0 \omega}{c_a^2} \nabla^2 \langle \rho_1 \mathbf{v}_1 \rangle = &- \boldsymbol{\nabla} \left(\frac{1}{2} \gamma \nabla^2 \left(\mathrm{Re}\left\{ \tilde{\rho}_1 \right\} \right)^2 \right) - \boldsymbol{\nabla} \left(\frac{1}{2} \gamma \nabla^2 \left(\mathrm{Im}\left\{ \tilde{\rho}_1 \right\} \right)^2 \right) \\ &+ \nabla^2 \left(\mathrm{Re}\left\{ \tilde{\rho}_1 \right\} \boldsymbol{\nabla} \mathrm{Im}\left\{ \tilde{\rho}_1 \right\} \right) - \nabla^2 \left(\mathrm{Im}\left\{ \tilde{\rho}_1 \right\} \boldsymbol{\nabla} \mathrm{Re}\left\{ \tilde{\rho}_1 \right\} \right). \end{aligned} \tag{5.31}$$

Again, two of the terms can be added to $\boldsymbol{\nabla} \langle p_{2\mathrm{eff}} \rangle$.

5.2.3 The decomposed Navier–Stokes equation for $\langle \mathbf{v}_{2\text{inc}} \rangle$

By introducing yet another pressure gradient $\boldsymbol{\nabla} \left\langle p_{2\text{repi}} \right\rangle$ we can now combine Eqs. (5.17), (5.27) and (5.31) and define

$$\begin{aligned}\boldsymbol{\nabla} \left\langle p_{2\text{repi}} \right\rangle \equiv & \boldsymbol{\nabla} \langle p_2 \rangle + \frac{1}{2}\rho_0 \boldsymbol{\nabla} \left\langle |\mathbf{v}_1|^2 \right\rangle - \frac{c_a^2}{2\rho_0} \boldsymbol{\nabla} \left\langle |\rho_1|^2 \right\rangle \\ & + \frac{\gamma\beta c_a^2}{(1+\beta)\omega} \boldsymbol{\nabla} \left(\boldsymbol{\nabla} \cdot \langle \rho_1 \mathbf{v}_1 \rangle \right) - \frac{\gamma^2 c_a^4}{4(1+\beta)\rho_0 \omega^2} \boldsymbol{\nabla} \left(\nabla^2 \mathrm{Re}\left\{\tilde{\rho}_1\right\}^2 + \nabla^2 \mathrm{Im}\left\{\tilde{\rho}_1\right\}^2 \right), \end{aligned} \tag{5.32}$$

where we have expressed all occurring η in terms of γ. As expected, the dominating terms are analogous to the result found in the inviscid theory by Eq. (2.85), and only large values of γ will alter $\langle p_2 \rangle$ from the inviscid counterpart.

We are now able to write up the Navier–Stokes equation with a body force density consisting purely of terms of the same order of magnitude and solve this for $\boldsymbol{\nabla} \left\langle p_{2\text{repi}} \right\rangle$ and $\langle \mathbf{v}_{2\text{inc}} \rangle$ in conjunction with the viscous counterpart to the continuity equation Eq. (5.3). If we combine the Navier–Stokes equation given in Eq. (5.16) with the decomposed terms from Eqs. (5.27), (5.31) and (5.32) we thereby eventually find the decomposed Navier–Stokes equation,

$$\begin{aligned}\boldsymbol{\nabla} \left\langle p_{2\text{repi}} \right\rangle = & \frac{\gamma\rho_0 c_a^2}{(1+\beta)\omega} \nabla^2 \langle \mathbf{v}_{2\text{inc}} \rangle + \frac{\gamma c_a^2}{2\rho_0} \left(\mathrm{Re}\left\{\tilde{\rho}_1\right\} \boldsymbol{\nabla} \mathrm{Im}\left\{\tilde{\rho}_1\right\} - \mathrm{Im}\left\{\tilde{\rho}_1\right\} \boldsymbol{\nabla} \mathrm{Re}\left\{\tilde{\rho}_1\right\} \right) \\ & - \frac{\gamma c_a^4}{2(1+\beta)\rho_0 \omega^2} \left(\nabla^2 \left[\mathrm{Re}\left\{\tilde{\rho}_1\right\} \boldsymbol{\nabla} \mathrm{Im}\left\{\tilde{\rho}_1\right\} \right] - \nabla^2 \left[\mathrm{Im}\left\{\tilde{\rho}_1\right\} \boldsymbol{\nabla} \mathrm{Re}\left\{\tilde{\rho}_1\right\} \right] \right). \end{aligned} \tag{5.33}$$

As a check of consistency a short glance at Eq. (5.33) reveals that no irrotational body force exists for $\gamma = 0$ as expected. To estimate the expected order of magnitude, we can use that the length scale of the gradient is equivalent to the wavenumber Eq. (2.35). By a quick calculation we get the following estimate for standing waves

$$| \langle \mathbf{v}_{2\text{inc}} \rangle | \sim \gamma c_a \frac{|\rho_1|^2}{\rho_0^2} \sim \gamma \frac{|v_1|^2}{c_a}. \tag{5.34}$$

This result implies that the incompressible component for a standing wave is governed by the small phase shift induced by the viscosity.

When we have solved for these quantities we can find the full second-order velocity by substituting back

$$\langle \mathbf{v}_2 \rangle = -\frac{1}{\rho_0} \langle \rho_1 \mathbf{v}_1 \rangle + \left\langle \mathbf{v}_{2,\text{inc}} \right\rangle. \tag{5.35}$$

Similar calculations can be done for $\boldsymbol{\nabla} \langle p_2 \rangle$ using Eq. (5.32). As all terms depend on ρ_1, and $\langle p_2 \rangle = 0$ for $\rho_1 = 0$, we can remove the gradients and compute $\langle p_2 \rangle$ directly. However, numerically we do not use any boundary conditions on $\left\langle p_{2\text{repi}} \right\rangle$ and thus cleverly chosen constraints should be applied, if the viscous terms become significant. The numerical implementation and solutions of Eq. (5.33) are given in Chap. 7.

5.2.4 Decomposition without introducing $\langle \mathbf{v}_{2\text{inc}} \rangle$

In the previous sections the equations were decomposed to solve for $\langle \mathbf{v}_{2\text{inc}} \rangle$. However, alternatively we can choose to solve directly for $\langle \mathbf{v}_2 \rangle$. In this manner we can also compare the two methods and determine if one is better suited for numerical implementation.

Take the Navier–Stokes equation Eq. (5.15) and collect any gradient term not containing $\langle \mathbf{v}_2 \rangle$ to obtain

$$\boldsymbol{\nabla} \langle p_2 \rangle + \frac{\rho_0}{2} \boldsymbol{\nabla} \left\langle |\mathbf{v}_1|^2 \right\rangle = - \langle \rho_1 \partial_t \mathbf{v}_1 \rangle + \eta \nabla^2 \langle \mathbf{v}_2 \rangle + \beta \eta \boldsymbol{\nabla} \langle \boldsymbol{\nabla} \cdot \mathbf{v}_2 \rangle \,. \tag{5.36}$$

Thus, the only body force with irrotational components driving this system is

$$- \langle \rho_1 \partial_t \mathbf{v}_1 \rangle \,, \tag{5.37}$$

which can be decomposed with the result given in Eq. (5.27). In analogy to the incompressible calculations we can define a new pressure gradient,

$$\boldsymbol{\nabla} \left\langle p_{2\text{rep}} \right\rangle \equiv \boldsymbol{\nabla} \langle p_2 \rangle + \frac{\rho_0}{2} \boldsymbol{\nabla} \left\langle |\mathbf{v}_1|^2 \right\rangle - \frac{c_a^2}{2\rho_0} \boldsymbol{\nabla} \left\langle |\rho_1|^2 \right\rangle . \tag{5.38}$$

Hereby a new Navier–Stokes equation can be established by combining Eqs. (5.27), (5.36) and (5.38),

$$\begin{aligned} \boldsymbol{\nabla} \left\langle p_{2\text{rep}} \right\rangle =& \frac{\gamma \rho_0 c_a^2}{(1+\beta)\omega} \nabla^2 \langle \mathbf{v}_2 \rangle + \frac{\gamma \beta \rho_0 c_a^2}{(1+\beta)\omega} \boldsymbol{\nabla} \langle \boldsymbol{\nabla} \cdot \mathbf{v}_2 \rangle \\ &+ \frac{\gamma c_a^2}{2\rho_0} \left(\mathrm{Re}\left\{ \tilde{\rho}_1 \right\} \mathrm{Im}\left\{ \boldsymbol{\nabla} \tilde{\rho}_1 \right\} - \mathrm{Im}\left\{ \tilde{\rho}_1 \right\} \mathrm{Re}\left\{ \boldsymbol{\nabla} \tilde{\rho}_1 \right\} \right) , \end{aligned} \tag{5.39}$$

which can now be coupled and solved together with the continuity equation. To subsequently find $\langle p_2 \rangle$ we use the same approach as in Sec. 5.2.3.

It should be emphasized that the analysis done in the past sections do only apply to an irrotational first-order velocity. However, it is possible to extend the analysis to cover the general case, where $\mathbf{v}_1$ can be decomposed by a scalar and vector potential. As we will not use this in our numerical analysis, the derivations are not given here but are outlined in App. D.

Before turning to the numerical implementation and analysis we will now outline another approach for determination of the streaming velocity.

5.3 Boundary layer theory

In the past sections we have concentrated on the bulk dynamics where the governing length scale is the wavelength, which we know to be on the order of $\lambda \sim 10^{-4} - 10^{-3}$ m for MHz ultrasound in water. But in a viscous system we also have another length scale, namely the momentum diffusion length δ_ν given by Eq. (3.20). Within this length scale on the order of 10^{-6} m the velocity changes due to viscous stress from zero at the boundary to the velocity otherwise found by a slip condition. Since $\lambda \gg \delta_\nu$ it was in Sec. 3.1.4 assumed

that bulk effects could be treated with slip boundary conditions rather than the no-slip. Combining this with the fact that it numerically is very hard to resolve both length scales at the same time implies that we in the treatment of bulk effects in Chap. 7 keep this assumption.

However, if we on the other hand do have a small boundary layer in the first-order fields the same must be the case for the second-order effects, which entails the existence of a time-independent boundary layer flow. The acoustic streaming near boundaries have previously been reported by amongst others Rayleigh [7] and Nyborg [17] and as such the basic theory is well known. In the next section the fundamental theory will briefly be presented, closely following the methods of Landau and Lifshitz (LL) [39], who notice that the acoustic streaming due to boundary layer flow is especially pronounced under the condition [39]

$$\lambda \gg h \gg \delta_\nu, \tag{5.40}$$

where h is a characteristic length scale of a confined flow region. From this we can deduce that the boundary layer streaming scales favorably with our microsystems, since the chamber height h under normal conditions obeys $\lambda > h \gg \delta_\nu$.

5.3.1 Governing equations

When dealing with laminar boundary layer theory, the Navier–Stokes equation reduces to Prandtl's incompressible boundary layer equations [39, 44],

$$\partial_t v_{bx} + (\mathbf{v}_b \cdot \boldsymbol{\nabla})\, v_{bx} = -\frac{1}{\rho}\partial_x p + \nu \partial_z^2 v_{bx} \tag{5.41a}$$

$$\partial_t v_{by} + (\mathbf{v}_b \cdot \boldsymbol{\nabla})\, v_{by} = -\frac{1}{\rho}\partial_y p + \nu \partial_z^2 v_{by} \tag{5.41b}$$

$$\partial_t v_{bz} + (\mathbf{v}_b \cdot \boldsymbol{\nabla})\, v_{bz} = \nu \partial_z^2 v_{bz} \tag{5.41c}$$

where v_{bx}, v_{by} and v_{bz} are the three components of the boundary layer velocity, and p is the bulk pressure distribution. The formulation in Eqs. (5.41) is valid for a time-dependent, incompressible flow along a boundary in the xy-plane as sketched in Fig. 5.1. At first sight it seems contradictory that we consider incompressible flow in an acoustic problem. However, as argued by Landau and Lifshitz [39] incompressibility is justified when both of the following conditions are fulfilled

$$v \ll c_a \tag{5.42a}$$

$$\tau \gg \frac{\ell_d}{c_a}. \tag{5.42b}$$

Here τ is the characteristic time scale and ℓ_d is the characteristic dynamic length scale. In the case of an oscillating boundary layer these are $\tau = \omega^{-1}$ and $\ell_d = \delta_\nu$, respectively[2]. We have already necessitated the first condition in Chap. 2, and since $\delta_\nu \ll \lambda$ both conditions for incompressibility are fulfilled in the boundary layer to first and second order.

[2]Strictly speaking we should distinguish between frequency and angular frequency. For estimates, however, this is not of importance.

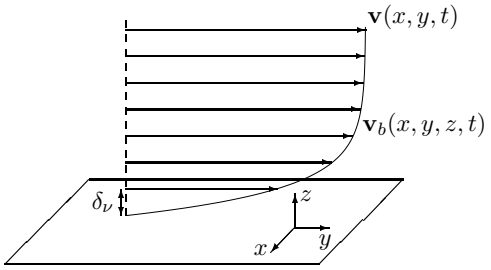

Figure 5.1: Sketch of the boundary layer velocity $\mathbf{v}_b$ in boundary layer of characteristic height δ_ν. The boundary layer velocity approaches the inviscid bulk velocity $\mathbf{v}$.

In boundary layers the pressure is essentially constant in the direction perpendicular to the surface. Thus, the pressure in the boundary layer is equal to the pressure in the bulk, where we assume an inviscid flow. From the inviscid Navier–Stokes equation we have

$$\boldsymbol{\nabla} p = -\rho \partial_t v - \rho(\mathbf{v}\cdot\boldsymbol{\nabla})\mathbf{v}, \tag{5.43}$$

which can be combined with Eqs. (5.41) to give

$$\partial_t v_{bx} + (\mathbf{v}_b\cdot\boldsymbol{\nabla})\, v_{bx} = \partial_t v_x + v_x\partial_x v_x + v_y\partial_y v_x + \nu\partial_z^2 v_{bx} \tag{5.44a}$$
$$\partial_t v_{by} + (\mathbf{v}_b\cdot\boldsymbol{\nabla})\, v_{by} = \partial_t v_y + v_x\partial_x v_y + v_y\partial_y v_y + \nu\partial_z^2 v_{by} \tag{5.44b}$$
$$\partial_t v_{bz} + (\mathbf{v}_b\cdot\boldsymbol{\nabla})\, v_{bz} = \nu\partial_z^2 v_{bz}. \tag{5.44c}$$

Here $v_x = v_x(x,y,t)$ and $v_y = v_y(x,y,t)$ are the inviscid velocity components outside the boundary layer.

5.3.2 Perturbation in boundary layer theory

We now apply the same perturbation approach as used in Chap. 2 to obtain equations of first and second order. To first order the equations are easily found from Eqs. (5.44) to be

$$\partial_t v_{1bx} - \nu\partial_z^2 v_{1bx} = \partial_t v_{10x} \tag{5.45a}$$
$$\partial_t v_{1by} - \nu\partial_z^2 v_{1by} = \partial_t v_{10y} \tag{5.45b}$$
$$\partial_t v_{1bz} - \nu\partial_z^2 v_{1bz} = 0. \tag{5.45c}$$

Likewise the second-order equations are readily set up, where we to make things short only present the time-averaged versions,

$$\nu\partial_z^2 \langle v_{2bx}\rangle = \langle(\mathbf{v}_{1b}\cdot\boldsymbol{\nabla})\, v_{1bx}\rangle - \langle v_{10x}\partial_x v_{10x}\rangle - \left\langle v_{10y}\partial_y v_{10x}\right\rangle \tag{5.46a}$$
$$\nu\partial_z^2 \left\langle v_{2by}\right\rangle = \left\langle(\mathbf{v}_{1b}\cdot\boldsymbol{\nabla})\, v_{1by}\right\rangle - \left\langle v_{10x}\partial_x v_{10y}\right\rangle - \left\langle v_{10y}\partial_y v_{10y}\right\rangle \tag{5.46b}$$
$$\nu\partial_z^2 \langle v_{2bz}\rangle = \langle(\mathbf{v}_{1b}\cdot\boldsymbol{\nabla})\, v_{1bz}\rangle\,. \tag{5.46c}$$

In conjunction with an incompressible continuity equation we hereby have the governing equations necessary to solve for a time-independent second-order boundary layer velocity. Since the boundary layer theory is based on an inviscid flow outside the layer, this has the advantage that we do not need to consider any viscous damping in the bulk but can restrict ourselves to the inviscid Helmholtz equation in order to find the driving terms.

To estimate the magnitude of the streaming velocity in the outer part of the boundary layer, we can consider the length scales in e.g. Eq. (5.46a). In the $x-$ and y-direction the derivatives scale inversely with the acoustic wavelength whereas the z-derivative is inverse to δ_ν,

$$\begin{aligned} \partial_x \approx \partial_y &\sim \frac{\omega}{2\pi c_a} \\ \partial_z &\sim \sqrt{\frac{\omega}{2\nu}}. \end{aligned} \tag{5.47}$$

If the bulk first-order velocity has an amplitude U we thereby find

$$U\frac{\omega}{2\pi c_a}U \sim \nu\frac{\omega}{2\nu}|\,\langle v_{2bx}\rangle\,|, \tag{5.48}$$

which is readily seen to give

$$|\,\langle v_{2bx}\rangle\,| \sim \frac{U^2}{\pi c_a}. \tag{5.49}$$

This estimate, which of course also holds for the y-component, is similar to the inviscid traveling wave solution found in Eq. (5.9), although Eq. (5.49) is valid for both standing and traveling waves. It might seem surprising that the boundary streaming velocity, which stems from viscous effects, does not depend on viscosity in similarity to the inviscid estimates. This can be explained by a phenomenological point of view, since the viscosity is both responsible for the momentum transfer driving the streaming as well as viscous damping of the system. In equilibrium these two effects will be balanced and, as they are both governed by viscosity, the streaming velocity will be independent of viscosity. With an expected first-order amplitude on the order of $U \sim 10^{-4}c_a$ the boundary streaming would amount to $|\,\langle v_{2bx}\rangle\,| \sim 10^{-5}\ \mathrm{m\,s^{-1}}$, which is equivalent to a Reynolds number of $Re \sim 10^{-3}$ in our shallow microsystems if the boundary layer streaming velocity is taken to be representative in the entire domain.

Examples of 2D boundary layer flows can be found in e.g. [7, 39], and in Chap. 7 a generalization to 3D will be discussed including a examples of a numerical solution scheme, where the boundary layer velocity can be used as a slip-velocity for computation of the bulk flow. However, in order to do this we must be acquainted with the numerical methods to which the next chapter is dedicated.

Chapter 6

Numerical implementation in Comsol Multiphysics

In order to apply the theory presented in the previous chapters for modeling arbitrarily shaped microsystems we are compelled to employ numerical tools. A variety of numerical methods and software packages are available for different tasks, and in the following we will use the finite element method (FEM). For this purpose the program Comsol Multiphysics^{TM} Version 3.3 (Comsol) will be utilized, and in this chapter some of the general aspects to be aware of will be described, whereas simulations applied to second-order acoustofluidics in microsystems are presented in the next chapters.

6.1 Graphical user interface and scripting

Comsol is a very powerful and versatile FEM tool equipped with a number of predefined physics modes within the fields of e.g. diffusion, electrostatics and fluid mechanics [56] allowing the user to readily solve a large range of standard problems directly from a graphical user interface (GUI). In essence this is done by drawing the structures as in any standard CAD program in either 1D, 2D or 3D whereafter the relevant physical parameters can be applied to the domains and boundary conditions to the boundaries. With the right choice of solvers and mesh resolution, simple problems can hereafter be solved by the push of a button.

However, the problems we are going to solve cannot be considered standard problems and therefore we cannot restrict ourselves to one of the physics modes but have to set up most of the equation systems ourselves. From the GUI this can be done using one of the PDE application modes described in the following sections. Hereby we can combine our own equation system with the user friendly GUI drawing capabilities.

Though allowing for easy setup of many customized problems, the graphical approach has certain limitations when it comes to e.g. systematic investigations, postprocessing and other specialized features. In that case we can turn to scripting, where we can choose either to expand and customize a problem exported from the GUI or write up the entire problem from scratch.

In this work both approaches have been used although we shall not distinguish between the two as the final result is basically the same. MATLAB is used as scripting environment, which allows us to take advantage of the built-in MATLAB functions at the expense of a slight decrease in computational resources. Before going into detail with some of the technicalities of scripting we will present the mathematical representation of coupled PDEs.

6.2 Equation representation

In COMSOL one can choose between three different ways of representing a PDE and boundary conditions, namely the coefficient form, general form, and weak form. We shall in this thesis not discuss the advantages of the individual representations but primarily turn our attention towards the general form.

The formulation of a PDE in the general form is as follows for the m^{th} variable

$$\boldsymbol{\nabla} \cdot \boldsymbol{\Gamma}_m = f_m, \qquad \forall\, (x, y, z) \in \Omega \tag{6.1}$$

where $\boldsymbol{\Gamma}_m$ is denoted the flux vector [56] and f_m is a scalar source field. Depending on the number of dependent variables being either pure scalars or scalar vector components, one or more flux vectors are required to describe an equation system. In a vector equation each flux vector can be regarded components of a tensor, which in case of the Navier–Stokes equation would be the stress tensor.

The Neumann and Dirichlet boundary conditions are implemented as

$$-\mathbf{n} \cdot \boldsymbol{\Gamma}_m = G + \frac{\partial R_n}{\partial u_m}\mu_n, \qquad \forall\, (x, y, z) \in \partial\Omega \tag{6.2a}$$

$$R_n = 0, \qquad \forall\, (x, y, z) \in \partial\Omega, \tag{6.2b}$$

where u_m is the dependent variable and μ_n a Lagrange multiplier [56] for the n^{th} boundary element.

The implementation of an equation in the general form is not unique but in some instances the sequence and choice of representation in systems of multiple variables can affect the boundary conditions [56], which one has to be aware of.

6.2.1 Example: The Helmholtz equation

As an illustrative example we can write up a 2D Helmholtz equation as given by Eq. (2.39). If solving for the pressure p in a single domain we have a scalar equation in one variable why we only need one flux vector, and the equation can be formulated as

$$\boldsymbol{\Gamma} = \begin{bmatrix} \partial_x p \\ \partial_y p \end{bmatrix} \tag{6.3a}$$

$$f = -\frac{\omega^2}{c_a^2} p. \tag{6.3b}$$

In the simplest configuration we can assume either an infinitely hard boundary corresponding to a homogeneous Neumann condition or alternatively an infinitely soft boundary corresponding to a homogeneous Dirichlet condition, which have to be defined for each boundary segment surrounding our domain. Inhomogeneous and combined boundary conditions can be defined in the same manner based on Eqs. (6.2).

6.3 Structure of a finite element problem

Now the different parts of a script necessary for defining and solving an equation system will be presented, using the 2D Helmholtz equation with a Neumann condition in a circular geometry as example. The following source code examples are based on a script exported from the GUI and subsequently customized. The entire script can be found in App. G and a corresponding simpler script only containing the necessary components is given in App. H.

Before defining the problem we start by clearing the workspace.

```
% Reset and clear environment
clear all, close all, clc, flclear fem
```

Hereafter MATLAB and COMSOL constants and variables are defined. In this case we define the frequency around which we want to search for eigenvalues and the speed of sound in the domain. In analogy with `fem.const` we can also define analytical expressions in `fem.expr`, which can ease notation for more complicated equation systems.

```
% Manually defined search frequency
fsearch=1e6;

% Constants
fem.const = {'c','1483'};
```

A necessity for solving a problem is a well-defined geometry. For this problem we only have a single domain being a circle with a radius of 1 mm centered at $(x, y) = (0, 0)$, but for more extensive problems several geometric domains can be defined to which one can subsequently apply individual physical parameters.

```
% Geometry
g1=ellip2('1e-3','1e-3','base','center','pos',{'0','0'},'rot','0');
```

The next step is to define the mesh, where it is particularly important to choose the correct mesh size. In general the resolution increases with decreasing mesh size, but the correspondingly increasing demands on memory and CPU sets natural limits on the mesh size. For acoustics the governing length scale is the wavelength and we should thus choose a mesh size able to resolve the wavelength, where ten or more points per wave length is an advisable minimum for reliable results. In the following we use a default triangular mesh, where the property `'hmax'` sets the maximum element size. Many other types and properties are available but will not be treated in details here.

```
% Initialize mesh
fem.mesh=meshinit(fem,'hmax',5e-5);
```

The geometry and resulting mesh is shown in Fig. 6.1

To tell COMSOL which equation system to use we must define the application mode being the general form, the dependent variables and the finite element type. In this example we use second-order Lagrange elements, but higher orders can be used on the expense of memory, which could be advantageous if the solution is to be used as input to another equation system.

```
appl.mode.class = 'FlPDEG';
appl.dim = {'p','p_t'};
appl.shape = {'shlag(2,''p'')'};
```

In contrast to the previous excerpts we now observe the syntax `appl.dim` and not `fem.dim`, which allows for several coupled systems each defined in an individual application mode `appl` but within the same `fem` environment. Thus, as we in this example do only consider the Helmholtz equation it is not strictly necessary to make use of application modes as is also demonstrated in App. H.

We now define the Neumann boundary condition by the command `bnd.type` and apply it to all four segments by `bnd.ind`.

```
bnd.type = 'neu';
bnd.ind = [1,1,1,1];
```

In general one can have different boundary conditions on individual parts of the perimeter and `bnd.type` converts to a list of conditions where `bnd.ind` points to the relevant elements of the list.

The components of $\mathbf{\Gamma}$ and f from Eqs. (6.3) can now be defined by the commands `equ.ga` and `equ.f`, respectively. As can be seen the name `'lambda'` is used for the angular frequency. This is due to the fact that `'lambda'` is the default name recognized as the eigenvalue by the COMSOL eigenvalue solver, although one can choose to rename the default value.

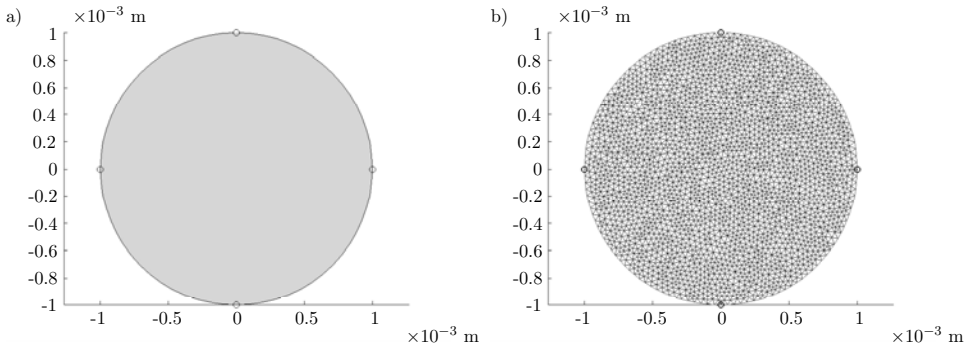

Figure 6.1: a) Geometry for the Helmholtz problem. Notice the segmentation of the boundary into four parts. b) The triangular mesh with maximum element size of 5×10^{-5} m.

```
18 equ.f = '-lambda^2/c^2*p';
19 equ.ga = {{{'px';'py'}}};
```

Here it is worth noting that derivatives of dependent variables can be written with the syntax $\partial_i p =$'pi' and $\partial_i \partial_j p =$'pij' where 'i' and 'j' are any of the independent variables x and y.

The two following commands combine the application modes into a full system and extends the mesh to the chosen finite elements as the last step before solving the problem.

```
20 % Multiphysics
21 fem=multiphysics(fem);
22 % Extend mesh
23 fem.xmesh=meshextend(fem);
```

Since the chosen boundary condition is equivalent to rigid walls the Helmholtz equation will be quantized as was shown in Sec. 3.1.2 and it is thus obvious to solve the problem with an eigenvalue solver.

```
25 % Solve problem for 6 eigenvalues
26 fem.sol=femeig(fem, ...
27     'solcomp',{'p'}, ...
28     'outcomp',{'p'}, ...
29     'neigs',6,...
30     'shift',2*pi*fsearch);
```

The eigenvalue solver has been specified to solve for and output 'p' by searching for six eigenvalues and corresponding eigenmodes around the angular frequency specified by the previously defined `fsearch`. As we have solved an eigenvalue problem, any solution can be multiplied with an arbitrary number and the amplitude is thus not defined. When using Comsol the amplitude is determined by a normalization after the degrees of freedom D as given in [57],

$$\frac{1}{N}\sum_{m}^{N}|D_m|^2 = 1. \tag{6.4}$$

Thus, it must be stressed that when analyzing output from a Comsol eigenvalue solver possible differences in amplitude between the solutions must not be interpreted as some eigenmodes being stronger than others as no such phenomenon can be defined in an eigenvalue problem. Distinction between strong and weak modes can only be determined when modeling an extended system including an actuator driven with a prescribed frequency.

The last step in the script is postprocessing where the results can be exported, processed and visualized in various ways. In Fig. 6.2 we have shown a surface plot of the first of the found eigenmode with the postprocessing function **postplot**.

6.4 Solvers

In the previous example we used the solver **femeig** to solve an eigenvalue problem. However, a collection of other solvers are available depending on the problem. In this thesis

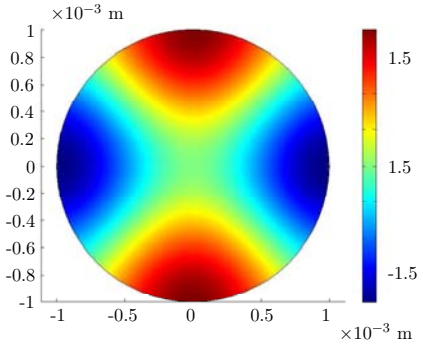

Figure 6.2: The solution corresponding to the Helmholtz equation with Neumann conditions for the eigenvalue $\omega = 4.5 \times 10^6$ s^{-1}. The solution is normalized by Eq. (6.4).

we will make use of the eigenvalue solver **femeig** as well as a stationary solver **femstatic**, which can solve linear as well as nonlinear problems. In the following a short overview of the relevant properties will be given.

We are already acquainted with the properties `'solcomp'` and `'outcomp'`. These determine which equation components to solve for and which to store in the solution object, respectively. In the Helmholtz example we only have one component `'p'` and thus these properties are superfluous, but in the next section we will see how they come into play when solving a coupled equation system.

Two properties that will be demonstrated later are `'init'` and `'u'`, which defines the initial value for the variables to solve for and the value of variables not solved for, respectively. Especially the last property is important, when one wants to build a solution on already computed values.

Independently of whether an eigenvalue or stationary solver is chosen, the problem will normally be split into a number linearized subsystems solved by linear system solvers [57], which can be specified with the property `'linsolver'`. These solvers are either iterative or direct and have impact on the solution process amongst other things in terms of stability, computation time and memory consumption, why it is important to choose the right solver for a given problem. We shall not dwell on algorithms and technicalities here but only report that from tests with the different solvers the default direct `UMFPACK` solver has been found the best overall choice in terms of speed and stability for the type of problems treated in this thesis although demanding a fairly high amount of memory.

6.4.1 Equation structure for eigensolver

In Chap. 2 three representations of the Helmholtz equation were found, namely the inviscid Eq. (2.39), the lossy Eq. (2.52) and the corresponding series expansion Eq. (2.56). In Sec. 6.3 we have already seen that the inviscid Helmholtz equation is easily implemented and solved as an eigenvalue problem. However, when it comes to the series expanded Helmholtz equation this has a general mathematical representation of the form

$$\nabla^2 \phi = -\omega^2 \left(a + b\omega\right)^2 \phi \tag{6.5}$$

where a and b are complex constants and ω a real angular frequency. This formulation is not found in the standard COMSOL application why it has to be investigated, if it is compatible with the solver. Extensive tests extending the inviscid Helmholtz equation by stepwise introducing complex constants and linear combinations of eigenvalues of different orders have been performed. As most of the intermediate results are not of interest for the problems we consider, we will not go into details with these but only conclude that it is not possible to obtain prudent results with the problems formulated as Eq. (6.5) in a COMSOL eigenvalue solver as was anticipated for a dissipative system in Sec. 2.3.1.

This is an important observation since we are thus forced to use the results of the inviscid Helmholtz equation as a basis for development of the viscous fields.

6.5 Coupling perturbed equation systems

We are interested in modeling second-order effects based on resonances in various geometries and must therefore find a way to couple between first-order and second-order equations. For this purpose COMSOL excels with its very efficient and user friendly multiphysics feature. With this it is possible to combine various equation systems to a fully coupled system, which can be solved with one of the COMSOL solvers. Examples of preconfigured applications in COMSOL of interest for LOC systems include fluid-structure and fluid-thermal interaction combining fluid mechanics with structural mechanics and heat transfer, respectively [56].

However, our perturbative system differs from most of the predefined applications in two ways. First of all our first-order fields must not be dependent on the second-order quantities as the perturbation approach implies a one-way coupling from first to second order. The other point is that we are aiming to couple an eigenvalue problem to a time-independent problem. These aspects entails the use of two different solvers in a consecutive manner.

In COMSOL this is not a standard configuration, but it can be implemented with some manually performed scripting. A number of different methods have been implemented and tested with varying success, where the following solver script has been found to be the best method. The method is of course not restricted to acoustofluidics but is a general method, which can be used for any system with a one-way coupling from an eigenvalue problem to a time-independent problem.

```
% Solve eigenvalue problem
fem.sol=femeig(fem, ...
    'solcomp',{'p'}, ...
    'outcomp',{'p'}, ...
    'neigs',neig, ...
    'shift',2*pi*fstart);
fem1=fem;

for solcount=1:length(fem1.sol.lambda)
    % Compute initial value
    sol1 = asseminit(fem1,'init',fem1,'solnum',solcount);
```

```
12      % Solve time-independent problem
13      fem.sol=femstatic(fem, ...
14          'init',sol1, ...
15          'u',sol1, ...
16          'solcomp',{'v2','u2','p2'}, ...
17          'outcomp',{'p','v2','u2','p2'});
18      % Save solution in dummy
19      uDummy(:,solcount)=fem.sol.u;
20  end
21  % Combine solutions and eigenvalues
22  fem.sol=femsol(uDummy,'lambda',fem1.sol.lambda);
23  clear uDummy; clear fem1;
```

Here we see a practical implementation of the solver properties `'u'`, `'init'`, `'solcomp'` and `'outcomp'` described in Sec. 6.4. The function **asseminit** creates a new solution object `sol1`, which can be used for passing initial values and variables to the **femstatic** solver. The property `'solnum'` allows us to take out the solutions from the eigenvalue solver one at a time, which is necessary as the stationary solver can only solve for one input. This further implies that the second solver must be called for each eigenmode, here implemented by a MATLAB **for** loop.

Unfortunately the eigenvalues are not transferred automatically. This can be rectified by creation of the temporary variable `uDummy`, which is combined with the eigenvalues to form the final solution object `fem.sol` by the function **femsol**. Hereby `fem.sol` contains the complete sets of solutions `'p'`, `'p2'`, `'u2'`, `'v2'`, and `'lambda'` with the number of sets defined by `neig`.

6.6 Minor technical pitfalls

During the implementation of various scripts a number of problems were encountered. Fortunately many of these give rise to either warnings, fatal errors or results appearing evidently wrong, whereby the flaws can be detected and solved. However, a few pitfalls not accompanied by any warnings or other immediate signs were found. These are primarily connected to the handling of differentiation and complex numbers.

First of all it is only possible to compute derivatives of the dependent variables up to second order. If derivatives higher than this are attempted COMSOL simply puts the derivative equal to zero in the entire domain, which for instance results in a null value for the Laplacian of the acoustic velocity based on a pressure eigenvalue solution as is realized from Eqs. (2.29) and (2.31). The deficiency can be resolved by setting up an intermediate weak form equation system with the second derivative as output. This new variable can be differentiated once or twice to give the third and fourth derivative of the original variable. Although stable the method is computationally heavy and should if possible be substituted by a proper preparatory analytical work. An example of such an implementation can be found in App. I.

The second issue concerns the differentiation of complex expressions and variables. Although mathematically speaking it should not matter if differentiation is done before or

after taking the real part, imaginary part or complex conjugate of an expression the order is important in COMSOL. When differentiating complex expressions one must always perform the differentiation before conjugating or taking real or imaginary part. This implies that `'conj(diff(p,x))'` is correct, whereas `'diff(conj(p),x)'` results in a null output. The syntax applies to both dependent variables and regular expressions such as `'sin(x)'`.

Although not directly being an error, a final detail to be aware of is the behavior of solutions near sharp geometric transitions such as a convex corner. For a Helmholtz equation solved with Neumann conditions in such a geometry, one can experience numerical difficulties if the derivatives of the solution are to be computed, as well as any system with slip conditions experience difficulties these places. This can partly be remedied by a corner smoothing method, which is a built-in feature in the COMSOL Navier–Stokes application mode [56]. As we will not employ this in the following the eager reader is referred to App. E and J for more details.

With the information in the previous sections we are now ready to treat the setup of the acoustofluidic equations in the next chapter.

Chapter 7

Streaming results in microsystems

In the following we will combine the theoretical work from the previous chapters with numerical implementations in COMSOL with the aim of simulating acoustic streaming in resonant microsystems. As a reference for validation or dismissal of the simulations we will use the work reported by Hagsäter *et al.* [1].

For the type of shallow resonating systems presented in Chap. 1, it has by Jensen [32] been shown that 2D models are very well suited for describing the acoustic eigenmodes as long as the wavelength is more than twice the height of the resonating chamber in which case dynamics in this dimension is highly suppressed. The modes we will consider in the following comply with this demand, and thus we shall restrict ourselves to two dimensions.

We begin by implementation of the first- and second-order equations for the streaming based on viscous bulk dynamics before we continue to a treatment of the boundary layer theory and end up with a short section on considerations for other loss mechanisms.

7.1 Implementation of first-order system

When setting up a model for the microsystems we must consider how much of the device and environment to include, which is a compromise between the exactness and computational needs. As the systems of our interest are water filled reservoirs in an acoustically hard silicon environment surrounded by air we can from the material parameters found in Table. 3.1 observe a significant mismatch in the characteristic impedance between water and silicon and silicon and air. Due to this mismatch we can approximate the silicon device with infinitely hard resonator wall without unacceptable deviations in the eigenmodes from a model including the silicon [32], and this simplified geometry will serve as our primary model in the following.

7.1.1 Actuation by accelerating walls

We know that the viscous system cannot be solved as an eigenvalue problem and we thus have to find a method for exciting the eigenmodes. Due to the two-dimensional restriction we cannot as such model a base mounted actuator and therefore we have to come up with a way to imitate an actuation mechanism and determine the excitation frequency.

One obvious approach is to take the non-driven inviscid eigenmodes as a starting point. Since the viscous damping coefficient is very low, the resonance frequency for the damped and undamped systems will essentially be the same as noticed in Sec. 3.1.3, and we can therefore use the inviscid eigenfrequency as our excitation frequency. To actuate the system we can choose to give the surrounding walls a normal acceleration as done in our 1D examples in Chap. 3. However, we do not know how the acceleration is to be geometrically distributed along the boundaries and if it must be individually specified for each eigenmode, which could be an issue for a damped system.

Again we can take advantage of the inviscid eigenmodes. When finding the these we assume the walls to be impermeable and acoustically and mechanically stiff. However, if we assume that the walls in our 2D model are no longer completely mechanically stiff although still acoustically hard, we could imagine their shape would be affected by the pressure found by the eigensolution as illustrated in Fig. 7.1 with a flexible membrane mounted on springs.

Using this model it is now reasonable to assume that we can drive a given damped resonance by forcing a normal acceleration on the walls with the same shape as the pressure distribution found from the undamped eigenmode. Initially we can test the model by solving two coupled inviscid Helmholtz equations with a solver implementation similar to the one presented in Sec. 6.5. If we denote the pressure from the two systems $p_{10}^{(1)}$ and $p_{10}^{(2)}$, respectively, the two boundary conditions are

$$\mathbf{n} \cdot (-\frac{1}{\rho_0} \boldsymbol{\nabla} p_{10}^{(1)}) = 0, \qquad \forall (x, y) \in \partial\Omega \tag{7.1a}$$

$$\mathbf{n} \cdot (-\frac{1}{\rho_0} \boldsymbol{\nabla} p_{10}^{(2)}) = C p_{10}^{(1)}, \qquad \forall (x, y) \in \partial\Omega, \tag{7.1b}$$

where C is an arbitrary amplitude scaling factor. An example of a simulation is given in Fig. 7.2 showing normalized plots, i.e. amplitudes of the order of unity, for $p_{10}^{(1)}$ and $p_{10}^{(2)}$ as well as the difference between these. The difference is on the order of 10^{-11}, which is very satisfactory for a numerical simulation considered the actuated system is only restricted from divergence due to the numerical resolution. Alternative spatial distributions of the acceleration along the boundaries have also been tested to be able to recreate the eigenmode, but the reported method has been found to be slightly more accurate.

7.1.2 Actuation of viscous system

With this we can now apply the same approach for actuating a viscous system. As the viscous system is not to be solved as an eigenvalue problem, it can be represented in

Figure 7.1: Schematic illustration of the shape of a flexible wall impacted by standing waves.

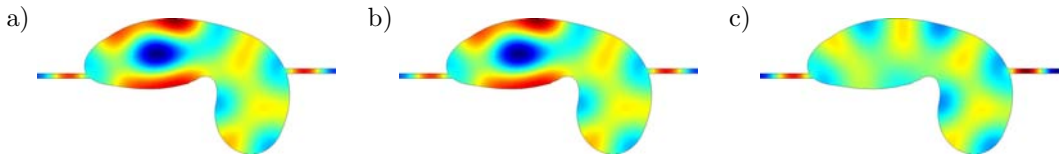

Figure 7.2: Normalized solution of the inviscid Helmholtz equation solved with COMSOL in an arbitrary geometry as a) eigenvalue problems in $p_{10}^{(1)}$ with hard walls and b) stationary problem in $p_{10}^{(2)}$ with normal acceleration coupled from the eigenvalue solution. c) shows the difference between the two normalized pressure plots, which is on the order of 10^{-11}. The simulations use second-order Lagrange elements with a maximum mesh size of $\sim 15 \times 10^{-3}\lambda$ and the red areas are maxima and blue minima.

several ways using either the coupled continuity and Navier–Stokes equations Eqs. (2.13) and (2.12) or the lossy Helmholtz equation with or without series expansion as given in Eqs. (2.52) and (2.56). One might argue that the Navier–Stokes equation should be the implementation of choice, since this does not restrict $\mathbf{v}_1$ to a gradient as is the case when using the Helmholtz equation in ρ_1 followed by a calculation of $\mathbf{v}_1$ from Eq. (2.76). However, due to the low viscous damping the latter approach is justified by Sec. 2.4.

In contrast to the boundary condition in Eq. (7.1b) a viscous Helmholtz equation must now employ Eq. (2.76) as an acceleration condition. Assuming a normal wall velocity v_w we thereby get the viscous equivalent condition to Eq. (7.1b)

$$\mathbf{n} \cdot \boldsymbol{\nabla} p_1 = \mathrm{i}\frac{\rho_0 \omega}{(1 - \mathrm{i}\gamma)} v_w, \qquad \forall (x, y) \in \partial\Omega, \tag{7.2}$$

where v_w for a system driven by an inviscid solution could be $v_w = Cp_{10}$ in analogy to Eq. (7.1b). Models coupling a numerically determined boundary velocity to the continuity and Navier–Stokes equations as well as to the lossy Helmholtz equation in various geometries have been implemented and tested. In the following, however, a simpler approach based on the analytical solution for a square found in Sec. 3.1.4 will be presented, since this enables us to compare numerical and analytical results.

The lossy Helmholtz equation is implemented in the exact same way as the inviscid example in Chap. 6 with the exception that it is solved as an actuated stationary problem with the boundary condition given in Eq. (7.2) and the inviscid wave number k_0 in the Helmholtz equation is replaced by the corresponding viscous wave number

$$k = \frac{k_0}{\sqrt{1 - \mathrm{i}\gamma}}. \tag{7.3}$$

The implemented script can be found in App. K.

It is obvious that we due to the viscous damping term need to resolve two different orders of magnitude simultaneously, which can be a problem for a numerical solution. As seen from Fig. 7.3 this is manifested as a solution where the numerically computed viscous contribution differs significantly from the analytical result. The simulation has

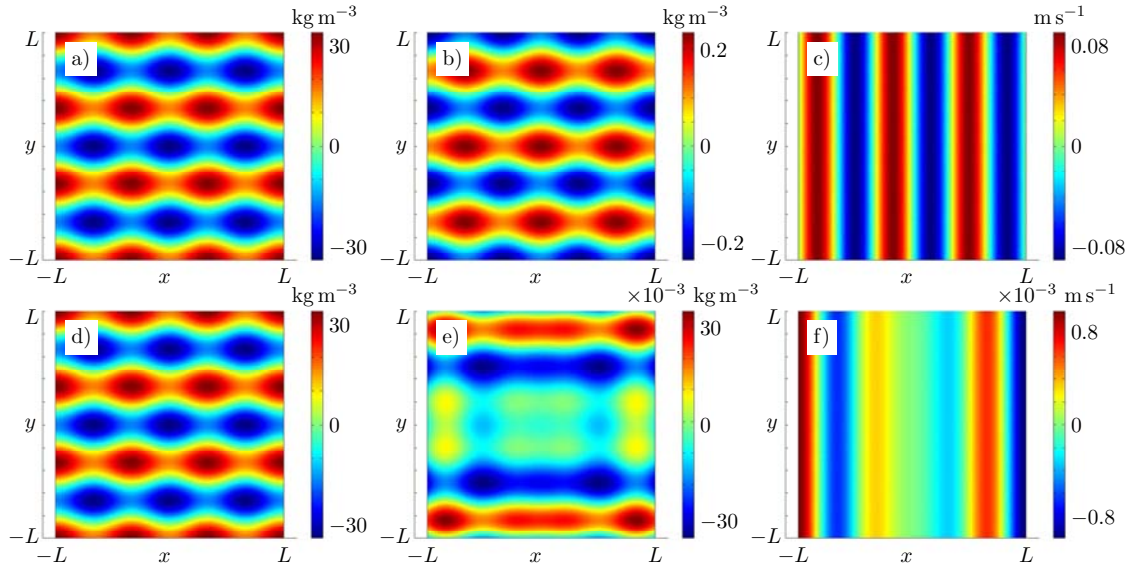

Figure 7.3: Comparison of numerically and analytically solved lossy Helmholtz equation in a water filled square of side length $2L = 2$ mm actuated at $\omega \approx 1.3 \times 10^7$ s^{-1} with a damping coefficient of $\gamma \approx 1.7 \times 10^{-5}$. The upper row shows the numerically computed fields a) Re $\{\rho_1\}$, b) Im $\{\rho_1\}$ and c) Re $\{v_{1x}\}$. The lower row d)-f) shows the corresponding analytically determined fields. It is obvious from b) and e) and c) and f) that the numerical simulation cannot resolve the two orders of magnitude simultaneously. The simulation use second-order Lagrange elements with a maximum mesh size of $\sim 5 \times 10^{-2}\lambda$.

been performed with second-order Lagrange elements with a maximum element size of 'hmax' $\sim 5 \times 10^{-2}\lambda$ in the standard 2×2 mm^2 water-filled chamber at an angular frequency of $\omega \approx 1.3 \times 10^7$ s^{-1} corresponding to a damping coefficient of $\gamma \approx 1.7 \times 10^{-5}$.

By increasing the viscosity with all other parameters kept constant the numerical and analytical solutions do converge after a few orders of magnitude increase, but for realistic damping coefficients the method is not suitable. The same conclusion holds for implementations of the continuity and Navier–Stokes equations, which furthermore have the disadvantage of boundary conditions directly in $\mathbf{n} \cdot \mathbf{v}_1$ calling for the use of corner smoothing methods in complex geometries. Furthermore, since we must resolve two different orders of magnitude simultaneously the method is also highly sensitive to the numerical conditions in terms of amongst other things mesh size.

7.1.3 Double perturbation method

Since no numerically stable solution was found in the previous section, we now investigate another approach, namely the double perturbation scheme introduced in Sec. 2.4, where we know the source terms ρ_{10} and $\mathbf{v}_{10}$ from the inviscid Helmholtz equation. As the resonance boundary conditions being a Neumann condition in ρ_{10}, which is equivalent to a no-stress condition in velocity, are fulfilled with the inviscid solution, the only boundary condition suitable for the viscous part $\mathbf{v}_{11}$ is a Dirichlet condition in $\mathbf{n} \cdot \mathbf{v}_{11}$ in order not

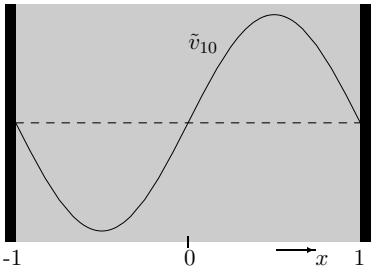

Figure 7.4: 1D normalized system with inviscid resonance $\tilde{v}_{10}$ between two acoustically hard walls.

to alter the value of $\mathbf{v}_1$ in the normal direction on the boundary. If the system is assumed not to be actuated, the Dirichlet condition would be trivial in both $\mathbf{v}_{10}$ and $\mathbf{v}_{11}$, whereas an actuated system can have inhomogeneous Dirichlet conditions in $\mathbf{v}_{11}$.

7.1.4 Double perturbation at resonance

For a full numerical implementation using the inviscid Helmholtz equation as a basis for driving the full system, a possible solution scheme could be implemented as the follows,

- Find ρ_{10} and $\mathbf{v}_{10}$ from the inviscid Helmholtz equation in ρ_{10}.
- Compute ρ_{11} and $\mathbf{v}_{11}$ from Eqs. (2.65) and (2.66) with a normal Dirichlet condition.
- Compute ρ_1 and $\mathbf{v}_1$ from Eqs. (2.60b) and (2.60c).

In such an implementation with acoustically hard resonator boundaries it is obvious that the boundary conditions entail zero normal velocity in $\mathbf{n}\cdot\mathbf{v}_{10}$. To examine the consequences of this we consider Eq. (2.74), which for simplicity is given in one dimension,

$$\partial_x^2 v_{11} = -k_0^2 v_{11} - \mathrm{i}\gamma k_0^2 v_{10}. \tag{7.4}$$

Now, let us consider a normalized 1D system with hard walls as sketched in Fig. 7.4, where the inviscid resonance $\tilde{v}_{10} = U \sin \pi x$ has been established.

Given Eq. (7.4) is a linear ordinary differential equation (ODE), the solution can be composed by a homogeneous and inhomogeneous solution found to be the following for the chosen inviscid resonance at $k_0 = \pi$

$$\tilde{v}_{11} = K_1 \cos \pi x + K_2 \sin \pi x + \mathrm{i}\frac{1}{2}\gamma U \left(\pi x \cos \pi x - \frac{1}{2} \sin \pi x \right), \tag{7.5}$$

where K_1 and K_2 are unknown constants. If we initially assume the system not to be actuated, we must apply trivial Dirichlet conditions at $x = \pm 1$ with the result

$$\mathrm{i}\frac{1}{2}\pi\gamma U - K_1 = -\mathrm{i}\frac{1}{2}\pi\gamma U - K_1. \tag{7.6}$$

This leads to the, at first sight, peculiar demand

$$\gamma U = 0 \tag{7.7}$$

stating that it is not possible to sustain a viscous system without any actuation. If we apply the previously used actuation with antisymmetric walls $\tilde{v}_{11}(\pm 1) = \pm\omega\ell$, we find that the homogeneous solution of Eq. (7.5) cannot satisfy the condition as the cosine term is symmetric and the sine terms is zero at the boundaries. Thus the boundary conditions must be satisfied by the inhomogeneous part of the solution. It is readily found that

$$K_1 = 0, \tag{7.8}$$

which leads to the total solution for $\tilde{v}_1 = \tilde{v}_{10} + \tilde{v}_{11}$

$$\tilde{\mathbf{v}}_1 = U \sin \pi x + \mathrm{i}\frac{1}{2}\pi\gamma U x \cos \pi x + \left(-\mathrm{i}\frac{1}{4}\gamma U + K_2\right) \sin \pi x. \tag{7.9}$$

Although to fit this with the boundary conditions $\tilde{\mathbf{v}}_1(\pm 1) = \pm\omega\ell$ allows only for a certain value of U, we still do not have any restriction on K_2 making the solution inconsistent with the one found analytically in Eq. (3.14a). This is a noteworthy example of a problem, which can be solved directly by analytical means but fails when perturbed, in contrast to most problems, where perturbation is applied to aid the solution process. It can, however, be shown that the series expanded velocity Eq. (3.15) at resonance fulfills Eq. (7.4) although it is not possible to compute the solution directly from Eq. (7.4).

7.1.5 Double perturbation off resonance

Let us now reverse the situation and let the inviscid velocity $\mathbf{v}_{10}$ be actuated off resonance, which is possible without divergence. With the anti-symmetric solution found in Eq. (3.5) the general solution to Eq. (7.4) in a system with actuators at $x = \pm L$ becomes

$$\tilde{v}_{11} = \left(K_1 + \mathrm{i}\frac{1}{2}k_0 U\gamma x \frac{1}{\sin k_0 L}\right) \cos k_0 x + \left(K_2 - \mathrm{i}\frac{1}{4}U\gamma \frac{1}{\sin k_0 L}\right) \sin k_0 x. \tag{7.10}$$

It is now clear, that a trivial Dirichlet condition on $\tilde{v}_{11}$ will couple $\tilde{v}_{11}$ uniquely to $\tilde{v}_{10}$ as neither the sine nor cosine are zero at the boundaries.

To implement this in COMSOL we can use either the representation given in Eq. (2.74) or the Navier–Stokes and continuity equations directly from Eqs. (2.65) and (2.66). Both have been tested with the same result, but the latter method has the advantage of simultaneously solving for both velocity and pressure distribution. In this case we rewrite the time derivative using the $\mathrm{e}^{-\mathrm{i}\omega t}$ convention to find

$$-\mathrm{i}\omega\rho_{11} = -\rho_0 \boldsymbol{\nabla} \cdot \mathbf{v}_{11} \tag{7.11}$$

$$-\mathrm{i}\omega\rho_0 \mathbf{v}_{11} = -c_a^2 \boldsymbol{\nabla}\rho_{11} + \eta\nabla^2 \mathbf{v}_{10} + \beta\eta \boldsymbol{\nabla}(\boldsymbol{\nabla} \cdot \mathbf{v}_{10}). \tag{7.12}$$

A 2D implementation in general form is straightforward with the continuity equation as

$$\boldsymbol{\Gamma}_{\mathrm{cont}} = \mathbf{0} \tag{7.13a}$$

$$f_{\mathrm{cont}} = \mathrm{i}\omega\rho_{11} - \rho_0(\partial_x v_{11x} + \partial_y v_{11y}). \tag{7.13b}$$

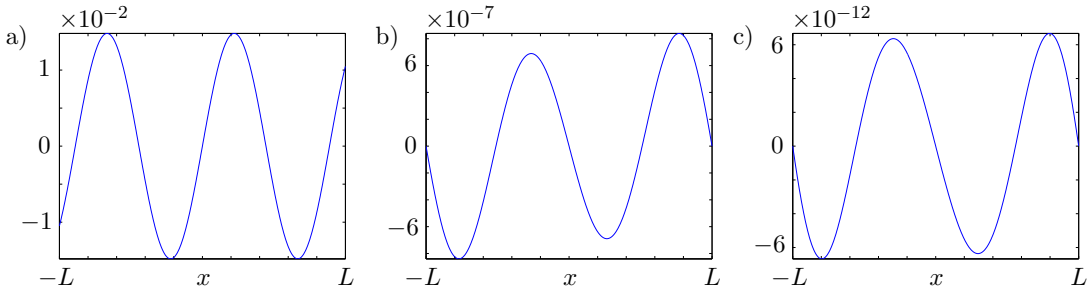

Figure 7.5: 1D solution of double perturbed first-order off-resonance system solved in COMSOL with analytical input. The viscous damping coefficient is $\gamma \sim 10^{-5}$, frequency fits $k_0 L = \frac{9}{4}\pi$ and the system is actuated by anti-symmetric moving walls at $x = \pm L$. a) The inviscid input function $\tilde{v}_{10}$ given in Eq. (3.5) leading to b) the numerically solved viscous part $\tilde{v}_{11}$. In c) is shown the difference between $\tilde{v}_{11}$ solved numerically and calculated from an analytical series solution Eq. (3.14a). A total of 500 mesh elements have been used.

Similarly we can implement the Navier–Stokes equation in a very simple formulation, since it does not contain any derivatives of $\mathbf{v}_{11}$

$$\mathbf{\Gamma}_{\mathrm{NS},x} = \begin{bmatrix} c_a^2 \rho_{11} \\ 0 \end{bmatrix}, \quad f_{\mathrm{NS},x} = \mathrm{i}\omega\rho_0 v_{11x} + F_{11x} \tag{7.14a}$$

$$\mathbf{\Gamma}_{\mathrm{NS},y} = \begin{bmatrix} 0 \\ c_a^2 \rho_{11} \end{bmatrix}, \quad f_{\mathrm{NS},y} = \mathrm{i}\omega\rho_0 v_{11y} + F_{11y}, \tag{7.14b}$$

where the components of $\mathbf{F}_{11}$ can be deduced from Eq. (2.67). The boundary conditions for v_{11x} are homogeneous Dirichlet conditions whereas ρ_{11} is not restricted.

Although 2D simulations have been made, we are not interested in off-resonance modes. Thus, in the following we only present a 1D example for a visualization of the method, as 1D results are easier to interpret and allows for a more refined mesh. In Fig. 7.5 a simulation of the 1D equivalent to Eqs. (7.13) and Eqs. (7.14) is shown for a system of length $2L = 2$ mm with a wave number arbitrarily chosen off resonance to $k_0 L = \frac{9}{4}\pi$. Using the properties of water, this corresponds to a damping coefficient of $\gamma \sim 10^{-5}$.

As can be seen from the error plot showing the difference between the numerical solution of $\tilde{v}_{11}$ and the corresponding imaginary part of the series expanded analytical solution Eq. (3.14a) the method is numerically very precise for small values of γ. Hereby we can conclude that the double perturbation scheme is well suited for determination of viscous fields in off-resonance systems and could be envisioned as a numerically stable method for e.g. viscous transmission calculations in low-damped systems. The implemented script is given in App. L.

Other approaches to solve the viscous resonant first-order problem have been investigated. These include manually added complex displacements to the inviscid fields, double perturbation with actuated inviscid fields as well as models for the double perturbation scheme with extended geometries. However, none of these have shown satisfactory general results and therefore we will not spend further time on the details.

7.2 Implementation of viscous second-order system

Since the previous sections have shown us that it has not been possible to develop a reliable model for computation of the viscous first-order fields, we cannot use these numerical results as source terms for the second-order effects based on bulk dynamics. This is of course a drawback in the process of developing a tool for analysis of these effects in arbitrarily shaped microsystems, which can only be efficiently executed by numerical computations.

However, for a conceptual treatment of the streaming equations derived in Chap. 5 it is sufficient with a single input eigenmode. Thus we can employ the analytical solution derived in Sec. 3.1.4 as source term to model the behavior in a shallow rectangular chamber. As this partly resembles the eigenmode in Fig. 1.2 we still have an approximate experimental reference for comparison. Furthermore, the numerical errors will be reduced when basing the source terms on analytical expressions.

7.2.1 Converting expressions to Comsol compatible format

Before considering how to represent the equations we must make sure that our syntax complies with Comsol. This becomes important when treating the source terms, where we from Chap. 5 have found these to consist of combinations of products of complex and differential operators. Due to Comsol's inexpedient complex differentiation syntax we must therefore expand all differentiation terms to products of derivatives rather than derivatives of products, as we in the former case can exploit $\partial_i \mathrm{Re}\{f\} = \mathrm{Re}\{\partial_i f\}$.

For both Eqs. (5.14), (5.33) and (5.39) the body forces must be split into $x-$ and $y-$components which are expanded individually. As an example we can from Eq. (5.33) expand the term

$$\nabla^2 \left(\mathrm{Re}\{\tilde{\rho}_1\} \boldsymbol{\nabla} \mathrm{Im}\{\tilde{\rho}_1\}\right). \tag{7.15}$$

Use the following identity to expand Eq. (7.15)

$$\nabla^2(f\boldsymbol{\nabla}g) = f\nabla^2\boldsymbol{\nabla}g + (\boldsymbol{\nabla}g)\,\nabla^2 f + 2(\boldsymbol{\nabla}f)\cdot(\boldsymbol{\nabla}(\boldsymbol{\nabla}g)). \tag{7.16}$$

Taking only the x-component, this can now be written as

$$\nabla^2(f\partial_x g) = f(\partial_x^3 g + \partial_y^2\partial_x g) + \partial_x g(\partial_x^2 f + \partial_y^2 f) + 2(\partial_x f\partial_x^2 g + \partial_y f\partial_y\partial_x g), \tag{7.17}$$

where a similar result of course holds for the y-component as well as analogous calculations can be done for the remaining body force terms in Eqs. (5.14), (5.33) and (5.39). With this formulation it is now easy to differentiate before taking real and imaginary parts, respectively. We also notice that with every terms expressed by products of ρ_1, we get up to third derivatives in ρ_1. With reference to Sec. 6.6 this poses a problem for numerically determined first-order fields, but for the analytical input the intermediate weak form step can be omitted for calculations of the derivatives.

7.2.2 Implementing full system

In Chap. 5 it was hinted that a direct implementation of Eqs. (2.86) and (2.97) can lead to numerical difficulties for low-damped standing waves. Despite of this we choose to implement the system to test this hypothesis, and furthermore the implementation will still be suitable for systems, where the structure of the first-order fields is different.

With the general form the equations can be constructed in COMSOL in various ways, but in the following only one of the implemented versions will be presented. In the direct implementation we solve for three dependent variables, namely $\langle v_{2x}\rangle$, $\left\langle v_{2y}\right\rangle$, and $\langle p_2\rangle$ being the two cartesian components of the streaming velocity and the second-order pressure, respectively. The continuity equation Eq. (2.86) is in general form implemented as

$$\boldsymbol{\Gamma}_{\text{cont}} = \begin{bmatrix} 0 \\ 0 \end{bmatrix} \tag{7.18a}$$

$$f_{\text{cont}} = \partial_x \langle v_{2x}\rangle + \partial_y \left\langle v_{2y}\right\rangle + \frac{1}{2\rho_0}\text{Re}\left\{\tilde{\rho}_1 \left(\partial_x \tilde{v}_{1x}\right)^* + \tilde{v}_{1x}^* \partial_x \tilde{\rho}_1 + \tilde{\rho}_1 \left(\partial_y \tilde{v}_{1y}\right)^* + \tilde{v}_{1y}^* \partial_y \tilde{\rho}_1\right\}, \tag{7.18b}$$

where we have expanded the term $\boldsymbol{\nabla}\cdot\langle\rho_1\mathbf{v}_1\rangle$ to a notation compatible with COMSOL. The Navier–Stokes equation must be split into cartesian coordinates and constitutes together with the continuity equation three coupled systems to be solved for. The implementation is in part analogous to the one found in [32] and is done by including all dependent variables in the flux vectors leaving only the body force components on the right-hand side,

$$\boldsymbol{\Gamma}_{\text{NS},x} = \begin{bmatrix} -\langle p_2\rangle + \eta(1+\beta)\partial_x \langle v_{2x}\rangle \\ \eta\partial_y \langle v_{2x}\rangle + \beta\eta\partial_x v_{2y} \end{bmatrix}, \quad f_{\text{NS},x} = \langle F_x\rangle \tag{7.19a}$$

$$\boldsymbol{\Gamma}_{\text{NS},y} = \begin{bmatrix} \eta\partial_x \left\langle v_{2y}\right\rangle + \beta\eta\partial_y \langle v_{2x}\rangle \\ -\langle p_2\rangle + \eta(1+\beta)\partial_y \left\langle v_{2y}\right\rangle \end{bmatrix}, \quad f_{\text{NS},y} = \left\langle F_y\right\rangle. \tag{7.19b}$$

The body force terms are of course expanded to a suitable representation in the same manner as in the continuity equation. The Dirichlet boundary condition on $\langle\mathbf{J}_2\rangle$ is implemented on all boundaries in accordance to Eq. (6.2b),

$$R_{\langle p_2\rangle} = 0 \tag{7.20a}$$

$$R_{\langle v_{2x}\rangle} = \rho_0 \langle v_{2x}\rangle + \langle\rho_1 v_{1x}\rangle \tag{7.20b}$$

$$R_{\langle v_{2y}\rangle} = \rho_0 \left\langle v_{2y}\right\rangle + \left\langle\rho_1 v_{1y}\right\rangle, \tag{7.20c}$$

where we notice that $\langle p_2\rangle$ is not restricted. As we do not use a numerically computed eigenmode for the source terms, the first-order fields are simple given as expressions using `fem.globalexpr`. The full implementation can be found in App. M.

When solving the full system without decomposition, we get the velocity results shown in Fig. 7.6, whereof it is clear that the streaming velocity is completely blurred by numerical noise, which renders the vector plot of the velocity field useless.

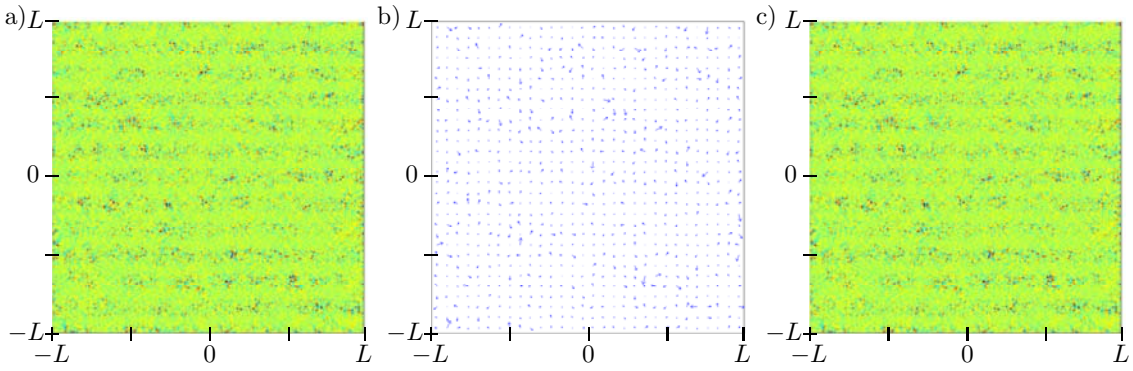

Figure 7.6: Numerical result of simulation of streaming velocity solved by equation system without decomposition, showing a) surface plot of $\langle v_{2x} \rangle$, b) vector streaming field and c) surface plot of $\left\langle v_{2y} \right\rangle$, respectively. The magnitude of the velocity is 10^{-5} m s^{-1} for a first-order pressure of $|p_1| \approx 10^5$ Pa driven at $\omega \approx 1.4 \times 10^7$ s^{-1} giving $\gamma \approx 1.7 \times 10^{-5}$ for water in a chamber with side length $2L = 2$ mm. The results are completely dominated by numerical noise.

The simulations have been performed with the standard material parameters for water in a chamber with side length $2L = 2 \times 10^{-3}$ m. For a first-order solution with $\lambda = 2/3L$ this implies $\omega = 1.4 \times 10^7$ s^{-1} and $\gamma = 1.7 \times 10^{-5}$. A maximum mesh element size of 35 µm corresponding to a resolution of approximately twenty mesh points per wavelength have been used, which is sufficient to resolve a proper conditioned system. Thus we can conclude that the dominating scalar potential in the body force precludes the computation of the streaming velocity.

On the contrary we should not expect any problems in calculating the second-order pressure. This is shown in Fig. 7.7 where both the numerically and analytically computed results is seen. The analytical solution does not take the contribution from the Laplacian of the streaming velocity into account, but since $\langle p_2 \rangle$ is dominated by the $\langle \Phi_F \rangle$ this is of no importance. As expected we are forced to use the decomposed equations in order to

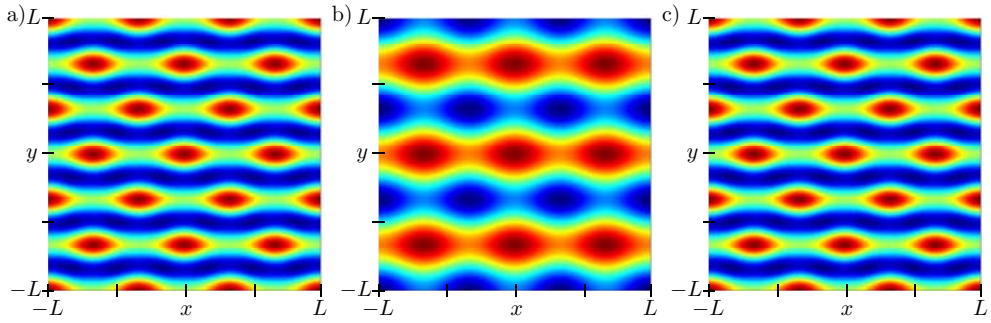

Figure 7.7: a) Numerical computation of $\langle p_2 \rangle$, b) $\mathrm{Re}\{\tilde{p}_1\}$, and c) Analytical calculation of $\langle p_2 \rangle$. Numerical and analytical calculations agree with each other as the damping is low. The amplitudes are $|p_1| \approx 10^5$ Pa and $|\langle p_2 \rangle| \approx 1$ with the same settings as in Fig. 7.6. Red areas are local maxima an blue are minima.

resolve the streaming velocity.

7.2.3 Implementation of decomposed systems

The decomposed systems both with and without explicit inclusion of $\langle \mathbf{v}_{2\mathrm{inc}} \rangle$ are implemented in a similar way as the full system. The incompressible continuity equation is implemented as

$$\boldsymbol{\Gamma}_{\mathrm{cont,inc}} = \mathbf{0} \tag{7.21a}$$

$$f_{\mathrm{cont,inc}} = \partial_x \langle v_{2\mathrm{inc}x} \rangle + \partial_y \left\langle v_{2\mathrm{inc}y} \right\rangle, \tag{7.21b}$$

whereas the decomposed Navier–Stokes equation Eq. (5.33) is implemented as

$$\boldsymbol{\Gamma}_{\mathrm{NSinc,x}} = \begin{bmatrix} -\left\langle p_{2\mathrm{repi}} \right\rangle + \eta \partial_x \langle v_{2\mathrm{inc}x} \rangle \\ \eta \partial_y \langle v_{2\mathrm{inc}x} \rangle \end{bmatrix}, \quad f_{\mathrm{NSinc},x} = -B_{Fx} \tag{7.22a}$$

$$\boldsymbol{\Gamma}_{\mathrm{NSinc,y}} = \begin{bmatrix} \eta \partial_x \left\langle v_{2\mathrm{inc}y} \right\rangle \\ -\left\langle p_{2\mathrm{repi}} \right\rangle + \eta \partial_y \left\langle v_{2\mathrm{inc}y} \right\rangle \end{bmatrix}, \quad f_{\mathrm{NSinc},y} = -B_{Fy}. \tag{7.22b}$$

Here $\mathbf{B}_F$ has been introduced as shorthand notation for the body force density terms in Eq. (5.33). The boundary conditions being no-slip in $\langle \mathbf{v}_{2\mathrm{inc}} \rangle$ are implemented in analogy to Eqs. (7.20), and the full implementation is found in App. N

For the decomposed system given by Eqs. (2.86) and (5.39), the implementation is identical to the full system Eqs. (7.18) and (7.19) with the exception that we solve for $\left\langle p_{2\mathrm{rep}} \right\rangle$ rather than $\langle p_2 \rangle$ and the body force has been altered is to the one found in Eq. (5.39). Thus, we shall not repeat the implementation here but refer to the source code given in App. O.

7.2.4 Comparison of numerical stability

In order to be able to compare the three implemented systems we must artificially increase the viscosity a certain amount as Sec. 7.2.2 has shown that comparisons to the full equation system will otherwise be impossible. Thus, we increase the viscosity three orders of magnitude leading to a attenuation coefficient of $\gamma = 1.7 \times 10^{-2}$, when all other parameters are kept the same as in Sec. 7.2.2. This value for the damping should be resolvable by Comsol in the implementation of the full equation system.

In Fig. 7.8 a comparison of the three implementations is given by a surface plot showing $\langle v_{2x} \rangle$ computed for $\langle \mathbf{v}_2 \rangle$ with and without decomposition, respectively. Between the surface plots is an interpolated cross sectional plot shown for all three implementations. It is clear that the two methods of decomposing the Navier–Stokes equation are equally efficient for reducing the level of numerical noise, whereas the directly implemented method still has a considerable amount of noise even for this fairly high value of $\gamma \sim 10^{-2}$. However, decreasing the damping to a realistic level does not affect the resolution of the decomposed systems, whereas the direct implementation fails as shown previously.

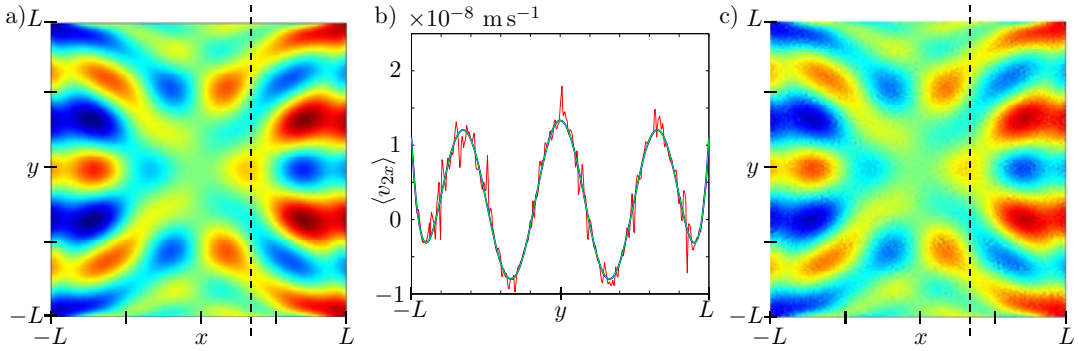

Figure 7.8: Surface plot of $\langle v_{2x} \rangle$ for $\gamma = 1.7 \times 10^{-2}$ for a) decomposed system Eq. (5.39) and c) full system Eq. (5.14). As illustrated by b) the cross sectional plot along the dotted lines, the full system represented by the red fluctuating line converges towards the decomposed solutions plotted as the identical blue and green lines. All parameters except γ are as used in previous examples for a first-order pressure of $|p_1| \sim 10^5$ Pa.

We can get an estimate of the necessary attenuation coefficient for a reliable result of the direct method by a convergence test comparing the direct method with the decomposed system. Such a test is shown in Fig. 7.9 with the measure of convergence being the total mean of the relative deviation between full and decomposed velocity in each interpolated grid point

$$\Delta_c \equiv \text{mean}\left(\frac{|g_{\text{decomp}} - g_{\text{full}}|}{|g_{\text{decomp}}|}\right), \tag{7.23}$$

where Fig. 7.9 uses $g = \langle v_{2x} \rangle$. It can be seen that convergence is not achieved until $\gamma \sim 10^{-1}$.

We have hereby shown that the decomposition method is valuable for enhancing the numerical stability when the body force is dominated by a scalar potential. This solution scheme is of course not restricted to this particular problem of viscous plane waves but applies to any problem with the same structure.

7.2.5 Evaluation of streaming results

Although the decomposition has proved to be numerically efficient this is not tantamount to a physically correct model. We now return to the appropriate value for the viscosity of water and evaluate the results obtained by the decomposed systems, where we shall not distinguish between the two decomposed models as no significant difference between their results have been found. In Fig. 7.10 is shown three velocity fields, namely $\langle \mathbf{v}_2 \rangle$ and the compressible and incompressible components of this.

The amplitudes of both compressible and incompressible components are on the same order of magnitude, and thus none of the two dominates the streaming. In this simulation a source pressure of $|p_1| \approx 10^5$ Pa has been used, giving rise to a streaming velocity of $|\langle \mathbf{v}_2 \rangle| \approx 5 \times 10^{-11}$ m s^{-1}. Given $\gamma = 1.7 \times 10^{-2}$ this is in perfect agreement with the

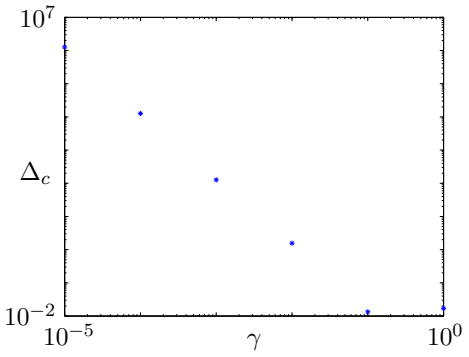

Figure 7.9: Convergence of the direct implementation of the full system in relation to the decomposed system based on Eq. (5.39). Δ_c is computed for $g = \langle v_{2x} \rangle$. Notice the excessive noise for low-damped water like systems and convergence for $\gamma \sim 10^{-1}$.

estimate found in Eq. (5.34). Other values of viscosity and amplitude of first-order fields have been tested all complying with Eq. (5.34), and we can conclude that in this system both the compressible and incompressible component scale with viscosity and the square of the first-order pressure.

At first sight this scaling can seem contradictory to the results found in Eqs. (5.9) and (5.49), which were both independent of viscosity. However, the scaling can be traced back to the underlying expression for the first-order fields Eqs. (3.15) and (3.16), where the amplitude of one of the two harmonic terms in pressure and velocity, respectively, depends on γ. Thus, the three estimates Eqs. (5.9), (5.49) and (5.34) are consistent as the appearance of γ is explicitly coupled to the first-order phase and amplitude, why $\langle \mathbf{v}_2 \rangle$ conceptually only depends on these two quantities.

If we consider the spatial appearance of the three vector fields we obviously find that although the first-order pressure eigenmode with reasonable approximation resembles the measurements shown in Fig. 1.2 the streaming does not at all correspond to the experimen-

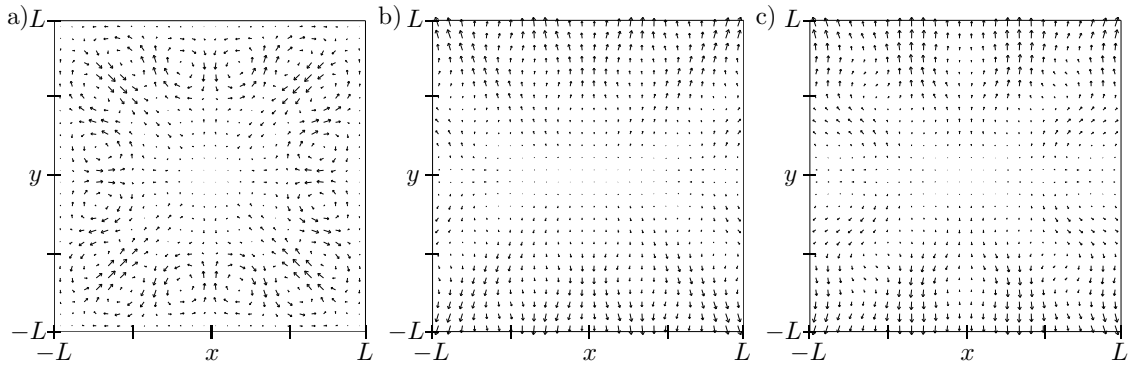

Figure 7.10: Vector representation of the streaming velocity components with vector lengths proportional to velocity, a) $\langle \mathbf{v}_{2\text{inc}} \rangle$, b) $\langle \mathbf{v}_2 \rangle - \langle \mathbf{v}_{2\text{inc}} \rangle = -\rho_0^{-1} \langle \rho_1 \mathbf{v}_1 \rangle$, and c) $\langle \mathbf{v}_2 \rangle$. Results do not resemble experiments and due to mass flux condition velocity seems to penetrate the walls.

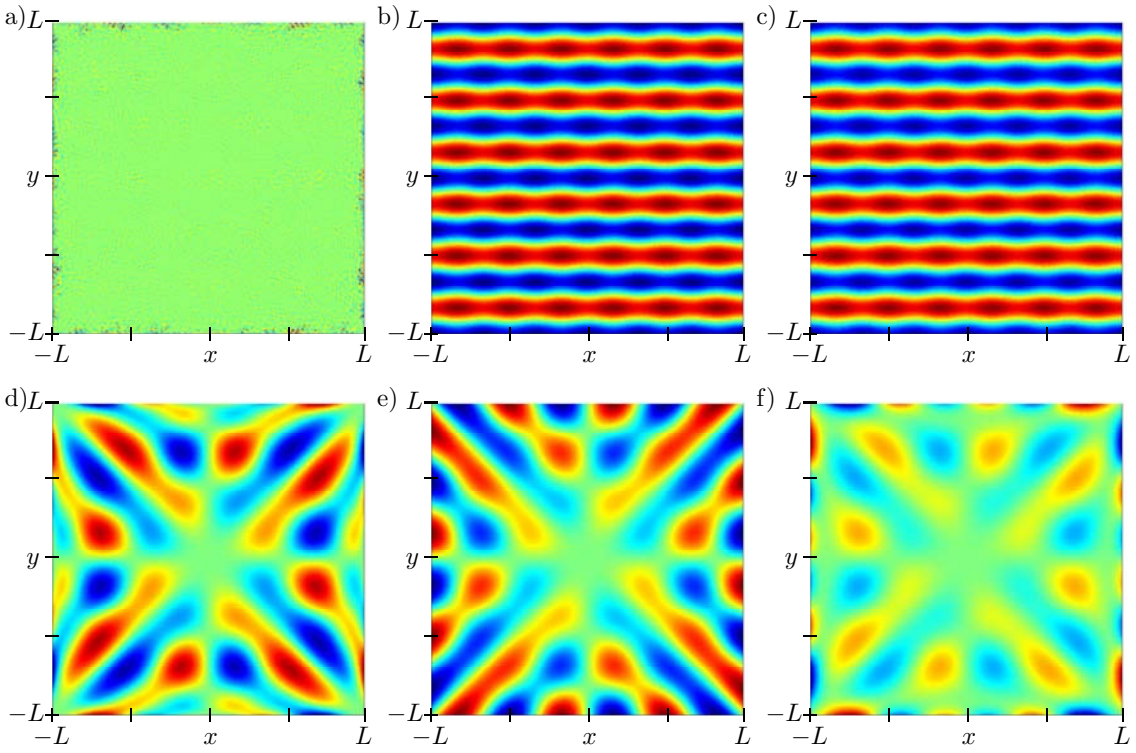

Figure 7.11: Divergence: a) $\boldsymbol{\nabla}\cdot\langle\mathbf{v}_{2\text{inc}}\rangle$, b) $-\boldsymbol{\nabla}\cdot\rho_0^{-1}\langle\rho_1\mathbf{v}_1\rangle$, c) $\boldsymbol{\nabla}\cdot\langle\mathbf{v}_2\rangle$, and vorticity: d) $\boldsymbol{\nabla}\times\langle\mathbf{v}_{2\text{inc}}\rangle$, e) $-\boldsymbol{\nabla}\times\rho_0^{-1}\langle\rho_1\mathbf{v}_1\rangle$, f) $\boldsymbol{\nabla}\times\langle\mathbf{v}_2\rangle$. The incompressible component is of course solenoidal and only displays numerical noise, whereas none are irrotational. The magnitude of the divergence for compressible components is approx. 10^{-7} s^{-1} and vorticity approx. $10^{-7}-10^{-6}$ s^{-1} with the vorticity of the incompressible component being about twice the magnitude of the compressible for $|p_1|\sim 10^5$ Pa. Individual color scales are used for each plot with red as local maxima and blue as minima.

tal observations. As an alternative visualization we can plot the divergence and vorticity rather than the vector fields, where the time averaged vorticity is defined as

$$\langle\boldsymbol{\omega}_2\rangle \equiv \boldsymbol{\nabla}\times\langle\mathbf{v}_2\rangle\,. \tag{7.24}$$

Hereby we get the results given in Fig. 7.11, where the incompressible component naturally is solenoidal except for a minor amount of numerical noise. In contrast to this both the compressible and incompressible component contributes to the vorticity with the magnitude of the incompressible velocity being approximately twice the compressible component. The contribution of $\langle\omega_{2\text{inc}}\rangle$ is most distinct at the boundaries as seen from Fig. 7.11 f) induced by the no-flux condition. Although we do observe vortices, the strength of these do not dominate the flow and due to the divergence being of the same order of magnitude we get a significant outwards velocity at the boundaries, although the mass flux is zero.

We could assert that the reason for the streaming simulations not being in satisfactory agreement with measurements is due to the choice of a first-order field with a high degree

of symmetry. However, as long as the domain is assumed to be surrounded by acoustically impermeable walls any breaking of the symmetry is not suspected to heavily alter neither the mathematical structure of the body force density nor the amplitude estimate given in Eq. (5.34).

In [1] the measured streaming velocity is on the order of $|\langle \mathbf{v}_2 \rangle| \sim 10^{-5}\ \mathrm{m\,s^{-1}}$. If we insert this in Eq. (5.34) the estimated sound pressure necessary to establish this streaming velocity in such a microsystem is found to be $|p_1| \sim 5 \times 10^7$ Pa. Such a pressure is not realistic, and combining this with the fact that the computed pattern did not resemble measurements, we can deduce that the utilized model is not sufficient to describe the acoustic streaming and the magnitude of the velocity is so small that bulk viscous damping can be neglected in streaming calculations for standing waves. Therefore we now turn to the boundary layer theory.

7.3 Streaming from boundary layer theory

So far we have only considered 2D models with boundary conditions surrounding a resonating chamber, which is sufficient for determination of the resonance modes. However, when it comes to the boundary layer theory the two far largest surfaces on which a boundary layer builds up are the top and bottom of the chamber, that has not taken into account previously.

In the following we outline a solution scheme for solving the full 3D problem and present a classical 2D solution subsequently extended to a square geometry.

7.3.1 General solution for first-order fields

Since the purpose of the first-order boundary layer is to adjust the simple inviscid slip condition to the physically correct no-slip condition we can readily define the boundary conditions for $\mathbf{v}_{1b}$, if we for simplify adopt the geometry used in Sec. 5.3.1

$$\mathbf{v}_{1b}(x, y, z = 0) = 0 \tag{7.25a}$$

$$\mathbf{v}_{1b}(x, y, z = \infty) = \mathbf{v}_{10}, \tag{7.25b}$$

where $\mathbf{v}_{10}$ is the inviscid bulk velocity. Although the outer condition is formally stated at infinity, a reasonable value for practical calculations can be approximated by a few times the momentum diffusion length.

A harmonically oscillating first-order velocity field along the boundary in the xy-plane can be formally expressed as

$$\mathbf{v}_{10}(x, y) = \tilde{v}_{10x} \mathrm{e}^{-\mathrm{i}\omega t} \hat{\mathbf{x}} + \tilde{v}_{10y} \mathrm{e}^{-\mathrm{i}\omega t} \hat{\mathbf{y}}, \tag{7.26}$$

where $\tilde{v}_{10x}$ and $\tilde{v}_{10y}$ are arbitrary functions of x and y. Based on this, we can construct a general set of solutions to the boundary layer equations given in Eqs. (5.45) and the incompressible continuity equation $\boldsymbol{\nabla} \cdot \mathbf{v}_{1b} = 0$. The solutions parallel to the surface are

found as a generalization of the example by LL [39] to be exponentially approaching the inviscid bulk velocity as follows,

$$v_{1bx} = \tilde{v}_{10x}\left(1 - \mathrm{e}^{-\varkappa z}\right)\mathrm{e}^{-\mathrm{i}\omega t} \tag{7.27a}$$

$$v_{1by} = \tilde{v}_{10y}\left(1 - \mathrm{e}^{-\varkappa z}\right)\mathrm{e}^{-\mathrm{i}\omega t} \tag{7.27b}$$

where we have introduced the boundary decay number $\varkappa$ [39],

$$\varkappa \equiv \frac{1-\mathrm{i}}{\delta_\nu} = \sqrt{\frac{-\mathrm{i}\omega}{\nu}}. \tag{7.28}$$

It should be noticed that we do not consider the z-component as we are only interested in the solutions parallel to the boundary. Since Eqs. (7.27) are general results for any harmonic field we do not need to compute $\mathbf{v}_{1b}$ numerically from Eqs. (5.45), but can use Eqs. (7.27) directly, provided $\mathbf{v}_{10}$ is known.

7.3.2 Solution scheme for numerical implementation

The second-order boundary layer equations from Eqs. (5.46) are not as simple as the corresponding first-order equations and might call for a numerical solution in the general case. In the following we will therefore outline a proposed solution scheme for solving the boundary layer induced streaming problem in an arbitrary, shallow microfluidic system.

The first step is to solve the Helmholtz equation in p_{10}, which, as previously, can be done in 2D, since we assume no dynamics perpendicular to the chamber top and bottom. This gives us the inviscid first-order bulk velocity $\mathbf{v}_{10}$.

Now we must solve for the boundary layer velocity, which calls for a 3D model. However, with the boundary layer length scale being much smaller than the general chamber geometry we must restrict ourselves to a pseudo 3D shell model as illustrated in Fig. 7.12. Letting the shell thickness w be a few times the momentum diffusion length δ_ν gives us a decent approximation to an infinite distance from the chamber walls. Furthermore, the 2D bulk velocity allows us to restrict the simulations to half the chamber height due to symmetry.

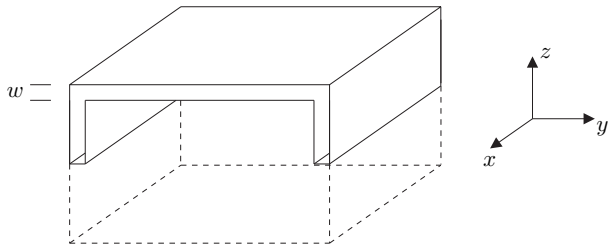

Figure 7.12: Conceptual sketch of a thin computational shell domain of thickness $w \sim \delta_\nu$ inside a larger microfluidic chamber. The shell can be meshed and used to solve for the second-order boundary layer velocity $\langle \mathbf{v}_{2b} \rangle$ with the application of a Dirichlet condition on the outer surfaces and a Neumann on the inner.

The first-order boundary layer velocity $\mathbf{v}_{1b}$ is constructed manually from Eqs. (7.27) and used as source term for the second-order terms $\langle \mathbf{v}_{2b} \rangle$ in Eqs. (5.46). In contrast to the first-order terms we have no knowledge of the value of $\langle \mathbf{v}_{2b} \rangle$ in the bulk, whereas the no-slip condition is still governing at the wall. However, we do know that the streaming velocity must be finite, and thereby we can define the boundary conditions at the inner (0) and outer (∞) edge of the shell as

$$\langle \mathbf{v}_{2b} \rangle (0) = 0 \tag{7.29}$$

$$\mathbf{n} \cdot \boldsymbol{\nabla} \langle \mathbf{v}_{2b} \rangle (\infty) = 0. \tag{7.30}$$

The last step is now to create a full 3D model and pass the boundary layer velocity $\langle \mathbf{v}_{2b} \rangle (\infty)$ as a slip velocity condition for a stationary, incompressible Navier–Stokes and continuity equation from which we can solve for the entire streaming field in the bulk. As the slip velocity boundary conditions give no conditions on the pressure in the Navier–Stokes equation, the numerical stability of the last step can be improved by adding an arbitrary point constraint to the pressure.

7.3.3 A classic streaming solution for infinite plates

Although the aforementioned solution scheme due to limited time has not yet been implemented we can still obtain information on the boundary layer streaming from a classic instructive example, where we combine analytical and numerical methods.

Let us consider two infinite parallel plates separated by a distance $2h$ as illustrated in Fig. 7.13. If a standing wave with one-dimensional dynamics is given by

$$v_{10}(y) = U \cos(k_0 y) \mathrm{e}^{-\mathrm{i}\omega t}, \tag{7.31}$$

it has by amongst others Rayleigh [7] and Landau and Lifshitz [39] been shown that the corresponding second-order boundary layer velocity parallel to the plates at the outer part of the boundary layer is given by

$$\langle v_{2b}(y) \rangle = \frac{3U^2}{8c_a} \sin(2k_0 y). \tag{7.32}$$

Since $\langle v_{2b}(y) \rangle$ is a second-order quantity it is obvious that we have obtained a doubling of spatial periodicity compared to the first-order field. Furthermore, from the conservation

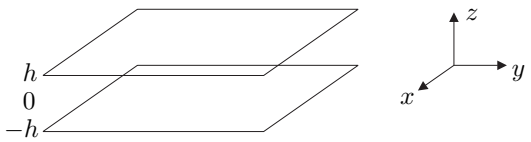

Figure 7.13: Geometry consisting of two infinitely large plates separated by a distance $2h$. A standing wave given by Eq. (7.31) will give rise to time-independent boundary layer velocity components, which can be used to solve the streaming problem between the plates.

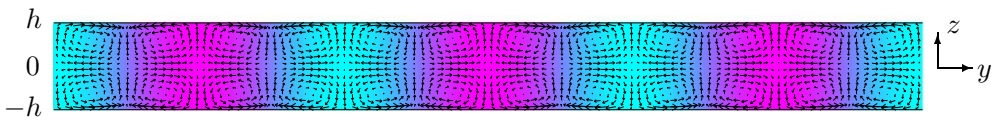

Figure 7.14: 2D streaming pattern between two infinite plates due to a boundary layer velocity Eq. (7.32) on both top and bottom induced by a standing wave given by Eq. (7.31). The vector plot shows the streaming and the surface plot is the first-order standing wave at $t = 0$ with local minima at cyan and maxima at magenta. The problem is solved numerically using COMSOL with an analytical slip boundary velocity of arbitrary amplitude.

of mass we can deduce that the spatially alternating boundary layer velocity must induce velocity components perpendicular to the plates as well.

Although the full analytical solution of the streaming velocity between the plates is well-known [39], we will present a numerical result to illustrate the capability of COMSOL to solve streaming problems from a slip velocity.

In Fig. 7.14 we have shown a vector plot of the streaming velocity based on the slip velocity at $z = \pm h$ given in Eq. (7.32). We observe the how 4×2 vortices are formed within each wavelength of the first-order standing wave illustrated by the surface plot. The figure shows an excerpt of a longer domain with symmetry conditions at the end and a pressure point constraint for numerical stability. The parameters are arbitrary, although ensuring a low Reynolds number, Re$\sim 5 \times 10^{-4}$ and a long wavelength $\lambda > 2h$.

This example shows us that rotational streaming velocities are induced even in the simplest possible geometry with an irrotational first-order eigenmode.

7.3.4 Streaming in a two-dimensional square

Let us now extend the simple infinite plate example to a geometry partly resembling our 2×2 mm^2 reference chamber. If we disregard the top and bottom plate, we can approximate the geometry by an infinitely deep chamber with boundary streaming effects induced exclusively by the surrounding walls parallel to the xy- and xz-planes using the geometry definition analogous to Fig. 7.13. This allows us to conduct the analysis as a 2D simulation.

Since the y- and z-components of $\mathbf{v}_{10}$ in resonance are zero at the xz- and xy-boundary, respectively, we are permitted to use the same boundary conditions as used for the infinite plates, however now with a specified boundary layer velocity in the z-direction as well. Letting the walls be positioned at $y = \pm L$ and $z = \pm L$ our boundary conditions using the non-actuated inviscid analogy to the resonance mode given by Eqs. (3.23) are

$$\left\langle \mathbf{v}_{2by}(y) \right\rangle = \frac{3U^2}{8c_a} \sin 2k_0 y, \qquad z = \pm L \tag{7.33a}$$

$$\langle \mathbf{v}_{2bz}(z) \rangle = \frac{3rU^2}{8c_a} \sin 2k_0 z, \qquad y = \pm L \tag{7.33b}$$

where we use $k_0 = 3\pi L^{-1}$ corresponding to three waves per chamber sidelength of $2L$.

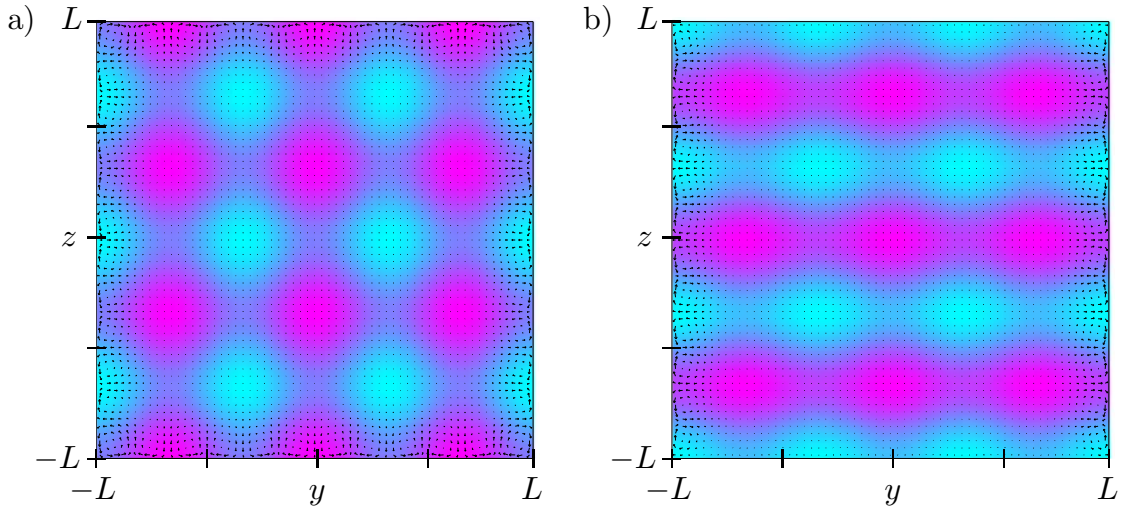

Figure 7.15: Acoustic streaming in an infinitely deep square induced by the boundary layer velocities Eqs. (7.33). The vector plot shows $\langle \mathbf{v}_2 \rangle$ and the surface plot is p_{10} at $t = 0$ where both plots have $k_0 L = 3\pi$ and a) have a threefold stronger amplitude of $\mathbf{v}_{10}$ in the z-component whereas b) have the same amplitudes in each direction but with opposite sign. Cyan are local minima and magenta are maxima.

In Fig. 7.15 we have plotted the solution both for the previously used resonance with amplitude factor $r = 3$ and for a mode with $r = 1$ and reversed sign on $\langle v_{2bz} \rangle$ in order to avoid the boundary streaming velocity to enter the corner of the square from both y- and z direction. The streaming velocity is given as a vector plot on top of the inviscid pressure distribution.

We can now make two significant observations. First of all we see a pattern of twelve vortices along the edges for a first-order wavelength of one third of the chamber length. As a pair of out- an ingoing velocity components for each half wavelength is to exist due to conservation of mass, the twelve vortices are to be expected due to the second-order doubling of spatial periodicity. However, if we compare to the measurement presented in Fig. 1.2 we only find six vortices in each dimension for this wavelength leading us to the conclusion that the observed streaming pattern cannot be ascribed to the boundary effect along the perimeter of the chamber.

Furthermore we observe that the dynamics are confined to a region near the boundaries in contrast to the infinite plate example with vortices extending to the center of the geometry. This has to do with the fact that the pressure p in the incompressible flow induced by the boundary velocity obeys a Laplace equation, $\nabla^2 p = 0$. In any infinite system where this holds in conjunction with a slip velocity harmonically varying along the boundary it can be shown that the velocity field decays exponentially from the boundaries at a rate of k_0 [33]. Although our square system is not infinite the extent relative to the decay length is large, and since it does no longer comply with the condition $\lambda \gg 2L$, the decay is now distinct.

7.3.5 Streaming in a three-dimensional chamber

If we include the top- and bottom plate as outlined in Fig. 7.12, between which we still have the condition $2h < \lambda$, it must be expected that the dynamics of the streaming extend to the entire chamber as was found with the infinite plates in Fig. 7.14.

However, from this example we know that the dominating vortices are oriented perpendicular to the surface, which must also be expected to be true for waves with 2D dynamics along the surface. Since our inviscid analytical first-order velocity field is irrotational, the same can be assumed to be true for the induced second-order boundary velocity. Thus, the only vortex components in planes parallel to the top and bottom of the chamber are to be caused by the boundary layer velocity along the chamber perimeter, which we in Fig. 7.15 have shown to be confined to the vicinity of the boundary. Moreover, if the top and bottom plates would induce vortices rotating parallel to the plate, we would still expect a doubling of the periodicity and hence get a 12×12-pattern rather than the observed 6×6-pattern in Fig. 1.2. The dynamics could of course be investigated further by simulations, but unfortunately time has not allowed for this.

7.4 Streaming induced by transmission loss

For the results considered so far the models have assumed perfect acoustic reflection at the walls, which is achieved for either a perfectly hard or soft walls, where we have used the former. However, in an experimental setup there are other sources for losses than viscous damping, namely energy transfer to the surroundings. This loss, being a transmission rather than damping loss, can be both to the surrounding air, and even more important also through the mechanical contact to the setup, whereby it can introduce phase shifts and traveling wave components. As the energy flux given by the transmission loss is highly dependent on the connection to the surroundings, this could to some extent explain that the strength and stability of the measured streaming is sensitive to frequency and experimental conditions [1].

The principal formulation of the system could to first extent be made by terminating one end of the simple transmission example treated in Fig. 3.5 with a reflecting actuator. With reference to this, we will hereby be able to find and maintain a resonance in domain A simultaneously with an energy flux transmitted into domain B, which will entail a phase shift between pressure and velocity in domain A different from $\frac{1}{2}\pi$.

To simulate such losses numerically we can initially consider a 2D geometry with inclusion of the surrounding silicon chip and model the outer boundaries of this to resemble an infinitely domain of air. As introduced in Chap. 3 the transmission between domains is characterized by the specific acoustic impedance z_s, which turns the boundary condition into a combined condition. This is implemented in COMSOL's acoustic application mode as [56]

$$\mathbf{n} \cdot \left(-\frac{1}{\rho_0} \boldsymbol{\nabla} p_1 \right) - \frac{\mathrm{i}\omega p_1}{z_{s,i}} = 0, \tag{7.34}$$

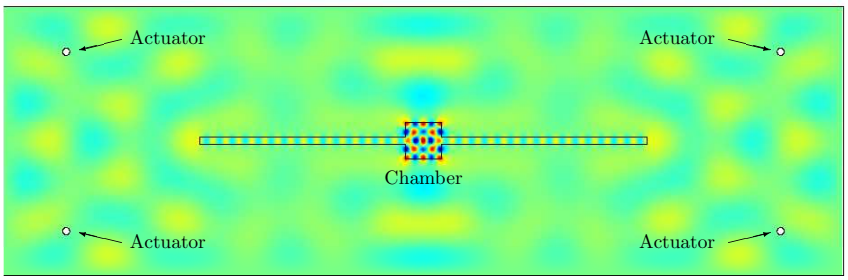

Figure 7.16: 2D model of a water-filled resonator surrounded by a silicon chip with impedance boundary conditions on the outer edges imitating surrounding air. The system is actuated by four circular accelerating boundaries and recreates a resonance in the chamber. This actuator geometry has the advantage of not introducing any disturbance of importance to the standing wave pattern. The surface plot shows the acoustic pressure with arbitrary amplitude and local maxima in red areas and minima in blue.

where $z_{s,i}$ is the input impedance [56] of the infinite domain surrounding the boundaries. Unfortunately ω figures in the impedance condition which precludes the possibility for solving the problem as an eigenvalue problem in analogy to the lossy Helmholtz equation.

A way to overcome this can be done by initially solving an eigenvalue problem with a Dirichlet condition resembling vacuum. Afterwards we can extend the problem with inclusion of transmission to various materials along the chip perimeter and solve this with a stationary solver at the idealized eigenfrequencies. If the energy of the lossless eigenmode is primarily localized to the resonating chamber, we can expect that the addition of infinite domains to the chip perimeter will not significantly change the eigenfrequency of these modes.

However, one issue connected to this approach is that an actuator must be added to the system in order to excite the eigenmodes, and we could expect the energy transfer to be dependent on the design of the actuator.

Preliminary simulations have been performed on different geometries, where an example with four small circular actuators is shown in Fig. 7.16. This actuator geometry will not introduce any significant disturbance to the eigenmodes but is still sufficient to recreate the resonance. Simulations show that the term $\langle p_{10}\mathbf{v}_{10}\rangle$ can contain significant irrotational components without any spatial doubling of periodicity leading one to believe this to be true for $\langle \mathbf{v}_2 \rangle$ as well. However, due to limitations in time the model has not been thoroughly investigated or verified why we shall not report further on the results.

7.5 Summary

To recapitulate we have found that the theory based on viscous damping does not correspond to experiments neither with respect to visual appearance nor magnitude and can be inferred to be an insignificant effect. Although the estimated velocity amplitudes Eq. (5.49) induced by boundary layer theory fit the measured velocities, the theory presented so far cannot account for the observed pattern. Hereby we must draw the conclusion that none

of these two mechanisms seem to be applicable for description of the streaming.

The proposed model with significant losses to the surroundings show indications of being a plausible alternative, which should be investigated more thoroughly.

Chapter 8

Application to a separation chip

In this chapter we will use some of the previously covered theory with primary focus on the radiation forces to describe effects observed in a flow-through particle separation chip made in the group of Thomas Laurell at Lund University. Experimental results on this and similar chips have previously been reported [28, 31] and in the following these results are extended with measurements made at DTU Nanotech by S.M. Hagsäter and A. Lenshof[1], and issues relevant for the function of such a device will be discussed.

Besides the acoustic radiation force we will also consider the influence of a superimposed Poiseuille flow on the acoustic field and outline a method for computing a quantitative measure of the separation efficiency of the device.

8.1 Chip design and function

The separation chip, schematically shown in Fig. 8.1, is a rather simple yet elegant device in silicon and glass [28] for sorting erythrocytes from lipid particles. Analogous to the previously treated chamber systems an acoustic resonance is being set up with the same actuation principles as shown in Fig. 1.1 in order to induce acoustic radiation forces. For this system the frequency is adjusted to fit half a wavelength across the channel as indicated in Fig. 8.1 b) whereby hard, dense erythrocytes are forced to pressure nodes in the center of the channel and the softer lipid particles are forced towards the channel walls as was described in Sec. 4.3.1.

A pressure is simultaneously applied to the left input giving rise to a laminar Poiseuille flow. Due to the laminar behavior the lipid particles and erythrocytes will subsequent to the acoustic separation be transported in a stratified flow, whereby the two types of particles can be collected in center and side outlets, respectively.

[1] S.M. Hagsäter and A. Lenshof are Ph.D. students in the groups of J.P. Kutter at the Technical University of Denmark and T. Laurell at Lund University, respectively.

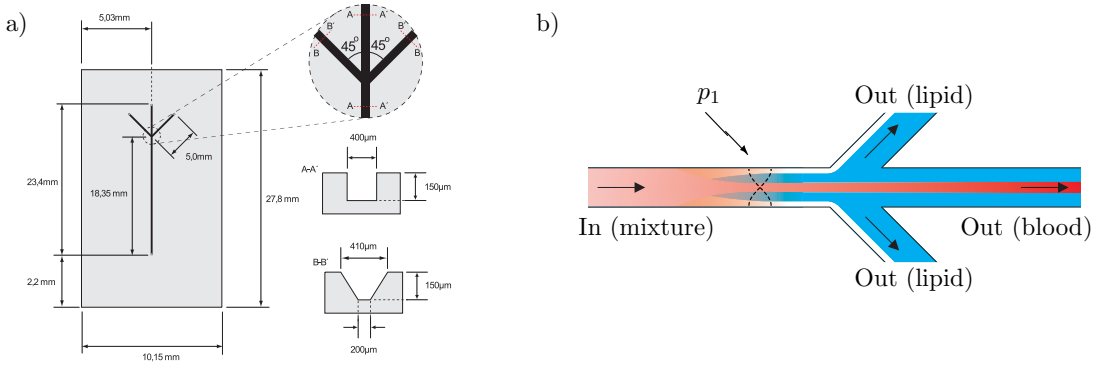

Figure 8.1: Overview and principle of operation of the separation device. In a) the geometry of the channel system and silicon base is given. b) shows the principle of operation of the flow-through device with standing waves across the separation channel of length $L = 18.35$ mm going from inlet to intersection. Red blood cells (red) are collected at the center and lipid particles (white) forced to the sidewalls whereafter the particles are flushed with the water (blue) to individual outlets. Image a) adapted from [2].

8.1.1 Measurements and material parameters

Since the main focus in this thesis is on the theoretical and numerical issues related to the device we will not go into details with the experimental methods but only summarize on the measurements that have been performed.

Although the device is intended to separate two types of particles, only measurements with one particle type at a time were performed at different eigenmodes. Measurements on particle dynamics were made with PIV [1] in a system without an applied Poiseuille flow. Hereby the motion due to radiation forces can be observed and quantified in the transient phase before particles have gathered at pressure nodes or antinodes.

Radiation measurements were performed on a Blood Mimicing Fluid from Danish Phantom Design [61] containing Orgasol© polyamide (PA) beads [59], which are assumed to be PA 6/12 type in water. Streaming measurements were made on polystyrene (PS) beads [2]. The material parameters and radiation coefficients for the two polymer particle types and red blood cells in water are given in Table. 8.1 from where it can be observed

Property	a	κ	ρ_0	$\mathcal{C}_\rho$	$\mathcal{C}_\kappa$
Unit	µm	10^{-11} Pa^{-1}	10^3 kg m^{-3}	10^{-2}	10^{-1}
PS	0.5	33	1.05	-3.4	2.7
PA 6/12	2.5	37	1.06	-4.0	1.9
Erythrocytes	~ 3	31-37	1.06-1.14	-4.0 – -8.7	3.1 – 1.9

Table 8.1: Parameters for acoustic radiation computations on micron sized particles based on data from [2, 58, 59] for polymers and [60] for erythrocytes, respectively. The radiation coefficients assume water at room temperature as suspension medium.

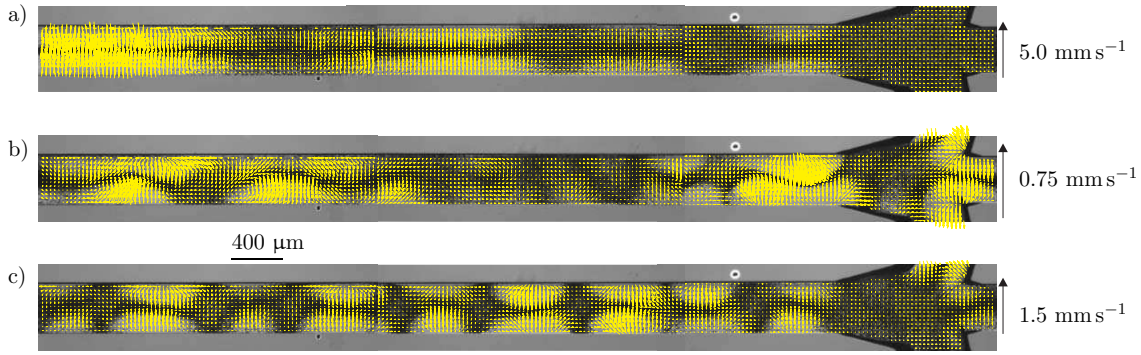

Figure 8.2: PIV measurement (yellow arrows) of transient particle velocities of PA beads in water due to acoustic radiation forces and the corresponding eigenmode pattern (gray scale). The three modes are found at a) 1.86 MHz, b) 1.96 MHz, and c) 2.05 MHz. Only the upper third of the full separation channel length is shown and we notice the irregular intersection geometry in the right part of the images. Images adapted from [2].

that all particles have equal sign of radiation coefficient and will be forced towards pressure nodes.

Besides the measurements on a quiescent system the device was also operated in flow-through mode in order to measure the separation efficiency $\mathcal{E}$ for each eigenmode with $\mathcal{E}$ defined as [2]

$$\mathcal{E} \equiv \frac{N_{\text{center}}}{N_{\text{center}} + N_{\text{waste}}}. \tag{8.1}$$

Here N refers to the number of particles collected at each outlet, and it is seen that a perfect focusing device would have a separation efficiency of $\mathcal{E} = 1$. For flow-through measurements, volume flow rates Q of 0.1 mL min^{-1}, 0.2 mL min^{-1}, and 0.4 mL min^{-1} were used.

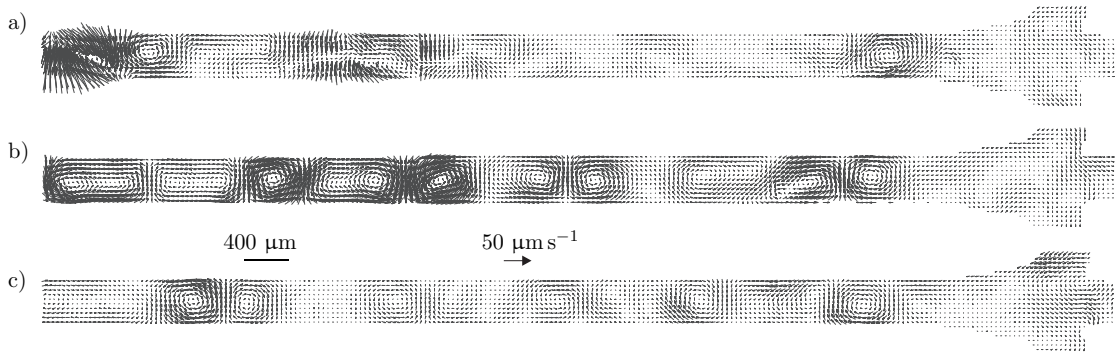

Figure 8.3: PIV measurement of the acoustic streaming velocity corresponding to the three modes at a) 1.86 MHz, b) 1.96 MHz, and c) 2.05 MHz, which are also illustrated in Fig. 8.2. The streaming has been visualized by the small PS beads. Only the upper third of the full separation channel length is shown. Images adapted from [2].

The three eigenmodes and measurements we will treat are shown in Fig. 8.2 for the particle velocity induced by the radiation force on the large PA beads. The corresponding streaming pattern is shown in Fig. 8.3 visualized by PS particles, and we will comment on the observations when comparing measurements and simulations.

8.2 The acoustics model

We will now discuss how to model the system to calculate the acoustic eigenmodes and radiation forces.

8.2.1 Acoustics with superposed flow

Before considering any numerical design, we should notice that the acoustic theory developed in Chap. 2 applies to a quiescent system with $\mathbf{v}_0 = \mathbf{0}$ as opposed to the present system with $\mathbf{v}_0 \neq \mathbf{0}$ in operation mode. Fortunately we do not need to redo the basic theory but can, following the method by Landau and Lifshitz [39], introduce a coordinate transformation to a coordinate system translated with the velocity $\mathbf{v}$ relative to our well-known quiescent system. The relation between the position vector $\mathbf{r}'$ in the moving system and $\mathbf{r}$ in the static system is $\mathbf{r}' = \mathbf{r} - \mathbf{v}t$, which, by insertion in the expression for a harmonic wave, can be shown to give the following relation [39],

$$\omega = k_0 c_a + \mathbf{v} \cdot \mathbf{k}_0. \tag{8.2}$$

With $\mathbf{v}$ being our Poiseuille flow velocity, $|\mathbf{v}| \ll c_a$, it is now seen that the superposed flow does only induce little deviation from the corresponding quiescent state. Thus, as a reasonable approximation it can in general be assumed that the resonance states are unaffected by the Poiseuille flow in low Reynolds number microsystems allowing us to solve for the two effects independently of each other. The same condition has been assumed valid by Townsend *et al.* [62, 63] for modeling particle tracing in a similar device.

8.2.2 Geometry for simulations

Since no effects of viscosity are included, the acoustics are governed by the standard Helmholtz equation found in Eq. (2.39). In analogy to Chap. 7 we restrict ourselves to 2D simulations since the frequencies given in Fig. 8.2 correspond to $\lambda \sim 8 \times 10^{-4}$ m thereby fulfilling the 2D condition $\lambda > 2h$ with h being the channel height of 1.5×10^{-4} m.

For the present geometry we do however have a challenge since the side channels due to fabrication issues do not have vertical side walls as seen in Fig. 8.1, as well as the intersection between the channels is not well-defined, which is observed from Fig. 8.2. The sloped sidewalls call for a 3D model, but due to the irregular geometry at the intersection this would not gain sufficiently more accuracy on the details of the eigenmodes than a 2D model. Different models to account for this geometry have been made and tested, and the presented acoustic model uses a side channel width of 300 µm corresponding approximately to the width at half the channel height, being a reasonable compromise between the top and bottom value of the side channel.

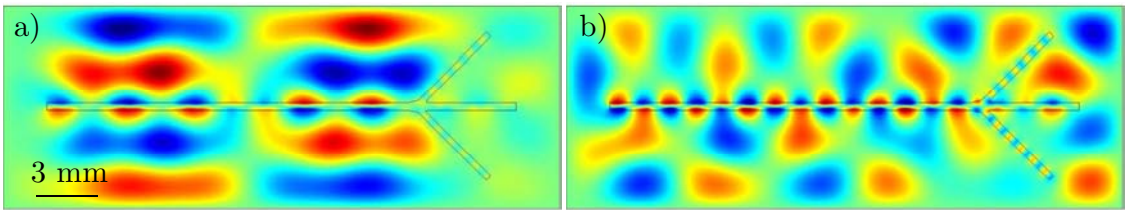

Figure 8.4: COMSOL simulation of two first-order pressure eigenmodes at a) 1.97 MHz and b) 2.05 MHz. The images show a 2D full chip simulation with silicon chip and water filled channels using the material parameters from Table. 3.1. We see both an almost symmetric and an asymmetric eigenmode, but the simulations do not resemble the measurements in Fig. 8.2 very well. Red areas correspond to local maxima and blue to minima.

8.2.3 Appearance and properties of the eigenmodes

As seen from Fig. 8.2 the measured eigenmodes are not completely symmetrical, which is especially pronounced for Fig. 8.2 b). From Jensen [32] it is known that such asymmetric modes can be induced by breaking the symmetry in the channel system and the position of the channel system on the silicon chip itself. For this particular device both of these conditions are present and simulations with and without the surrounding silicon have been performed. Since the asymmetry in the channel system is confined to the region near the channel intersection it was expected that asymmetric modes were more pronounced in the full model.

In Fig. 8.4 two modes near the relevant eigenfrequencies are shown and we notice that both near symmetric and asymmetric patterns are observed as expected. However, if we compare the number of nodal points along the separation channel a discrepancy between simulations and measurements is observed, where the simulations greatly underestimate the number of standing waves along the channel. This was found to be the general picture for a large number of eigenmodes.

Reducing the model only to include the channel system we find a better correspondence between the number of nodal points and frequency when comparing simulations and measurements, although there is still a slight tendency to underestimate the number in the simulations within a reasonable frequency span between measured and simulated eigenfrequencies. This is shown in Fig. 8.5, where we also find an asymmetric mode quite similar to the one shown in Fig. 8.2 b). Hereby we can conclude that the simplest 2D model in this case gives better predictions of the actual behavior of the device, although asymmetric modes were seldom found. It should, however, be noticed that the not very well-defined geometry of this device entails a far larger deviation between simulated and observed eigenmodes than what can be obtained for the chambers in [1] as can be seen from Fig. 1.2 and App. F. Thus, if design improvements are to be made on the basis of simulations one could consider to change fabrication methods to the ones used in [1] for reduced deviation between intended and actual geometry. Simulations on a symmetric device have been made as well, which lead only to symmetric eigenmodes proving that even small deviations in geometry can alter the dynamics in the entire device.

In previously published papers [28,29,31] the 2D dynamics of the separation system has

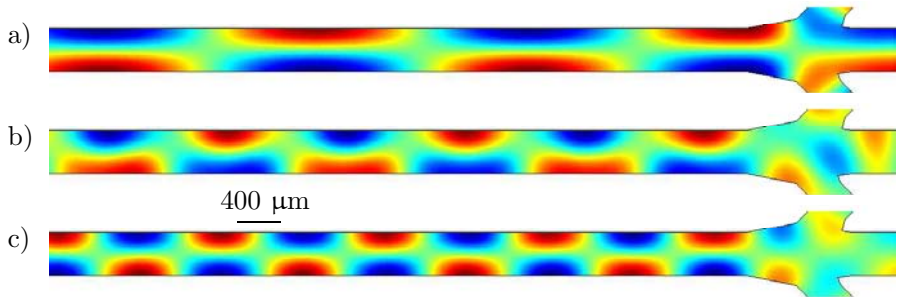

Figure 8.5: Comsol simulation of three first-order pressure eigenmodes at a) 1.89 MHz, b) 1.97 MHz, and c) 2.09 MHz. The images show the same selection of the channel system as in Fig. 8.2 and we recognize some correspondence between measurements and simulations both for frequency and spatial appearance of the modes, although a) deviates significantly from the measurement at the intersection. Simulations are made with water at 20°C as medium and red areas are pressure maxima and blue are minima.

not been taken into account, but the resonance has been assumed to be a single standing wave transverse to the channel without any longitudinal variation. However, in reality we do have standing waves along the channel as well, and the system dynamics are thus governed by two length scales being the transverse wavelength λ_t and the longitudinal λ_l. Due to these length scales we can thereby estimate the expected resonance frequencies from Eq. (3.10), rewritten as

$$f = c_a \sqrt{\lambda_t^{-2} + \lambda_l^{-2}}. \tag{8.3}$$

Since we are only interested in the standing waves confined to the separation channel we can make a rough estimate of the possible resonance frequencies by assuming λ_t to be fractions of the channel width w and λ_l to be fractions of the length L, which are taken to be $w = 400$ µm and $L = 18.35$ mm. Based on Eq. (8.3) we can find the first 50 eigenfrequencies for both $\lambda_t = 2w$ and $\lambda_t \to \infty$, which are shown in Fig. 8.6 together with the first 150 eigenfrequencies for the numerical simulation including the asymmetric intersection and the three outlet channels.

Although the two graphs cannot be directly compared due the difference in geometrical complexity we do observe some similarities. They both exhibit a kink near 1.85 MHz caused by the first transition into a transverse mode of $\lambda_t = 2w$. This gives the plateau of small frequency gaps between two adjacent longitudinal modes as long as the transverse mode dominates, that is $\lambda_t < \lambda_l$. If a specific longitudinal mode for some reason turns out to be better suited for a specific purpose it is important that we are able to excite and maintain this mode during operation. However, due to the small frequency gap the present system is quite sensitive towards for instance temperature variations.

As an example we can calculate the transition from $\lambda_l = \frac{1}{5}L$ to $\lambda_l = \frac{1}{4}L$ for $\lambda_t = 2w$, which for constant temperature gives $f_5/f_4 = 1.008$. This frequency ratio is equivalent to the ratio of the speed of sound for a temperature change from 25°C to 20°C [40] amounting to $c_{a25}/c_{a20} = 1497/1485 = 1.01$, whereby an actuated system can change

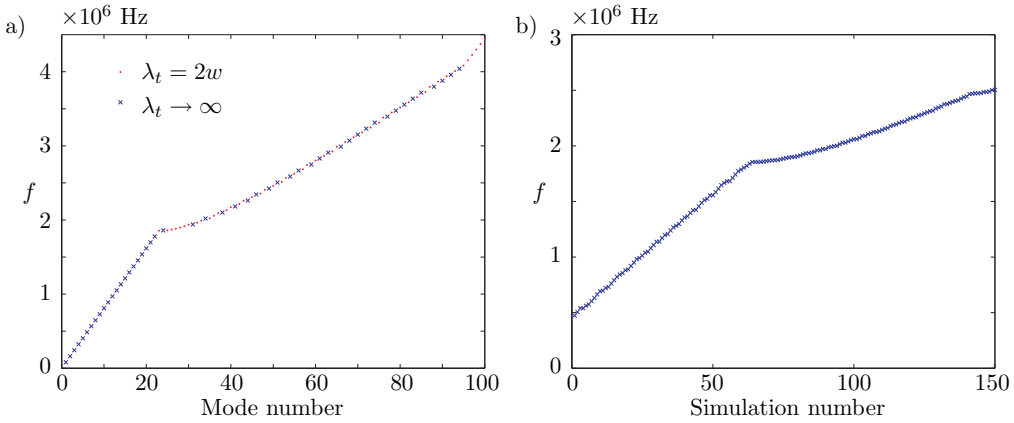

Figure 8.6: The eigenfrequency distribution for a) a straight channel with the 50 first modes for $\lambda_t \to \infty$ and 50 first for $\lambda_t = 2w$ calculated from Eq. (8.3) and sorted by increasing frequency. In b) 150 eigenfrequencies for the separation chip's channel system computed by COMSOL are shown. Although geometrically different both plots show a kink at the first transition from $\lambda_t \to \infty$ to $\lambda_t = 2w$ followed by a flat plateau. In both a) and b) water at 20°C is the propagation medium.

from one mode to another possibly resulting in a change of the separation efficiency if temperature is not controlled. Since the mode shifts are least separated in frequency for the lowest longitudinal modes one might consider to run the system at a higher mode and avoid operation near the plateau in order to increase temperature tolerance.

8.3 Comparing theory and experiment

Having numerically found eigenmodes that roughly fit the measured patterns, we are now ready to compare simulations and measurements and finally determine particle paths from inlet to outlet.

8.3.1 Equation of motion for tracer particles

Since the PIV measurements are based on particle velocities we must initially set up an equation of motion for the tracer particles. The equation of motion is constructed directly from Newton's second law of motion, where we disregard any forces but the Stokes drag force due to the acoustic streaming and Poiseuille flow and the acoustic radiation force. Letting the particle velocity be $\mathbf{u}$ and the fluid velocity $\mathbf{v}$ we thereby find the following for a particle of radius a and mass m

$$m\partial_t \mathbf{u} = 6\pi\eta a(\mathbf{v} - \mathbf{u}) + \mathbf{F}_a, \tag{8.4}$$

where we have used the formulation for Stokes drag from [33], and the acoustic radiation force is given in Eqs. (4.34) and (4.35). Using $m = \frac{4}{3}\pi a^3 \rho_0^{(p)}$ to express the mass of the particle and introducing the characteristic scales for length L_0 and velocity U_0 a non-

dimensional equivalent of Eq. (8.4) can be written as

$$\mathrm{St}\hat{\partial}_t\hat{\mathbf{u}} + \hat{\mathbf{u}} = \hat{\mathbf{v}} + \frac{1}{6\pi\hat{a}\hat{\eta}}\hat{\mathbf{F}}_a, \tag{8.5}$$

where we have introduced the particle Stokes Number [64]

$$\mathrm{St} \equiv \frac{2\rho_0^{(p)}a^2}{9\eta}\frac{U_0}{L_0}. \tag{8.6}$$

An estimate of the Stokes number can be found using the characteristic Poiseuille velocity $U_0 \sim QS^{-1}$ with S being the channel cross section. For a flow rate of 0.4 mL min^{-1} this amounts to $U_0 \sim 10^{-1}$ m s^{-1}. Combining this with the smallest length scale upon which dynamics are changing in the acoustic field, where a representative length scale would be half the channel width $L_0 \sim 10^{-4}$ m, the estimate of the Stokes number becomes St$\approx 10^{-3}$. From this it follows that disregarding particle inertia is a good approximation and leaves us the steady state equation of motion

$$\mathbf{u} = \mathbf{v} - \frac{\rho_0 a^2}{3\eta}\boldsymbol{\nabla}\left(\frac{\langle p_{10}^2\rangle}{3\rho_0^2 c_a^2}\mathcal{C}_\kappa + \frac{\langle v_{10}^2\rangle}{2}\mathcal{C}_\rho\right) \tag{8.7}$$

giving a linear relation between the particle velocity $\mathbf{u}$, fluid velocity $\mathbf{v}$ and radiation force $\mathbf{F}_a$. Thus, if we compute the Poiseuille flow profile, the acoustic streaming and acoustic radiation force, the particle paths can subsequently be found using a standard numerical integration method based on e.g. Euler or Runge-Kutta schemes.

8.3.2 Estimating streaming from the radiation force

If no steady flow is present in the system, the equation of motion Eq. (8.7) reduces to

$$\mathbf{u} = -\frac{\rho_0 a^2}{3\eta}\boldsymbol{\nabla}\left(\frac{\langle p_{10}^2\rangle}{3\rho_0^2 c_a^2}\mathcal{C}_\kappa + \frac{\langle v_{10}^2\rangle}{2}\mathcal{C}_\rho\right). \tag{8.8}$$

Thus, by measuring the particle velocity $\mathbf{u}$ we can from the material properties calculate the radiation force $\mathbf{F}_a$ and subsequently the magnitude of the acoustic fields p_1 and $\mathbf{v}_1$. Hereby we are also able to estimate the magnitude of the acoustic streaming velocity from Eq. (5.9) or Eq. (5.49)

$$|\mathbf{v}_2| \sim \frac{|\langle v_{10}^2\rangle|}{\pi c_a}. \tag{8.9}$$

To simplify matters we can use Eqs. (2.29) and (2.31) to express $\mathbf{v}_{10}$ in terms of p_{10} leading to

$$\mathbf{u} = -\frac{a^2\rho_0}{3\eta}\boldsymbol{\nabla}\left(\frac{\langle p_{10}^2\rangle}{3\rho_0 c_a^2}\mathcal{C}_\kappa + \frac{\left\langle\left(-\frac{\mathrm{i}}{\rho_0\omega}\boldsymbol{\nabla}p_{10}\right)^2\right\rangle}{2}\mathcal{C}_\rho\right). \tag{8.10}$$

Since we are only interested in estimating the amplitude of the fields, we can use that $|\boldsymbol{\nabla}| \sim 2k_0 = 2c_a/\omega$, and after a small amount of algebra we are left with the following estimate relating the measured particle velocities to the acoustic first-order pressure,

$$|\mathbf{u}| \approx \frac{a^2\omega}{3\eta\rho_0 c_a^3}\left(\frac{1}{3}\mathcal{C}_\kappa + \frac{1}{2}\mathcal{C}_\rho\right)\left|p_{10}^2\right| \tag{8.11}$$

The first-order velocity $\mathbf{v}_{10}$ can likewise be estimated from

$$|\mathbf{v}_{10}| = \frac{1}{\rho_0 c_a}|p_{10}|. \tag{8.12}$$

In Table. 8.2 the measured and estimated quantities are summarized for the six measurements given in Figs. 8.2 and 8.3, where $\mathbf{u}_m$ is the radiation induced velocity from Fig. 8.2 and $|\langle\mathbf{v}_{2m}\rangle|$ is the measured streaming velocity from Fig. 8.3. The remaining quantities are estimates based on the radiation measurements.

We can now see that the estimated first-order fields are generally in accordance with the results reported by Spengler *et al.* [38], who made a similar estimate by balancing radiation forces and gravity. However, the lowest mode, mode a), is seen to be a few times stronger. If we compare the measured and estimated streaming velocities, it is for modes b) and c) found that the two velocities correspond within a factor of five, which is satisfactory for the fairly rough estimates, although any clear-cut correlation is not seen. The same correspondence can also be shown to true for the measurements in the square chamber in Fig. 1.2, where estimates and measurement correspond within a factor of two. Thus, although we should be careful not to draw any definitive conclusions from this very limited amount of data, these observations support the theory that the observed streaming patterns are of second order and scale as expected from Eq. (5.49), independently of viscosity. Yet, we cannot account for the actual streaming pattern, which both in Figs. 1.2 and 8.3 lack the anticipated doubling of periodicity, as well as the cause of the significant discrepancy between estimated and measured streaming velocity for mode a) is unknown.

Another important observation is that mode a) exhibits a much stronger coupling in parts of the channel than the two other modes although mode a) was actually excited by a lower power of $P = 0.2$ W than modes b) and c) actuated by $P = 0.5$ W [2]. Such a behavior, which experimentally expressed itself in a much higher separation efficiency, cannot

Property	f	$\mathbf{u}_m$	$\lvert\langle\mathbf{v}_{2m}\rangle\rvert$	$\lvert p_{10e}\rvert$	$\lvert\mathbf{v}_{10e}\rvert$	$\lvert\langle\mathbf{v}_{2e}\rangle\rvert$
Unit	MHz	$\mu\mathrm{m\,s^{-1}}$	$\mu\mathrm{m\,s^{-1}}$	10^6 Pa	$\mathrm{m\,s^{-1}}$	$\mu\mathrm{m\,s^{-1}}$
Mode a)	1.86	2200	85	2.5	1.7	900
Mode b)	1.96	220	50	0.7	0.5	80
Mode c)	2.05	400	25	1.0	0.7	150

Table 8.2: Measured and computed and calculated properties from the three eigenmodes shown in Figs. 8.2 and 8.3. $\mathbf{u}_m$ is the radiation induces velocity, $\langle\mathbf{v}_2\rangle$ is streaming velocity and p_{10} and $\mathbf{v}_{10}$ are acoustic first-order fields. Indices m and e correspond to measured and estimated.

be determined from an eigenvalue analysis but emphasizes the importance of stabilizing the device within a specific longitudinal mode.

8.3.3 Dominating mechanism

The present device is designed for utilization of radiation forces and it is therefore important to know within which limits the dynamics are governed by the radiation force, since the small tracers in Fig. 8.3 demonstrate that the streaming velocity is an inherent part of the nonlinear acoustics and can affect the functionality of any acoustofluidic device.

Especially if particles of a wide size distribution are to be manipulated it is important to know, if radiation forces or viscous drag from the streaming dominates. A balance equation between the two forces can be obtained from Eq. (8.7) if we set $\mathbf{v} = \langle \mathbf{v}_2 \rangle$, $\mathbf{u} = \mathbf{0}$ and combine this with the estimates from Eqs. (8.11), (8.9) and (8.12),

$$\frac{|p_{10}^2|}{2\rho_0^2 c_a^3} = \frac{a^2\omega}{3\eta\rho_0 c_a^3}\left(\frac{1}{3}\mathcal{C}_\kappa + \frac{1}{2}\mathcal{C}_\rho\right)\left|p_{10}^2\right|. \tag{8.13}$$

From this it is easy to determine the critical particle radius a_c where the transition from streaming to radiation occurs,

$$a_c \approx \sqrt{\frac{3\eta}{2\rho_0\omega}\left(\frac{1}{3}\mathcal{C}_\kappa + \frac{1}{2}\mathcal{C}_\rho\right)^{-1}}. \tag{8.14}$$

Here we identify a rational scaling with viscosity increasing the Stokes drag contribution and the angular frequency increasing the radiation contribution as this is related to the gradient of the radiation force potential. It is also seen that the expression is independent of the amplitude of the first-order fields, which is quite fortunate since any change in amplitude due to e.g. actuator coupling issues will not induce a change in the overall particle selectivity. On the other hand the size selectivity can be adjusted through the frequency as long as the general condition $k_0 a \ll 1$ is obeyed.

For the given separation system at a frequency of $f = 2$ MHz the critical radius for a polyamide particle can be estimated to $a_c \sim 1.7$ µm and correspondingly for a polystyrene particle $a_c \sim 1.3$ µm, which is between the two particle sizes used in experiments and thus consistent with the observed change of governing dynamics between Figs. 8.2 and 8.3. Although the magnitude of the streaming is expected to scale with the first-order fields in same way as the radiation force, the actual spatial pattern of streaming and radiation do not necessarily correspond to each other and we might have areas of low radiation forces where the streaming dominates and vice versa. By a close examination of Fig. 8.2 b) we actually do find indications of circular motion as shown in Fig. 8.7, where any vortices are likely to be due to acoustic streaming, since the radiation force is based on a scalar potential.

This could affect the function of the device if an unfortunate design gives rise to an acoustic remixing subsequent to the particle separation. Thus, even though the devices are based on radiation forces, for design optimizations it will be valuable to be able to model both radiation and streaming for particle tracing through Eq. (8.7).

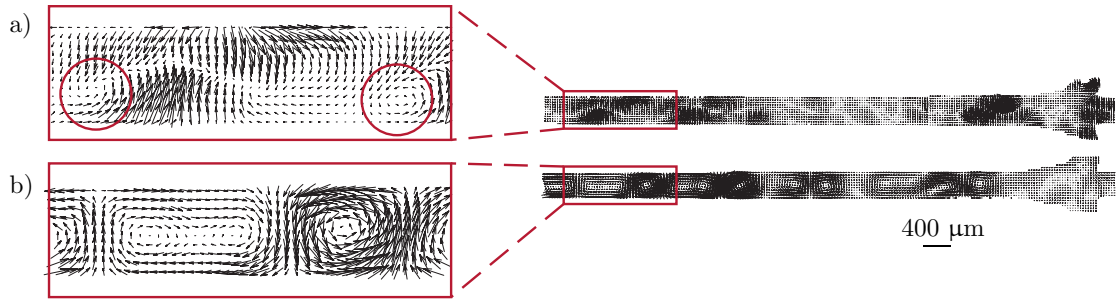

Figure 8.7: Close-up on the radiation a) on 2.5 µm particles and streaming b) measurements with 0.5 µm particles for the eigenmode at 1.96 MHz corresponding to Fig. 8.2 b) and Fig. 8.3 b). Vortices in the radiation measurement a), indicating that the large particles are also affected by the streaming, are marked by the red circles. Measurements courtesy of Hagsäter *et al.* [2].

8.3.4 Radiation forces and separation efficiency

Based on the numerically computed eigenmode from Fig. 8.5 we can compare the induced velocity calculated from the radiation force Eq. (8.8) to the measured radiation force velocity from Fig. 8.2 b). A close-up near the intersection is shown in Fig. 8.8, where a partial agreement between measurement and simulation can be observed. There are however discrepancies, which calls for the use of a model geometrically in better agreement with the real device. Similar plots for the circular chambers used in [1] are given in App. F, where better correspondence is found. From this we can deduce that the inviscid 2D models combined with the radiation force equation Eq. (4.34) can be used as a design tool for geometrically well-defined shallow devices, whereas the results are more uncertain for devices that are not height invariant and include unknown asymmetric geometries.

If we intend to combine the radiation force field with a Poiseuille flow for particle tracing in order to predict the separation efficiency we cannot simply superpose the two fields in a numerical simulation, since the radiation force is based on an eigensolution. Thus for a prediction of the separation efficiency we must determine the radiation amplitude by either making an extended numerical model including an actuator, which is both computationally heavy and doubtful to give a sufficiently precise description of the real

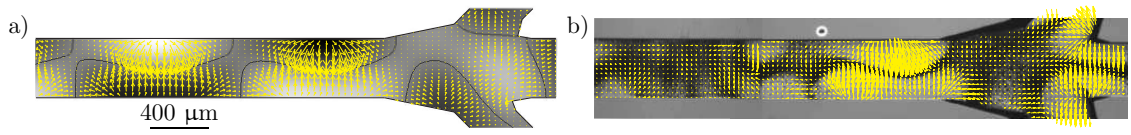

Figure 8.8: Close-up of the radiation force illustrated by vector plots scaling with velocity. In a) the numerically computed solution at 1.97 MHz is combined with a gray-scale surface plot of the first-order pressure field and corresponding black nodal lines, and in b) the measured force at 1.96 MHz is combined with micrographs of the particle formation at nodal lines. The pressure in a) has local maxima at white areas and minima at black with an arbitrary amplitude. Image b) is adapted from Hagsäter *et al.* [2].

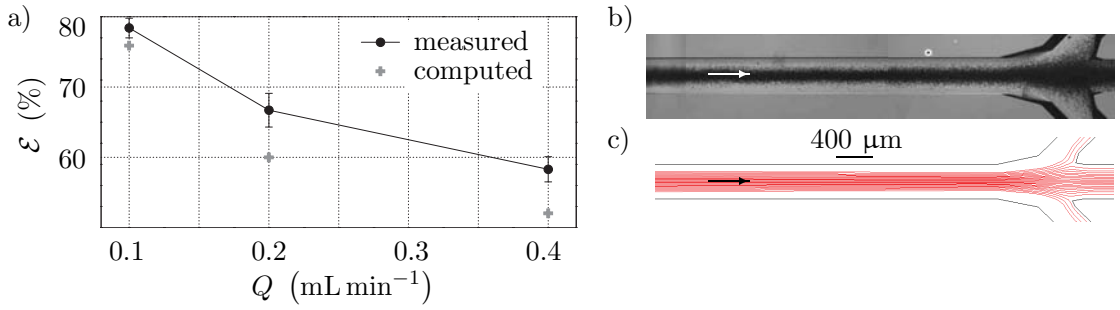

Figure 8.9: Demonstration of particle tracing to estimate the separation efficiency $\mathcal{E}$ for the computed eigenmode at 1.97 MHz and compared to measurements at 1.96 MHz. In a) measurements from [2] are plotted together with simulations for tracing of 25 particles. Panels b) and c) show the measured and computed particle band at a flow rate of $Q = 0.1$ mL min^{-1}. Images a) and b) adapted from Hagsäter *et al.* [2].

device, or alternatively base the amplitudes on a reasonable guess, i.e. $|\mathbf{v}_{10}| \sim 10^{-4} c_a$, or previous measurements to which the computed eigenmode pattern can be fitted. The latter approach has been used to make a model combining a Poiseuille flow with the acoustic radiation force based on the measured amplitudes in Fig. 8.2. Using COMSOL's built-in postprocessing Runge-Kutta 45 solver a collection of particles released at the inlet can be traced by time-integrating Eq. (8.7) whereafter the separation efficiency can be roughly estimated by simply counting the number of particles terminated at the three outlets.

However, since the model does not take streaming velocities into account and the 2D geometry leads to an inaccurate determination of the Poiseuille flow, the model should not be used for anything but a coarse indicator of the system behavior. Despite the discrepancies between the simulated and measured eigenmodes Fig. 8.9 shows an example of the method, where the separation efficiency has been estimated by tracing 25 particles through the radiation force fields at $f = 1.97$ MHz for different flow rates and compared to measurements from [2]. Due to the limited amount of particles and the simplified model, the results shown are only to proof the concept of the computation method, which of course show a decreasing separation efficiency $\mathcal{E}$ for increasing flow rate Q. Thus, for devices, which are geometrically better suited for modeling, the tracing method might turn out useful for instructive design characterization although inclusion of other mechanisms, with the streaming velocity being the most important, should be incorporated.

8.4 Summary

In short the analysis have pointed out that several separation modes exist within a small frequency span, which can be troublesome if these have different separation efficiencies. To improve the device one could consider to alter the geometry in order to decrease the number of possible closely situated separation modes, as well as a more well-defined height invariant geometry is expected to improve the correspondence between measurements and 2D models. Another important point is the comparison of velocities induced by streaming

and radiation, which have rendered it probable that the general treatment of the streaming velocity is correct with regards to the magnitude although the streaming pattern cannot be computed.

Chapter 9

Conclusion and outlook

9.1 Conclusion

The work presented in this thesis can be categorized into mathematical analysis, numerical implementation and comparison to real systems, which have been applied to both acoustic streaming and acoustic radiation in resonant microfluidic systems.

Regarding the acoustic streaming, three different mechanisms for inducing the effect have been proposed, namely viscous damping in the bulk fluid, creation of boundary layers due to viscous stress, and losses by energy transmission to the surroundings.

A thorough analysis of the second-order equations governing the viscous loss mechanism revealed that the mathematical structure of these rendered it impossible to solve them directly for the streaming at resonance by numerical means. This problem was successfully resolved by an analytical decomposition of the equations and subsequent implementation in Comsol. The outcome of the simulations, however, showed that viscous damping cannot account for the experimentally observed streaming results reported by [1] but is a far too weak effect to be of any significance. This implies, on the other hand, that we do not need to compute the viscous first-order fields, simplifying simulations considerably.

Subsequently a basic analysis of the boundary layer theory was conducted from which it was found that estimates based on this approach can explain the magnitude of the observed streaming. However, a discrepancy in terms of periodicity doubling between the experimentally determined flow pattern [1] and anticipations based on a simple analysis indicated that the boundary layer theory cannot explain the flow fields either.

The third mechanism for describing the streaming, in terms of energy transmission to the surroundings, has only been touched upon at the end of the project, but initial simulations indicate this to be a more promising approach than viscous losses and boundary layer effects.

Concerning the radiation force, the general theory has been presented and summarized based on a compilation of different papers. From this, a formulation applicable to small compressible particles in inviscid standing wave fields has been used as a postprocessing extension of numerically determined first-order acoustic fields. Such an approach has shown that calculations of the radiation force in a microfluidic system is possible from 2D

eigenmode simulations, where the results are qualitatively in accordance with experimental data, provided the geometry of the resonator is well defined. Since the computations rely on eigenmodes we have not been concerned with the amplitudes although we have shortly touched upon different coupling models.

In order to relate the theoretical work to applications we have exploited some of the methods to analyze an already existing microfluidic separation device [28, 31]. Employing both simple analytical approaches as well as numerical simulations we found that the analysis could reveal important characteristics of the device and give hints for design and operation alterations.

Thus, our initial goal of developing methods suitable for designing and evaluating arbitrarily shaped acoustofluidic resonance systems has partly been achieved, since we with a decent accuracy can model the spatial distribution of the radiation force in an inviscid approximation for shallow acoustic microfluidic resonators.

9.2 Outlook

Given that we have not succeeded to compute the acoustic streaming at resonance, this is an obvious point of departure for future work on acoustofluidics. A natural basis will be a more generalized and thorough investigation of the transmission loss approach, which seems to be a promising path for the development of a new streaming model. Being based on energy transmission, it might be beneficial to formulate the model in terms of energy flux and mass flux rather than velocities and pressure, although the underlying physics of course is the same.

Another interesting topic is the effects neglected in the radiation section. Here it could be worth to investigate the consequences of the fact that the critical radius for the conversion from radiation to streaming dominance is close to the momentum diffusion length, where viscous radiation effects come into play. Furthermore, the Bjerknes forces are an issue, which could be imagined to be of particular interest for particle traps, where a high degree of control of the radiation force is desired.

Besides the theoretical perspectives, it would also be beneficial with more experimental data in order to evaluate the accuracy of the method for calculation of radiation forces in a number of very well-defined geometries.

The same applies for the streaming, where it would be interesting to investigate, if we ever get the doubling of spatial periodicity as expected from the second-order theory treated so far, or if the streaming is related to the structure of the first-order field. If the latter turns out to be the case, it could finally, from an application point of view, be interesting to exploit this for the development of an acoustically driven chaotic mixer based on a switching between two different eigenmodes, where we can design for a specific set of modes using the first-order Helmholtz equation.

Appendix A

Decomposition of $\mathbf{v}_1$

In this appendix it is shown how the first-order velocity can be decomposed by a scalar and vector potential.

As we know that $\mathbf{v}_1$ is a gradient in the inviscid case, it can be expected that the dominating part of $\mathbf{v}_1$ in the viscous case can also be described by a gradient. Thus, we can always choose to decompose $\mathbf{v}_1$ after a gradient and some unknown extra velocity,

$$\mathbf{v}_1 = \boldsymbol{\nabla}\phi_1 + \mathbf{v}_r, \tag{A.1}$$

where we have made no assumptions on the structure of $\mathbf{v}_r$. With the decomposition in Eq. (A.1) the continuity equation to first order becomes

$$\begin{aligned} \partial_t \rho_1 &= -\rho_0 \boldsymbol{\nabla}\cdot\mathbf{v}_1 \\ &= -\rho_0 \nabla^2\phi_1 - \rho_0 \boldsymbol{\nabla}\cdot\mathbf{v}_r. \end{aligned} \tag{A.2}$$

With time-harmonic first-order quantities we hereby find

$$\nabla^2\phi_1 = \frac{\mathrm{i}\omega\rho_1}{\rho_0} - \boldsymbol{\nabla}\cdot\mathbf{v}_r. \tag{A.3}$$

Combining the Navier–Stokes equation and the equation of state Eqs. (2.12) and (2.14) with time-harmonic behavior leads to

$$-\mathrm{i}\omega\rho_0\mathbf{v}_1 = -c_a^2\boldsymbol{\nabla}\rho_1 + \eta\nabla^2\mathbf{v}_1 + \beta\eta\boldsymbol{\nabla}(\boldsymbol{\nabla}\cdot\mathbf{v}_1). \tag{A.4}$$

If we substitute the decomposed velocity given by Eq. (A.1), we find

$$-\mathrm{i}\omega\rho_0\mathbf{v}_1 = -c_a^2\boldsymbol{\nabla}\rho_1 + \eta\nabla^2\boldsymbol{\nabla}\phi_1 + \eta\nabla^2\mathbf{v}_r + \beta\eta\boldsymbol{\nabla}(\nabla^2\phi_1) + \beta\eta\boldsymbol{\nabla}(\boldsymbol{\nabla}\cdot\mathbf{v}_r). \tag{A.5}$$

Insert the expression for $\nabla^2\phi_1$ obtained from Eq. (A.3) and use $\nabla^2\boldsymbol{\nabla} = \boldsymbol{\nabla}\nabla^2$.

$$\begin{aligned} -\mathrm{i}\omega\rho_0\mathbf{v}_1 &= -c_a^2\boldsymbol{\nabla}\rho_1 + (1+\beta)\eta\boldsymbol{\nabla}\left(\frac{\mathrm{i}\omega\rho_1}{\rho_0} - \boldsymbol{\nabla}\cdot\mathbf{v}_r\right) + \eta\nabla^2\mathbf{v}_r + \beta\eta\boldsymbol{\nabla}(\boldsymbol{\nabla}\cdot\mathbf{v}_r) \\ &= \left(-c_a^2 + \frac{\mathrm{i}(1+\beta)\eta\omega}{\rho_0}\right)\boldsymbol{\nabla}\rho_1 - (1+\beta)\eta\boldsymbol{\nabla}(\boldsymbol{\nabla}\cdot\mathbf{v}_r) + \beta\eta\boldsymbol{\nabla}(\boldsymbol{\nabla}\cdot\mathbf{v}_r) + \eta\nabla^2\mathbf{v}_r \\ &= \left(-c_a^2 + \frac{\mathrm{i}(1+\beta)\eta\omega}{\rho_0}\right)\boldsymbol{\nabla}\rho_1 - \eta\boldsymbol{\nabla}(\boldsymbol{\nabla}\cdot\mathbf{v}_r) + \eta\nabla^2\mathbf{v}_r. \end{aligned} \tag{A.6}$$

Introducing γ as defined in Eq. (2.53) we get,

$$-\mathrm{i}\omega\rho_0\mathbf{v}_1 = -c_a^2\left(1-\mathrm{i}\gamma\right)\boldsymbol{\nabla}\rho_1 + \eta\left(\nabla^2\mathbf{v}_r - \boldsymbol{\nabla}(\boldsymbol{\nabla}\cdot\mathbf{v}_r)\right). \tag{A.7}$$

Now $\mathbf{v}_1$ can be isolated to get

$$\mathbf{v}_1 = -\frac{\mathrm{i}c_a^2\left(1-\mathrm{i}\gamma\right)}{\omega\rho_0}\boldsymbol{\nabla}\rho_1 + \frac{\mathrm{i}\eta}{\rho_0\omega}\left(\nabla^2\mathbf{v}_r - \boldsymbol{\nabla}(\boldsymbol{\nabla}\cdot\mathbf{v}_r)\right). \tag{A.8}$$

We notice that if $\mathbf{v}_r = \boldsymbol{\nabla}\phi_r$ the last terms disappear as expected due to the fact that we in this case have $\mathbf{v}_1 = \boldsymbol{\nabla}\phi_1 \equiv K\boldsymbol{\nabla}\rho_1$, where

$$K \equiv -\frac{\mathrm{i}c_a^2\left(1-\mathrm{i}\gamma\right)}{\omega\rho_0}. \tag{A.9}$$

As $\mathbf{v}_r = \mathbf{0}$ for $\gamma = 0$ we can also deduce that the last terms must scale with γ.

To ease notation, we can redefine the terms containing $\mathbf{v}_r$ as these are not known anyways. With the definition

$$\mathbf{v}_u \equiv \frac{\mathrm{i}\eta}{\rho_0\omega}\left(\nabla^2\mathbf{v}_r - \boldsymbol{\nabla}(\boldsymbol{\nabla}\cdot\mathbf{v}_r)\right), \tag{A.10}$$

we thus have shown that in general $\mathbf{v}_1$ can be decomposed after

$$\mathbf{v}_1 = -\frac{\mathrm{i}c_a^2\left(1-\mathrm{i}\gamma\right)}{\omega\rho_0}\boldsymbol{\nabla}\rho_1 + \mathbf{v}_u, \tag{A.11}$$

where we know that $\mathbf{v}_u$ is small compared to the dominating components of the gradient term. Taking the divergence of Eq. (A.11) leads to

$$\boldsymbol{\nabla}\cdot\mathbf{v}_1 = -\frac{\mathrm{i}(1-\mathrm{i}\gamma)c_a^2}{\omega\rho_0}\nabla^2\rho_1 + \boldsymbol{\nabla}\cdot\mathbf{v}_u. \tag{A.12}$$

From this we can now isolate $\nabla^2\rho_1$,

$$\nabla^2\rho_1 = -\frac{\omega\rho_0}{\mathrm{i}(1-\mathrm{i}\gamma)c_a^2}\boldsymbol{\nabla}\cdot\mathbf{v}_1 + \frac{\omega\rho_0}{\mathrm{i}(1-\mathrm{i}\gamma)c_a^2}\boldsymbol{\nabla}\cdot\mathbf{v}_u. \tag{A.13}$$

We have previously in Eq. (2.52) shown the lossy Helmholtz equation for e.g. ρ_1 to be

$$\nabla^2\rho_1 = -\frac{\omega^2}{c_a^2(1-\mathrm{i}\gamma)}\rho_1. \tag{A.14}$$

Combining this with Eq. (A.13) leads to

$$-\frac{\rho_0\omega}{(1-\mathrm{i}\gamma)c_a^2}\boldsymbol{\nabla}\cdot\mathbf{v}_1 + \frac{\rho_0\omega}{\mathrm{i}(1-\mathrm{i}\gamma)c_a^2}\boldsymbol{\nabla}\cdot\mathbf{v}_u = -\frac{\omega^2}{c_a^2(1-\mathrm{i}\gamma)}\rho_1 \tag{A.15}$$

which is readily reduced to

$$-\rho_0 \boldsymbol{\nabla} \cdot \mathbf{v}_1 + \rho_0 \boldsymbol{\nabla} \cdot \mathbf{v}_u = -\mathrm{i}\omega\rho_1. \tag{A.16}$$

This is a continuity equation. However, comparing to the original continuity equation Eq. (A.2) we see that for Eq. (A.16) to be fulfilled, we must have

$$\boldsymbol{\nabla} \cdot \mathbf{v}_u = 0. \tag{A.17}$$

This implies that $\mathbf{v}_u$ can be constructed from a vector potential and thus we can conclude from Eq. (A.11) that $\mathbf{v}_1$ can be decomposed into a gradient and curl component,

$$\mathbf{v}_1 = \boldsymbol{\nabla}\phi_1 + \boldsymbol{\nabla} \times \mathbf{A}_1. \tag{A.18}$$

Appendix B

Combined actuator system

The following appendix contains the treatment of an actuator model based on a combined force-driven mechanical actuator. This is a classical acoustic approach for treating actuators and the methods and models presented in the following are based on and follows to a large extent the similar combined driver-pipe example given by Kinsler [35, chap. 10].

B.1 Combined actuator system

The simple actuation method used in Chap. 3 implies an actuator velocity growing linearly with frequency. As shown this has led to unreasonably large values of pressure and velocity both with and without the inclusion of viscous damping. This indicates that our model have been too simple regarding the actuation mechanism which in general will be dependent on the frequency response of the system due to internal impedances.

To reveal some of these aspects we can treat the simple example of a harmonically forced, damped, linear mechanical oscillator driving some fluid in a closed tube as illustrated in Fig. B.1. This classical example could also model the behavior of a speaker driving a resonator tube or some musical instrument [35].

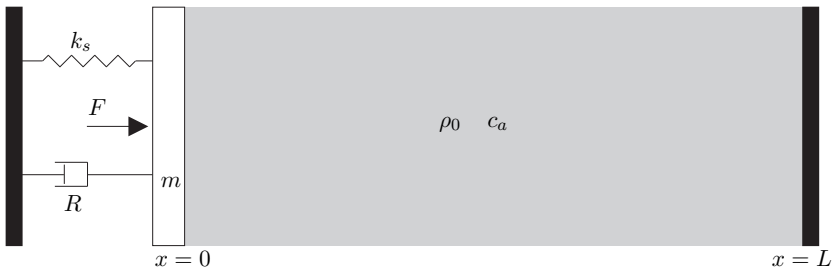

Figure B.1: A combined fluidic resonator and actuator system modeled by a forced, damped, linear oscillator connected to a tube at $x = 0$. The tube is rigidly closed at $x = L$ and the displacement of the oscillator is assumed much smaller than the tube length.

Following the classic acoustic approach as in [35], we assume the cross sectional area S to be sufficiently small so only plane waves will be allowed to propagate. The equation

of motion for the mass oscillating with displacement ξ can be written up directly as

$$m\partial_t^2\xi = -k_s\xi - R\partial_t\xi - Sp_{10}(0,t) + F, \tag{B.1}$$

where we have assumed the displacement of the actuator negligible in comparison to the tube length L so the force from the fluid essentially can be expressed by $p_{10}(0,t)$. The remaining terms stem from the spring stiffness k_s, the viscous damper with damping coefficient R and the driving force, which is assumed harmonic, $F = F_0\mathrm{e}^{-\mathrm{i}\omega t}$.

Due to continuity of the velocity at $x = 0$ we must demand the fluid velocity to equal the velocity of the mass,

$$\partial_t\xi = v_{10}(0,t) \equiv v|_0, \tag{B.2}$$

where the last equality is introduced for notational convenience. Hereby we can rewrite the equation of motion in terms of $v|_0$ and $p|_0$,

$$m\partial_t v|_0 = -k_s\int v|_0 dt - Rv|_0 - Sp|_0 + F. \tag{B.3}$$

As the system is harmonically driven, all time dependencies are of the form $\mathrm{e}^{-\mathrm{i}\omega t}$, which allows us to make the substitutions

$$\partial_t = -\mathrm{i}\omega \tag{B.4}$$

$$\int dt = \frac{\mathrm{i}}{\omega}, \tag{B.5}$$

now yielding

$$-\mathrm{i}\omega m v|_0 = -\frac{\mathrm{i}k_s}{\omega}v|_0 = -Rv|_0 = -Sp|_0 + F. \tag{B.6}$$

This allows us to derive an expression for the excitation force,

$$\begin{aligned} F &= \left[-\mathrm{i}\omega m + \frac{\mathrm{i}k_s}{\omega} + R + S\frac{p|_0}{v|_0}\right] v|_0 \\ &= \left[-\mathrm{i}\omega m + \frac{\mathrm{i}k_s}{\omega} + R + Sz_a|_0\right] v|_0, \end{aligned} \tag{B.7}$$

where we have introduced the specific acoustic impedance z_a defined in Sec. 3.2.1. As the mechanical impedance is defined as [36]

$$Z_m = \frac{F}{v}, \tag{B.8}$$

we easily deduce the total mechanical input impedance of the system from Eq. (B.7),

$$Z_{m0} = -\mathrm{i}\omega m + \frac{\mathrm{i}k_s}{\omega} + R + Sz_a|_0. \tag{B.9}$$

This is an important quantity which can be used for determination of the resonance frequencies of the system. However, before proceeding to this, let us first determine the solution of the acoustic field in the tube. Since we have assumed plane waves, the general solution can be expressed as

$$v_{10} = A\mathrm{e}^{\mathrm{i}(k_0 x - \omega t)} + B\mathrm{e}^{\mathrm{i}(-k_0 x - \omega t)}. \tag{B.10}$$

As we have a rigid wall at $x = L$ and as the pressure at $x = 0$ can be expressed in terms of the actuator parameters from Eq. (B.7), we can now set up two boundary conditions,

$$v_{10}(L, t) = 0 \tag{B.11a}$$

$$p_{10}(0, t) = \frac{1}{S}\left[-\mathrm{i}\omega m v|_0 + \frac{\mathrm{i}k_s}{\omega} v|_0 + R v|_0 - F\right]. \tag{B.11b}$$

Now, from Eqs. (2.14), (2.13) and (B.10) we find that

$$p_{10} = \rho_0 c_a \left[A\mathrm{e}^{\mathrm{i}(k_0 x - \omega t)} - B\mathrm{e}^{\mathrm{i}(-k_0 x - \omega t)}\right]. \tag{B.12}$$

From this we can now find

$$p|_0 = \rho_0 c_a \left[A - B\right] \mathrm{e}^{-\mathrm{i}\omega t} \tag{B.13}$$

$$v|_0 = \left[A + B\right] \mathrm{e}^{-\mathrm{i}\omega t}, \tag{B.14}$$

which by insertion in the boundary conditions leads to

$$\rho_0 c_a (A - B) = \frac{1}{S}\left[(A + B)\left[-\mathrm{i}\omega m + \frac{\mathrm{i}k_s}{\omega} + R\right] - F\right] \tag{B.15}$$

$$A\mathrm{e}^{\mathrm{i}(k_0 L - \omega t)} + B\mathrm{e}^{\mathrm{i}(-k_0 L - \omega t)} = 0. \tag{B.16}$$

From Eq. (B.16) we get

$$A = -B\frac{\mathrm{e}^{\mathrm{i}(-k_0 L - \omega t)}}{\mathrm{e}^{\mathrm{i}(k_0 L - \omega t)}} = -B\mathrm{e}^{-2\mathrm{i}k_0 L}. \tag{B.17}$$

Inserting this into Eq. (B.15) and isolating B leads to

$$B = -\frac{F}{S}\left[-\rho_0 c_a \left(1 + \mathrm{e}^{-2\mathrm{i}k_0 L}\right) + \frac{1}{S}\left(1 - \mathrm{e}^{-2\mathrm{i}k_0 L}\right)\left[\mathrm{i}\omega m - \frac{\mathrm{i}k_s}{\omega} - R\right]\right]^{-1}. \tag{B.18}$$

Now A is readily determined from Eq. (B.17) as

$$A = \mathrm{e}^{-2\mathrm{i}k_0 L}\frac{F}{S}\left[-\rho_0 c_a \left(1 + \mathrm{e}^{-2\mathrm{i}k_0 L}\right) + \frac{1}{S}\left(1 - \mathrm{e}^{-2\mathrm{i}k_0 L}\right)\left[\mathrm{i}\omega m - \frac{\mathrm{i}k_s}{\omega} - R\right]\right]^{-1}. \tag{B.19}$$

Hereby we have found the analytical expression for the velocity and pressure field in the combined tube and actuator system by Eqs. (B.10), (B.12), (B.18) and (B.19),

$$v_{10}(x, t) = \mathcal{F}\left(\mathrm{e}^{-2\mathrm{i}k_0 L}\mathrm{e}^{\mathrm{i}k_0 x} - \mathrm{e}^{-\mathrm{i}k_0 x}\right)\mathrm{e}^{-\mathrm{i}\omega t} \tag{B.20}$$

$$p_{10}(x, t) = \rho_0 c_a \mathcal{F}\left(\mathrm{e}^{-2\mathrm{i}k_0 L}\mathrm{e}^{\mathrm{i}k_0 x} + \mathrm{e}^{-\mathrm{i}k_0 x}\right)\mathrm{e}^{-\mathrm{i}\omega t}, \tag{B.21}$$

where $\mathcal{F}$ has been defined as

$$\mathcal{F} \equiv \frac{F}{S}\left[-\rho_0 c_a\left(1+\mathrm{e}^{-2\mathrm{i}k_0L}\right)+\frac{1}{S}\left(1-\mathrm{e}^{-2\mathrm{i}k_0L}\right)\left[\mathrm{i}\omega m-\frac{\mathrm{i}k_s}{\omega}-R\right]\right]^{-1}. \tag{B.22}$$

It is now easy to see that the specific acoustic impedance at $x=0$ can be expressed as

$$z_a = \rho_0 c_a \frac{\mathrm{e}^{-2\mathrm{i}k_0L}+1}{\mathrm{e}^{-2\mathrm{i}k_0L}-1} = \mathrm{i}\rho_0 c_a \cot k_0 L. \tag{B.23}$$

This means that the tube itself has resonances for

$$\cot k_0 L = 0, \tag{B.24}$$

leading to the solutions

$$k_0 L = \frac{\pi}{2}(2n-1), \qquad n=1,2,3,\ldots \tag{B.25}$$

$$\omega = \frac{c_a}{L}\frac{\pi}{2}(2n-1), \qquad n=1,2,3,\ldots \tag{B.26}$$

$$\tag{B.27}$$

This result is equivalent to wavelengths that have the following relation to the length of the tube,

$$\lambda = \frac{4L}{2n-1}, \qquad n=1,2,3,\ldots \tag{B.28}$$

and an analogous result can be found for the anti resonances. Similarly the actuator itself has resonance for

$$\omega = \sqrt{\frac{k_s}{m}}. \tag{B.29}$$

The resonances of the entire system are found from Eq. (B.9) by setting the reactance, which is defined as the imaginary part of the impedance, equal to zero as the resistance, being the real part of the impedance, is independent of frequency,

$$\mathrm{Im}\left\{Z_{m0}\right\} = 0. \tag{B.30}$$

Combining Eqs. (B.9) and (B.23) we get

$$-m\omega + \frac{k_s}{\omega} + S\rho_0 c_a \cot k_0 L = 0 \tag{B.31}$$

$$-mkc_a + \frac{k_s}{kc} + S\rho_0 c_a \cot k_0 L = 0. \tag{B.32}$$

Following [35, chap. 10.6] we can by rearranging the terms and introducing two cleverly chosen parameters rewrite Eq. (B.32) into a transcendental equation in k_0L,

$$\cot k_0 L = r_m k_0 L - \frac{r_s}{k_0 L}, \tag{B.33}$$

where the two new parameters r_m and r_s are given by

$$r_m = \frac{m}{SL\rho_0} \tag{B.34}$$

$$r_s = \frac{k_s L}{S\rho_0 c_a^2}, \tag{B.35}$$

and, as pointed out in [35], are the actuator to fluid ratio of mass and spring stiffness, respectively. The mass ratio is immediately recognized, and the spring ratio can be clarified by use of the following expression relating the speed of sound c_a for liquids to the bulk modulus K_0 and density ρ_0 [44],

$$c_a^2 = \frac{K_0}{\rho_0}. \tag{B.36}$$

This relation yields

$$r_s = \frac{k_s L}{SK_0}. \tag{B.37}$$

As with most transcendental equations, Eq. (B.33) cannot be solved directly but one must rely on numerical or graphical methods. The latter method, where solutions are found by intersection of the right and left hand side of Eq. (B.33), is an intuitively easy approach and gives a good foundation for understanding the impact of the two parameters r_m and r_s.

In Fig. B.2 the left and right hand side of Eq. (B.33) have been plotted for two different combinations of r_m and r_s. Fig. B.2 (a) represents a heavy and rigid actuator and we see that the solutions to the transcendental equation are rapidly approaching the vertical asymptotes for the cotangent part which occur for integers of π. This corresponds to a tube and wavelength relation of the form

$$n\frac{\lambda}{2} = L, \qquad n = 1, 2, 3, \ldots, \tag{B.38}$$

which is the classic example of resonances for standing plane waves between two rigid surfaces. Such a behavior is in line with expectations for an actuator dominated system. In Fig. B.2 (b) the system is now dominated by the fluid and we see that the resonances are closer to the ones found for a open pipe in Eq. (B.25) and only slowly approaching the resonances for a closed system.

Having treated the resonances we can now investigate the behavior of the velocity at the actuator for different frequencies. Disregarding the time factor $\mathrm{e}^{-\mathrm{i}\omega t}$ we can plot the real part $v_{\max,0}$ of Eq. (B.20) for $x = 0$. Due to complicated composition of the velocity solution, we shall not write it but only plot the solution. The result for the same values of r_m and r_s as used in Fig. B.2 are shown in Fig. B.3 where the velocity is given in arbitrary units. As expected the velocity of the actuator is dependent on the frequency, peaking a the system resonance. The values of ρ_0, c_a, S, L, F, R, k_s and m utilized for the two plots are chosen rather arbitrarily in order to emphasize the two extremes of actuator

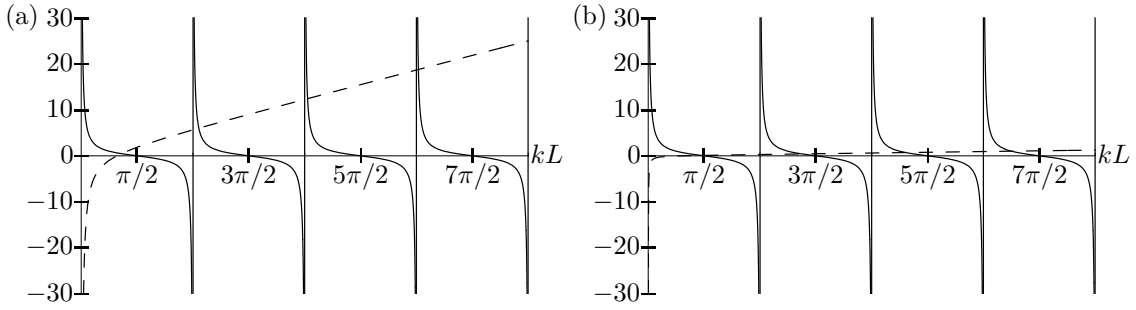

Figure B.2: Left and right hand side of Eq. (B.33) plotted as solid and dashed line, respectively. In (a) we have $r_m = 2$ and $r_s = 2$, whereas in (b) the corresponding values are $r_m = 0.1$ and $r_s = 0.1$. This corresponds to a actuator and fluid dominated system, respectively and gives rise to resonances close to the ones corresponding to a system rigidly closed in both ends or only in one end, respectively.

r_m	r_s	c_a	ρ_0	R	k_s	m	F	L	S
2	2	100	1	30	20	20	10	100	0.1
0.1	0.1	100	1	10	10	0.1	10	10	0.1

Table B.1: Values in SI units for the system plotted in Fig. B.2 and Fig. B.3, respectively.

and fluid dominated systems, respectively. Depending on the parameters, the behavior of course changes where especially the damping have an impact on the driver velocity profile, despite not changing the resonance frequencies. The values used for actuator dominated behavior are given in Table. B.1.

Although we have now included internal impedance in the actuator, the model, however, is still not sufficient as we have not considered the viscous damping. Furthermore, we have assumed the force to be constant without thought for the actual power consumption required for driving the system. In a real device this might be a limiting factor, especially at resonance.

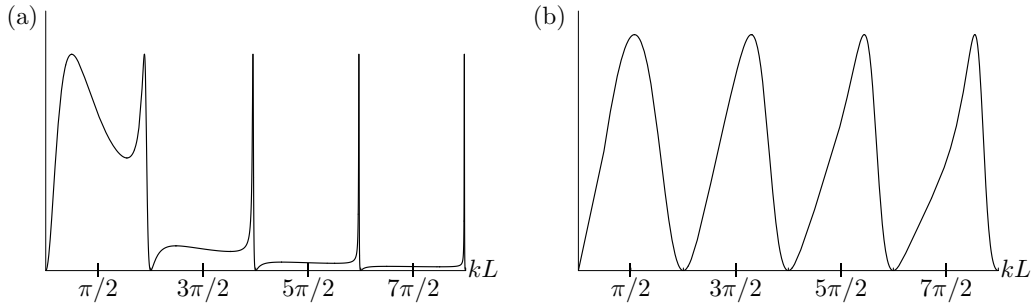

Figure B.3: The velocity, of the actuator in arbitrary units. The values of r_m and r_s in (a) and (b), respectively, are the same as used in Fig. B.2 (a) and (b) and we observe peaks at the resonances where the system is easy to drive for the given force.

B.2 Combined actuator system with viscous damping

Considering the system treated in Sec. B.1 but with inclusion of viscous damping, the basic equation of motion is the same as Eq. (B.1). This means that solving the damped system is directly equivalent to solving the analogous undamped problem with the exception that the wave number k_0 must now be substituted with its complex counterpart

$$k = k_0(1 + \mathrm{i}\frac{1}{2}\gamma), \tag{B.39}$$

found from the modified Helmholtz equation Eq. (2.56) with γ defined in Eq. (2.53). Without further ado we can therefore skip the math and go directly to Eq. (B.12), where we find

$$p_1 = \frac{\rho_0 c_a^2}{\omega} k \left[A\mathrm{e}^{\mathrm{i}(kx-\omega t)} - B\mathrm{e}^{\mathrm{i}(-kx-\omega t)} \right]. \tag{B.40}$$

The calculations follow the inviscid case, and we can therefore readily recognize the specific acoustic impedance from the first part of Eq. (B.23) by substituting k for k_0 and $c_a^2 k/\omega$ for c_a,

$$z_a = \rho_0 \frac{c_a^2 k}{\omega} \frac{\mathrm{e}^{-2\mathrm{i}kL} + 1}{\mathrm{e}^{-2\mathrm{i}kL} - 1} \tag{B.41}$$

$$= \frac{\rho_0 c_a^2 k_0 (1 + \mathrm{i}\frac{1}{2}\gamma)}{\omega} \frac{\mathrm{e}^{k_0\gamma L}\mathrm{e}^{-2\mathrm{i}k_0 L} + 1}{\mathrm{e}^{2k_0\gamma L}\mathrm{e}^{-2\mathrm{i}k_0 L} - 1} \tag{B.42}$$

$$= \rho_0 c_a \left(1 + \mathrm{i}\frac{1}{2}\gamma\right) \frac{\mathrm{e}^{k_0\gamma L}\left(\cos 2k_0 L - \mathrm{i}\sin 2k_0 L\right) + 1}{\mathrm{e}^{k_0\gamma L}\left(\cos 2k_0 L - \mathrm{i}\sin 2k_0 L\right) - 1} \tag{B.43}$$

By tedious algebraic manipulation we can split the expression into real and imaginary parts,

$$\begin{aligned} z_a =& \frac{\rho_0 c_a}{k_0\left[\cos 2k_0 L - \cosh k_0\gamma L\right]} \times \\ & \left[\frac{1}{2}k_0\gamma \sin 2k_0 L - k_0 \sinh k_0\gamma L - \mathrm{i}\left(k_0 \sin 2k_0 L + \frac{1}{2}k_0\gamma \sinh k_0\gamma L\right)\right], \end{aligned} \tag{B.44}$$

as we have previously estimated typical values for γ to be on the order of 10^{-5} it is a reasonable assumption that $\frac{1}{2}k_0\gamma L \ll 1$, which yields

$$z_a \approx \frac{\rho_0 c_a}{\cos 2k_0 L - 1}\left[\frac{1}{2}\gamma \sin 2k_0 L - k_0\gamma L - \mathrm{i}\left(\sin 2k_0 L + \frac{1}{2}\gamma^2 k_0 L\right)\right], \tag{B.45}$$

where $\gamma = 0$ leads to the inviscid result found in Eq. (B.23). Hereby the system dynamics can be analyzed. We will not do this however, since remaining analysis methods are analogous to the inviscid case.

Appendix C

Extended calculations for radiation force

This appendix contains calculations connected to the derivation of the acoustic radiation force on a spherical object in a plane standing wave field. The calculations closely follow the derivations by Yosioka and Kawasima [19] with the addition of intermediate results. The essential parts of these calculations are given in a condensed format in Sec. 4.3 and some left out details are found in [19].

C.1 Basic equations

For a plane acoustic field along the z-axis, there will be no φ-dependence. By projection along $\hat{\mathbf{z}}$ in spherical coordinates we find for normal and tangential components, respectively, that

$$\mathbf{n} \cdot \hat{\mathbf{z}} = \hat{\mathbf{r}} \cdot \hat{\mathbf{z}} = \cos\theta \tag{C.1a}$$

$$\mathbf{t} \cdot \hat{\mathbf{z}} = \hat{\boldsymbol{\theta}} \cdot \hat{\mathbf{z}} = -\sin\theta. \tag{C.1b}$$

Thereby we get the following from Eq. (4.16)

$$\begin{aligned}\langle F_a \rangle = &-2\pi a^2 \rho_0 \left\langle \int_0^\pi v_r^2 \cos\theta \sin\theta d\theta \right\rangle + 2\pi a^2 \left\langle \int_0^\pi \rho_0 v_r v_\theta \sin^2\theta d\theta \right\rangle \\ &+\pi a^2 \rho_0 \left\langle \int_0^\pi v_{10}^2 \cos\theta \sin\theta d\theta \right\rangle - \pi a^2 \frac{\rho_0}{c_a^2} \left\langle \int_0^\pi (\partial_t \phi_{10})^2 \cos\theta \sin\theta d\theta \right\rangle,\end{aligned} \tag{C.2}$$

where we for simplicity have not expressed the velocity in terms of potentials but exploited

$$\mathbf{v}_{10} = v_t \mathbf{t} + v_n \mathbf{n} = v_\theta \hat{\boldsymbol{\theta}} + v_r \hat{\mathbf{r}}. \tag{C.3}$$

If we rewrite Eq. (C.2) in terms of the potential ϕ_{10}, which will be convenient for subsequent calculations, this is in spherical coordinates with no φ-dependence related to $\mathbf{v}_{10}$ by

$$\mathbf{v}_{10} = \boldsymbol{\nabla}\phi_{10} = \hat{\mathbf{r}}\partial_r \phi_{10} + \hat{\boldsymbol{\theta}} \frac{1}{r} \partial_\theta \phi_{10}. \tag{C.4}$$

The third term on the right hand side of Eq. (C.2) can by using Eq. (C.4) be expressed as

$$\pi a^2 \rho_0 \left\langle \int_0^\pi v_{10}^2 \cos\theta \sin\theta d\theta \right\rangle = \\ \pi a^2 \rho_0 \left\langle \int_0^\pi \left[(\partial_r \phi_{10})_{r=a}^2 + \frac{1}{a^2} (\partial_\theta \phi_{10})_{r=a}^2 \right] \cos\theta \sin\theta d\theta \right\rangle . \tag{C.5}$$

Similarly from Eqs. (C.3) and (C.4) we can easily rewrite the first term in Eq. (C.2) to

$$-2\pi a^2 \rho_0 \left\langle \int_0^\pi v_r^2 \cos\theta \sin\theta d\theta \right\rangle = \\ -2\pi a^2 \rho_0 \left\langle \int_0^\pi (\partial_r \phi_{10})_{r=a}^2 \cos\theta \sin\theta d\theta \right\rangle . \tag{C.6}$$

Combining the first term of Eq. (C.5) with Eq. (C.6) we can define

$$\langle F_r \rangle = -\pi a^2 \rho_0 \left\langle \int_0^\pi (\partial_r \phi_{10})_{r=a}^2 \cos\theta \sin\theta d\theta \right\rangle . \tag{C.7}$$

Analogous rewriting can be performed for the second term,

$$\begin{aligned} \langle F_{\theta r} \rangle &= 2\pi a^2 \rho_0 \left\langle \int_0^\pi v_r v_\theta \sin^2\theta d\theta \right\rangle \\ &= 2\pi a^2 \rho_0 \left\langle \int_0^\pi (\partial_r \phi_{10})_{r=a} \frac{1}{a} (\partial_\theta \phi_{10})_{r=a} \sin^2\theta d\theta \right\rangle \\ &= 2\pi a \rho_0 \left\langle \int_0^\pi (\partial_r \phi_{10})_{r=a} (\partial_\theta \phi_{10})_{r=a} \sin^2\theta d\theta \right\rangle . \end{aligned} \tag{C.8}$$

The remaining part of Eq. (C.5) can be defined as

$$\begin{aligned} \langle F_\theta \rangle &= \pi a^2 \rho_0 \left\langle \int_0^\pi \frac{1}{a^2} (\partial_\theta \phi_{10})_{r=a}^2 \cos\theta \sin\theta d\theta \right\rangle \\ &= \pi \rho_0 \left\langle \int_0^\pi (\partial_\theta \phi_{10})_{r=a}^2 \cos\theta \sin\theta d\theta \right\rangle . \end{aligned} \tag{C.9}$$

Finally the contribution from the time derived potential can be written directly as

$$\left\langle F_\phi \right\rangle = -\pi a^2 \frac{\rho_0}{c_a^2} \left\langle \int_0^\pi (\partial_t \phi_{10})_{r=a}^2 \cos\theta \sin\theta d\theta \right\rangle . \tag{C.10}$$

Thus the time averaged force on the particle can now be found from

$$\langle F_a \rangle = \langle F_r \rangle + \langle F_{\theta r} \rangle + \langle F_\theta \rangle + \left\langle F_\phi \right\rangle . \tag{C.11}$$

C.2 Force in terms of potential inside sphere

As the first order velocity potential $\phi_{10}^{(p)}$ inside the sphere is of a simpler nature than the outer potential, it is algebraically advantageous to express $\langle F_a \rangle$ by $\phi_{10}^{(p)}$. This is easily

obtained by exploiting the physical boundary conditions to be fulfilled on the surface namely continuity in normal velocity and pressure,

$$(\partial_r \phi_{10})_{r=a} = (\partial_r \phi_{10}^{(p)})_{r=a} \tag{C.12a}$$

$$\rho_0(\partial_t \phi_{10})_{r=a} = \rho_0^{(p)}(\partial_t \phi_{10}^{(p)})_{r=a} \Rightarrow (\partial_t \phi_{10})_{r=a} = \alpha(\partial_t \phi_{10}^{(p)})_{r=a} \tag{C.12b}$$

$$\rho_0(\partial_\theta \phi_{10})_{r=a} = \rho_0^{(p)}(\partial_\theta \phi_{10}^{(p)})_{r=a} \Rightarrow (\partial_\theta \phi_{10})_{r=a} = \alpha(\partial_\theta \phi_{10}^{(p)})_{r=a}, \tag{C.12c}$$

where the last equality is a consequence of Eq. (C.12b). For further algebraic manipulation it is advisable to make the variable transformation $\mu = \cos\theta$, $d\mu = -\sin\theta d\theta$ leading to the following, where time averaging is implicitly done but not written for each term,

$$F_r = -\pi a^2 \rho_0 \int_{-1}^{1} (\partial_r \phi_{10}^{(p)})^2 \mu d\mu \tag{C.13}$$

$$\begin{aligned} F_\theta &= \pi \rho_0 \int_{-1}^{1} (\alpha \partial_\theta \phi_{10}^{(p)})^2 \mu d\mu \\ &= \pi \rho_0 \alpha^2 \int_{-1}^{1} (\partial_\mu \phi_{10}^{(p)})^2 \sin^2\theta \mu d\mu \\ &= \pi \rho_0 \alpha^2 \int_{-1}^{1} (\partial_\mu \phi_{10}^{(p)})^2 (1-\mu^2) \mu d\mu \end{aligned} \tag{C.14}$$

$$\begin{aligned} F_{r\theta} &= -2\pi a \rho_0 \int_{-1}^{1} (\partial_r \phi_{10}^{(p)})(\alpha \partial_\theta \phi_{10}^{(p)}) \sin\theta d\mu \\ &= -2\pi a \alpha \rho_0 \int_{-1}^{1} (\partial_r \phi_{10}^{(p)})(\partial_\mu \phi_{10}^{(p)})(1-\mu^2) d\mu \end{aligned} \tag{C.15}$$

$$\begin{aligned} F_\phi &= \pi a^2 \frac{\rho_0}{c_a^2} \int_{-1}^{1} \left(\partial_t \phi_{10}^{(p)}\right)^2 \alpha^2 \mu d\mu \\ &= -\pi a^2 \alpha^2 \frac{\rho_0}{c_a^2} \int_{-1}^{1} \left(\partial_t \phi_{10}^{(p)}\right)^2 \mu d\mu. \end{aligned} \tag{C.16}$$

Here use have been made of the relation $\sin^2\theta = 1 - \cos^2\theta = 1 - \mu^2$ and

$$\frac{\partial \phi}{\partial \theta} = \frac{\partial \mu}{\partial \theta}\frac{\partial \phi}{\partial \mu} = -\sin\theta \partial_\mu \phi. \tag{C.17}$$

C.3 Scattering on spherical particle

As the spherical particle is impinged by the acoustic wave, a spherical wave propagating from the particle will be induced. Hereby the potential outside the particle will consist of both the incoming potential ϕ_{10i} and the scattered ϕ_{10s}

$$\phi_{10} = \phi_{10i} + \phi_{10s}. \tag{C.18}$$

Such a scattering is a classical mathematical problem, which in spherical coordinates can be expressed by infinite series of products of spherical Bessel functions j_n and Hankel functions h_n as well as Legendre polynomials. Treatment of the general theory can be

found in various mathematical textbooks [46] and the scattering in connection to acoustics can be found in [19] and [47].

The trivial derivations will not be given here, but we will only state the solution in terms of the potential inside the sphere, which can be found from the potential in Eq. (C.18) by applying continuity in pressure and velocity [19]. Let the incoming potential relative to the particle position be given as the following in cartesian coordinates

$$\phi_{10i} = Uk_0^{-1}\mathrm{e}^{\mathrm{i}\omega t}(\mathrm{e}^{\mathrm{i}k_0(z+h)} + \mathrm{e}^{-\mathrm{i}k_0(z+h)}), \tag{C.19}$$

where h is the position of the particle relative to a reference plane as initially used by King [8] and U is a velocity amplitude. Hereby the internal potential can be written as [19]

$$\phi_{10}^{(p)} = \sum_{n=0}^{\infty}(2n+1)\mathrm{e}^{\mathrm{i}\omega t}(-\mathrm{i})^n B_n j_n(k_0^{(p)}a)P_n(\cos\theta), \tag{C.20}$$

where B_n is a coefficient to be determined from the boundary conditions. Notice that we use the $\mathrm{e}^{\mathrm{i}\omega t}$ convention in order to keep consistency with the reference [19], although the previously used $\mathrm{e}^{-\mathrm{i}\omega t}$ convention could be used as well. This is merely a mathematical choice affecting among other things the type of Hankel functions of the external potentials.

C.4 Calculation of coefficients

Use the real physical solution of the potential Eq. (C.20) and define

$$\begin{aligned}\mathrm{Re}\left\{\phi_{10}^{(p)}\right\} &= \mathrm{Re}\left\{\sum_{n=0}^{\infty}(2n+1)e^{i\omega t}(-\mathrm{i})^n B_n j_n(k_0^{(p)}a)P_n(\cos\theta)\right\}\\ &\equiv \sum_{n=0}^{\infty}(2n+1)M_n P_n(\cos\theta),\end{aligned} \tag{C.21}$$

with the radial derivative

$$\begin{aligned}\mathrm{Re}\left\{\partial_r\phi_{10}^{(p)}\right\} &= \mathrm{Re}\left\{\sum_{n=0}^{\infty}(2n+1)e^{\mathrm{i}\omega t}(-i)^n B_n k_0^{(p)} j_n'(k_0^{(p)}a)P_n(\cos\theta)\right\}\\ &\equiv \sum_{n=0}^{\infty}(2n+1)K_n P_n(\cos\theta).\end{aligned} \tag{C.22}$$

If we exploit the following identity for Legendre polynomials

$$\int_{-1}^{1}\mu P_n(\mu)P_l(\mu)d\mu = \begin{cases}\frac{2(l+1)}{(2l+1)(2l+3)} & , \quad n = l+1\\ \frac{2l}{(2l-1)(2l+1)} & , \quad n = l-1,\\ 0 & , \quad \text{otherwise}\end{cases} \tag{C.23}$$

we immediately see that only terms with $n = l \pm 1$ survive and we can thus write

$$\begin{aligned} F_r &= -\pi a^2 \rho_0 \int_{-1}^{1} \left(\sum_{n=0}^{\infty} (2n+1) K_n P_n(\mu) \right)^2 \mu d\mu \\ &= -\pi a^2 \rho_0 \sum_{n=0}^{\infty} 2(2n+1) K_n (2(n+1)+1) K_{n+1} \frac{2(n+1)}{(2n+1)(2n+3)} \\ &= -2\pi a^2 \rho_0 \sum_{n=0}^{\infty} 2(n+1) K_n K_{n+1} \end{aligned} \tag{C.24}$$

Similarly for P_ϕ where $\left(\mathrm{Re}\left\{ \partial_t \phi_{10}^{(p)} \right\} \right)^2 = \omega^2 \sin^2 \theta(\cdot)$

$$\begin{aligned} F_\phi &= -\frac{\pi a^2 \alpha^2 \rho_0}{c_a^2} \int_{-1}^{1} \left(\partial_t \phi_{10}^{(p)} \right)^2 \mu d\mu \\ &= -\frac{\pi a^2 \alpha^2 \omega^2 \rho_0}{c_a^2} \sum_{n=0}^{\infty} 2(2n+1) M_m (2n+3) M_{n+1} \frac{2(n+1)}{(2n+1)(2n+3)} \\ &= -2\pi a^2 \alpha^2 k_0^2 \rho_0 \sum_{n=0}^{\infty} 2(n+1) M_n M_{n+1} \end{aligned} \tag{C.25}$$

The following recurrence relation holds for Legendre polynomials,

$$\begin{aligned} (1-\mu^2) \partial_\mu P_n(\mu) &= -n\mu P_n(\mu) + n P_{n-1}(\mu) \\ &= (n+1)\mu P_n(\mu) - (n+1) P_{n+1}(\mu). \end{aligned} \tag{C.26}$$

The orthogonality relation

$$\int_{-1}^{1} P_n(\mu) P_l(\mu) d\mu = \frac{2}{2n+1} \delta_{nl}, \tag{C.27}$$

with δ_{nl} being the Kronecker delta allows only terms with $P_n^2(\mu)$ survive leading to terms with $K_{n+1} M_n$. Together with a few integral relations, calculations similar to Eqs. (C.24) and (C.25) can be shown to give [19],

$$\begin{aligned} F_{r\theta} = &- 2\pi a \alpha \rho_0 \sum_{n=0}^{\infty} 2(n+1)(n+2) K_n M_{n+1} \\ &+ 2\pi a \alpha \rho_0 \sum_{n=0}^{\infty} 2n(n+1) K_{n+1} M_n \end{aligned} \tag{C.28}$$

$$F_\theta = 2\pi \alpha^2 \rho_0 \sum_{n=0}^{\infty} 2n(n+1)(n+2) M_n M_{n+1} \tag{C.29}$$

C.5 Radiation on small spheres

If the spatial extension of the sphere is small in comparison to the wavelength, that is $(k_0 a)^2,\ (k_0^{(p)} a)^2 \ll 1$, any term higher than $n = 2$ will not contribute to M_n and K_n found from Eqs. (C.21) and (C.22) [19]. Thus we can now from Eqs. (C.24)-(C.29) find the force contributions on the particle as

$$F_r = -2\pi a^2 \rho_0 \left[2K_0 K_1 + 4K_1 K_2\right] \tag{C.30a}$$
$$F_\theta = 2\pi \alpha^2 \rho_0 \left[12 M_1 M_2\right] \tag{C.30b}$$
$$F_{r\theta} = -2\pi a\alpha \rho_0 \left[4K_0 M_1 + 12 K_1 M_2\right] + 2\pi a\alpha \rho_0 \left[4 M_1 K_2\right] \tag{C.30c}$$
$$F_\phi = -2\pi k_0^2 a^2 \alpha^2 \rho_0 \left[2M_0 M_1 + 4 M_1 M_2\right]. \tag{C.30d}$$

The total force is thereby

$$\begin{aligned} F_a = -2\pi\rho_0 \Big[& 2a^2 (K_0 K_1 + 2K_1 K_2) \\ & - 4a\alpha \left(M_1 K_2 - K_0 M_1 - 3K_1 M_2\right) \\ & -2\alpha^2 \left(6 M_1 M_2 - (k_0 a)^2 \left(M_0 M_1 + 2 M_1 M_2\right)\right)\Big]. \end{aligned} \tag{C.31}$$

All cross terms between M_n and K_n can be rewritten in terms of either M_n or K_n by exploiting the following relation for spherical Bessel functions

$$\partial_x j_n(x) = \frac{n}{x} j_n(x) - j_{n+1}(x), \tag{C.32}$$

which by applying the chain rule becomes

$$\partial_x j_n(k_0 x) = k_0 \frac{d}{d(k_0 x)} j_n(k_0 x) = k_0 j_n'(k_0 x) = \frac{n}{x} j_n(x) - k_0 j_{n+1}(k_0 x). \tag{C.33}$$

From Eqs. (C.21) and (C.22) we easily find that

$$K_n = k_0^{(p)} M_n', \tag{C.34}$$

and hereby we can by exploiting Eq. (C.33) write

$$K_n = \frac{n}{a} M_n(k_0^{(p)} a) - k_0^{(p)} M_{n+1}(k_0^{(p)} a) \equiv \frac{n}{a} M_n - k_0^{(p)} M_{n+1}. \tag{C.35}$$

We can now write up K_0, K_1 and K_2 in terms of M_n,

$$K_0 = -k_0^{(p)} M_1 \tag{C.36}$$
$$K_1 = \frac{1}{a} M_1 - k_0^{(p)} M_2 \tag{C.37}$$
$$\begin{aligned} K_2 &= \frac{2}{a} M_2 - k_0^{(p)} M_3 \\ &= -\frac{3}{a} M_2 + k_0^{(p)} M_1, \end{aligned} \tag{C.38}$$

where we for the last equality have exploited the recurrence relation

$$j_{n+1}(x) = \frac{(2n+1)}{x} j_n(x) - j_{n-1}(x). \tag{C.39}$$

Finally we get the following expression for the force

$$\begin{aligned} F_a = -2\pi\rho_0 \Big[& 2a^2(1+2\alpha)K_0K_1 - 4a^2(\alpha-1)K_1K_2 \\ & +2(k_0a)^2\alpha^2 M_0M_1 + 12\alpha(1-\alpha)M_1M_2 \Big]. \end{aligned} \tag{C.40}$$

C.6 Writing out terms for small sphere

If we assume that $\alpha = \mathcal{O}(1)$, which is valid for e.g. cells and tracer beads in water the expressions for aK_n and M_n can be found by series expansion to second order in $(k_0a)^2$ and $(k_0^{(p)}s)^2$, that is to fourth order in (k_0a) and $(k_0^{(p)}s)$. Subsequently the insignificant terms can be discarded. For a plane standing wave like Eq. (C.19), we can use now use the expressions from the appendix in Yosioka and Kawasima [19] to write up aK_0 as

$$aK_0 = \mathrm{Re}\left\{ Uk_0^{-1} e^{\mathrm{i}(-hk_0+\omega t)} \left(1 + e^{\mathrm{i}2hk_0}\right) \times \right. \tag{C.41}$$

$$\left. \frac{(\cos(k_0a) + \mathrm{i}\sin(k_0a)) \left(k_0^{(p)}a\cos(k_0^{(p)}a) - \sin(k_0^{(p)}a)\right)}{k_0^{(p)}a\cos(k_0^{(p)}a) + (\alpha - 1 + \mathrm{i}\alpha k_0a)\sin(k_0^{(p)}a)} \right\}. \tag{C.42}$$

Employing the series expansion we find

$$aK_0 = \frac{1}{540\alpha^2} Uk_0^{-1}(k_0^{(p)}a)^2\cos(k_0h)\times \tag{C.43}$$

$$\begin{aligned} & \Big[-[5(24 - 36(k_0a)^2 + 53(k_0a)^4)(k_0^{(p)}a)^2 \\ & + 3(8 - 4(k_0a)^2 + 3(k_0a)^4)(15 + (k_0^{(p)}a)^2)\alpha]\cos(\omega t) \\ & +4k_0a[30\alpha(k_0a)^2 + (k_0^{(p)}a)^2(-30 + (k_0a)^2(55 + 2\alpha))]\sin(\omega t) \Big] \end{aligned} \tag{C.44}$$

By discarding the insignificant terms we find the simplified expression

$$aK_0 = 2Uk_0^{-1}\cos(k_0h)\left[-\frac{(k_0^{(p)}a)^2}{3\alpha}\cos(\omega t) - \frac{(k_0^{(p)}a)^4 k_0a(1-\vartheta^2\alpha)}{9\alpha^2}\sin(\omega t) \right], \tag{C.45}$$

where $\alpha = \rho_0^{(p)}/\rho_0$ and $\vartheta = k_0/k_0^{(p)}$. Similar calculations can be executed for K_1, K_2, M_0, M_1 and M_2 giving the following results.

$$aK_1 = 2Uk_0^{-1}\sin(k_0h)\left[-\frac{k_0a}{1+2\alpha}\cos(\omega t) + \frac{(k_0a)^4(1-\alpha)}{3(1+2\alpha)^2}\sin(\omega t)\right] \tag{C.46}$$

$$aK_2 = 4Uk_0^{-1}\cos(k_0h)\left[-\frac{(k_0a)^2}{6+9\alpha}\cos(\omega t) + \frac{2(k_0a)^7(1-\alpha)}{135(2+3\alpha)^2}\sin(\omega t)\right] \tag{C.47}$$

$$M_0 = 2Uk_0^{-1}\cos(k_0h)\left[\frac{1}{\alpha}\cos(\omega t) + \frac{(k_0^{(p)}a)^2k_0a(1-\alpha\vartheta^2)}{3\alpha^2}\sin(\omega t)\right] \tag{C.48}$$

$$M_1 = 2Uk_0^{-1}\sin(k_0h)\left[-\frac{k_0a}{1+2\alpha}\cos(\omega t) + \frac{(k_0a)^4(1-\alpha)}{3(1+2\alpha)^2}\sin(\omega t)\right] \tag{C.49}$$

$$M_2 = 2Uk_0^{-1}\cos(k_0h)\left[-\frac{(k_0a)^2}{6+9\alpha}\cos(\omega t) + \frac{2(k_0a)^7(1-\alpha)}{135(2+3\alpha)^2}\sin(\omega t)\right]. \tag{C.50}$$

The expressions for aK_2 and M_2 has been found by separately expanding numerator and denominator to fifth order in $(k_0a)^2$ and $(k_0^{(p)}a)^2$.

By inserting these expression into Eq. (C.40) and time averaging we can after trivial algebraic manipulation find the following expression

$$\langle F_a\rangle = \frac{4\pi(k_0a)^3\rho_0U^2k_0^{-2}\sin(2k_0h)}{405\alpha^2(1+2\alpha)^2(2+3\alpha)\vartheta^4}\times \tag{C.51}$$

$$\Big[4(k_0a)^8(\alpha-1)^3\alpha^2\vartheta^4 + 135\alpha[2+\alpha(7+6\alpha)]\vartheta^2[-1-2\alpha+\alpha(-2+5\alpha)\vartheta^2]$$
$$-15(k_0a)^6(\alpha-1)(2+3\alpha)(\alpha\vartheta^2-1)[-1+\alpha(-2+3\alpha\vartheta^2)]\Big] \tag{C.52}$$

As $(k_0a)^2 \ll 1$ we can now see that several terms in Eq. (C.52) are insignificant. Discarding these terms we are now left with

$$\langle F_a\rangle = 4\pi a^3U^2k_0\rho_0\mathcal{C}(\alpha,\vartheta)\sin(2k_0h), \tag{C.53}$$

where $\mathcal{C}(\alpha,\vartheta)$ is a dimensionless material dependent factor given by

$$\mathcal{C}(\alpha,\vartheta) = \frac{-2+5\alpha}{3+6\alpha} - \frac{1}{3\alpha\vartheta^2}. \tag{C.54}$$

This can be rewritten to a system where the potential is defined relative to origo, i.e. $\phi_{10i} = Uk_0^{-1}\cos(k_0z)\cos(\omega t)$, which gives the result

$$\langle F_a\rangle = 4\pi a^3U^2k_0\rho_0\mathcal{C}(\alpha,\vartheta)\sin(2k_0z). \tag{C.55}$$

Appendix D

Decomposing second-order equations in general case

In Chap. 5 we have decomposed the second-order Navier–Stokes equation in the special case $\mathbf{v}_1 = \boldsymbol{\nabla}\phi_1$. However, this can only be assumed to be true in the low viscosity case. We will now treat the case, where we have not made this restriction on $\mathbf{v}_1$.

The only gradient terms in the second-order Navier–Stokes equation Eq. (5.14) are $\boldsymbol{\nabla}\langle p_2\rangle$ and $\beta\eta\boldsymbol{\nabla}\langle\boldsymbol{\nabla}\cdot\mathbf{v}_2\rangle$ which we cannot combine to some $\boldsymbol{\nabla}\left\langle p_{2,\mathrm{eff}}\right\rangle$, as we cannot combine two unknown terms. Thus no terms can readily be unified to a common gradient term.

However, we know from App. A that $\mathbf{v}_1$ can be decomposed after potentials. The expression for $\mathbf{v}_1$ given in Eq. (A.11) can now be inserted in the second-order continuity and Navier–Stokes equations. For the continuity equation we find

$$\boldsymbol{\nabla}\cdot\langle\mathbf{v}_2\rangle = -\frac{1}{\rho_0}\boldsymbol{\nabla}\cdot\langle\rho_1\mathbf{v}_1\rangle \tag{D.1}$$

$$= -\frac{1}{\rho_0}\boldsymbol{\nabla}\cdot\langle\rho_1\boldsymbol{\nabla}\phi_1 + \rho_1\mathbf{v}_r\rangle \tag{D.2}$$

$$= -\frac{1}{\rho_0}\boldsymbol{\nabla}\cdot\left\langle -\rho_1\left(\frac{\mathrm{i}c_a^2(1-\mathrm{i}\gamma)}{\omega\rho_0}\boldsymbol{\nabla}\rho_1\right) + \rho_1\mathbf{v}_u\right\rangle. \tag{D.3}$$

The Navier–Stokes equation is

$$\langle\rho_1\partial_t\mathbf{v}_1\rangle + \rho_0\langle(\mathbf{v}_1\cdot\boldsymbol{\nabla})\mathbf{v}_1\rangle = -\boldsymbol{\nabla}\langle p_2\rangle + \eta\nabla^2\langle\mathbf{v}_2\rangle + \beta\eta\boldsymbol{\nabla}\langle\boldsymbol{\nabla}\cdot\mathbf{v}_2\rangle, \tag{D.4}$$

which becomes

$$\left\langle -\rho_1\left(\frac{c_a^2(1-i\gamma)}{\rho_0}\boldsymbol{\nabla}\rho_1\right) - \rho_1(\mathrm{i}\omega\mathbf{v}_u)\right\rangle \tag{D.5}$$

$$+\rho_0\left\langle\left(\left[-\frac{\mathrm{i}(1-\mathrm{i}\gamma)c_a^2}{\rho_0\omega}\boldsymbol{\nabla}\rho_1 + \mathbf{v}_u\right]\cdot\boldsymbol{\nabla}\right)\left(-\frac{\mathrm{i}(1-\mathrm{i}\gamma)c_a^2}{\rho_0\omega}\boldsymbol{\nabla}\rho_1 + \mathbf{v}_u\right)\right\rangle \tag{D.6}$$

$$= -\boldsymbol{\nabla}\langle p_2\rangle + \eta\nabla^2\langle\mathbf{v}_2\rangle + \beta\eta\boldsymbol{\nabla}\langle\boldsymbol{\nabla}\cdot\mathbf{v}_2\rangle. \tag{D.7}$$

We can now use $\langle AB + CD\rangle = \langle AB\rangle + \langle CD\rangle$ to separate terms. In this way the continuity equation becomes

$$\boldsymbol{\nabla}\cdot\langle\mathbf{v}_2\rangle = \frac{c_a^2}{\omega\rho_0^2}\boldsymbol{\nabla}\left\langle\rho_1\left(\mathrm{i}(1-\mathrm{i}\gamma)\boldsymbol{\nabla}\rho_1\right)\right\rangle - \frac{1}{\rho_0}\boldsymbol{\nabla}\left\langle\rho_1\mathbf{v}_u\right\rangle. \tag{D.8}$$

The Navier–Stokes equation expands to

$$-\frac{c_a^2}{\rho_0}\left\langle\rho_1\left(1-\mathrm{i}\gamma\right)\boldsymbol{\nabla}\rho_1\right\rangle - \left\langle\rho_1(\mathrm{i}\omega\mathbf{v}_u)\right\rangle \tag{D.9}$$

$$+\rho_0\left\langle\left(\left[-\frac{\mathrm{i}(1-\mathrm{i}\gamma)c_a^2}{\rho_0\omega}\boldsymbol{\nabla}\rho_1\right]\cdot\boldsymbol{\nabla}\right)\left(-\frac{\mathrm{i}(1-\mathrm{i}\gamma)c_a^2}{\rho_0\omega}\boldsymbol{\nabla}\rho_1\right)\right\rangle \tag{D.10}$$

$$+\rho_0\left\langle\left(\mathbf{v}_u\cdot\boldsymbol{\nabla}\right)\left[-\frac{\mathrm{i}(1-\mathrm{i}\gamma)c_a^2}{\rho_0\omega}\boldsymbol{\nabla}\rho_1\right]\right\rangle \tag{D.11}$$

$$+\rho_0\left\langle\left(\left[-\frac{\mathrm{i}(1-\mathrm{i}\gamma)c_a^2}{\rho_0\omega}\boldsymbol{\nabla}\rho_1\right]\cdot\boldsymbol{\nabla}\right)\mathbf{v}_u\right\rangle + \rho_0\left\langle\left(\mathbf{v}_u\cdot\boldsymbol{\nabla}\right)\mathbf{v}_u\right\rangle \tag{D.12}$$

$$= -\boldsymbol{\nabla}\left\langle p_2\right\rangle + \eta\nabla^2\left\langle\mathbf{v}_2\right\rangle + \beta\eta\boldsymbol{\nabla}\left\langle\boldsymbol{\nabla}\cdot\mathbf{v}_2\right\rangle. \tag{D.13}$$

Compared to the special case with $\mathbf{v}_1 = \boldsymbol{\nabla}\phi_1$, we now have four extra terms on the left hand side contributing to the body force, namely

$$-\left\langle\rho_1(\mathrm{i}\omega\mathbf{v}_u)\right\rangle + \rho_0\left\langle\left(\mathbf{v}_u\cdot\boldsymbol{\nabla}\right)\mathbf{v}_u\right\rangle \tag{D.14}$$

$$+\rho_0\left\langle\left(\mathbf{v}_u\cdot\boldsymbol{\nabla}\right)\left[-\frac{\mathrm{i}(1-\mathrm{i}\gamma)c_a^2}{\rho_0\omega}\boldsymbol{\nabla}\rho_1\right]\right\rangle \tag{D.15}$$

$$+\rho_0\left\langle\left(\left[-\frac{\mathrm{i}(1-\mathrm{i}\gamma)c_a^2}{\rho_0\omega}\boldsymbol{\nabla}\rho_1\right]\cdot\boldsymbol{\nabla}\right)\mathbf{v}_u\right\rangle, \tag{D.16}$$

where the second term can be neglected as this has the order of magnitude $|\mathbf{v}_u|^2$ and $|\mathbf{v}_u| \sim \gamma|\mathbf{v}_g|$, where $\mathbf{v}_g$ is the gradient term.

As the rest of the equation is equal to the situation with $\mathbf{v}_1 = \boldsymbol{\nabla}\phi_1$ the analysis from Sec. 5.2.4 can be transferred directly. The four terms in Eq. (D.16) do not need to be decomposed as they all contain $\mathbf{v}_u$ and thus cannot be expected to exceed the body force terms of Eq. (5.39) in magnitude.

If we know both ρ_1 and $\mathbf{v}_1$ by e.g. solving the continuity and Navier–Stokes equations to first order, we are able to identify the extra terms to the body force which stems from $\mathbf{v}_u$ by substraction

$$\mathbf{v}_u = \mathbf{v}_1 - K\boldsymbol{\nabla}\rho_1, \tag{D.17}$$

where K has been defined in Eq. (5.22). Hereby we can solve the decomposed system in the general case for a viscous system at resonance.

Appendix E

Introduction to corner smoothing

This appendix contains a little introduction to the concepts of corner smoothing. The implementation is based on COMSOL's own corner smoothing method found in the Navier–Stokes application mode.

In some of our examples we have solved the Navier–Stokes equation with a slip condition in the velocity, i.e. $\mathbf{v}_1 \cdot \mathbf{n} = 0$, from the argumentation that the momentum diffusion length is so diminutive that it is negligible to first order. However, the slip condition can numerically fail at corners and other places where boundary segments interconnect as we in these places do not have a unambiguous definition of the normal vector. Instead there is a risk of having two normal vectors in different directions as shown at the tip of a wedge in Fig. E.1. As a consequence of this the two normal vectors can span a plane and thereby we restrict the full velocity to zero at the intersections by constituting a local no-slip condition. Especially at convex corners this is most unfortunate as we physically can expect high velocities at these local points.

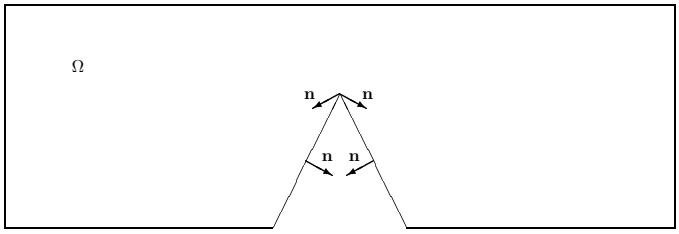

Figure E.1: Numerically, outwards normal vectors can be defined in two different directions where boundary segments intersect. This locally turns a slip condition into a no-slip condition.

To solve this problem we can employ a method similar to the built-in corner smoothing in COMSOL's incompressible Navier–Stokes application mode [56]. The fundamental principle in this method is to define a new normal vector $\mathbf{n}_w$ as a set of finite element variables n_{wx} and n_{wy} at the boundaries. These are coupled to the built-in normal vectors by the weak constraint

$$\mathbf{n} = \mathbf{n}_w. \tag{E.1}$$

As these normal vectors are not necessarily unit vectors, we introduce the normalized vector components

$$n_{wwx} \equiv \texttt{nojac}\left(\frac{n_{wx}}{\sqrt{n_{wx}^2 + n_{wy}^2}}\right) \tag{E.2}$$

$$n_{wwy} \equiv \texttt{nojac}\left(\frac{n_{wy}}{\sqrt{n_{wx}^2 + n_{wy}^2}}\right), \tag{E.3}$$

where the `nojac`–operator excludes the computation from contributing to the Jacobian of the system [57]. This new set of unit normal vectors can now be used in the Dirichlet slip condition as

$$\mathbf{v}_1 \cdot \mathbf{n}_{ww} = 0, \tag{E.4}$$

which in cartesian coordinates is implemented as

$$v_{1x} n_{wwx} + v_{1y} n_{wwy} = 0, \tag{E.5}$$

or, if the wall vibrates with a normal velocity v_{wall},

$$v_{1x} n_{wwx} + v_{1y} n_{wwy} = v_{\text{wall}}. \tag{E.6}$$

With this method we do numerically convert the corners to a smoother transition thus avoiding non-physical no-slip condition.

Appendix F

Radiation results in round chamber

This appendix contains plot for comparison of simulation and measurement of the steady state velocity $\mathbf{v}_r$ induced by the acoustic radiation force in a round chamber. Further experimental details and results are found in Hagsäter *et al.* [1]. The chamber is 200 µm deep, 2 mm in diameter and connected to 400 µm wide and 11.85 mm long inlet channels.

2D simulations on the entire channel system have been made with hard wall boundary conditions to determine the acoustic pressure distribution at resonance from the Helmholtz equation. The domain uses water at 20°C as propagation medium, and the amplitudes of the pressure fields are arbitrary due to the eigenvalue problem.

The velocity $\mathbf{v}_r$ induced from the radiation force is found from Eq. (8.8) using the material properties of water with PA beads.

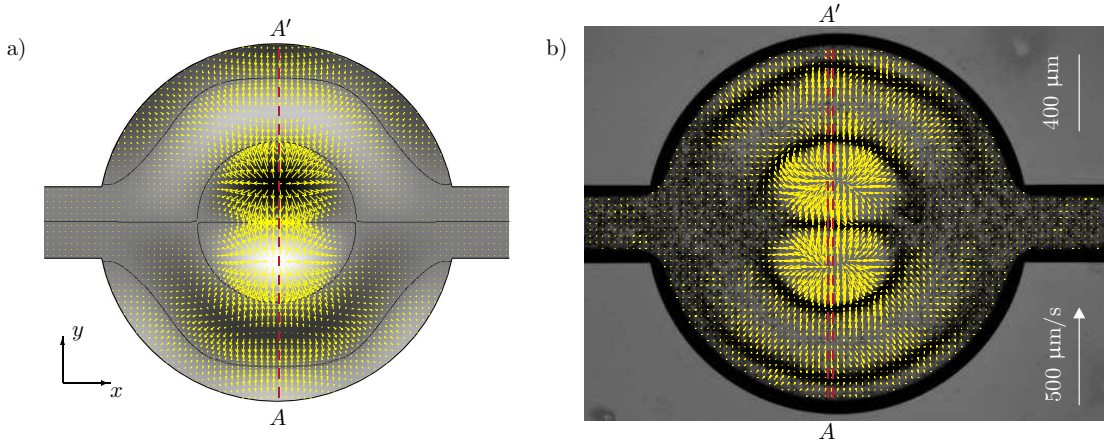

Figure F.1: Radiation force induced velocity and first-order pressure field for numerical and experimental results. a) Numerical result showing grayscale surface plot of pressure distribution and nodal lines overlayed with radiation force vector plot at $f = 2.14$ MHz. b) Experimental result illustrating radiation force and particle formation in nodal lines at $f = 1.94$ MHz. The slashed lines indicate position for cross sectional plot in Fig. F.2. Image b) adapted from [1].

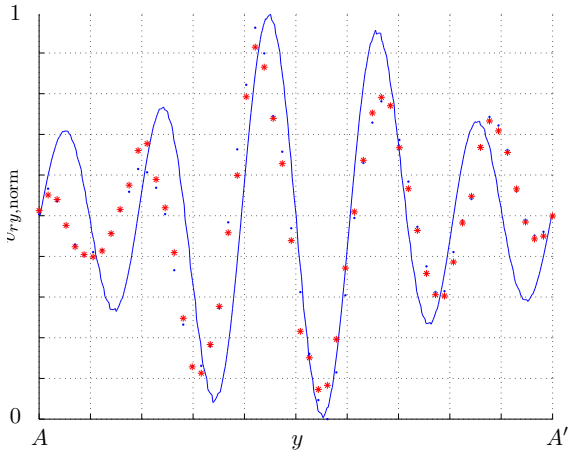

Figure F.2: Comparison of y-component of the normalized radiation force velocity $v_{ry,\mathrm{norm}}$ along the lines from A to A' shown in Fig. F.1. Numerical results is the solid line and experimental results are asterisks and dots for measurements to the left and right of the center line, respectively. The results have maximum amplitudes normalized to unity. Experimental data courtesy of S.M. Hagsäter.

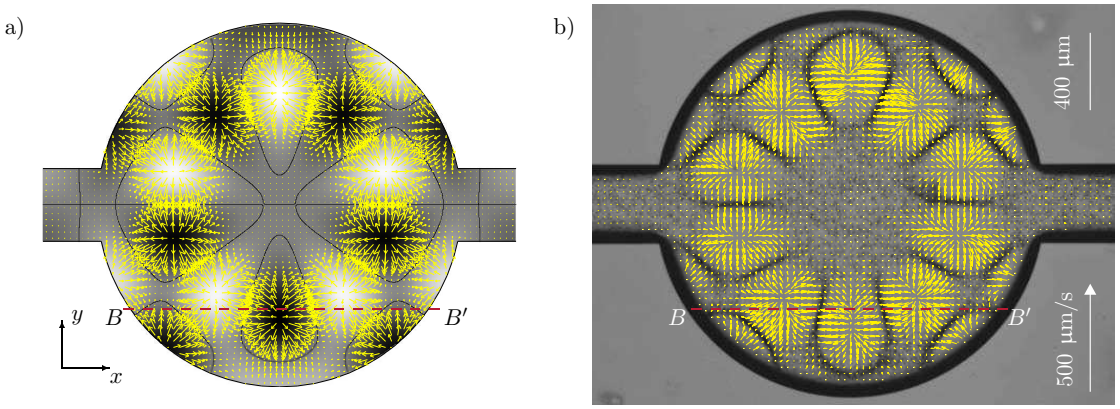

Figure F.3: Radiation force induced velocity and first-order pressure field for numerical and experimental results. a) Numerical result showing grayscale surface plot of pressure distribution and nodal lines overlayed with radiation force vector plot at $f = 2.49$ MHz. b) Experimental result illustrating radiation force and particle formation in nodal lines at $f = 2.42$ MHz. The slashed lines indicate position for cross sectional plot in Fig. F.4. Image b) adapted from [1].

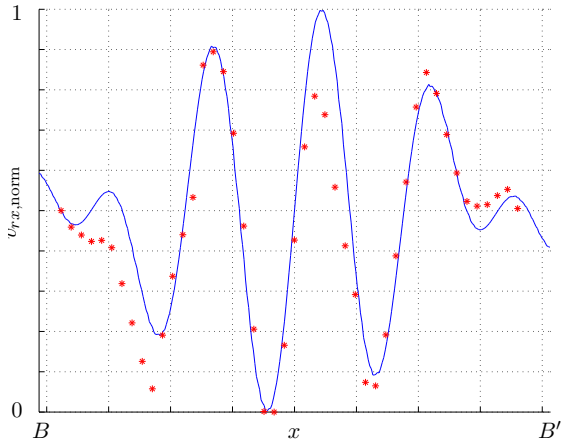

Figure F.4: Comparison of x-component of the normalized radiation force velocity $v_{rx,\mathrm{norm}}$ along the lines from B to B' shown in Fig. F.3. Numerical results is the solid line and experimental results are asterisks. The results have maximum amplitudes normalized to unity. Experimental data courtesy of S.M. Hagsäter.

Appendix G

Comsol: Helmholtz equation from GUI

```
%%% Small script for solving the Helmholtz equation in a circular 2
    D domain
%%% with an eigenvalue solver. Exported and customized from GUI.
%%% MSc student Peder Skafte-Pedersen, TMF, DTU Nanotech, 2007.

% Reset and clear environment
clear all, close all, clc, flclear fem

% Manually defined search frequency
fsearch=1e6;

% Constants
fem.const = {'c','1483'};

% Geometry
g1=ellip2('1e-3','1e-3','base','center','pos',{'0','0'},'rot','0');

% Analyzed geometry
clear s
s.objs={g1};
fem.draw=struct('s',s);
fem.geom=geomcsg(fem);

% Initialize mesh
fem.mesh=meshinit(fem,'hmax',5e-5);

% Application mode 1, 2D Helmholtz
clear appl
appl.mode.class = 'FlPDEG';
appl.dim = {'p','p_t'};
appl.shape = {'shlag(2,''p'')'};
appl.assignsuffix = '_g';
```

```
clear bnd
bnd.type = 'neu';
bnd.ind = [1,1,1,1];
appl.bnd = bnd;
clear equ
equ.da = 0;
equ.f = '-lambda^2/c^2*p';
equ.ga = {{{'px';'py'}}};
equ.ind = [1];
appl.equ = equ;
fem.appl{1} = appl;
fem.frame = {'ref'};
fem.border = 1;
clear units;
units.basesystem = 'SI';
fem.units = units;

% Multiphysics
fem=multiphysics(fem);
% Extend mesh
fem.xmesh=meshextend(fem);

% Solve problem for 6 eigenvalues
fem.sol=femeig(fem, ...
    'solcomp',{'p'}, ...
    'outcomp',{'p'}, ...
    'neigs',6,...
    'shift',2*pi*fsearch);

% Save fem structure
fem0=fem;

% Show results
disp('omega'),disp(fem.sol.lambda')

figure
postplot(fem, ...
    'tridata',{'p','cont','internal'}, ...
    'trimap','jet(1024)', ...
    'solnum',1);
```

Appendix H

Comsol: Helmholtz equation, simple version

```
%%% Small script for solving the Helmholtz equation in a circular 2
    D domain
%%% with an eigenvalue solver. Heavily reduced and altered.
%%% MSc student Peder Skafte-Pedersen, TMF, DTU Nanotech, 2007.

% Reset and clear environment
clear all, close all, clc, flclear fem

% Manually defined search frequency
fsearch=1e6;

% Geometry
fem.geom=ellip2('1e-3','1e-3');

% Constants
fem.const = {'c','1483'};

% Initialize mesh
fem.mesh=meshinit(fem,'hmax',5e-5);

% Variables
fem.dim = {'p'};
% Element type
fem.shape = [2];

% Formulation
fem.form = 'general';
% Equation definition
fem.equ.f = {{'-lambda^2/c^2*p'}};
fem.equ.ga = {{{'px';'py'}}};

% Boundary type
```

```
32 fem.bnd.type = 'neu';
33 % Boundary assignment
34 fem.bnd.ind = [1,1,1,1];
35
36 % Differentiate
37 fem=femdiff(fem);
38
39 % Extend mesh
40 fem.xmesh=meshextend(fem);
41
42 % Solve problem
43 fem.sol=femeig(fem, ...
44     'neigs',6,...
45     'shift',2*pi*fsearch);
46
47 % Save current fem structure for restart purposes
48 fem0=fem;
49
50 % Plot solution
51 postsurf(fem,'p',...
52     'solnum',1);
```

Appendix I

Comsol: Computing higher derivatives

The following script computes the second spatial derivative of a dependent variable using an intermediate equation system in weak form. The script is adapted from a formulation proposed by PhD student Martin Heller, DTU Nanotech.

```
%%% Demonstration of the weak mode for computation of higher
    derivatives.
%%% This script solves the Helmholtz equation as an eigenvalue
    problem and
%%% computes the second derivative in x and y for one eigenmode.
%%% MSc student Peder Skafte-Pedersen, TMF, DTU Nanotech, 2007.

% Clear environment
clear all, close all, flclear fem, clc

%%% Settings %%%
% Mesh size
MaxMesh=2e-5;
% Search frequency
fstart=1.33e6;
% Number of eigenvalues
neig=5;
% Eigensolution to analyze
eignumber=4;

% Geometry (simple square)
g1=rect2(2e-3,2e-3,'base','center','pos',[0,0]);

% Analyzed geometry
clear s
s.objs={g1};
s.name={'R1'};
s.tags={'g1'};
```

```
27
28 fem.draw=struct('s',s);
29 fem.geom=geomcsg(fem);
30
31 % Initialize mesh
32 fem.mesh=meshinit(fem, ...
33     'hmax',MaxMesh);
34
35 % Constants
36 fem.const = {'cw','1483'};
37
38 % Application mode 1 -- Inviscid first-order Helmholtz
39 clear appl
40 appl.mode.class = 'FlPDEG';
41 appl.dim = {'p','p_t'};
42 app.shape = {'shlag(2,''p'')'};
43 appl.assignsuffix = '_g';
44 clear bnd
45 bnd.type = 'neu';
46 bnd.ind = [1,1,1,1];
47 appl.bnd = bnd;
48 clear equ
49 equ.da = 0;
50 equ.f = 'lambda^2/cw^2*p';
51 equ.ind = [1];
52 appl.equ = equ;
53 fem.appl{1} = appl;
54
55 % Application mode 2 -- Second x-derivative
56 clear appl
57 appl.mode.class = 'FlPDEW';
58 appl.dim = {'p_xx','p_xx_t'};
59 app.shape = {'shlag(2,''p_xx'')'};
60 appl.assignsuffix = '_w';
61 clear prop
62 clear weakconstr
63 weakconstr.value = 'off';
64 weakconstr.dim = {'lm3','lm4'};
65 prop.weakconstr = weakconstr;
66 appl.prop = prop;
67 clear bnd
68 bnd.weak = '-test(p_xx)*px*nx';
69 bnd.constr = '0';
70 bnd.ind = [1,1,1,1];
71 appl.bnd = bnd;
72 clear equ
73 equ.weak = 'test(p_xx)*p_xx+test(p_xxx)*px';
74 equ.dweak = 0;
75 equ.ind = [1];
```

```
76  appl.equ = equ;
77  fem.appl{2} = appl;
78
79  % Application mode 3 -- Second y-derivative
80  clear appl
81  appl.mode.class = 'FlPDEW';
82  appl.dim = {'p_yy','p_yy_t'};
83  app.shape = {'shlag(2,''p_yy'')'};
84  appl.assignsuffix = '_w';
85  clear prop
86  clear weakconstr
87  weakconstr.value = 'off';
88  weakconstr.dim = {'lm5','lm6'};
89  prop.weakconstr = weakconstr;
90  appl.prop = prop;
91  clear bnd
92  bnd.weak = '-test(p_yy)*py*ny';
93  bnd.constr = '0';
94  bnd.ind = [1,1,1,1];
95  appl.bnd = bnd;
96  clear equ
97  equ.weak = 'test(p_yy)*p_yy+test(p_yyy)*py';
98  equ.dweak = 0;
99  equ.ind = [1];
100 appl.equ = equ;
101 fem.appl{3} = appl;
102
103 fem.frame = {'ref'};
104 fem.border = 1;
105 clear units;
106 units.basesystem = 'SI';
107 fem.units = units;
108
109 % Multiphysics
110 fem=multiphysics(fem);
111
112 % Extend mesh
113 fem.xmesh=meshextend(fem);
114
115 % Solver script
116 fem.sol=femeig(fem, ...
117      'solcomp',{'p'}, ...
118      'outcomp',{'p'}, ...
119      'neigs',neig, ...
120      'shift',fstart*2*pi);
121
122 fem1=fem;
123 sol1 = asseminit(fem1,'init',fem1,'solnum',eignumber);
124
```

```
125 fem.sol=femstatic(fem,...
126     'init',sol1,...
127     'u',sol1,...
128     'solcomp',{'p_xx','p_yy'}, ...
129     'outcomp',{'p_xx','p_yy','p'});
130 fem.sol=femsol(fem.sol.u,'lambda',fem1.sol.lambda(eignumber));
131 fem2=fem;
132 flclear fem1
133
134 % Plot solution
135 figure
136 postplot(fem, ...
137     'tridata',{'pxx','cont','internal'}, ...
138     'trimap','jet(1024)', ...
139     'title','Surface: pxx');
140
141 figure
142 postplot(fem, ...
143     'tridata',{'p_xx','cont','internal'}, ...
144     'trimap','jet(1024)', ...
145     'title','Surface: p_xx');
```

Appendix J

Comsol: Corner smoothing

Implementation of corner smoothing in Comsol.

```
%%% Script for implementation of no-slip condition with corner
    smoothing.
%%% The script solves a harmonically driven sound field expressed
    by the
%%% continuity and harmonic Navier-Stokes equation. The stress
    tensor only
%%% contains shear components and the smoothing implementation is
    based on
%%% COMSOL's similar method for the Navier-Stokes application mode.
%%% MSc student Peder Skafte-Pedersen, TMF, DTU Nanotech, 2007.

% Reset environment
flclear fem, clear all; close all; clc
% Load geometry
flbinaryfile='NoSlipSmoothTest.mphm';

% Constants
fem.const = {'eta','1e-3*1e5', ...
    'beta','5/3', ...
    'c','1483', ...
    'rho','998', ...
    'gamma','omega*eta*(1+beta)/(rho*c^2)', ...
    'n','1', ...
    'omega','2*pi*n*c/5e-3'};

% Geometry
clear draw
g4=flbinary('g4','draw',flbinaryfile);
draw.s.objs = {g4};
draw.s.name = {'CO2'};
draw.s.tags = {'g4'};
fem.draw = draw;
fem.geom = geomcsg(fem);
```

```
30
31 % Initialize mesh
32 fem.mesh=meshinit(fem, ...
33     'hmax',6e-5);
34
35 % Application mode 1
36 clear appl
37 appl.mode.class = 'FlPDEG';
38 appl.dim = {'u','v','p','nxw','nyw','u_t','v_t','p_t','nxw_t','
      nyw_t'};
39 appl.shape = {'shlag(2,''u'')','shlag(2,''v'')','shlag(1,''p'')'};
40 appl.assignsuffix = '_g';
41 clear prop
42 clear weakconstr
43 weakconstr.value = 'off';
44 weakconstr.dim = {'lm1','lm2','lm3','lm4','lm5','lm6','lm7','lm8','
      lm9','lm10'};
45 prop.weakconstr = weakconstr;
46 appl.prop = prop;
47 fem.frame = {'ref'};
48
49 % Shape functions
50 fem.shape = {'shlag(2,''u'')','shlag(2,''v'')','shlag(1,''p'')','
      shlag(1,''nxw'')','shlag(1,''nyw'')'};
51
52 % Integration order
53 fem.gporder = {4,2,0};
54
55 % Constraint order
56 fem.cporder = {2,1,0};
57
58 % Equation form
59 fem.form = 'general';
60 clear units;
61 units.basesystem = 'SI';
62 fem.units = units;
63
64 % Subdomain settings
65 clear equ
66 equ.init = {{1;0;0}};
67 equ.shape = [1;2;3];
68 equ.cporder = {{1;1;2}};
69 equ.da = 0;
70 equ.gporder = {{1;1;2}};
71 equ.weak = 0;
72 equ.f = {{'beta*eta*(uxx+vxy)+i*omega*rho*u-px';'beta*eta*(uxy+vyy)
      +i*omega*rho*v-py'; ...
73     'p+i*rho*c^2*(ux+vy)/omega'}};
74 equ.ga = {{{'-eta*ux';'-eta*uy'};{'-eta*vx';'-eta*vy'};{0;0}}};
```

```
75  equ.sshapedim = 1;
76  equ.dinit = 0;
77  equ.ind = [1];
78  equ.dim = {'u','v','p'};
79
80  % Interior mesh boundary settings
81  equ.bnd.gporder = 1;
82  equ.bnd.weak = 0;
83  equ.bnd.ind = [1];
84
85  % Interior mesh boundary expressions
86  equ.bnd.expr = {};
87  fem.equ = equ;
88
89  % Boundary settings
90  clear bnd
91  bnd.init = {{'';'';'';'nx_g';'ny_g'}};
92  bnd.r = {'-u*nxww_g-v*nyww_g+1','-u*nxww_g-v*nyww_g'}; % Smoothed
93  bnd.shape = [1;2;3;4;5];
94  bnd.dweak = 0;
95  bnd.constr = {{0;0;0;'nx_g-nxw';'ny_g-nyw'}};
96  bnd.sshape = 1;
97  bnd.cporder = {{1;1;2;2;2}};
98  bnd.g = {{'-K_x+Kw_x';'-K_y+Kw_y';0;0;0}}; % Smoothed
99  bnd.gporder = {{1;1;2;2;2}};
100 bnd.weak = 0;
101 bnd.sshapedim = 1;
102 bnd.dinit = {{}};
103 bnd.ind = [1,2,2,2,2,2,2];
104 bnd.dim = {'u','v','p','nxw','nyw'};
105 bnd.var = {'nx_g','nx', ...
106     'ny_g','ny'};
107
108 % Boundary expressions
109 bnd.expr = {'nxww_g','nojac(nxw/sqrt(nxw^2+nyw^2))', ...
110     'nyww_g','nojac(nyw/sqrt(nxw^2+nyw^2))',...
111     'K_x','eta*ux*nx_g+eta*uy*ny_g',...
112     'K_y','eta*vx*nx_g+eta*vy*ny_g',...
113     'Kw_x','eta*ux*nxww_g+eta*uy*nyww_g',...
114     'Kw_y','eta*vx*nxww_g+eta*vy*nyww_g'};
115 fem.bnd = bnd;
116
117 % Solution form
118 fem.solform = 'weak';
119
120 % Multiphysics
121 fem=multiphysics(fem,...
122     'bdl',[], ...
123     'sdl',[]);
```

```
124
125 % Extend mesh
126 fem.xmesh=meshextend(fem);
127
128 % Solve problem
129 fem.sol=femstatic(fem, ...
130     'solcomp',{'nxw','nyw','u','p','v'}, ...
131     'outcomp',{'nxw','nyw','u','p','v'});
```

Appendix K

Comsol: Lossy Helmholtz

Implementation of 2D lossy Helmholtz equation in a square driven by anti-phase moving walls. Analytical solution given for comparison.

```
%%% Script for solving the viscous Helmholtz equation with the standard
%%% analytical solution as boundary condition, i.e. antisymmetric moving
%%% walls with velocity amplitude ratio of 3. The analytical solution is
%%% given as global expression as well for comparison. Results in short: The
%%% numerical solution does not converge unless we go up very high in
%%% damping, i.e. gamma ~ 10^-2. Solved for the viscous first-order density
%%% (rho_1=pv)
%%% MSc student Peder Skafte-Pedersen, TMF, DTU Nanotech, 2007.

% Reset workspace
clear all, close all, clc, flclear fem

% Geometry (square)
g2=rect2('2e-3','2e-3','base','center','pos',{'0','0'},'rot','0');

% Analyzed geometry
clear s
s.objs={g2};
s.name={'R1'};
s.tags={'g2'};

fem.draw=struct('s',s);
fem.geom=geomcsg(fem);

% Constants
fem.const = {'cw','1483', ...
```

```
  'rho','998', ...
  'eta','1e-3', ...
  'beta','5/3', ...
  'k','3*pi/1e-3', ...
  'omega','k*cw', ...
  'gammadamp','eta*(1+beta)*omega/(rho*cw^2)', ...
  'vw','1e-3', ...
  'Kfactor','i*rho*omega/(cw^2*(1-i*gammadamp))', ...
  'kv','k/sqrt(1-i*gammadamp)'};

% Initialize mesh
fem.mesh=meshinit(fem, ...
                  'hmax',[1.5e-5]);

% Application mode (Viscous Helmholtz)
clear appl
appl.mode.class = 'FlPDEG';
appl.dim = {'pv','pv_t'};
appl.assignsuffix = '_g';
clear bnd
bnd.type = 'neu';
bnd.g = {'3*Kfactor*vw','Kfactor*vw'};
bnd.ind = [2,1,1,2];
appl.bnd = bnd;
clear equ
equ.da = 0;
equ.f = 'sourcehelm';
equ.ga = {{{'gammax';'gammay'}}};
equ.ind = [1];
appl.equ = equ;
fem.appl{1} = appl;
fem.frame = {'ref'};
fem.border = 1;
clear units;
units.basesystem = 'SI';
fem.units = units;

% Global expressions
fem.globalexpr = {'gammax','pvx',...
    'gammay','pvy',...
    'sourcehelm','-omega^2/cw^2*1/(1-i*gammadamp)*pv',...
    'v1xexact','-vw*sin(kv*x)/sin(kv*1e-3)',...
    'v1yexact','-3*vw*sin(kv*y)/sin(kv*1e-3)',...
    'rhoexact','i*vw*kv*rho/(omega*sin(kv*1e-3))*(cos(kv*x)+3*cos(
       kv*y))',...
    'v1xcomp','1/Kfactor*pvx',...
    'v1ycomp','1/Kfactor*pvy'};

% Multiphysics
```

```
75 fem=multiphysics(fem);
76
77 % Extend mesh
78 fem.xmesh=meshextend(fem);
79
80 % Solve problem
81 fem.sol=femstatic(fem, ...
82                   'solcomp',{'pv'}, ...
83                   'outcomp',{'pv'});
84
85 % Save current fem structure for restart purposes
86 fem0=fem;
87
88 % Plot solution
89
90 % Numerical results
91 figure
92 postplot(fem, ...
93          'tridata',{'imag(pv)','cont','internal'}, ...
94          'trimap','jet(1024)', ...
95          'title','Surface: imag(pv)',...
```

Appendix L

Comsol: Double perturbation

Implementation of 1D double perturbed viscous first-order system off resonance with analytical inviscid input velocity.

```
%%% Script for solving the viscous first-order fields off-resonance by a
%%% double perturbation scheme. The model builds on the inviscid analytically
%%% resolved first-order field with accelerated walls at plus and minus L. A
%%% Trivial Dirichlet is used to solve for the viscous part of the system.
%%% 1D-model for high resolution.
%%% MSc student Peder Skafte-Pedersen, TMF, DTU Nanotech, 2007.

% Reset workspace
clear all, close all, flclear fem, clc

% Half domain length (SI units)
Lhalf=1e-3;
% Mesh points
Mpoint=500;

% Geometry
g1=solid1([-Lhalf,Lhalf]);

% Analyzed geometry
clear s
s.objs={g1};
s.name={'I1'};
s.tags={'g1'};

fem.draw=struct('s',s);
fem.geom=geomcsg(fem);

% Constants (Water systems off resonance)
```

```
fem.const = {'L',Lhalf, ...
    'eta','1e-3', ...
    'beta','5/3', ...
    'gamma','eta*(1+beta)*omega/(rho*c^2)', ...
    'c','1483', ...
    'k','9/4*pi/L', ...
    'omega','k*c', ...
    'rho','998', ...
    'l','1e-9'};

% Initialize mesh
fem.mesh=meshinit(fem, ...
    'hmax',2*Lhalf/Mpoint);

% Application mode (General, double perturbation in continuity and
   Navier-Stokes)
clear appl
appl.mode.class = 'FlPDEG';
appl.dim = {'u11','p11','u11_t','p11_t'};
appl.gporder = 4;
appl.cporder = 2;
appl.assignsuffix = '_g';
clear bnd
bnd.type = 'dir';
bnd.r = '-u11';
bnd.ind = [1,1];
appl.bnd = bnd;
clear equ
equ.da = 0;
equ.f = {{'fx';'fp'}};
equ.ga = {{'gammaxx';0}};
equ.ind = [1];
appl.equ = equ;
fem.appl{1} = appl;
fem.frame = {'ref'};
fem.border = 1;
clear units;
units.basesystem = 'SI';
fem.units = units;

% Global expressions
fem.globalexpr = {'F11x','eta*(diff(diff(u10,x),x))+beta*eta*(diff(
   diff(u10,x),x))',...
                'fx','i*omega*rho*u11+F11x',...
                'fp','i*omega*p11-rho*(u11x)',...
                'gammaxx','c^2*p11',...
                'u10','omega*l/sin(k*L)*sin(k*x)',...
                'u1series','omega*l*(sin(k*x)+i*k*gamma/2*x*cos(k*x
                   ))/(sin(k*L)+i*k*gamma/2*L*cos(k*L))',...
```

```
75                  'u1exact','omega*l*sin(k*x/sqrt(1-i*gamma))/sin(k*L
                       /sqrt(1-i*gamma))'};
76
77  % Multiphysics
78  fem=multiphysics(fem);
79
80  % Extend mesh
81  fem.xmesh=meshextend(fem);
82
83  % Solve problem
84  fem.sol=femstatic(fem, ...
85      'solcomp',{'u11','p11'}, ...
86      'outcomp',{'u11','p11'});
87
88  % Save current fem structure for restart purposes
89  fem0=fem;
90
91  % Plot solution
92
93  figure
94  postlin(fem,'imag(u11+u10)');
```

Appendix M

Comsol: Second-order direct implementation

Direct implementation of the time-averaged second-order continuity and Navier–Stokes equations Eqs. (2.86) and (2.97) with an analytical first-order input.

```
function SecondOrderAnalyticalInput(dummy)

%%% Implementation of second-order NS and continuity without
    decomposition.
%%% The system is solved for v_2 and p_2rep (which for notational
    ease is
%%% called (u2,v2) and p2). The analytical inpit is the square
    chamber with
%%% walls vibrating in antiphase at resonance similar to the TGJ
%%% implementation. Implemented as function to be called by
    external
%%% script.
%%% MSc student Peder Skafte-Pedersen, TMF, DTU Nanotech, 2007.

% Prepare system by cleaning up
flclear fem
if nargin==0
    clear all
    PlotSave=0; % Boolean for saving plots
end
close all
clc

global fem
global etascale
if nargin==0
    etascale=1e0;
end

% Geometry
```

```
g2=rect2('2e-3','2e-3','base','center','pos',{'0','0'},'rot','0');

% Analyzed geometry
clear s
s.objs={g2};
s.name={'R1'};
s.tags={'g2'};

fem.draw=struct('s',s);
fem.geom=geomcsg(fem);

% Constants (Viscosity altered)
fem.const = {'L','1e-3',...
    'rhow','998.2', ...
    'cw','1483', ...
    'beta','5/3', ...
    'eta',1e-3*etascale, ...
    'omega','cw*n*pi/L', ...
    'gammadamp','omega*(1+beta)*eta/(rhow*cw^2)', ...
    'r','3',...
    'n','3',...
    'k','omega/(cw*sqrt(1-i*gammadamp))',...
    'l','1e-13',...
    'K','-i*omega/(rhow*k^2)'};

% Initialize mesh
fem.mesh=meshinit(fem, ...
    'hmax',[3e-5]);

% (Default values are not included)

% Application mode 1
clear appl
appl.mode.class = 'FlPDEG';
appl.dim = {'u2','v2','p2','u2_t','v2_t','p2_t'};
appl.shape = {'shlag(2,''u2'')','shlag(2,''v2'')','shlag(1,''p2'')'
   };
appl.assignsuffix = '_g';
clear prop
clear weakconstr
weakconstr.value = 'off';
weakconstr.dim = {'lm2','lm3','lm4','lm5','lm6','lm7'};
prop.weakconstr = weakconstr;
appl.prop = prop;
clear bnd
bnd.r = {{'J2X';'J2Y';'0'}}; % No-slip in mass flux
bnd.ind = [1,1,1,1];
appl.bnd = bnd;
clear equ
```

```
75 equ.da = 0;
76 equ.f = {{'Fx';'Fy';'u2x+v2y-S'}};
77 equ.ga = {{{'gammaxx';'gammaxy'};{'gammayx';'gammayy'};{0;0}}};
78 equ.ind = [1];
79 appl.equ = equ;
80 fem.appl{1} = appl;
81 fem.frame = {'ref'};
82
83 % Global expressions
84 fem.globalexpr = {
85     'pv','-i*rhow*k*omega*l*cw^2/(omega*sin(k*L))*(cos(k*x)+r*cos(k
       *y))',...
86     'vx','omega*l/sin(k*L)*sin(k*x)',...
87     'vy','r*omega*l/sin(k*L)*sin(k*y)',...
88     'gammaxx','-p2+(beta+1)*eta*u2x' ...
89     'gammaxy','eta*(u2y+beta*v2x)' ...
90     'gammayx','eta*(v2x+beta*u2y)' ...
91     'gammayy','-p2+(beta+1)*eta*v2y', ...
92     'S','-1/(2*cw^2*rhow)*real(diff(pv,x)*conj(vx)+pv*conj(diff(vx,
       x))+diff(pv,y)*conj(vy)+pv*conj(diff(vy,y)))',...
93     'Fx','rhow/2*real((vx*conj(diff(vx,x))+vy*conj(diff(vx,y)))+vx
       *(conj(diff(vx,x))+conj(diff(vy,y))))',...
94     'Fy','rhow/2*real((vx*conj(diff(vy,x))+vy*conj(diff(vy,y)))+vy
       *(conj(diff(vx,x))+conj(diff(vy,y))))', ...
95     'J2X','rhow*u2+1/(2*cw^2)*real(pv*conj(vx))',...
96     'J2Y','rhow*v2+1/(2*cw^2)*real(pv*conj(vy))',...
97     'p2analytFpart','-1/2*rhow*1/2*real((vx*conj(vx)+vy*conj(vy)))
       +1/(2*rhow*cw^2)*1/2*real((1+i*gammadamp)*pv*conj(pv))',...
98     'p2analytBpart','-(1+beta)*eta/(4*rhow*cw^4)*real(K*(2*diff(pv,
       x)*conj(diff(pv,x))+pv*conj(diff(diff(pv,x),x))+conj(pv)*
       diff(diff(pv,x),x)+2*diff(pv,y)*conj(diff(pv,y))+pv*conj(
       diff(diff(pv,y),y))+conj(pv)*diff(diff(pv,y),y)))',...
99     'p2analyt','p2analytFpart+p2analytBpart'};
100
101 % Multiphysics
102 fem=multiphysics(fem);
103
104 % Extend mesh
105 fem.xmesh=meshextend(fem);
106
107 % Solve problem
108 fem.sol=femstatic(fem, ...
109     'solcomp',{'v2','u2','p2'}, ...
110     'outcomp',{'v2','u2','p2'});
111
112 % Save current fem structure for restart purposes
113 fem0=fem;
114
115 if nargin==0
```

```
116     % Plot solution
117     figure
118     postplot(fem, ...
119         'tridata',{'real(pv)','cont','internal'}, ...
120         'trimap','jet(1024)', ...
121         'title','Surface: real of p');
122 end
```

Appendix N

Comsol: Second-order decomposed incompressible

Implementation of the time-averaged decomposed second-order continuity and Navier–Stokes equations Eqs. (5.3) and (5.33) with an analytical first-order input.

```
function SecondOrderSmallBodyForceAnalyticalInputIncomp(dummy)

%%% Implementation of second-order NS and continuity with small
    body force.
%%% The system is solved for v_2inc and p_2rep (which for
    notational ease is
%%% called (u2,v2) and p2). First-order quantities must comply with
     the
%%% restriction that the velocity can be expressed as gradient
    field. In
%%% this case we use the square chamber with walls vibrating in
    antiphase
%%% at resonance similar to the TGJ implementation. Implemented as
    function
%%% to be called by external script.
%%% MSc student Peder Skafte-Pedersen, TMF, DTU Nanotech, 2007.

% Prepare system by cleaning up
flclear fem
if nargin==0
clear all
PlotSave=0; % Boolean for saving plots
end
close all
clc

global fem
global etascale
if nargin==0
    etascale=1e0;
```

```
25 end
26
27 % Geometry
28 g2=rect2('2e-3','2e-3','base','center','pos',{'0','0'},'rot','0');
29
30 % Analyzed geometry
31 clear s
32 s.objs={g2};
33 s.name={'R1'};
34 s.tags={'g2'};
35
36 fem.draw=struct('s',s);
37 fem.geom=geomcsg(fem);
38
39 % Constants
40 fem.const = {'L','1e-3',...
41     'rhow','998.2', ...
42     'cw','1483', ...
43     'beta','5/3', ...
44     'eta',1e-3*etascale, ...
45     'omega','cw*n*pi/L', ...
46     'gamma','omega*(1+beta)*eta/(rhow*cw^2)', ...
47     'r','3',...
48     'n','3',...
49     'k','omega/(cw*sqrt(1-i*gamma))',...
50     'l','1e-13',...
51     'K','-i*omega/(rhow*k^2)'};
52
53 % Initialize mesh
54 fem.mesh=meshinit(fem, ...
55     'hmax',[3.5e-5]);
56
57 % (Default values are not included)
58
59 % Application mode 1, second-order NS & continuity
60 clear appl
61 appl.mode.class = 'FlPDEG';
62 appl.dim = {'u2','v2','p2','u2_t','v2_t','p2_t'};
63 appl.shape = {'shlag(2,''u2'')','shlag(2,''v2'')','shlag(1,''p2'')'
       };
64 appl.assignsuffix = '_g';
65 clear prop
66 clear weakconstr
67 weakconstr.value = 'off';
68 weakconstr.dim = {'lm2','lm3','lm4','lm5','lm6','lm7'};
69 prop.weakconstr = weakconstr;
70 appl.prop = prop;
71 clear bnd
72 bnd.r = {{'u2';'v2';'0'}}; % No-slip
```

```
73  bnd.ind = [1,1,1,1];
74  appl.bnd = bnd;
75  clear equ
76  equ.da = 0;
77  equ.f = {{'-BFx';'-BFy';'u2x+v2y'}};
78  equ.ga = {{{'gammaxx';'gammaxy'};{'gammayx';'gammayy'};{0;0}}};
79  equ.ind = [1];
80  appl.equ = equ;
81  fem.appl{1} = appl;
82  fem.frame = {'ref'};
83
84  % Global expressions, rhov=rho_viscous, vx=v_(1,x), vy=v_(1,y).
85
86  fem.globalexpr = {
87      'rhov','-i*rhow*k*omega*l/(omega*sin(k*L))*(cos(k*x)+r*cos(k*y)
        )',...
88      'vx','omega*l/sin(k*L)*sin(k*x)',...
89      'vy','r*omega*l/sin(k*L)*sin(k*y)',...
90      'gammaxx','-p2+eta*u2x', ...
91      'gammaxy','eta*u2y', ...
92      'gammayx','eta*v2x', ...
93      'gammayy','-p2+eta*v2y', ...
94      'BFx1','real(rhov)*imag(diff(rhov,x))-imag(rhov)*real(diff(rhov
        ,x))',...
95      'BFx2','real(rhov)*(imag(diff(diff(diff(rhov,x),x),x))+imag(
        diff(diff(diff(rhov,x),y),y)))+imag(diff(rhov,x))*(real(diff
        (diff(rhov,x),x))+real(diff(diff(rhov,y),y)))+2*(real(diff(
        rhov,x))*imag(diff(diff(rhov,x),x))+real(diff(rhov,y))*imag(
        diff(diff(rhov,x),y)))',...
96      'BFx3','imag(rhov)*(real(diff(diff(diff(rhov,x),x),x))+real(
        diff(diff(diff(rhov,x),y),y)))+real(diff(rhov,x))*(imag(diff
        (diff(rhov,x),x))+imag(diff(diff(rhov,y),y)))+2*(imag(diff(
        rhov,x))*real(diff(diff(rhov,x),x))+imag(diff(rhov,y))*real(
        diff(diff(rhov,x),y)))',...
97      'BFx','gamma*cw^2/(2*rhow)*BFx1-(eta*cw^2)/(2*rhow^2*omega)*(
        BFx2-BFx3)',...
98      'BFy1','real(rhov)*imag(diff(rhov,y))-imag(rhov)*real(diff(rhov
        ,y))',...
99      'BFy2','real(rhov)*(imag(diff(diff(diff(rhov,y),x),x))+imag(
        diff(diff(diff(rhov,y),y),y)))+imag(diff(rhov,y))*(real(diff
        (diff(rhov,x),x))+real(diff(diff(rhov,y),y)))+2*(real(diff(
        rhov,x))*imag(diff(diff(rhov,x),y))+real(diff(rhov,y))*imag(
        diff(diff(rhov,y),y)))',...
100     'BFy3','imag(rhov)*(real(diff(diff(diff(rhov,y),x),x))+real(
        diff(diff(diff(rhov,y),y),y)))+real(diff(rhov,y))*(imag(diff
        (diff(rhov,x),x))+imag(diff(diff(rhov,y),y)))+2*(imag(diff(
        rhov,x))*real(diff(diff(rhov,x),y))+imag(diff(rhov,y))*real(
        diff(diff(rhov,y),y)))',...
```

```
101     'BFy','gamma*cw^2/(2*rhow)*BFy1-(eta*cw^2)/(2*rhow^2*omega)*(
            BFy2-BFy3)',...
102     'rho1vx','-1/(2*rhow)*real(rhov*conj(vx))',...
103     'rho1vy','-1/(2*rhow)*real(rhov*conj(vy))',...
104     'p2full','p2-rhow/4*real(vx*conj(vx)+vy*conj(vy))+cw^2/(4*rhow)
            *real(rhov*conj(rhov))-beta*eta/(rhow*2)*real(conj(vx)*diff(
            rhov,x)+rhov*conj(diff(vx,x))+conj(vy)*diff(rhov,y)+rhov*
            conj(diff(vy,y)))+gamma*eta*cw^2/(4*rhow^2*omega)*(2*real(
            rhov)*real(diff(diff(rhov,x),x))+2*real(diff(rhov,x))^2+2*
            real(rhov)*real(diff(diff(rhov,y),y))+2*real(diff(rhov,y))
            ^2+2*imag(rhov)*imag(diff(diff(rhov,x),x))+2*imag(diff(rhov,
            x))^2+2*imag(rhov)*imag(diff(diff(rhov,y),y))+2*imag(diff(
            rhov,y))^2)',...
105     'u2full','u2+rho1vx',...
106     'v2full','v2+rho1vy'
107     };
108
109 % Multiphysics
110 fem=multiphysics(fem);
111
112 % Extend mesh
113 fem.xmesh=meshextend(fem);
114
115 % Solve problem
116 fem.sol=femstatic(fem, ...
117     'solcomp',{'v2','u2','p2'}, ...
118     'outcomp',{'v2','u2','p2'});
119
120 % Save current fem structure for restart purposes
121 fem0=fem;
122
123 if nargin==0
124 % Plot solution
125 figure
126 postplot(fem, ...
127     'tridata',{'real(rhov)','cont','internal'}, ...
128     'trimap','jet(1024)', ...
129     'title','Surface: real of rho_1');
130 end
```

Appendix O

Comsol: Second-order decomposed

Implementation of the time-averaged decomposed second-order continuity and Navier–Stokes equations Eqs. (2.86) and (5.39) with an analytical first-order input.

```
function SecondOrderSmallBodyForceAnalyticalInput(dummy)

%%% Implementation of second-order NS and continuity with small
    body force.
%%% The system is solved for v_2 and p_2rep (which for notational
    ease is
%%% called (u2,v2) and p2). First-order quantities must comply with
     the
%%% restriction that the velocity can be expressed as gradient
    field. In
%%% this case we use the square chamber with walls vibrating in
    antiphase
%%% at resonance similar to the TGJ implementation. Implemented as
    function
%%% to be called by external script.
%%% MSc student Peder Skafte-Pedersen, TMF, DTU Nanotech, 2007.

% Prepare system by cleaning up
flclear fem
if nargin==0
clear all
PlotSave=0; % Boolean for saving plots
end
close all, clc

global fem
global etascale
if nargin==0
    etascale=1e0;
end

% Geometry
```

```
27 g2=rect2('2e-3','2e-3','base','center','pos',{'0','0'},'rot','0');
28
29 % Analyzed geometry
30 clear s
31 s.objs={g2};
32 s.name={'R1'};
33 s.tags={'g2'};
34
35 fem.draw=struct('s',s);
36 fem.geom=geomcsg(fem);
37
38 % Constants
39 fem.const = {'L','1e-3',...
40     'rhow','998.2', ...
41     'cw','1483', ...
42     'beta','5/3', ...
43     'eta',1e-3*etascale, ...
44     'omega','cw*n*pi/L', ...
45     'gamma','omega*(1+beta)*eta/(rhow*cw^2)', ...
46     'r','3',...
47     'n','3',...
48     'k','omega/(cw*sqrt(1-i*gamma))',...
49     'l','1e-13',...
50     'K','-i*omega/(rhow*k^2)'};
51
52 % Initialize mesh
53 fem.mesh=meshinit(fem, ...
54     'hmax',[3.5e-5]);
55
56 % Application mode 1, second-order NS & continuity
57 clear appl
58 appl.mode.class = 'FlPDEG';
59 appl.dim = {'u2','v2','p2','u2_t','v2_t','p2_t'};
60 appl.shape = {'shlag(2,''u2'')','shlag(2,''v2'')','shlag(1,''p2'')'
      };
61 appl.assignsuffix = '_g';
62 clear prop
63 clear weakconstr
64 weakconstr.value = 'off';
65 weakconstr.dim = {'lm2','lm3','lm4','lm5','lm6','lm7'};
66 prop.weakconstr = weakconstr;
67 appl.prop = prop;
68 clear bnd
69 bnd.r = {{'J2X';'J2Y';'0'}}; % No-slip
70 bnd.ind = [1,1,1,1];
71 appl.bnd = bnd;
72 clear equ
73 equ.da = 0;
74 equ.f = {{'-Fx';'-Fy';'u2x+v2y-S'}};
```

```
75 equ.ga = {{{'gammaxx';'gammaxy'};{'gammayx';'gammayy'};{0;0}}};
76 equ.ind = [1];
77 appl.equ = equ;
78 fem.appl{1} = appl;
79 fem.frame = {'ref'};
80 % Global expressions (No Taylor expanded first-order - i.e. exact
       with slip condition)
81 fem.globalexpr = {
82     'rhov','-i*rhow*k*omega*l/(omega*sin(k*L))*(cos(k*x)+r*cos(k*y)
          )',...
83     'vx','omega*l/sin(k*L)*sin(k*x)',...
84     'vy','r*omega*l/sin(k*L)*sin(k*y)',...
85     'gammaxx','-p2+eta*(1+beta)*u2x' ...
86     'gammaxy','eta*u2y+beta*eta*v2x' ...
87     'gammayx','eta*v2x+beta*eta*u2y' ...
88     'gammayy','-p2+eta*(1+beta)*v2y', ...
89     'S','-1/(2*rhow)*real(diff(rhov,x)*conj(vx)+rhov*conj(diff(vx,x
          ))+diff(rhov,y)*conj(vy)+rhov*conj(diff(vy,y)))',...
90     'Fx','gamma*cw^2/(2*rhow)*(real(rhov)*imag(diff(rhov,x))-imag(
          rhov)*real(diff(rhov,x)))',...
91     'Fy','gamma*cw^2/(2*rhow)*(real(rhov)*imag(diff(rhov,y))-imag(
          rhov)*real(diff(rhov,y)))',...
92     'J2X','rhow*u2+1/(2)*real(rhov*conj(vx))',...
93     'J2Y','rhow*v2+1/(2)*real(rhov*conj(vy))',...
94     'rhovx','-1/(2*rhow)*real(rhov*conj(vx))',...
95     'rhovy','-1/(2*rhow)*real(rhov*conj(vy))',...
96     'p2full','p2-rhow/4*real(vx*conj(vx)+vy*conj(vy))+cw^2/(4*rhow)
          *real(rhov*conj(rhov))'
97      };
98
99 % Multiphysics
100 fem=multiphysics(fem);
101
102 % Extend mesh
103 fem.xmesh=meshextend(fem);
104
105 % Solve problem
106 fem.sol=femstatic(fem, ...
107     'solcomp',{'v2','u2','p2'}, ...
108     'outcomp',{'v2','u2','p2'});
109
110 % Save current fem structure for restart purposes
111 fem0=fem;
112
113 if nargin==0
114 % Plot solution
115 figure
116 postplot(fem, ...
117     'tridata',{'real(rhov)','cont','internal'}, ...
```

```
118     'trimap','jet(1024)', ...
119     'title','Surface: real of rho_1');
120 end
```

Bibliography

[1] S. M. Hagsäter, T. Glasdam Jensen, H. Bruus, and J. P. Kutter. Acoustic resonances in microfluidic chips: full-image micro-PIV experiments and numerical simulations. *Lab on a Chip*, 7(10):1336–1344, 2007.

[2] S. M. Hagsäter, A. Lenshof, P. Skafte-Pedersen, J.P. Kutter, T. Laurell, and H. Bruus. Acoustic resonances in straight microchannels: Beyond the 1D-approximation. *Lab on a Chip*, 2008. Submitted.

[3] I. Gitlin, A. D. Stroock, G. M. Whitesides, and A. Ajdari. Pumping based on transverse electrokinetic effects. *Appl. Phys. Lett.*, 83:1486, 2003.

[4] Ok Chan Jeong and S. Konishi. Fabrication and drive test of pneumatic PDMS micro pump. *Sensors and Actuators A (Physical)*, 135(2):849–56, 2007.

[5] Nam-Trung Nguyen and Zhigang Wu. Micromixers—a review. *Journal of Micromechanics and Microengineering*, 15(2):R1–R16, 2005.

[6] M. Faraday. On a Peculiar Class of Acoustical Figures; and on Certain Forms Assumed by Groups of Particles upon Vibrating Elastic Surfaces. *Philosophical Transactions of the Royal Society of London*, 121:299–340, 1831.

[7] L. Rayleigh. On the Circulation of Air Observed in Kundt's Tubes, and on Some Allied Acoustical Problems. *Philosophical Transactions Series I*, 175:1–21, 1884.

[8] Louis V. King. On the Acoustic Radiation Pressure on Spheres. *Proceedings of the Royal Society of London. Series A, Mathematical and Physical Sciences*, Vol. 147, No. 861:212–240, Nov. 15, 1934.

[9] Carl Eckart. Vortices and Streams Caused by Sound Waves. *Phys. Rev.*, 73(1):68–76, Jan 1948.

[10] J.J. Markham, Robert T. Beyer, and R. B. Lindsay. Absorption of Sound in Fluids. *Reviews of Modern Physics*, 23(4):353–411, 1951.

[11] J.J. Markham. Second-Order Acoustic Fields: Streaming with Viscosity and Relaxation. *Physical Review*, 86(4):497–502, 1952.

[12] J.J. Markham. Second-Order Acoustic Fields: Energy Relations. *Physical Review*, 86(5):712–714, 1952.

[13] J.J. Markham. Second-Order Acoustic Fields: Relations Between Density and Pressure. *Physical Review*, 86(5):710–711, 1952.

[14] J.J. Markham. Second-Order Acoustic Fields: Relations between Energy and Intensity. *Physical Review*, 89(5):972–977, 1953.

[15] W. L. Nyborg. Acoustic streaming due to attenuated plane waves. *Journal of the Acoustical Society of America*, 25:68–75, 1953.

[16] W. L. Nyborg. Acoustic streaming equations: laws of rotational motion for fluid elements. *Acoustical Society of America – Journal*, 25(5):938–944, 1953.

[17] W. L. Nyborg. Acoustic streaming near a boundary. *Journal of the Acoustical Society of America*, 30(4):329–339, 1958.

[18] W. L. Nyborg. Radiation pressure on a small rigid sphere. *Journal of the Acoustical Society of America*, 42(5):947–952, 1967.

[19] K. Yosioka and Y. Kawasima. Acoustic radiation pressure on a compressible sphere. *Acustica*, 5(3):167–173, 1955.

[20] Hongyu Yu and Eun Sok Kim. Noninvasive acoustic-wave microfluidic driver. In *Proc. Fifteenth IEEE International Conference on Micro Electro Mechanical Systems*, pages 125–128, 2002.

[21] Zhen Yang, Sohei Matsumoto, Hiroshi Goto, Mikio Matsumoto, and Ryutaro Maeda. Ultrasonic micromixer for microfluidic systems. *Sensors and Actuators A: Physical*, 93(3):266–272, 2001.

[22] Martin Bengtsson and Thomas Laurell. Ultrasonic agitation in microchannels. *Analytical and Bioanalytical Chemistry*, 378(7):1716–1721, 2004.

[23] Ling-Sheng Jang, Shih-Hui Chao, Mark R. Holl, and Deirdre R. Meldrum. Resonant mode-hopping micromixing. *Sensors and Actuators A: Physical*, 138(1):179–186, 2007.

[24] H. Jagannathan, G.G. Yaralioglu, A.S. Ergun, and B.T. Khuri-Yakub. Acoustic heating and thermometry in microfluidic channels. In *Proc. MEMS-03 Kyoto Micro Electro Mechanical Systems IEEE The Sixteenth Annual International Conference on*, pages 474–477, 2003.

[25] Tobias Lilliehorn, Urban Simu, Mikael Nilsson, Monica Almqvist, Tadeusz Stepinski, Thomas Laurell, Johan Nilsson, and Stefan Johansson. Trapping of microparticles in the near field of an ultrasonic transducer. *Ultrasonics*, 43(5):293–303, 2005.

[26] T. Kozuka, T. Tuziuti, H. Mitome, and T. Fukuda. Non-contact micromanipulation using an ultrasonic standing wave field. In *Proc. 'An Investigation of Micro Structures, Sensors, Actuators, Machines and Systems'. IEEE The Ninth Annual International Workshop on Micro Electro Mechanical Systems, MEMS '96*, pages 435–440, 11–15 Feb. 1996.

[27] Yoshiki Yamakoshi and Yuji Noguchi. Micro particle trapping by opposite phases ultrasonic travelling waves. *Ultrasonics*, 36(8):873–878, 1998.

[28] Andreas Nilsson, Filip Petersson, Henrik Jönsson, and Thomas Laurell. Acoustic control of suspended particles in micro fluidic chips. *Lab on a Chip*, 4(2):131–135, 2004.

[29] Filip Petersson, Andreas Nilsson, Cecilia Holm, Henrik Jonsson, and Thomas Laurell. Continuous separation of lipid particles from erythrocytes by means of laminar flow and acoustic standing wave forces. *Lab on a Chip*, 5(1):20–22, 2005.

[30] J. Hultström, O. Manneberg, K. Dopf, H.M. Hertz, H. Brismar, and M. Wiklund. Proliferation and viability of adherent cells manipulated by standing-wave ultrasound in a microfluidic chip. *Ultrasound in Medicine & Biology*, 33(1):145–151, 2007.

[31] Filip Petersson, Andreas Nilsson, Cecilia Holm, Henrik Jönsson, and Thomas Laurell. Separation of lipids from blood utilizing ultrasonic standing waves in microfluidic channels. *The Analyst*, 129(10):938–943, 2004.

[32] Thomas Glasdam Jensen. Acoustic radiation in microfluidic systems. Master's thesis, MIC — Department of Micro and Nanotechnology, DTU — Technical University of Denmark, April 2007.

[33] Henrik Bruus. *Theoretical Microfluidics*. Oxford Master Series in Physics number 18. Oxford University Press, 2008. ISBN 978–0–19–923508–7.

[34] L.N. Liebermann. The second viscosity of liquids. *Physical Review*, 75:1415–1422, 1949.

[35] Lawrence E. Kinsler, Austin R. Frey, Alan B. Coppens, and James V. Sanders. *Fundamentals of Acoustics*. John Wiley & Sons, Inc., fourth edition, 2000. ISBN 978-0471-84789-2.

[36] Finn Jacobsen and Jean-Dominique Polack. An elementary introduction to acoustics. Printed at Acoustic Technology, Ørsted•DTU, Technical University of Denmark, August 2003. Note no 0112.

[37] FERROPERM PIEZOCERAMICS A/S. High quality components and materials for the electronic industry. www.ferroperm-piezo.com, May 2003. Full Catalogue, pdf.

[38] J.F. Spengler, M. Jekel, K.T. Christensen, R.J. Adrian, J.J. Hawkes, and W.T. Coakley. Observation of yeast cell movement and aggregation in a small-scale MHz-ultrasonic standing wave field. *Bioseparation*, 9(6):329–341, 2001.

[39] L.D. Landau and E.M. Lifshitz. *Fluid Mechanics*, volume 6 of *Course of Theoretical Physics*. Butterworth-Heinemann, second edition, 2006. ISBN 0-7506-2767.

[40] CRCnetBASE Product, Copyrigth© 2007 Taylor and Francis Group, LLC. CRC Handbook of Chemistry and Physics, 88th edition. Online version, accessed through DTV: Technical Knowledge Center of Denmark, http://www.hbcponline.com.globalproxy.cvt.dk/, 2007.

[41] L. V. King. On the Acoustic Radiation Pressure on Circular Discs: Inertia and Diffraction Corrections. *Royal Society of London Proceedings Series A*, 153:1–16, December 1935.

[42] T. Hasegawa, T. Kido, T. Iizuka, and C. Matsuoka. A general theory of Rayleigh and Langevin radiation pressures. *Journal of the Acoustical Society of Japan (E)*, 21(3):145–52, 2000.

[43] T. Hasegawa, Y. Hino, A. Annou, H. Noda, M. Kato, and N. Inoue. Acoustic radiation pressure acting on spherical and cylindrical shells. *Journal of the Acoustical Society of America*, 93(1):154–61, 1993.

[44] Frank M. White. *Viscous Fluid Flow*. McGraw-Hill, third edition, international edition, 2006. ISBN 007-124493-X.

[45] Jeremy J. Hawkes and W. Terence Coakley. Force field particle filter, combining ultrasound standing waves and laminar flow. *Sensors and Actuators B: Chemical*, 75(3):213–222, 2001.

[46] Susan M. Lea. *Mathematics for Physicists*. Brooks/Cole—Thomson Learning, 2004. ISBN 0-534-37997-4.

[47] James J. Jr. Faran. Sound Scattering by Solid Cylinders and Spheres. *The Journal of the Acoustical Society of America*, 23(4):405–418, 1951.

[48] Gunnar Christiansen, Erik Both, and Preben Østergaard Sørensen. *Mekanik*. Institut for Fysik, Danmarks Tekniske Universitet, 2000. ISBN 87-87669-18-8.

[49] L. P. Gor'kov. On the Forces Acting on a Small Particle in an Acoustical Field in an Ideal Fluid. *Soviet Physics Doklady*, 6:773–775, March 1962.

[50] P. J. Westervelt. The Theory of Steady Forces Caused by Sound Waves. *The Journal of the Acoustical Society of America*, 23(4):312–315, 1951.

[51] A.A. Doinikov. Acoustic radiation pressure on a rigid sphere in a viscous fluid. *Proceedings of the Royal Society of London, Series A (Mathematical and Physical Sciences)*, 447(1931):447–66, 1994.

[52] A.A. Doinikov. Radiation force due to a spherical sound field on a rigid sphere in a viscous fluid. *Journal of the Acoustical Society of America*, 96(5):3100–5, 1994.

[53] A.A. Doinikov. Theory of acoustic radiation pressure for actual fluids. *Physical Review E (Statistical Physics, Plasmas, Fluids, and Related Interdisciplinary Topics)*, 54(6):6297–303, 1996.

[54] Lawrence A. Crum. Bjerknes forces on bubbles in a stationary sound field. *J Acoust Soc Am*, 57(6):1363–1370, 1975.

[55] Filip Petersson. *On acoustic particle and cell manipulation in microfluidic systems.* PhD thesis, Department of Electrical Measurements, Lund Insitute of Technology, Lund University, May 2007.

[56] COMSOL AB. *COMSOL Multiphysics Modeling Guide*, August 2006. Version 3.3.

[57] COMSOL AB. *COMSOL Multiphysics User's Guide*, August 2006. Version 3.3.

[58] CRCnetBASE Product, Copyrigth© 2007 Taylor and Francis Group, LLC. Polymers: A property database. Online version, accessed through DTV: Technical Knowledge Center of Denmark, http://www.polymersdatabase.com.globalproxy.cvt.dk/, 2007.

[59] Arkema Orgasol© Powders. http://www.arkema-inc.com/index.cfm?pag=103, Orgasol© data brochure: http://www.arkema-inc.com/literature/pdf/197.pdf.

[60] Malika Toubal, Mohamed Asmani, Edouard Radziszewski, and Bertrand Nongaillard. Acoustic measurement of compressibility and thermal expansion coefficient of erythrocytes. *Physics in Medicine and Biology*, 44(5):1277–1287, 1999.

[61] Dansk Fantom Service. Homepage: http://www.fantom.suite.dk/home.html, Data for EU-DFS-BMF-ver.1: http://www.fantom.suite.dk/eu_bmf.htm.

[62] R.J. Townsend, M. Hill, N.R. Harris, and N.M. White. Modelling of particle paths passing through an ultrasonic standing wave. *Ultrasonics*, 42(1-9):319–324, 2004.

[63] R.J. Townsend, M. Hill, N.R. Harris, N.M. White, and S.P. Beeby. Numerical modelling of a microfluidic ultrasonic particle separator. *2005 NSTI Nanotechnology Conference and Trade Show. NSTI Nanotech 2005*, 1:194–7, 2005.

[64] I. Tuval, I. Mezic, F. Bottausci, Y.T. Zhang, N.C. MacDonald, and O. Piro. Control of particles in microelectrode devices. *Physical Review Letters*, 95(23):236002/1–4, 2005.